UNIVERSITÀ
DEGLI STUDI
FIRENZE

DOTTORATO DI RICERCA IN
SCIENZE CHIMICHE

CICLO XXVIII

COORDINATORE Prof. Andrea Goti

Single Molecule Magnets form an ab initio point of view: from single molecules to the adsorption on surfaces

Settore Scientifico Disciplinare CHIM/03

Dottorando:
Dott. Alessandro Lunghi

Tutore:
Dott. Federico Totti

Coordinatore:
Prof. Andrea Goti

Anni 2012/2015

Omettendo un numero arbitrario di fatti
si può dimostrare tutto.

List of Papers:

- "DFT Magnetic Characterization of a Fe_4 SMMs Series: From Isotropic Exchange Interactions to Multi-Spin Zero Field Splitting.", A. Lunghi and F. Totti, J. Mater. Chem. C, 2014, 2, 8333-8343.
- "Single Molecule Magnets Grafted on Gold: Evolution of Magnetic Properties From Ab Initio Molecular Dynamics.", A. Lunghi, MI Mauri, R. Sessoli and F. Totti, J. Mater. Chem. C, 2015, 2, 7294-7304.
- "Reduction of Spin Reversal Barrier in Single Molecule Magnets Through Thermal Bath Fluctuations." A. Lunghi, R. Sessoli, F. Totti and S. Sanvito, In preparation.
- "Spin-Phonon Relaxation Through Intra-Molecular Spin-Orbit Coupling Modulation." A. Lunghi, R. Sessoli, F. Totti and S. Sanvito, In preparation.
- "Tuning Isotropic Exchange Coupling Interactions Inside Single Molecule Magnets on Gold with Ion Dependent Metal Screening." A. Lunghi, R. Sessoli and F. Totti, In preparation.
- "Toward Mesoscale Properties of Self Assembled Monolayers of Single Molecule Magnets: development of an *ad hoc* force field and its DFT validation" G. Fernandez Garcia, A. Lunghi, R. Sessoli and F. Totti, In preparation.
- "Two Dimensional Crystals of SMMs: Packing Effects on Magnetism." G. Fernandez Garcia, A. Lunghi, R. Sessoli and F. Totti, In preparation.

Papers not included into the thesis:

- "cis-Pt $I_2(NH_3)_2$: a reappraisal." T. Marzo, S. Pillozzi, O. Hrabina, J. Kasparkova, V. Babrec, A. Arcangeli, G. Bartoli, M. Severi, A. Lunghi, F. Totti, C. Gabbiani, A.G. Quiroga, L. Messori, Dalton Trans., 2015, 44, 14896-14905.

Acknowledgments: I would like to thank all the staff of the LAboratory of Molecular Magnetism (LAMM), Prof. Roberta Sessoli, Prof. Lorenzo Sorace, Prof. Gianni Cardini and Prof. Roberto Righini for their constant help and for inspiring me with fruitful conversations. I also would like to thank Prof. Andrea Cornia and Dott. Erick Tancini for providing me experimental data to support my calculations. A special appreciation is due to Prof. Stefano Sanvito and its research group for giving me the opportunity to be their host at the Trinity College in Dublin. A very grateful thank is due to Dott. Guglielmo Fernandez Grarcia for developing with me all the results discussed in section 4.3. I thank the INSTM for funding my Ph.D. scholarship, European Research Council for funding through the Advanced Grant MolNanoMaS (no. 267746), Italian MIUR for support through FIRB project *Nanomagneti molecolari su superfici metalliche e magnetiche per applicazioni nella spintronica molecolare* (RBAP117RWN), and the CINECA awards under PRACE and ISCRA initiatives, for the availability of high performance computing resources and support ("DySMoMAu" and "SMMICroG" projects).

Abstract

At present, the possibility to employ Single Molecule Magnets (SMMs) properties in real technological devices is still a challenge. In order to reach this target a significant extension of their spin life-time and a rational tuning of their properties on demand is mandatory. In this Ph.D. thesis a comprehensive theoretical and computational assessment of the main open questions related to the microscopic quantum origins of SMMs properties has been done together with the development of an ab initio protocol based on both DFT and post HF schemes able to describe SMMs electronic structure in any sort of chemical environment. The multi-spin origin of the ground state in polynuclear SMMs has been discussed and the several involved spin terms assessed. A fundamental extension of spin relaxation theory has been developed in order to account for the real complexity of the spin environment made by phonons and other SMMs spins. Spin relaxation phenomena have been addressed tracking down the origin of the spin-flip effective barrier reduction, observed experimentally and never interpreted before. The determination of the main contribution of molecular internal degrees of freedom at the origin of spin relaxation has also been pointed out for the first time, paving the ground for a rational design of molecular structures to extend relaxation time-scales. Finally, the issues related to the conservation of SMMs properties once adsorbed on a metallic substrate have also been addressed. A combination of different computational schemes made possible to highlight the striking importance of electronic and structural rearrangements of SMMs once deposited. This effect, largely underestimated in literature, has been observed both for what concerns substrate/SMM and SMM/SMM interactions, demonstrating, for instance, the possibility to modulate the molecular orientation playing with the SMMs organic scaffold degrees of freedom.

Contents

Chapter 1

Introduction

Single molecule magnets (SMMs) are a class of molecular compounds which experience a slow relaxation rate of their magnetization vector.

The first evidence of a blocking temperature under which the orientation of a spin vector carried by a molecule shows a slow relaxation was obtained for the crystal of a mixed valence Mn_{12} cluster at the temperature (T) of 2 K[1]. The possibility to observe an hysteresis curve of molecular origin has been a fundamental discovery which paved the ground for a new research field with potential high impact applications in a large context of technological aree. The interest in SMMs spin dynamics lies in the origin of the phenomenon itself more than in its magnitude, as numerous magnetic materials with blocking temperatures well above a few K have been known by centuries. Classical magnets show their magnetic behavior in virtue of a phase transition which grants them a stable magnetic ground state, because of a long range correlation between spins composing the material, while magneto-crystalline anisotropy provides to their macroscopic magnetic moment a preferential direction in space. In SMMs, the same effect is basically reproduced on molecular scale but considering that the long range cooperative effect is excluded by the small number of paramagnetic ions involved, the long term magnetization is completely due to inherent molecular magnetic properties. Indeed, each molecule inside the crystal has an $S \neq 0$ ground state which behaves like an isolated magnetic moment ($\vec{\mathbf{M}}$), almost completely uncorrelated from those of other molecules, and nevertheless able to retain its direction in space thanks to the molecular easy axis kind of magnetic anisotropy. This class of systems

is generally composed by single or polynuclear transition metal clusters and recently it has been extended to lanthanides based molecules[2–4]. The microscopic origin of the axial magnetic anisotropy, which confers to SMMs their properties, is due by the presence of a strong spin-orbit coupling interaction felt by the unpaired electrons generating the global $S \neq 0$ ground state. The spin orbit coupling correlates the almost vanishing angular momenta of transition metals to the spin variables, whom will experience a non homogeneous angular potential energy bias. Therefore, the S ground state multiplet degeneracy is split with respect to the projection along the z quantization axis, which is labeled by S_z eigenvalues M_S. The easy axis anisotropy stabilizes M_s components according to fig. 1.1.

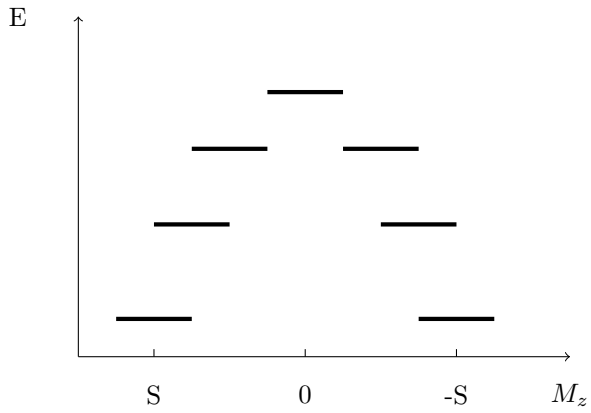

Figure 1.1: Horizontal black lines show the energy ladder of the spin states. The S_z expectation values are intended to be calculated for a molecule orientated with its easy axis along the z quantization axis.

Usually, the spin levels energy ladder is pictorially described as a double well potential energy surface function of the axial components of the ground state S_z operator. Clearly, the double well potential energy surface is only a classical analogy valid for huge values of magnetic moment (classical limit) and for typical small S the molecular states should be treated in a quantum theory framework. Loosely speaking, at finite T the two opposite spin polarizations would be statistically almost equivalently populated and the SMM would not show any residual magnetic moment. When driven out of equilibrium, *e.g.* by an external applied field, the SMM would show its spin magnetic properties due to the the unbalanced spin population of the two wells As for their classical bulk magnets counterpart, an easy axis magnetic anisotropy would tend to retain such polarized configuration where the magnetization vector lies

along the easy axis direction but, on the other hand, in the case of molecular magnets, the cooperativity between different spins is absent and the time scales needed to recover the equilibrium configuration with $\vec{\mathbf{M}} = 0$ become very short. However, besides this drawback, SMMs make possible to probe properties of pure molecular origin and due to this feature interesting effects not obtainable with common magnets become available. The combination of low dimensionality and extremely reduced sizes prompt these compounds at the center of an extremely multidisciplinary investigation with roots in material science, physics and, obviously, chemistry. Indeed, single molecule magnets give the unique chance to study spin related quantum effects in well-controlled systems, where synthetic chemistry can play a designing role and where the strengths of the various interactions can be monitored and tuned. For instance, in the context of the nano-revolution recently experienced by material science, SMMs represent a very promising alternative to the zero dimensional quantum dots usually built by metastable and not easily controlled entities like nanoparticles or magnetic impurities inside bulk hosts. The implementation of SMMs as nanomagnets for high-density information storage is their most intuitive application, making possible to shrink a bit size of orders of magnitudes with an increase in hard drive capabilities of at least by a factor of 100[5]. More exotic applications are also possible due to the quantum nature of the molecular spin. Indeed, the possibility to observe superposition of SMM eigenstates makes possible the use of SMMs as logic elements for quantum computing[6, 7]. So far, the proposition of algorithms able to exploit the manifold of the ground state spin level has been reported and big efforts to push spin relaxation time scale forward have been done, in order to match those required by practical applications.[8–12] Recently, a very promising emerging technological field has been taking place: spintronics[13]. This discipline, already used to built currently available M-RAM devices, exploits spin property of conducting electrons as an additional degree of freedom to carry information together with charge. Among the many success in this field, the most important one is due to the observation of the giant magnetoresistance effect, which granted the Nobel prize to Fert and Grünberg in 2007[14]. Another interesting advantage of using spins as information carriers is represented by the important reduction of devices energy loss and temperature increase they provide, as it represent one of the actual limits in the building of logical devices. The introduction of organic molecules in place of bulk materials in spintronic devices would represent a fundamental step forward for this discipline thanks to both the high synthetic versatility of molecules and their low cost, compared to magnetic metals and oxides[15, 16]. In this framework, the combination of the rich quantum behavior of SMMs and spintronic technologies represent an interesting evolution of

both these fields, which might also bring to the observation of new interesting effects over those already characterized[17].

However, to be implemented in real devices, a significant amount of work on SMMs is still needed. Among the many open research directions offered by the SMMs world the three most important field of debates are

I Origin of SMMs static magnetic properties;

II Origin of SMMs dynamical and transient properties;

III Implementation of SMMs in real devices.

The first two aree address the fundamental problem of understanding the origin of the SMMs behavior and are propaedeutic for all the aforementioned applications. Indeed, only a deep knowledge of the microscopic origin of SMMs properties would make possible a chemical tailoring strategy to tune their properties to the desired level. As already pointed out, the low dimensionality of SMMs grants them their fascinating properties but at the same time they experience the drawback of not being permanent magnets. Indeed, their magnetic properties are inherently transient and originates by a non-equilibrium spin dynamics. Their implementation in real devices, therefore, requires that a significant extension of their magnetization life-time should be achieved. In order to tackle such problem the understanding of the quantum origin of magnetism in molecular compounds is a mandatory step. Big efforts have devoted to this task in recent years, from both experimental and theoretical sides, with a great success for what concerns single ion molecular magnets. However, the description of polynuclear SMMs is still under debates and some uncertainty are still present, especially for what concerns those more elusive properties such, for example, the anisotropic exchange coupling inside transition metal polynuclear clusters. Although the study of static magnetic properties of SMMs is the most investigated aspect among the three introduced above, its consequences on spin dynamics properties are not yet well understood. One of the limiting factor in this field is represented by the lacking of theoretical models able to explain unambiguously the microscopic origin of the relaxation and consequently a certain amount of serendipity is still present in the designing process of new SMMs. The acquisition of a deeper knowledge in this field would be expected to dramatically push forward the possibility to engineer molecular structures to create more efficient SMMs. In view of their implementation on real devices, another set of problems must be addressed. For instance, in order to exploit single molecule magnets as I/O units a probing of their local properties must be fulfilled and in order to do that they need do to be deposited on a solid support *i.e.* surfaces. The possibility to

realize such a process has been recently provided but, however, a numerous amount of open questions arose. The most important one concerns the ability of SMMs to retain their properties once deposited on a substrate as both failing and successful adsorption attempts have been reported. Passing from a crystalline environment to an adsorbed scenario both structural and electronic properties of molecules could be affected with dramatic effects on their magnetism. However, the complexity of the processes involved do not make their assessment an easy task and even employing multiple experimental techniques many of them remain unsolved issues. Moreover, as observed for simple molecular system like phthalocyanines and porphyrins, the formation of an interface between the substrate and the molecular layer might introduce new features to this aggregate adding new properties not observable in the two components separately. The possibility to tune molecular properties through the interplay with substrates represent a very interesting playground which has been only slightly investigated for SMMs because of their complexity. However, recently, SMMs robust enough to retain their basic magnetic properties once adsorbed have been synthesized opening the possibility to employ the so called surface-magnetochemistry principles also in this field.

Although experimental investigations in these fields are intensively operative and their state of the art is constantly pushed forward, the theoretical side of their description is still in its early stages. Especially the possibility to include SMMs description in a solid ab initio computational framework has been made possible only in the last few years thanks to an extensive work on the specialization of density functional theory (DFT) and post Hatree Fock (postHF) methods to the calculation of magnetic properties[18, 19]. The possibility to model the complexity of SMMs accounting for important information obtained by first principle calculations is expected to dramatically improve the understanding of SMMs world and offers the unique chance to rationalize experimental findings and to give fundamental support to study elusive properties. In this thesis a comprehensive analysis of the aforementioned themes (I-II-III) will be provided. In chapter number 2 the research area I will be addressed. The description of the spin hamiltonian formalism will be introduced and its ab initio determination in the context of polynuclear transition metal SMMs will be investigated. The contents of this chapter will be propaedeutic for all the subsequent chapters. Topic related to the research area II will be addressed in the chapter 3, where the basic quantum theory of the spin relaxation will be revisited and extended to molecular crystal of SMMs. Concluding, in the chapter 4 results related to deposited SMMs issues (III) will be presented. As a final comment, the addressing of all the themes I-II-III in the same work also offers the possibility to investigate the

SMMs behavior from different point of views, usually addressed by different research communities with different backgrounds and methods of choice. An attempt to find a middle ground for a comprehensive discussion of all the different SMMs properties has been done and in order to reach such a goal a multidisciplinary approach has been exploited using different levels of theory for different tasks and at the same time trying to unify them under the same formalism. For instance, electronic structure modeling methods, well grounded in the computational chemists community, have been used together with stochastic approaches for the spin relaxation theory, which is usually more investigated by physicists community by means of classical statistical mechanics. Similarly, methods, like molecular dynamics, usually employed to study soft matter properties, have here been exploited to address typical surface science problems. In this respect, this project is intrinsically multidisciplinary also in its methodological contents. Indeed, different theoretical grounds, usually confined in their specific range of applicability will be here used together in order to get a balanced description of all the interactions involved, accordingly to the needed level of accuracy and to the problem size. A specific effort has been devoted to the tune of available computational schemes in order to make possible a realistic modeling of SMMs and their environment complexity, which necessarily requests large simulation cells, without scarifying the accuracy of the numerical methods. For instance a description of electronic structure by mean of density function theory (DFT) has been preferred to more expensive post-Hartree Fock (post-HF) schemes where the modeling of the SMMs surrounding has been necessary, while post-HF schemes have been preferred for isolated molecules made by only one paramagnetic ion. The same attention has been devoted to the choice of structural optimization schemes, selecting ab initio ones for system under 1000 atom per unit cell while employing a force field parametrization to extent size scales to tens of nm and time scales to ns.

Chapter 2

Polynuclear SSM Crystals

Contents

SMMs have been mostly investigated in their molecular crystalline phase and therefore the study of their bulk properties represents the natural starting point for the discussion before moving to more complex and exotic scenario. The access to high quality structural parameters provided by X-ray techniques makes possible to create detailed magneto structural correlations, which have been proved to be an unique tool for the rationalization of magnetic effects in molecular compounds. So far, although a comprehensive characterization of static magnetic properties of mononuclear SMMs has been done, a corresponding amount of work about multi ion transition metal clusters is still lacking and a few pieces for a complete and exhaustive description of their magnetic properties are still missing. The inherent complexity of these systems

is mainly due to the multiple interactions occurring inside their magnetic core, which elusively mix all together to create the observable global magnetic behavior, whose interpretation is an exceptional challenge for both experimental and theoretical sciences. From a practical point of view, the need to shed some lights on multi ion transition metal complexes comes from the appreciation that in order to enhance the effective spin reversal barrier a high level of molecular engineering is required and without a quite accurate chemical design of single ion environment and cluster structure, it is not possible to sum up several anisotropy contributions without observing cancellation effects. The case of the Mn_{19} cluster[20] is just a dramatic example. In this framework the need to understand and to predict how the single ion contributions sum[21] and how much the interaction between different spin centers can contribute to the final anisotropy value becomes crucial. In order to tackle this problem, a synergy between computational sciences and experimental investigations must be established. In this framework, the interaction between the experimental and theoretical sides requires the determination of a common playground where these two distinct worlds can interact. The spin hamiltonian formalism can represent such an opportunity since it has always been the basic tool for magnetic phenomena interpretation and big efforts are continuously devoted to the interpretation and determination of its parameters. For this reason, section 2.1 of this chapter will be entirely devoted to the description of its theoretical foundations and will be preparatory for all the following discussions. Indeed, all the results that will be displayed in the rest of this thesis will be always presented through this formalism in order to be readily comparable with the available liteature. The whole SMMs research is totally hinged on this formalism and in sections 2.2 and 2.3 the state of the art of its connection to the computational machinery of DFT and post-HF approaches will be outlined. Sections 2.4, 2.5, 2.6 and 2.7 will then be devoted to the application of these tools to specific multi ion complexes. Waldmann theoretically showed[22] that the spin flip energy barrier value does not sensitively depends on the ground state S value and on lights of this, ferrimagnetic systems represent the most popular and studied SMMs. The family of helical pitch complexes, also called ferric star complexes, will be at the center of this investigation due to the extensive characterization already available in literature and, starting from these results, an extensive characterization of their magnetic properties will be developed in order to fill the gaps still present in their description. This class of SMMs represent the perfect benchmark systems for the purpose of extending the knowledge on multi ion complexes without totally leaving the safe shore of experimental evidences. Indeed, the study of these SMM crystals has an additional propaedeutic value with respect to the intrinsic interest in their properties. The possibility to access, at least partially,

to reliable structural and magnetic experimental information makes possible to finely tune the computational techniques which will be also exploited in the next two chapters where the complexity of the task to be accomplished will be much more harder and little help from existing results will be available. The main challenge represented by this class of system is that the only experimental observable is the ground state anisotropy which hides into itself all the multi-spin structure of the zero field splitting. Many experimental strategies have been attempted to solve this puzzling situation. For instance, in the context of helical pitch SMMs, partial diamagnetic substitution of metallic ions and the chemical modulation of magnetic properties due to organic scaffold modifications have been the basic tools exploited to get information about the magneto structural correlations ruling these SMMs behavior.[23, 24] However, because of the large number of parameters required to completely specify the multi spin magnetic structure of these complexes, the real weight of some interactions inside the metallic core and their origin remain unknown. In section 2.4 will be presented the application of DFT simulations to the determination of magneto structural correlations inside an iso structural series of Fe_4 helical pitch molecules through the direct calculation of the multi spin hamiltonian parameters. These information will be also used to reproduce the ground state properties for a direct comparison with experimental data. This last procedure will be further analyzed in section 2.5 where the possibility to calculate higher order spin hamiltonian terms and their properties will be discussed. Section 2.6 will be devoted to the post Hartree Fock study of anisotropic exchange coupling tensor, as the last missing element in the helycal pitch multi spin hamiltonian. Section 2.7 will concern the study of extended magnetic atom chains (EMACs). This class of compound represents a less common class of polynuclear magnetic complexes and will give the opportunity to investigate the effects of direct metal-metal bonding to the overall SMM behavior.

2.1 Spin Hamiltonian Formalism

Although the origin of the spin hamiltonian formalism is mainly phenomenological, a theoretical foundation could be provided. The main idea of this formalism relies on the possibility to define a *Spin* system as an entity localized on a single center and with intrinsic properties, only marginally affected by the surrounding, that could be interrogated through external stimuli. From a theoretical point of view the same definition could be stated as the possibility to describe the system through a set of quantum operator variables $\vec{\mathbf{S}}$, whose algebra follows

$$[\hat{S}_i, \hat{S}_j] = i\hbar \hat{S}_k \delta_{ijk} \qquad [\hat{S}^2, \hat{S}_i] = 0 \tag{2.1}$$

$$\hat{S}_z|S^2 S_z\rangle = \hbar S_z|S^2 S_z\rangle \qquad \hat{S}^2|S^2 S_z\rangle = \hbar^2 S(S+1)|S^2 S_z\rangle \tag{2.2}$$

Clearly this definition needs to be fulfilled at all times, *i.e.* $[H, S^2] = 0$. This last condition is of paramount importance and summarizes the spin center definition: the hamiltonian H, which describes the spin system, has common eigenkets with the operator S^2 and its eigenkets can be labeled through S^2 eigenvalues.

Accordingly to the discussion above, independently on the chemical complexity of a system, if it fulfills the condition $[H, S^2] = 0$, it is possible to described its low lying eigenvalues and eigenvectors through eigenvalues and eigenvectors of a spin hamiltonian H_s built with spin operator variables. These are the only ingredients needed for the spin hamiltonian description. The hamiltonian is then shaped according to algebraic requirements. The spin hamiltonian for an isolated system should be invariant upon reference frame transformations, *i.e.* it must be a 0 rank tensor. In this context, the word *tensor* applies to reference frame rotation effects on spin operators. Therefore, the easiest description of the spin hamiltonian is in terms of spherical tensors T^k_q. Indeed, spherical tensors are operators, build from a combination of cartesian spin operators, which maintain their algebraic shape upon cartesian axis rotation. Nevertheless, spherical tensor operators possess the major drawback not to be hermitian and they need to be combined between themselves in order to produce hermitian operators, property that assures the hamiltonian to be hermitian itself. Although this is not mandatory, it is convenient in order for spin hamiltonian coefficients to be real and thus subject to ordering. Tennant's operators are a class of tesseral operators that are hermitian and at the same time possess a clear connection with the spherical tensors which have the correct rotational properties[25]:

$$O_0^k = T_0^k \tag{2.3}$$

$$O_q^k = \frac{1}{\sqrt{2}}((-1)^q T_q^k + T_{-q}^k) \tag{2.4}$$

$$O_{-q}^k = \frac{i}{\sqrt{2}}((-1)^{q+1} T_q^k + T_{-q}^k) \tag{2.5}$$

This is not the only possible choice and in literature there is a complete zoology of generalized Steven's operators which are commonly used to build spin hamiltonians[26]. From now on the letter T would be used in the spin hamiltonian formalism to indicate spherical tensor operator, while the letter O for the Tennant's operators, if not differently specified.

These operators could be used to build a completely general spin hamiltonian of the form:

$$H_s(\vec{\mathbf{S}}) = \sum_{k=0}^{2S} \sum_{q=-k}^{k} B_q^k \hat{O}_q^k(\vec{\mathbf{S}}) \tag{2.6}$$

The upper limit 2S for the index k comes from the null value of all the matrix elements $\langle SM_s|\hat{O}^k|SM_s^{'}\rangle$ according to the wigner-eckart theorem. The B_q^k coefficients are real numbers, accordingly to $\hat{O}_q^k(\vec{\mathbf{S}})$ properties, and their value is adjusted in order to reproduce the $2S+1$ lowest eigenvalues and eigenvectors of the hamiltonian H describing the system in terms of its first principles. The mapping between the real hamiltonian H and the spin hamiltonian is made by the relation

$$\langle SM_S|H|SM_S'\rangle = \langle SM_S|H_s|SM_S'\rangle \tag{2.7}$$

which paved the ground for the computational evaluation of spin hamiltonian coefficients.

Odd k index spherical tensors worth an additional comment. These operators change sign upon time-inversion symmetry operation

$$\langle lm|T_q^k|lm'\rangle = (-1)^k \langle lm|T_q^k|lm'\rangle \tag{2.8}$$

This imply that the corresponding B_q^k coefficients must do the same in order for H_s to be a 0-rank tensor. These terms are usually neglected from the description of

magnetic systems, except for the Dzyaloshinskii-Moriya interaction (*vide infra*), but it must be stressed that it should be done in force of their small value as there are not *a priori* reasons for their null value.

Before moving to the multi spin hamiltonian description it is useful to introduce the concept of spherical tensor norm. Sometimes, for analysis purposes, it is needed to reduce all the components of a spherical tensors into a single number, as it is common practice for cartesian vectors. In order to accomplish that, lets start noting that as H_s is a 0-rank tensor, all the X_q^k of a general spin hamiltonian $H_s = \sum_{kq} X_q^k \hat{T}_q^k$ must transform as T_q^k, and so, according to the composition theorem of spherical tensors we can use the relation

$$X_{lq} = \sum_{q'q''} \langle lq, l'l''|l'q'l''q''\rangle X_{l'q'} X_{l''q''} \tag{2.9}$$

Choosing l=0 and l'=l", the Clebsh-Gordan coefficients $\langle lq, l'l''|l'q'l''q''\rangle$ become:

$$\langle 00, l'l'|l'q'l'q''\rangle = \delta_{q',-q''} \frac{(-1)^{l'-q'}}{\sqrt{2l'+1}} \tag{2.10}$$

Exploiting the spherical tensor property $X^*_{l'q'} = (-1)^{q'} X_{l'-q'}$ we get in the end:

$$|T^{l'}| = X_{00} = \sum_{q'} \frac{(-1)^{l'}}{\sqrt{l'+1}} X^*_{l'q'} X_{l'q'} = \sum_{q'} \frac{(-1)^{l'}}{\sqrt{l'+1}} |X_{l'q'}|^2 \tag{2.11}$$

Eq. 2.11 is positive defined for all even order spherical tensors and negative defined for all odd order spherical tensors and therefore it can be used as norm definition for the coefficients of spin hamiltonian operators. This definition of norm will be used multiple time in the next sections and chapters.

Multi Spin Hamiltonian

For a multi spin system, the coupling theorem for single spin spherical tensors can used and obtain

$$T_q^k(s_1 s_2) = \sum_{q1,q2} < k1, k2, k, q|k1, k2, q1, q2 > T_{q1}^{k2}(s_1) T_{q2}^{k2}(s_2) \tag{2.12}$$

where from now on the lowercase letters will always indicate a spin from a multi spin system, while capital S letters will indicate the total spin variable $\vec{\mathbf{S}} = \sum_i \vec{\mathbf{s}}_i$. In the

context of single spin system the capital S letter will be used without ambiguity. Relation 2.12 could be used recursively an arbitrary number of times in order to produce v-plets combinations of spin operators, leading to a general multi-spin hamiltonian

$$H(s_1, ..., s_N) = \sum_v \sum_k \sum_{q=-k}^{k} B_{kq}(v) O_{kq}(v) \tag{2.13}$$

In order to clarify the meaning of the generalized multi-spin hamiltonian, lets study its connection with a more common form of multi-spin hamiltonian. When dealing with transition metal complexes made of N spins $\vec{\mathbf{s_i}}$, the low-lying energy spectrum is usually mapped to the eigenvalues of a multi-spin Hamiltonian of the form:

$$H(\{\vec{\mathbf{s_i}}\}_N) = \sum_{i=1}^{N} \beta_e \vec{\mathbf{B}} \cdot \mathbf{g_i} \cdot \vec{\mathbf{s_i}} + \sum_{i,j=1}^{N} \vec{\mathbf{s_i}} \cdot \mathbf{J_{ij}} \cdot \vec{\mathbf{s_j}} \tag{2.14}$$

The first term reported in equation 2.14, usually called magnetic Zeeman hamiltonian, describes the interaction between an external magnetic field $\vec{\mathbf{B}}$ and a single spin. This interaction is modulated by the Landé tensor $\mathbf{g}$. The tensor $\mathbf{J_{ij}}$ is usually decomposed into single body terms ($\mathbf{D_i}$ for $i = j$) and two body terms ($\mathbf{J_{ij}}$ with $i \neq j$). These two second rank cartesian tensors, which are respectively called single ion anisotropy tensor and exchange coupling tensor, describe the energy levels splitting of spins in zero external field and they embed all the effects of the surrounding chemical environment, whatever their nature is. The last one is usually further decomposed into an isotropic (Heisenberg hamiltonian) and an anisotropic part for each pair of spins (Anisotropic exchange hamiltonian and Dzyaloshinskii-Moriya hamiltonian):

$$\vec{\mathbf{s_i}} \cdot \mathbf{J_{ij}} \cdot \vec{\mathbf{s_j}} = J_{ij}(\vec{\mathbf{s_i}} \cdot \vec{\mathbf{s_j}}) + \vec{\mathbf{s_i}} \cdot \mathbf{D_{ij}} \cdot \vec{\mathbf{s_j}} + \mathbf{d_{ij}} \cdot (\vec{\mathbf{s_i}} \times \vec{\mathbf{s_j}}) \tag{2.15}$$

where

$$J_{ij} = Tr(\mathbf{J_{ij}})/3$$

$$\mathbf{D_{ij}} = \frac{1}{2}(\mathbf{J_{ij}} + \mathbf{J_{ji}}) \quad and \quad \mathbf{d_{ij}} = \frac{1}{2}(\mathbf{J_{ij}} - \mathbf{J_{ji}})$$

The isotropic exchange interaction constants J_{ij} are the only terms of the above spin Hamiltonian which do not depend on the orientation of the spins and they just lift the degeneracy of the various S^2 eigenfunctions (Heisenberg Hamiltonian). All the other terms, instead, describe anisotropic interactions and they arise from the non spherical symmetry of the interactions felt by the spins.

This four part of the spin hamiltonian could be obtained from the general hamiltonian 2.13 with a specific choice of v. Indeed, choosing appropriate combinations of couples of single spin operators

$$T^1(s_i) \otimes T^1(B) \rightarrow T^1(s_i, B) \equiv \text{Zeeman hamiltonian} \tag{2.16}$$
$$T^1(s_i) \otimes T^1(s_j) \rightarrow T^0(s_i, s_j) \equiv \text{Heisenberg hamiltonian} \tag{2.17}$$
$$T^1(s_i) \otimes T^1(s_j) \rightarrow T^1(s_i, s_j) \equiv \text{Dzyaloshinskii-Moriya hamiltonian} \tag{2.18}$$
$$T^1(s_i) \otimes T^1(s_j) \rightarrow T^2(s_i, s_j) \equiv \text{Anisotropic exchange hamiltonian} \tag{2.19}$$
$$T^1(s_i) \otimes T^1(s_i) \rightarrow T^2(s_i, s_i) \equiv \text{Single ion Anisotropic hamiltonian} \tag{2.20}$$

The spread of the cartesian notation for the multi spin hamiltonian terms makes them the most common forms for second order operators and the spherical tensor formalism is introduced only for the higher order terms. The anisotropic second order cartesian tensor terms are defined symmetric and traceless, so they have only five independent elements. From them, the anisotropy intensity and its distortions from perfect axial symmetry are conventionally introduced with the axial (D) and rhombic (E) parameters:

$$D = D_c - \frac{1}{2}(D_b + D_a) \qquad E = \frac{1}{2}|(D_b - D_a)| \tag{2.21}$$

where D_a, D_b and D_c are $\mathbf{D}$ eigenvalues chosen such as $0 < |E/D| < \frac{1}{3}$. The remaining parameters needed to completely describe $\mathbf{D}$ are inside its eigenvectors. The sign of the parameter D describes very important property of the system *i.e.* negative values correspond to easy-axis kind of anisotropy while positive values correspond to easy-plane kind of anisotropy.

Giant Spin Approximation

When dealing with systems with many spins (e.g. polynuclear clusters of interacting paramagnetic ions) the mathematical problem becomes easily inaccessible as H_s dimension is given by $\prod_i = s_i(s_i+1)$, where i scales over the spins considered. Moreover, as only the first few eigenvalues and eigenstates are usually needed, the mathematical treatment of this class of spin systems exploits the so called Giant Spin Approximation (GSA). This approximation can be introduced when the difference in energy between different multiplets (eigenvectors with the same S^2 expectation value) is much higher than the energy splitting of levels inside each multiplet, splitting which arises from

anisotropic terms (Strong Exchange limit). In that case the mixing of states between different multiplets is small and it is possible to consider each multiplet separately from the others [27]. In order to introduce the mathematical procedure used to perform this approximation, lets consider a multi-spin hamiltonian (MSH), written as a function of spherical tensors, composed only of single and double spin interactions

$$H(s_1, ..., s_N) = \sum_i \sum_{kq} X_q^k(s_i) T_q^k(s_i) + \sum_{ij} \sum_{kq} X_q^k(s_i s_j) T_q^k(s_i s_j) \tag{2.22}$$

The GSA is realized asking the identity between MSH and giant spin hamiltonian (GSH), the last one being algebraically equivalent to a single spin hamiltonian with value S:

$$\langle SM_S | H_{MS}(s_1, ..., s_N) | SM'_S \rangle = \langle SM_S | H_{GS}(S) | SM'_S \rangle \tag{2.23}$$

,where cross multiplet terms are assumed zero *i.e.* $\langle SM_S | H_{MS} | S'M'_{S'} \rangle = 0$.

Considering, for sake of clarity, only single spin tensors from the MSH and exploiting the wigner-eckart theorem

$$\langle SM_S | \sum_i \sum_{kq} X_q^k(s_i) T_q^k(s_i) | SM'_S \rangle = \tag{2.24}$$

$$\sum_i \sum_{kq} X_q^k(s_i) \langle SM_S || T^k(s_i) || SM'_S \rangle \frac{\langle SM_S, kS | kq, SM'_S \rangle}{\sqrt{2S+1}} \tag{2.25}$$

Alike, for the GSH

$$\langle SM_S | \sum_{kq} X_q^k(S) T_q^k(S) | SM'_S \rangle = \tag{2.26}$$

$$\sum_{kq} X_q^k(S) \langle SM_S || T^k(S) || SM'_S \rangle \frac{\langle SM_S, kS | kq, SM'_S \rangle}{\sqrt{2S+1}} \tag{2.27}$$

Matching Eq. 2.25 and Eq. 2.27 for each (k,q)

$$X_q^k(S) = \sum_i X_q^k(s_i) \frac{\langle SM_S || T^k(s_i) || SM'_S \rangle}{\langle SM_S || T^k(S) || SM'_S \rangle} \tag{2.28}$$

similarly for multi spin terms of MSH

$$X_q^k(S) = \sum_{ij} X_q^k(s_i s_j) \frac{\langle SM_S||T^k(s_i s_j)||SM'_S\rangle}{\langle SM_S||T^k(S)||SM'_S\rangle} \tag{2.29}$$

Eqs. 2.28 and 2.29 show that the GSH parameters could be evaluated from the MSH ones through a weighed sum. The translation from spherical to cartesian components, may be used for the very common situation which requires to project the symmetric and anisotropic hamiltonian 2.14 into

$$\mathbf{H_S} = \vec{\mathbf{S}} \cdot \mathbf{D_S} \cdot \vec{\mathbf{S}} \tag{2.30}$$

According to relations 2.28 and 2.29, $\mathbf{D_S}$ is related to the several terms $\mathbf{D_i}$ and $\mathbf{D_{ij}}$ by

$$\mathbf{D_S} = \sum_i d_i^S \mathbf{D_i} + \sum_{ij} d_{ij}^S \mathbf{D_{ij}} \tag{2.31}$$

with

$$d_i^S = \frac{\langle SM_S||T^k(s_i)||SM'_S\rangle}{\langle SM_S||T^k(S)||SM'_S\rangle}, \qquad d_{ij}^S = \frac{\langle SM_S||T^k(s_i s_j)||SM'_S\rangle}{\langle SM_S||T^k(S)||SM'_S\rangle} \tag{2.32}$$

Multi spin hamiltonian and giant spin hamiltonian definitions put the basis for a more detailed discussion about the spin hamiltonian formalism in general. The same spin addiction formalism just presented readily applies to the combination of single electron hamiltonians. Indeed, the single spin hamiltonian is nothing than a giant spin hamiltonian built from single spin hamiltonian of interacting electrons. According to the Russel-Sunders picture, when the distance between ground and excited state LS terms is big enough, with respect to the intra ground state multiplet level splitting, it is possible to conside the multiplet total S operator a good quantum number and the 2S+1 level of the ground LS terms can be regarded as level of a giant S spin. It is then clear that a hierarchy between intra spin first principles and spin-external world interactions must exists. Indeed, although the spin hamiltonian describes interactions between the spin and the external world, at the same time, part of these interactions spoil the nature of the spin itself. Specifically, all the anisotropic terms in a multi-spin hamiltonian do not commute with S^2 and therefore makes the total S operator

eigenvalues bad behaving quantum numbers. The condition *only marginally affected by the surrounding* appearing in the spin hamiltonian definition at the beginning of the section is then needed to be associated only to this kind of interactions. As it also comes from the discussion of the Russel-Sunders picture, the giant spin hamiltonian formulation could still be used if the anisotropic interactions are weak with respect to the isotropic ones. In this framework, the condition $[H_s, S^2] = 0$ could be relaxed to $[H_s, S^2] \sim 0$, in order to include in the formalism anisotropic effects.

2.2 QM - Spin Hamiltonian Mapping

The main consequence of the condition $[H_s, S^2] \sim 0$ is the necessity to interpret the spin hamiltonian as a perturbative series. This statement is at the basis of the mapping between electronic structure calculations and spin hamiltonian parameters. While isotropic interactions are generated by pure electrostatic interactions between electrons, all the anisotropic terms in the spin hamiltonian come from relativistic contributions, *i.e.* spin-orbit coupling (SOC) and spin-spin dipolar (SS) contribution. Lets consider Eq. 2.7 with $H = H_{BO} + H_{SOC}$, where H_{SOC} refers to the SOC hamiltonian interaction and H_{BO} refers to the Born-Oppenheimer hamiltonian. According to the above discussion, H_{SOC} must be regarded as a perturbation to the main contribution to the energy coming from the Born-Oppenheimer hamiltonian. Therefore,

$$\langle aSM_s|H|aSM_s^{'}\rangle = E_a\delta_{M_sM_s^{'}} + \langle aSM_s|H_{SOC}|aSM_s^{'}\rangle \tag{2.33}$$

$$-\sum_{bM_s^{''}} \frac{\langle aSM_s|H_{SOC}|bSM_s^{''}\rangle\langle bSM_s^{''}|H_{SOC}|aSM_s^{'}\rangle}{E_b - E_a} \tag{2.34}$$

, where a and b represent the label of the H eigenstate $|aSM_s\rangle$ including all the other degrees of freedom except for the spin one. The E_a value can be neglected as it only gives the energy scale. The mapping between H_s anisotropic terms and H_{SOC} perturbative series is done on the basis of algebraic correspondences. H_{SOC} could be written in the spherical basis as $H_{SOC} = \sum_q \sum_i (-1)^q h_{-q}(i) s_q(i)$, where h_{-q} contains angular momentum operators and coordinate dependent coefficients and the i sum runs over all the electrons in the system. The first order contribution is then

$$\langle aSM_s|H_{SOC}|aSM_s^{'}\rangle = \sum_q \sum_i (-1)^q \langle a|h_{-q}(i)|a\rangle\langle SM_s|s_q(i)|SM_s^{'}\rangle \tag{2.35}$$

$s_q(i)$ is a spherical tensor of the first order and therefore, according to the wigner-eckart theorem

$$\langle SM_s|s_q(i)|SM_s^{'}\rangle = \frac{\langle S||s(i)||S\rangle}{\sqrt{2S+1}}\langle SM_s 1S|1q, SM_s^{'}\rangle = \tag{2.36}$$

$$\frac{\langle S||s(i)||S\rangle}{\sqrt{2S+1}}\frac{\sqrt{2S+1}}{\langle S||T^1(S)||S\rangle}\langle SM_s|T_q^1(S)|SM_s^{'}\rangle = \tag{2.37}$$

$$\frac{\langle S||s(i)||S\rangle}{\sqrt{2S+1}}\frac{\sqrt{2S+1}}{\sqrt{2S+1}\sqrt{S(S+1)}}\langle SM_s|T_q^1(S)|SM_s^{'}\rangle = \tag{2.38}$$

$$\frac{\langle S||s(i)||S\rangle}{\sqrt{(2S+1)(S(S+1))}}\langle SM_s|T_q^1(S)|SM_s^{'}\rangle \tag{2.39}$$

Substituting the final expression of Eq. 2.39 in 2.35

$$\langle aSM_s|H_{SOC}|aSM_s^{'}\rangle = \tag{2.40}$$

$$\sum_q\sum_i(-1)^q\langle a|h_{-q}(i)|a\rangle\frac{\langle S||s(i)||S\rangle}{\sqrt{(2S+1)(S(S+1))}}\langle SM_s|T_q^1(S)|SM_s^{'}\rangle \tag{2.41}$$

Recognizing the algebraic form of $H_s = \sum_q X_q^1 T_q^1$ is then possible to make the mapping

$$X_q^1 = \sum_i(-1)^q\langle a|h_{-q}(i)|a\rangle\frac{\langle S||s(i)||S\rangle}{\sqrt{(2S+1)(S(S+1))}} \tag{2.42}$$

The calculated X_q^1 coefficients may be combined according to 2.5 to obtain the specific form of a generalized spin hamiltonian. At the best of my knowledge, this is the first time Eq. 2.42 has been reported.

The procedure just outlined could be recasted at different perturbational orders with different relativistic terms in H to produce a variety of spin hamiltonian terms. For instance, spin orbit coupling at the second order could be mapped into a spin hamiltonian of the form $\mathbf{H_S} = \vec{\mathbf{S}} \cdot \mathbf{D_S} \cdot \vec{\mathbf{S}}$[28], while mixing at the second order spin orbit coupling and electronic zeeman interactions gives the anisotropic landè factor in the spin hamiltonian $\mathbf{H_S} = \beta\vec{\mathbf{S}} \cdot \mathbf{g} \cdot \vec{\mathbf{B}}$[28]. As the spin hamiltonian formalism is strictly correct only in the weak anisotropy regime, the perturbation expansion upon which is based the mapping with the electronic structure is expected to break down when low lying electronic levels become almost degenerate to the ground state *i.e.* the angular momentum is not completely quenched. As it will be shown later, this is indeed the case of strongly anisotropic single ion transition metal complexes of Fe^{2+}, Co^{2+}

and Ni^{2+}. These cases fall into a gray area for the spin hamiltonian theory because perturbation theory is no longer strictly applicable but at the same time the ground state orbital angular momentum is partially quenched and it could not be used as a good quantum variable to produce a pseudo spin hamiltonian in terms of the total angular momentum J=L+S, as it is common practice for lanthanides compounds. In this case a spin hamiltonian of the form 2.6 could be retained but the mapping with the electronic structure is made by means of a *brute force* fitting. The low lying part of H spectrum could be written as function of its eigenvalues and eigenvectors

$$H = \sum_{k=1}^{2S+1} |k\rangle E_k \langle k| \tag{2.43}$$

Therefore, the mapping with the spin hamiltonian assumes the form

$$\langle SM_S|H_s|SM_{S'}\rangle = \sum_{k}^{2S+1} \langle SM_S|k\rangle E_k \langle k|SM_{S'}\rangle \tag{2.44}$$

This system of linear equation could be solved by means of a least square fit[29]. Although this relation is not *a priori* valid and the quality of the fitting should be evaluated each time, its range of applicability is larger with respect to the (more correct) perturbation treatment of relativistic interactions. For instance, it can also be exploited when higher order spin hamiltonian terms are needed to describes the system; this feature is particularly appealing as analytical expressions, like 2.42, are missing for these terms. At the same time, a clear connection between specific interaction included in H and spin hamiltonian terms is here lost and the correctness of H_s choice falls under the quality of the fit itself. Over parametrization problems could arise, especially when multi spin complexes are considered.

The mapping procedures just outlined are based on many body electronic structure algorithms. On the other hand, the calculation of magnetic properties from density functional or Hartee-Fock therory requires some precaution and the next section will be dedicated to the review of available DFT-SH mapping methods.

2.3 DFT - Spin Hamiltonian Mapping

The most studied term of the spin Hamiltonian, in a molecular orbital framework, is by far the isotropic exchange interaction. Probably the first attempts to define and calculate the exchange coupling constants go back to Löwdin [30, 31] but the first practical methods, which allow for an accurate J evaluation within the framework of DFT or Hartee Fock (HF), appeared in the literature a few decades ago with Noodleman [32], Yamaguchi [33] and Ginsberg [34]. The basic idea behind all these treatments relies on the mapping of the low lying energy levels obtained from DFT with the Heisenberg spin Hamiltonian. The main problem to puzzle out was that Unrestricted Kohn Sham (UKS) and UHF schemes, when used to describe multiplets different from the High Spin (HS) state, give a spin contaminated solution. If one is interested on the evaluation of spin properties, it becomes of fundamental importance to account for the differences between these kind of solutions, usually called broken symmetry (BS) solutions, and pure spin states. This problem was solved by Noodleman, who interpreted these BS solutions as eigenfunctions of the S_z operator. These eigenfunctions can be written as a weighted average of pure spin states which are orthogonal and non interacting with respect to the total Hamiltonian of the system. In this way Noodleman found out that it is possible to cancel out all the contributions of the multiplets between the HS and the BS just making the difference between the energy of the HS and BS state:

$$E_{HS} - E_{BS} = 2J_{12}s_1s_2 \tag{2.45}$$

To demonstrate this relation lets consider a system of two interacting spins which could be described by the $|S, S_z, s_1, s_2 >$ basis set. Within this scheme is possible to calculate the energy spin ladder of the Heisemberg spin hamiltonian as a function of the only multiplet S value since this interaction does not lift the S_z energy level degeneracy:

$$E(S) = \frac{J}{2}[S(S+1) - S^{Max}(S^{Max}+1) + 2s_1^{Max}s_2^{Max}] \tag{2.46}$$

Expression 2.46 could be readily used to evaluate E(HS) and obtain $E(HS) = Js_1s_2$. However, to compute energies evaluated within the DFT framework $E(BS)$) it should be interpreted the DFT solution as vectors of the form $|s_1, s_2, s_{z1}, s_{z2} >$:

$$E(BS) = < s_1, s_2, s_{z1}, s_{z2}|H|s_1, s_2, s_{1z}, s_{2z} >= \tag{2.47}$$

$$\sum_S c_S^2 < S^2, S_z, s_1, s_2|H|S^2, S_z, s_1, s_2 >= \tag{2.48}$$

$$\sum_S c_S^2 E(S) = \sum_S^{S_{max}} \frac{J}{2} c_S^2 \Big(S(S+1) - S_{max}(S_{max}+1) + 2s_1 s_2 \Big) \tag{2.49}$$

Utilizing now the relations $\sum_S c_S^2 = 1$ and $\sum_S c_S^2 S(S+1) =< S_z^2 >_{BS} + S_{max}$ and making the difference between E(HS) and E(BS)

$$E(HS) - E(BS) = 2J s_1 s_2 \tag{2.50}$$

The relation 2.50 is just the generalization for a generic spin pair of the relation found out by Noodleman [32] and was derived for the first time by Dai Et al[35].

This relation is theoretically correct for two well defined spins. All the limitations on the accuracy of this method arise from the impossibility to define properly a spin center and from the deficiencies of DFT to manage open shell systems. The first evaluation of anisotropy tensors from DFT is more recent and proposed by Pederson *et al.* [36]. In his pioneering work he used second order perturbation theory arguments to evaluate the contribution of spin-orbit coupling to the non relativistic ground state of a Mn_{12} cluster. An alternative formula was derived by Neese [37] within a response theory framework. These two formula are quite similar and essentially differ only in the prefactors of the angular momenta integrals. Recently Van Wüllen *et al.* [38] showed that Pederson and Neese's approaches to ZFS mapping of SOC contribution could be modified and with these modifications both method's formulae become identical to:

$$\begin{aligned} D_{KL} = \tfrac{1}{2S(2S-1)}\{ \quad & -\textstyle\sum_{i\uparrow,a\uparrow} < \phi_{i\uparrow}|h_K^{so}|\phi_{a\uparrow} > U^L_{a\uparrow i\uparrow} \\ & -\textstyle\sum_{i\downarrow,a\downarrow} < \phi_{i\downarrow}|h_K^{so}|\phi_{a\downarrow} > U^L_{a\downarrow i\downarrow} \\ & +\textstyle\sum_{i\uparrow,a\downarrow} < \phi_{i\uparrow}|h_K^{so}|\phi_{a\downarrow} > U^L_{a\downarrow i\uparrow} \\ & +\textstyle\sum_{i\downarrow,a\uparrow} < \phi_{i\downarrow}|h_K^{so}|\phi_{a\uparrow} > U^L_{a\uparrow i\downarrow} \quad \} \end{aligned} \tag{2.51}$$

Where ϕ stands for a generic spin orbital and the various U are linear response parameters. These several U parameters correspond to $< \phi_{a\uparrow}|h_K^{so}|\phi_{i\uparrow} > /(\epsilon_a - \epsilon_i)$ in absence of the explicit HF exchange term in the functional, otherwise they should be compute them from coupled perturbed equations. Another very important result was obtained by Neese [39], who showed the importance of the spin-spin interaction contribution to the single ion anisotropy tensor. This interaction could be handled

with MO calculations thanks to first order perturbation theory, which leads to the calculation of integrals

$$D_{KL}^{SS} = \frac{\alpha^2}{2S(2S-1)} \langle \Psi_0 | \sum_i \sum_{j \neq i} \frac{r_{ij}^2 \delta_{KL} - 3(r_{ij})_K (r_{ij})_L}{r_{ij}^5} \cdot (2\hat{s}_{zi}\hat{s}_{zj} - \hat{s}_{xi}\hat{s}_{xj} - \hat{s}_{yi}\hat{s}_{yj}) | \Psi_0 \rangle \tag{2.52}$$

where α is the fine structure constant, r is the distance vector between electrons and $|\Psi_0\rangle$ is the ground state wave function. In another article Van Wüllen [40] explained that the equations 2.51 and 2.52 could be applied only if the wave function obtained from DFT is a pure spin state. This is not the case when antiferromagnetic interactions occur between different magnetic centers and a single determinant description of the wave-function is used. In ref [40] it was suggested to switch off the spin orbit interaction over all but one magnetic center in order to evaluate the single ion anisotropy tensor for that specific ion. This procedure allows for the direct evaluation of the single ion tensor for all the ions into the cluster, carrying out a calculation with the formula 2.51 for all the ions one by one. The same authors have also recently published a methodology [41], similar in philosophy to the one proposed by Noodleman, for the isotropic exchange coupling constants, for the evaluation of the contributions of spin-spin and spin-orbit coupling to the anisotropy exchange tensors.

In the next section these procedures will be tested and expanded. The calculation of the single ion tensors will be done through a diamagnetic substitution of the various paramagnetic ions, as also suggested in [40], since it is a common experimental protocol for the extraction of single ion contributions [42]. For what concerns the inclusion of the anisotropic interactions between different spin centers ($\mathbf{D_{ij}}$) here I would like to show a different procedure from the one presented in [41]. The method is directly related to the strong exchange formulation of the HS state for two antiferromagnetically coupled spins, where $\mathbf{D_{HS}}$ is written as function of multi-spin Hamiltonian parameters (see Equation 2.30). Once the single ion tensors of a couple are obtained with the diamagnetic substitution method it is possible to extract the anisotropic exchange contribution as

$$\mathbf{D_{12}} = \frac{\mathbf{D_{HS}} - d_1^{HS}\mathbf{D_1} - d_2^{HS}\mathbf{D_2}}{d_{12}^{HS}} \tag{2.53}$$

where d_1^{HS},d_2^{HS} and d_{12}^{HS} are the projection coefficients that relate the various tensors to the global high spin state and $\mathbf{D_{HS}}$ is the anisotropy tensor for the dimer in its High Spin configuration. Using the diamagnetic substitution for all the magnetic centers

except two, it is thus possible to calculate the anisotropy tensor for the HS state of a dimer. Note that this operation could be safely handled with formula 2.51 since the high spin state could be written as a pure spin state, even utilizing mono determinant wave functions. It also should be pointed out that the GSA is especially valid for the HS state since the energy difference between adjacent states is E(S)-E(S-1)=JS, which is maximal for the HS state. This procedure has to be repeated for all the strongly interacting exchange coupled pairs. For all the other couples, where the SOC contribution to the anisotropic tensor could be neglected, the $\mathbf{D_{ij}}$ tensor is determined only by the dipolar through space interaction, which could be safely treated with the point dipole approximation:

$$\mathbf{D}_{ij}^{Dip} = \mu_B^2 \frac{\mathbf{g}_i \cdot \mathbf{g}_j - 3(\mathbf{g}_i \cdot \vec{\mathbf{r}})(\vec{\mathbf{r}} \cdot \mathbf{g}_j)}{r^3} \tag{2.54}$$

where r is the distance between the ions, $\vec{\mathbf{r}}$ the unit vector connecting them and $\mathbf{g_i}$ is Landé single ion tensor which can be evaluated from DFT at the same time of the single ion tensors $\mathbf{D_i}$, as described by Neese[43]. The main advantage of this procedure, with respect to the one proposed by Kessler *et al.*[41], is that it does not require any introduction of arbitrary chosen unknown parameters, choice which is expected to affect dramatically the results. Moreover, the application of eq. 2.53 does not require any other code implementation and could be exploited within the already available software.

2.4 Fe_4 SMM Series

Accordingly with the discussion of the last section, I want here to present a computational protocol to describe the axial zero field splitting parameters (D) for antiferromagnetically coupled paramagnetic ions, including the contribution of anisotropic exchange coupling interaction between magnetic centers. From a theoretical and computational point of view this approach represents a possible route to treat such systems in the DFT framework, whose range of applicability was only recently expanded to the realm of ferrimagnetic complexes. In this framework a comprehensive and detailed magneto-structural correlation analysis of a series of Fe_4 SMMs has been performed.

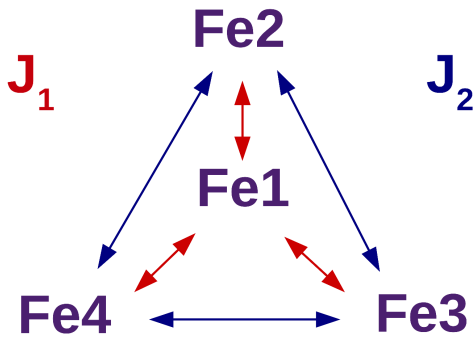

Figure 2.1: Fe^{3+} ions arrangement inside Ferric Star. Red arrows show the direct exchange interactions labeled by J_1 constants while the blue arrows shows the indirect interactions labeled by J_2 constant.

The studied molecules in this work are seven different synthetic analogs of the ferric star $[Fe_4(OMe)_6(dpm)_6]$ (Fe_4OMe) **(1)**[44]. These molecules differ one from another by the presence of one or two tripodal ligands $RC(CH_2O)_3$ (R-LIG) with different R groups which substitute three methoxide groups each in **(1)**. The molecules selected for this study are $[Fe_4(OEt)_3$(tBu-LIG)$(dpm)_6]$ (Fe_4tBu) **(2)**, $[Fe_4$(Ph-LIG)$_2(dpm)_6]$ (Fe_4Ph) **(3)** and $[Fe_4$(Me-LIG)$_2(dpm)_6]$ (Fe_4Me) **(4)**, from the work of Accorsi *et al.*[23] and $[Fe_4(AcS(CH_2)_5$-LIG$)_2(dpm)_6]$ (Polymorph No.1) (Fe_4C5) **(5)**, $[Fe_4$(AcS $(CH_2)_4$-LIG$)_2(dpm)_6]$ (Fe_4C4) **(6)**, $[Fe_4(AcS(CH_2)_3$-LIG$)_2(dpm)_6]$ (Polymorph No.1) (Fe_4C3) **(7)** and $[Fe_4(AcSCH_2$-LIG$)_2(dpm)_6]$ (Polymorph No.1) (Fe_4C1) **(8)** from Tancini's Ph.D thesis[45] (see Figure 2.2). The magnetic nature of these SMMs originates from four Fe^{3+} disposed on the same plane as pictorially described by the Figure 2.1. The interaction between the central (Fe_1 or Fe_c) and the peripheral (Fe_2, Fe_3, Fe_4 or briefly Fe_p) irons is made possible thanks to μ-alkoxo ligands that mediate a super-

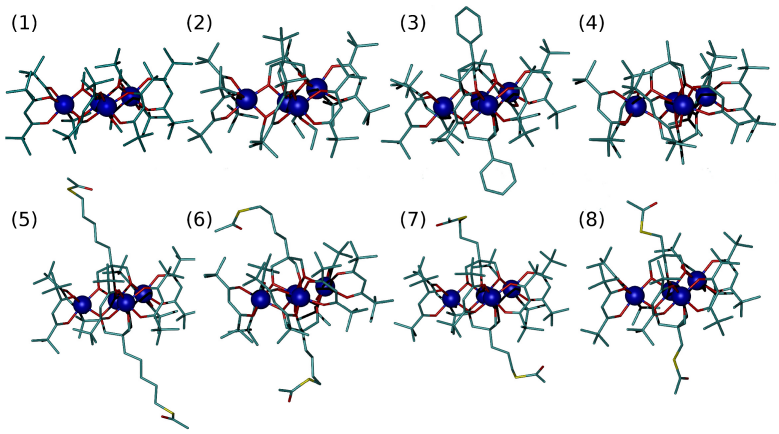

Figure 2.2: The Fe_4 series. Top line from left: Fe_4OMe **(1)**, Fe_4tBu **(2)**, Fe_4Ph **(3)**, Fe_4Me **(4)**; Bottom line from left: Fe_4C_5 **(5)**, Fe_4C_4 **(6)**, Fe_4C_3 **(7)**, Fe_4C_1 **(8)**. Hydrogen atoms were not reported for sake of clarity.

exchange coupling interaction. These SMMs, in their crystalline environment, have an $S = 5$ ground state which originates from the leading antiferromagnetic coupling between the central high spin Fe^{3+} ion (Fe_c or Fe_1) and the three peripheral high spin Fe^{3+} ions (Fe_p or Fe_2, Fe_3 and Fe_4). The Hamiltonian describing these isotropic interactions is written as

$$\begin{aligned} H =& J_{12}\vec{\mathbf{s}}_1 \cdot \vec{\mathbf{s}}_2 + J_{13}\vec{\mathbf{s}}_1 \cdot \vec{\mathbf{s}}_3 + J_{14}\vec{\mathbf{s}}_1 \cdot \vec{\mathbf{s}}_4 + \\ & J_2\big(\vec{\mathbf{s}}_2 \cdot \vec{\mathbf{s}}_3 + \vec{\mathbf{s}}_2 \cdot \vec{\mathbf{s}}_4 + \vec{\mathbf{s}}_3 \cdot \vec{\mathbf{s}}_4\big). \end{aligned} \tag{2.55}$$

Here, J_{1x} (x = 2-4) are the first and J_2 the second neighbor exchange interactions (J_2 is left three-fold since it is usually below 1 cm^{-1}). Usually experimental data are interpreted assuming a threefold symmetry of this hamiltonian *i.e.* the three J_{1x} (x = 2-4) constants are described by a means of their means value J_1. Experimentally J_1 is always found to be antiferromagnetic with values ranging from about 23 to 15 cm^{-1}, while J_2 is about a few wave-numbers and its value is strongly affected by experimental systematic errors[46]. The magnetic memory effect, *i.e.*, the opening of magnetic hysteresis loop, is originated by the degeneracy lifting of the ground state multiplet due to the anisotropy term of the spin Hamiltonian,

$$H = \sum_i \vec{\mathbf{s}}_i \cdot \mathbf{D_i} \cdot \vec{\mathbf{s}}_i + \sum_{i,j\neq i} \vec{\mathbf{s}}_i \cdot \mathbf{D_{ij}} \cdot \vec{\mathbf{s}}_j. \tag{2.56}$$

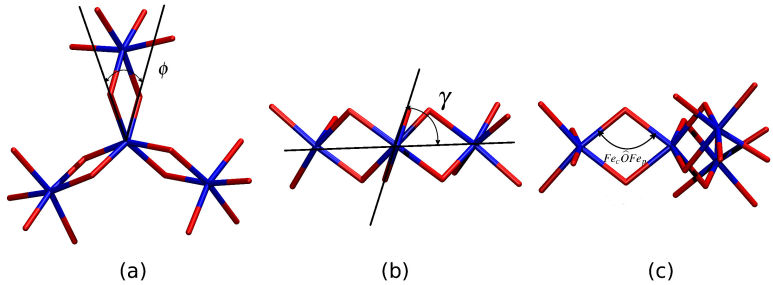

Figure 2.3: Graphical description of the trigonal rotation angle ϕ **(a)**, γ-pitch angle **(b)** and $Fe_c\widehat{O}Fe_p$ **(c)**.

In the above expression, i and j run over the spin ($\vec{\mathbf{s}}$) of the four iron ions. Alternatively, in the Giant Spin approximation (GSA), the same anisotropic physical behavior could be modeled as

$$H = \vec{\mathbf{S}} \cdot \mathbf{D}_{S=5} \cdot \vec{\mathbf{S}}, \tag{2.57}$$

where $\vec{\mathbf{S}}$ now stands for the ground state giant spin $S = 5$ vector. The $D_{S=5}$ axial constants are always found negative (easy-axis anisotropy) with values ranging between -0.206 and -0.449 cm^{-1}[23, 45]. By symmetry the rhombic $E_{S=5}$ values are quite small and often not even measured. Thanks to all these kinds of Fe_4 molecules synthesized through the years it is now possible to better understand the magneto-structural correlations that govern the global magnetic properties of this class of SMMs. For what concerns the relation between the exchange coupling constant J_1 and the geometrical structure, it has been found that the crucial structural parameter is the $Fe_c\widehat{O}Fe_p$ angle (see Figure2.3c), as already been found from studies about iron dimers [23, 47, 48]. All the iron ions in the Fe_4 SMMs posses a distorted O_h crystal field environment, which is the fundamental ingredient in order to have a single ion anisotropy. Since the central Fe^{+3} ion conserves its ternary symmetry, its distortions from the perfect O_h point-group symmetry are usually described with the two angles θ and ϕ, which correspond to the trigonal compression and rotation respectively (see Figure 2.3b). The effects of this kind of distortions on the anisotropy of Fe^{3+} ions have been already studied both from experimental and computational[49, 50] point of view and a few magneto-structural correlations have been also extracted. In particular it has been observed that, while the trigonal compression leads to positive D values, trigonal rotations lead to easy axis anisotropies. Since these molecules have

four magnetic centers, the resulting $\mathbf{D_S}$ is generated from the spin projected tensorial sum of the single-ion and exchange contributions (see Equation 2.32). Therefore, in order to understand magneto-structural correlations, geometric parameters that take into account both local O_h symmetry distortions and mutual tensors orientation are needed. Experimentally, a magneto-structural correlation between the **D** value and the so called γ-pitch [23] was found out. The helical γ-pitch is defined as the dihedral angle between the $Fe_cO_2Fe_p$ and Fe_4 planes (see Fig.2.3b) and it is directly correlated to the trigonal rotation of the central ion. Experimentally, it was observed that the enhancement of D is quite sensitive to the modulations of the γ-pitch. In order to explain the observed trend, it was suggested[23, 48] that such modulations causes changes in the D parameter for the central ion as well as in the magnitude and/or orientation of the anisotropy tensors for the peripheral ions. The reorientation of the peripheral tensors, which results in a different overall anisotropy, was considered a key ingredient.

Isotropic Exchange Coupling Constants

Usually the spin Hamiltonian used to fit experimental data is chosen according to an idealized $\mathbf{C}_3$ symmetry for the molecule. Except for **(2)** and **(3)**, which have a $\mathbf{D}_3$ and $\mathbf{C}_3$ molecular symmetry, respectively, this is only an approximation of the real molecular symmetry. Indeed, **(1)**, **(3)**, and **(5)** belong to the $\mathbf{C}_2$ symmetry point-group, while **(6)**, **(7)**, and **(8)** belongs to the $\mathbf{C}_1$ symmetry point-group. Despite this approximation about the real symmetry of the molecules, this approach does not introduce sensitive differences in the results since experiments actually sense only the J mean value. Therefore, although the used Heisenberg Hamiltonian (see Equation 2.97) is expressed with three explicit J_1 constants, only their mean value is reported here, in order to directly compare these results with the experimental ones. Calculated exchange coupling constants for the whole series are reported in Table 2.1 together with the experimental values found in literature [23, 45] and the value of $Fe_c\widehat{O}Fe_p$ angles averaged assuming a $\mathbf{C}_3$ symmetry of the molecule. The calculated exchange coupling constants are in good agreement with the experimental ones. The correlation coefficient between experimental and computed values is 0.932 while the mean error is 1.80 cm^{-1}. The goodness of these results is also supported by the high correlation between the $Fe_c\widehat{O}Fe_p$ and computed J_1 constants (see Tab. 2.2). The PBE0 functional is found to be particularly able to quantitatively predict the exchange coupling constants. In Table 2.1 are also reported the J_2 values together to the available experimental values. Although the absolute value for this interaction

Table 2.1: Calculated (PBE0) and experimental Exchange Coupling Constants.

	Fe_4OMe	Fe_4tBu	Fe_4Ph	Fe_4Me
J_1^{DFT}	23.37 cm^{-1}	22.04 cm^{-1}	13.10 cm^{-1}	16.47 cm^{-1}
J_1^{EXP}	21.10 cm^{-1} [a]	21.40(16) cm^{-1} [a]	16.37(12) cm^{-1} [a]	16.51(8) cm^{-1} [a]
J_2^{DFT}	0.24 cm^{-1}	0.32 cm^{-1}	0.24 cm^{-1}	0.25 cm^{-1}
J_2^{EXP}	-1.10 cm^{-1} [a]	-0.16(14) cm^{-1} [a]	0.29(11) cm^{-1} [a]	-0.62(8) cm^{-1} [a]
$Fe_c\widehat{O}Fe_p$	104.4 °	104.3 °	102.2 °	102.9 °

	Fe_4C5	Fe_4C4	Fe_4C3	Fe_4C1
J_1^{DFT}	15.96 cm^{-1}	12.63 cm^{-1}	11.08 cm^{-1}	12.41 cm^{-1}
J_1^{EXP}	16.74(4) cm^{-1} [b]	15.85(7) cm^{-1} [b]	16.49(9) cm^{-1} [b]	16.04(4) cm^{-1} [b]
J_2^{DFT}	0.24 cm^{-1}	0.21 cm^{-1}	0.49 cm^{-1}	0.18 cm^{-1}
J_2^{EXP}	0.05 cm^{-1} [b]	0.37 cm^{-1} [b]	0.40 cm^{-1} [b]	-0.07 cm^{-1} [b]
$Fe_c\widehat{O}Fe_p$	102.8 °	102.3 °	102.1 °	102.3 °

[a] Experimental values taken from [23];
[b] Experimental values taken from [45].

Table 2.2: Isotropic Exchange Coupling Constants Magneto-Structural correlations Analysis.

	Correlation	Slope	Std.Err	Std.Err%
J_{DFT}-J_{EXP}	0.932	1.86	1.80	10.24
J_{DFT}-$Fe_c\widehat{O}Fe_p$	0.991	-	-	-
J_{EXP}-$Fe_c\widehat{O}Fe_p$	0.963	-	-	-

is comparable with experimental findings, reported calculations predict a practically constant antiferromagnetic value for all the J_2 exchange coupling constants.

Anisotropic Single Ions Tensors

The Fe_4Ph molecule has been used as a benchmark to test PBE and PBE0 performances. Presented results are in partial agreement with the study of Duboc *et al.*[51], where they showed that hybrid functionals, like B3LYP, do not lead to a significant increase in accuracy. In this study PBE results by far superior compared to PBE0 for what concerns single ion tensor prediction and, because of that, single ion calculations for the other molecules have been carried out only with PBE. Results are shown in Table 2.3 where the values of axial and rhombic zfs parameters both for the central and peripheral ions are reported, together with Euler angles (ZYZ convention). In this context Euler angles describe the orientation of $\mathbf{D_{SI}}$ (single ion anisotropy tensor) eigenvectors with respect to the natural Cartesian frame of the Fe_4. For convention this reference frame is defined with the z axis parallel to the normal vector of the plane identified by the three peripheral iron ions; y along the $\mathbf{C}_2$ symmetry axis, while the eigenvectors of $\mathbf{D_{SI}}$ are ordered depending on their eigenvalues following the convention: medium-axis = x, easy-axis = y and hard-axis = z. It is clear that

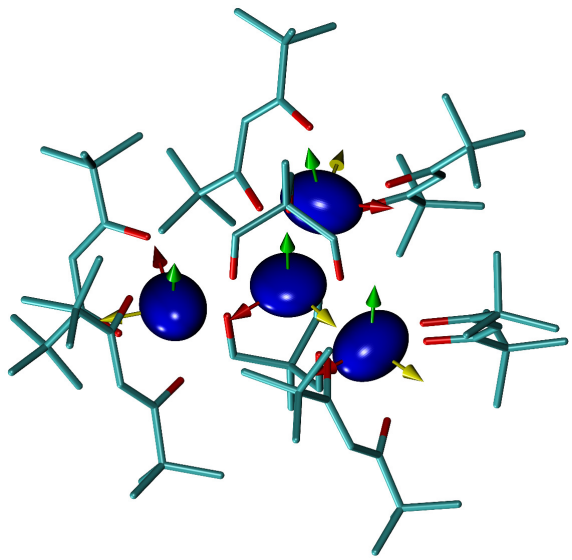

Figure 2.4: Calculated $\mathbf{D_{SI}}$ for Fe_4Me. Prolate ellipsoids stand for easy-plane anisotropies and oblate ellipsoids stand for easy-axis anisotropies. Local tensors eigenvectors were reported as red for the hard direction, yellow for the medium direction and green for the easy direction.

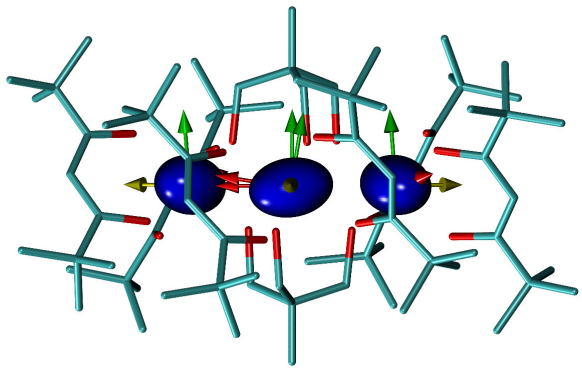

Figure 2.5: Calculated $\mathbf{D_{SI}}$ for Fe_4Me. Prolate ellipsoids stand for easy-plane anisotropies and oblate ellipsoids stand for easy-axis anisotropies. Local tensors eigenvectors were reported as red for the hard direction, yellow for the medium direction and green for the easy direction.

DFT can well reproduce the variations of Fe_c axial anisotropy on the substitution of OMe ligands of **(1)** with one tripodal ligand in **(2)** and with two tripodal ligands in **(3)**-**(8)**. These structural variations, indeed, produce a modification of the trigonal rotation angle ϕ, which enhances the easy axis nature of the central Fe^{3+}. Experimentally all these information about single ion contribution to the global $\mathbf{D_S}$ are quite complicated to be extracted. The only available information are about the peripheral irons and have been extracted from $FeGa_3Ph$ and Fe_3CrMe complexes[24, 52]. These data, reported in Table 2.3, show that DFT can reproduce, with a nice agreement, both their absolute values and their symmetry properties, predicting different D values for the two different kinds of Fe_p. Indeed only one Fe_p lies on the real/idealized C_2 symmetry axis while the other two equivalent irons do not ($Fe_{p'}$).

The direct calculations of single ion tensors, without any *a priori* assumption, allow the description of the non-collinear properties of magnetization easy axis. As expected by symmetry considerations, the easy axis of the central iron is found parallel to the pseudo-$\mathbf{C_3}$ symmetry axis. Since one Fe_p lies on a real/pseudo-$\mathbf{C_2}$ symmetry axis, one

Table 2.3: Calculated Single Ion Anisotropy Tensors and their orientations.

	D[b]			E/D[b]			β'[a]
	Fe_c	Fe_p [c]	$Fe_{p'}$ [c]	Fe_c	Fe_p [c]	$Fe_{p'}$ [c]	
Fe_4OMe	-0.240	1.038	1.028	0.023	0.064	0.061	25
Fe_4tBu	-0.307	0.841	0.841	~ 0	0.062	0.080	22
Fe_4Ph	-1.100	0.728	0.630	0.061	0.160	0.230	13
Fe_4Me	-1.084	0.828	0.848	0.004	0.170	0.148	9
Fe_4C5	-1.105	0.818	0.731	0.033	0.163	0.170	9
Fe_4C4	-1.070	0.555	0.780	0.036	0.258	0.147	7
Fe_4C3	-1.079	0.523	0.766	0.021	0.285	0.726	13
Fe_4C1	-1.072	0.682	0.609	0.005	0.197	0.217	7
Fe_3CrMe[d]	-	0.738(1)	0.738(1)	-	0.087	0.087	5
$FeGa_3$Ph[e]	-	0.710(5)	0.602(5)	-	0.108	0.168	-

[a] $\beta'=|\beta - 90|$ is here reported only for Fe_p;
[b] Values expressed in cm^{-1} and angles expressed in degree;
[c] Fe_p refers to the peripheral iron lying on the pseudo-$\mathbf{C}_2$ and $Fe_{p'}$ refers to irons which do not;
[d] Taken from article [52];
[e] Taken from article [24].

of its eigenvectors is correctly found to lie into the irons plane with its x-axis parallel to the y Cartesian axis, i.e. $\alpha = 0°$ (see Figure 2.4). Since this symmetry conditions is not strictly fulfilled by all the molecules, which have only an idealized $\mathbf{C}_2$ symmetry, some discrepancies have also been found. Indeed, the molecules **(1)** and **(8)** show an α value around 10° instead of $\sim 0°$. The other eigenvectors, corresponding to easy (y) and hard (z) axis, do not have any symmetry constraint and are found to be with the easy axis slightly rotated from the Cartesian z axis of an angle $\beta' = |90 - \beta|$ (see Figure 2.5). Finally, the angle γ is found to be $\sim -90°$. Thanks to the pseudo-$\mathbf{C}_3$ axis perpendicular to the irons plane, the eigenvectors of the two $Fe_{p'}$ are approximately related to the eigenvectors of Fe_p by a rotation of 120°. Recently all these information have become available for the Fe_3CrMe SMM thanks to the single crystal EPR investigation of Sorace *et al.*[52]. In Table 2.3 it is shown that both experimental investigation and these calculations agree on the orientation of the eigenvectors of peripheral irons. I would like to stress out that, in order to correctly and quantitatively predict multi nuclear complexes magnetic properties, it is of great importance not only to reproduce axial and rhombic parameters, but also the tensor eigenvectors orientations, since the tensorial summation operation, needed to extract the global magnetic behavior, strictly depends on all these parameters.

Anisotropic Exchange Coupling Tensors

The spin-spin interaction between different magnetic centers is usually calculated within the point-dipole approximation. In this framework spins interact only through space with an r^{-3} power law. As demonstrated by Riplinger *et al.*[53] for di-radical species and as also observed by Maurice *et al.*[54] for a copper acetate dimer in a computational study, the point-dipole approximation is no longer valid once delocalization and through bond spin-spin interaction occur. In Table 2.4 it is reported the axial value D of $\mathbf{D}_{ij}$ for Fe_4Ph, separated in its spin-spin (D_{SS}) and spin-orbit (D_{SOC}) contributions. Calculations have been done using both PBE and PBE0 functionals. For comparison, the D_{SS} values predicted by the point-dipole formula are also reported.

Table 2.4: Fe_4Ph D_{SOC} and D_{SS}. Comparison between PBE, PBE0 and point-dipole approximation.

	D_{SS} [a]			D_{SOC} [a]	
	PBE	PBE0	Point-Dipol	PBE	PBE0
Fe_c-Fe_p	-0.152	-0.160	-0.179	0.813	-0.219
Fe_c-$Fe_{p'}$	-0.153	-0.160	-0.180	1.040	-0.199
Fe_p-$Fe_{p'}$	-0.032	-0.034	-0.035	0.008	0.133
$Fe_{p'}$-$Fe_{p'}$	-0.034	-0.033	-0.033	0.014	-0.096

[a] Values expressed in cm^{-1};
[b] Fe_p refers to the peripheral iron lying on the $\mathbf{C}_2$ and $Fe_{p'}$ refers to irons which do not.

For what concerns the spin-spin contribution to D (D_{SS}), in Table 2.4 it is possible to note how both PBE and PBE0 give similar results. At the same time they both deviate from the predictions of the point-dipole formula when dealing with strongly exchange coupled irons (Fe_c-Fe_p). As expected, the point-dipole formula predicts values in agreement with DFT only when delocalization effects and through bond interactions are negligible, as for the couples Fe_p-Fe_p. The easy axis of this interaction is correctly predicted parallel to the Fe-Fe direction. Less satisfactory is the determination of the anisotropic exchange interaction D_{SOC}. The only available experimental value for this kind of interaction between Fe^{3+} ions is the one available for an iron dimer[42], where the anisotropic exchange coupling has been estimated to be -0.159 cm^{-1}. With respect to this value PBE completely fails, both for what concerns the sign and the size of the interaction. PBE0 gives a completely different result from PBE and at least the sign of the axial anisotropy parameter is found in agreement. However, also in this case the absolute value of D_{SOC} is overestimated. In Table 2.5 values of D_{SS} for all the molecules have been reported, computed with PBE for the exchange coupled

irons and with point-dipole formula for the others. This receipt will be used for all the next calculations.

Table 2.5: Calculated Exchange Coupling Anisotropy Tensors.

	$\mathbf{D_{SS}}$ [a]		$(\mathbf{E/D})_{\mathbf{SS}}$ [a]	
	Fe_c-Fe_p [b]	Fe_p-Fe_p [b]	Fe_c-Fe_p [b]	Fe_p-Fe_p [b]
Fe_4OMe	-0.145	-0.031	0.070	0.000
Fe_4tBu	-0.147	-0.033	0.074	0.000
Fe_4Ph	-0.152	-0.034	0.086	0.000
Fe_4Me	-0.152	-0.034	0.086	0.000
Fe_4C5	-0.152	-0.032	0.086	0.000
Fe_4C4	-0.151	-0.035	0.087	0.000
Fe_4C3	-0.149	-0.033	0.086	0.000
Fe_4C1	-0.150	-0.034	0.083	0.000

[a] Values expressed in cm^{-1}.
[b] Fe_p here refers to a generic peripheral iron.

Spin Projected Anisotropic Tensors and Magneto-Structural Correlations

Now that the multi-spin nature of the zero field splitting for all the Fe_4 SMMs have been computed, it is possible to collapse all these information into the spin projected anisotropy tensor. The $d_i^{S=5}$ and $d_{ij}^{S=5}$ coefficients could be always numerically evaluated[55] once the isotropic exchange structure is known, by direct diagonalization of the Heisenberg Hamiltonian expressed in a basis set that spans the complete Hilbert space of dimension $\prod_i^N (2s_i + 1)$. Although these systems span point groups from **C1** to **D3**, in all cases the symmetry of the core can be approximated to a pseudo **C3** symmetry. In this framework, it is possible to find a spin coupling scheme ($|\mathbf{s_1}, \mathbf{s_2}, \mathbf{S_{12}}, \mathbf{s_3}, \mathbf{S_{123}}, \mathbf{s_4}, \mathbf{S}>$) which defines a representation that already diagonalizes the Heisenberg Hamiltonian: $|\frac{5}{2}, \frac{5}{2}, 5, \frac{5}{2}, \frac{15}{2}, \frac{5}{2}, 5>$. This basis set is then used to numerically calculate the several projection coefficients which are:

$$\begin{array}{lllll} d_c & = & 0.1282 & d_p & = & 0.1868 \\ d_{cp} & = & -0.1816 & d_{pp} & = & 0.2335 \end{array}$$

These coefficients, together with anisotropic tensors, are then inserted in Equation 2.31 and the results are summarized in Table 2.6. As expected, even if the dominating part of the total axial anisotropy comes from single ion contributions, $D_{SI}^{S=5}$, the spin-spin part is not negligible. This two body interaction is, however, constant along

Table 2.6: Calculated and Experimental Anisotropic Tensors for the S=5 Magnetic Ground State.

	Fe_4OMe	Fe_4tBu	Fe_4Ph	Fe_4Me
$D_{SI}^{S=5}$	-0.158 cm^{-1}	-0.223 cm^{-1}	-0.419 cm^{-1}	-0.462 cm^{-1}
$D_{SI}^{S=5}(c)$	-0.038 cm^{-1}	-0.039 cm^{-1}	-0.141 cm^{-1}	-0.139 cm^{-1}
$D_{SI}^{S=5}(p)$ [c]	-0.128 cm^{-1}	-0.183 cm^{-1}	-0.278 cm^{-1}	-0.323 cm^{-1}
$D_{SI+SS}^{S=5}$	-0.181 cm^{-1}	-0.244 cm^{-1}	-0.442 cm^{-1}	-0.485 cm^{-1}
$D_{EXP}^{S=5}$	-0.206(1) cm^{-1} [a]	-0.270(1) cm^{-1} [a]	-0.421(1) cm^{-1} [a]	-0.445(1) cm^{-1} [a]
$E_{SI+SS}^{S=5}$	0.007 cm^{-1}	0.000 cm^{-1}	0.002 cm^{-1}	0.003 cm^{-1}
$E_{EXP}^{S=5}$	–	–	0.023 cm^{-1} [a]	<0.009 cm^{-1} [a]
$\gamma - pitch$	63.24 °	65.82 °	68.93 °	70.63 °

	Fe_4C5	Fe_4C4	Fe_4C3	Fe_4C1
$D_{SI}^{S=5}$	-0.443 cm^{-1}	-0.417 cm^{-1}	-0.413 cm^{-1}	-0.405 cm^{-1}
$D_{SI}^{S=5}(c)$	-0.142 cm^{-1}	-0.137 cm^{-1}	-0.138 cm^{-1}	-0.137 cm^{-1}
$D_{SI}^{S=5}(p)$ [c]	-0.302 cm^{-1}	-0.280 cm^{-1}	-0.275 cm^{-1}	-0.268 cm^{-1}
$D_{SI+SS}^{S=5}$	-0.467 cm^{-1}	-0.440 cm^{-1}	-0.436 cm^{-1}	-0.428 cm^{-1}
$D_{EXP}^{S=5}$	-0.451(4) cm^{-1} [b]	-0.440(11) cm^{-1} [b]	-0.415(5) cm^{-1} [b]	-0.426(3) cm^{-1} [b]
$E_{SI+SS}^{S=5}$	0.007 cm^{-1}	0.024 cm^{-1}	0.027 cm^{-1}	0.005 cm^{-1}
$E_{EXP}^{S=5}$	–	–	–	–
$\gamma - pitch$	70.45 °	68.41 °	69.42 °	68.84 °

[a] Values from the work of Accorsi *et al.*[23];
[b] Values from Tancini's Ph.D thesis [45];
[c] D_p here stands for the sum of all the three peripheral single ion tensors.

Table 2.7: S=5 Ground State Anisotropic Tensors Magneto-Structural Correlations Analysis.

	Correlation	Slope	Std.Err	Std.Err%
$D^{S=5}_{SI+SS}$-$D^{S=5}_{EXP}$	0.993	1.21	0.014	3.64
$D^{S=5}_{SI+SS}$-γ pitch	0.973	-	-	-
$D^{S=5}_{SI}(p)$-γ pitch	0.986	-	-	-
$D^{S=5}_{EXP}$-γ pitch	0.960	-	-	-

the whole series, as it principally depends on Fe-Fe distances (see Table 2.5). The contribution $D^{S=5}_{SI+SS}$, which includes both single ion and exchange spin-spin contributions, is found to nicely reproduce the experimental $D^{S=5}$ values. The linear regression analysis reported in Table 2.6 shows a very good agreement, indeed. The Std. Error is found to be 0.014 cm^{-1}, which is comparable to experimental errors. The rhombic parameters are found to be much smaller with respect to D values. Only two experimental values are available and they are in qualitative agreement with the computed findings (see Table 2.6). In order to individuate which is the leading contribution to the magnetic ground-state anisotropy, the total $D^{S=5}_{SI}$ value has been decomposed into the Fe_p and Fe_c contributions ($D^{S=5}_{SI}(c)$ and $D^{S=5}_{SI}(p)$, respectively). The Fe_c already possesses an easy-axis single ion anisotropy collinear to the symmetry axis of the entire molecule and so directly contributes to the global $D^{S=5}$. On the contrary, the peripheral irons have an easy-plane anisotropy but they still contribute to the final easy-axis anisotropy value thanks to the orthogonality of their easy-plane with the symmetry axis of the molecule. Indeed, thanks to the pseudo-$\mathbf{C}_3$ symmetry axis, the plane contributions to the final D cancel out and only the easy-axis contribution, that acts in the direction normal to the irons's plane, is effectively enhanced in the sum process. As already noted by Oshio *et al.*[21] this is a general feature about the sum of single ion contributions to the global anisotropy of transition metal clusters and could be exploited in order to obtain easy axis contribution from easy-plane anisotropies. Although the high negative value of the axial anisotropy of Fe_c, its contribution to the global anisotropy is less than 50% of the total Fe_p contributions. Such a result can be explained by the smaller projection coefficient and by the presence of three Fe_p contributions. It is possible to observe a substantial increase of $D^{S=5}_{SI}(c)$ passing from **(1)**-**(2)** to **(3)**-**(8)**, where the pseudo-$\mathbf{C_3}$ symmetry is enforced, but between **(1)** and **(2)** and inside the group **(3)**-**(8)** there are no significant variations of $D^{S=5}_{SI}(c)$ on γ-pitch modulations. On the contrary, $D^{S=5}_{SI}(p)$ not only contributes more than

$D_{SI}^{S=5}(c)$, but it is also responsible for the magneto-structural correlation with γ-pitch as its correlation coefficient attests (see Table 2.6). As discussed in section 2.4, the γ-pitch geometrical parameter combines contributions both from the trigonal rotation of the central iron and from the non-collinearity and different magnitude of anisotropy of the peripheral ones. Since all these contributions are simultaneously modulated through the series in an uncorrelated fashion, the γ-pitch could not explain by itself all the single ion features of the Fe_4 complex. Therefore a complete analysis by means of the multi-spin Hamiltonian, as the one showed in this work, is needed. For the sake of completeness I would also like to make a few comments on the contribution of the anisotropic exchange (SOC contribution) to the global $D^{S=5}$. In section 6.3 it was stated that the PBE functional completely fails on the estimation of this property and thus it was not included in the analysis of the Giant-Spin Hamiltonian for the ground state multiplet. On the contrary, the values of D_{SOC} obtained with the functional PBE0 are in partial agreement with the few experimental findings available in literature. For this reason it has been evaluated a $\mathbf{D}^{S=5}$ tensor composed by $\mathbf{D}_{SI}$ and $\mathbf{D}_{SS}$ contribution from PBE calculations and the SOC contribution to the anisotropic exchange interaction from PBE0 calculation. This procedure have been exploited only for the molecule **(3)**. The resulting axial and rhombic anisotropy parameters are: D=-0.395 cm^{-1} and E/D=0.033. The comparison of these values with those reported in Table 2.6 shows that the introduction of the PBE0 D_{SOC} lowers the axial anisotropy $D^{S=5}$ but with respect to the experimental data the absolute value of the deviation of PBE and PBE0 are similar, 6.2% and 5.0%, respectively. Since the very small amount of both experimental and computational data it is not possible, at this stage, to prove the correctness of the D_{SOC} evaluated from PBE0, and a deeper analysis of this contribution is is provided in the next chapter.

Conclusions

A comprehensive magnetic characterization performed at DFT level for a selected series of star shaped Fe_4 SMMs have been presented. The already established procedure to compute single ion anisotropy tensors has been exploited and extended in order to include the determination of exchange anisotropy tensors, both spin-spin and SOC contributions. It should be also stressed out that this procedure is not only related to the DFT framework, since it avoids BS solutions, but it could be directly used to map every kind of electronic structure calculation to the multi-spin Hamiltonian of Equation 2.14. This means that it shows a practical way to evaluate exchange anisotropy tensors also in the framework of high level post-HF methods like CASSCF/NEVPT2

or CASSCF/DDCI, which will be shown later. This approach differs from the one proposed very recently by Van Wüllen [41] which is based on the exploitation of a number of Broken Symmetry solutions. In this framework, the presented computed multi-spin parameters have been calculated on X-ray structures and a nice agreement has been found with the available experimental findings, supporting the reliability of the computational protocol. Confirmations on the correlation between $Fe\widehat{O}Fe$ angle and the J_1 has been also found. New insights have been brought, instead, to the correlation of the D with the γ-pitch angle. A detailed analysis of the anisotropy parameters led to the conclusion that although the contribution of central iron to the D can be strongly influenced by the tripodal ligands, the main responsible of the different anisotropy properties observed in the series are the peripherals ions. Their contribution comes both from the non-collinearity and from the absolute value of their single ion anisotropy tensors, properties which are simultaneously modulated through the series. Although this work was principally devoted to the determination of the nature of magneto-structural correlations for the Fe_4 SMM, it has been also provided a few information about DFT reliability over the determination of isotropic exchange and ZFS interactions for μ-alkoxo bridged Fe^{3+} ions. Both J and D determination from DFT are found to be quite accurate with Std. errors of 1.80 cm^{-1} for J and 0.018 cm^{-1} for D. In conclusion, the computational protocol here proposed seems to be robust enough to be used also as predictive tool as witnessed by the good results obtained in describing the fine complex magnetic structure of the Fe_4 SMMs series.

2.5 Beyond the Giant Spin Approximation

In the last section the GSA was employed in order to project the single ion and exchange anisotropy tensor on the ground state multiplet. Principles of validity for this procedure have been outlined in the section devoted to the spin hamiltonian formalism, where it was clearly pointed out the importance of the large exchange limit $J >> D$. Although many transition metal clusters usually have exchange interactions much stronger than anisotropy splitting, experimental evidences of GSA breaking exist[52, 56, 57]. These evidences arise in anomalies in EPR experiments which are not accountable with the spin hamiltonian terms coming from the GSA. To reproduce these spectra features the introduction of higher order terms in the GSH is thus needed. The origin of these additional terms has been demonstrated to be connected to the S-mixing[58, 59]. This effect arises from the mixing between MSH solutions with different S^2 expectation value. Indeed, when the isotropic exchange introduce a small multiplet separation, the anisotropic terms of the spin hamiltonian couple them and generate a system which is no longer an S^2 eigenstate.

An intuitive approach to the S-mixing requires a perturbative description of the multi spin hamiltonain anisotropic terms in the giant spin basis set. This procedure readily generalized the perturbative approach exploited by Neese *et al.*[28] to project spin orbit contributions into the usual $H_s = \vec{\mathbf{S}} \cdot \mathbf{D} \cdot \vec{\mathbf{S}}$ hamiltonian and was used for the first time in this context by Liviotti *et al.*[59]. Lets start recalling that the multi spin hamiltonian is connected to the giant spin one through the usual matrix elements mapping relation2.13:

$$\langle SM_S|H_{GS}(S)|SM'_S\rangle = \langle SM_S|H_{MS}(s_1,...,s_N)|SM'_S\rangle \tag{2.58}$$

In order to make clear from a mathematical point of view the origin of these higher order GSH terms lets study the mapping between these two spin hamiltonians

$$H_{MS} = \sum_{ij} J_{ij}(\vec{\mathbf{s}}_i \cdot \vec{\mathbf{s}}_j) + \sum_{ij} \vec{\mathbf{s}}_i \cdot \mathbf{D}_{ij} \cdot \vec{\mathbf{s}}_j \tag{2.59}$$

$$H_{GS} = \sum_{q} B_q^2 T_q^2 + \sum_{q} B_q^4 T_q^4 \tag{2.60}$$

The left side of eq. 2.58 could be evaluated straightforwardly with the aim of the Wigner-Eckart theorem as S^2 commute with H_{GS}. The same it is not possible for the

right side term of eq. 2.58. However, $|SM_S\rangle$ is eigenket of the isotropic part of the MSH and therefore a perturbative approach is applicable. *i.e.* the $H_1 = \sum_{ij} \vec{\mathbf{s}}_i \cdot \mathbf{D}_{ij} \cdot \vec{\mathbf{s}}_j$ part of the hamiltonian on the right side of eq. 2.58 is treated as a perturbation of the reference 0-order hamiltonian $H_0 = \sum_{ij} J_{ij}(\vec{\mathbf{s}}_i \cdot \vec{\mathbf{s}}_j)$. Restraining the formalism at the second order

$$\langle SM_S|H_{MS}|SM'_S\rangle = E_S + \langle SM_S|H_1|SM'_S\rangle \tag{2.61}$$

$$- \sum_{S''M''_{S''}} \frac{1}{\Delta_{S''S}} \langle SM_S|H_1|S''M_{S''}\rangle\langle S''M_{S''}|H_1|SM'_S\rangle \tag{2.62}$$

For infinite exchange $\Delta_{S''S} \to \infty$ the GSA scenario (see eq. 2.23) is obtained and it thus could be considered as the first order approximation of a general treatment of the S-mixing. In order to show that a MSH containing second order terms is able to give rise to giant spin hamiltonian of the kind $B^4_q T^4_q(S)$, let's decompose $T^4_q(S)$ by means of the projection theorem into two second order terms:

$$T^4_q(S) = \sum_{q_1 q_2} \langle 4q, 22|1q_1, 1q_2\rangle T^2_{q_1}(S) T^2_{q_2}(S) \tag{2.63}$$

Including this transformation in the left side matrix element of eq. 2.58

$$\langle SM_S|H_{GS}(S)|SM'_S\rangle = \sum_q B^4_q \langle SM_S|T^4_q(S)|SM'_S\rangle = \tag{2.64}$$

$$\sum_q B^4_q \sum_{q_1 q_2} \langle 4q, 22|1q_1, 1q_2\rangle \sum_{M''} \langle SM_S|T^2_{q_1}(S)|SM''_S\rangle\langle SM''_S|T^2_{q_2}(S)|SM'_S\rangle \tag{2.65}$$

This last relation is of the correct algebraic form to be compared with the last term in eq. 2.62. However it is not already clear how the mapping could be done. In order to do that the last term in eq. 2.62 should be converted in a form which present explicitly the part $\sum_{M''} \langle SM_S|T^2_{q_1}(S)|SM''_S\rangle\langle SM''_S|T^2_{q_2}(S)|SM'_S\rangle$. In order to get this result let's start considering only the S" excited states equal to S. In this case

$$\langle SM_S|H_1|SM''_S\rangle\langle SM''_S|H_1|SM'_S\rangle = \tag{2.66}$$

$$\sum_{ij} \sum_{q_1 q_2} B^2_{q_1}(s_i s_j) B^2_{q_2}(s_i s_j) \langle SM_S|T^2_{q_1}(s_i s_j)|SM''_S\rangle\langle SM''_S|T^2_{q_2}(s_i s_j)|SM'_S\rangle \tag{2.67}$$

The conversion of $\langle SM_S|T^2_{q_1}(s_is_j)|SM''_S\rangle$ and $\langle SM''_S|T^2_{q_2}(s_is_j)|SM'_S\rangle$ into functions depending only on the total spin variable S could be accomplished thanks to relations

$$\langle SM_S|T^2_q(s_is_j)|SM''_S\rangle = \langle SM_S|T^2_q(S)|SM''_S\rangle \frac{\langle SM_S||T^k(s_is_j)||SM'_S\rangle}{\langle SM_S||T^k(S)||SM'_S\rangle} \tag{2.68}$$

Inserting this last relation into 2.67 and then into 2.62

$$\sum_{S''=S}\sum_{M_{S''}} \frac{1}{\Delta_{S''S}}\langle SM_S|H_1|S''M_{S''}\rangle\langle S''M_{S''}|H_1|SM'_S\rangle = \tag{2.69}$$

$$\sum_{q_1q_2}\sum_{ij}\sum_{S''=S} \frac{B^2_{q_1}\sum(s_is_j)B^2_{q_2}(s_is_j)}{\Delta_{S''S}} \frac{\langle SM_S||T^k(s_is_j)||SM'_S\rangle}{\langle SM_S||T^k(S)||SM'_S\rangle} \tag{2.70}$$

$$\sum_{M''}\langle SM_S|T^2_{q_1}(S)|SM''_S\rangle\langle SM''_S|T^2_{q_2}(S)|SM'_S\rangle \tag{2.71}$$

and finally, matching the expressions 2.65 and 2.71

$$\sum_q B^4_q\langle 4q,22|1q_1,1q_2\rangle = \tag{2.72}$$

$$-\sum_{ij}\sum_{S''=S} \frac{B^2_{q_1}\sum(s_is_j)B^2_{q_2}(s_is_j)}{\Delta_{S''S}} \frac{\langle SM_S||T^k(s_is_j)||SM'_S\rangle}{\langle SM_S||T^k(S)||SM'_S\rangle} \tag{2.73}$$

Before to proceed another discussion of the perturbation treatment just presented is required. The second order perturbation expression of the MSH has been mapped to the fourth order GSH thanks to the spherical tensor projection theorem. However, this was not the only possible choice as from the sum of two second order spherical tensors is possible to generate all the spherical tensors of order between 0 and 4. In this scenario a generalization of the expression 2.73 to

$$\sum_q B^2_q\langle 2q,22|1q_1,1q_2\rangle + \sum_q B^4_q\langle 4q,22|1q_1,1q_2\rangle = \tag{2.74}$$

$$-\sum_{ij}\sum_{S''=S} \frac{B^2_{q_1}\sum(s_is_j)B^2_{q_2}(s_is_j)}{\Delta_{S''S}} \frac{\langle SM_S||T^k(s_is_j)||SM'_S\rangle}{\langle SM_S||T^k(S)||SM'_S\rangle} \tag{2.75}$$

is thus possible. This argument shows that S-mixing not only generates higher order GSH terms but it also affects the regular second order ones. Similar expressions to 2.73 and 2.75, for cases with $S'' \neq S$, could be derived but the algebra is much more involved and cumbersome. The same issue particularly applies to the study of higher order perturbation theory and for practical purpose a different approach for the higher order giant spin terms determination is needed. The simpler one follows the same procedure outlined in the first section of this chapter to fit the electronic energy ladder with a single spin hamiltonian. Here, the low lying spectrum obtained from the diagonalization of the MSH could be fitted with a generalized GSH, through a simple linear least square approach.

The Fe_3Cr SMM has been used to study experimentally the origin of higher order giant spin hamiltonian terms inside the helical-pitch SMM family[52]. This compound is structurally identical to the Fe_4 system except for substitution of the central Fe ion with a Cr^{+3} one. Magnetic interactions inside the magnetic core of this molecules are very similar to the original Fe_4 one and lend to this SMM an S=6 ground state and an easy axis global anisotropy. This molecule could be used as benchmark system to analyse the effect of S-mixing, their correlation with the non collinearity of peripheral iron ion easy axis and their magnitude dependency from the main isotropic exchange coupling constant linking the central chromium and the peripheral iron ions. In order to study the effect of S-mixing on the Fe_3Cr the experimental D_{3h} symmetry adapted multi spin hamiltonian parameters are going to be used. The second order anisotropic tensors of the peripheral iron ions have also been realigned with the C_3 symmetry axis of the molecule *i.e.* the β' angle of the latter discussion on the Fe_4 series has been set to zero. The mapping with the GSH has been done through a direct fit of the first 2S+1 (with S=6) roots of the diagonalization of this hamiltonian. The GSH has been chosen to contain second, fourth and sixth order terms.

$$H_{GS} = \sum_q B_q^2 O_q^2(S) + \sum_q B_q^4 O_q^4(S) + \sum_q B_q^6 O_q^6(S) \tag{2.76}$$

Starting from the study of GSH parameters dependence on the excited states energy splitting, fig. 2.6 shows the residual sum of square for the fit as function of the isotropic exchange coupling constant between the chromium ion and the peripheral iron ions. Notably, the accuracy of the fitting increases as the energy separation with the excited states increases, showing that despite the introduction of fourth and sixth order giant spin operator the fit of the low lying part of the multi spin spectrum could not be exactly be fitted by a generalized giant spin hamiltonian unless the GSA

validity is approached.

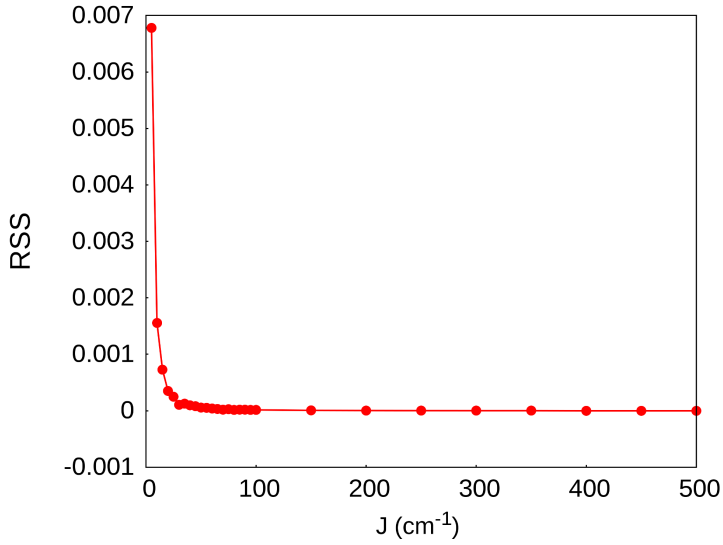

Figure 2.6: Residual sum of squares resulting from the least square linear fit of the giant spin hamiltonian.

Fig. 2.7, 2.8 and 2.9 reports the evolution with J of the norms of the second, fourth and sixth order giant spin operators, respectively.

All of these three trends show a remarkable $\sim 1/J$ behavior, which approaches zero in the second and third case and approaches a finite value for the second order case. The 1/J behavior is in line with the second order perturbative approach used above to introduce the S-mixing effect. Moreover, as pointed out in the same discussion, it is here demonstrated that the S-mixing does not only introduce higher order giant spin terms in the spin hamiltonian but also affects the second order ones predicted by the GSA. One interesting consequences of this last effect is that the S-mixing introduces every kind of terms in the spin hamiltonian, symmetry forbidden included. Eq. 2.75 could help to shed some light on this last point. According to Sorace *et al.*[52], for the D_{3h} symmetry of the problem under study, the only allowed fourth order terms would be the $B_0^4(S)$ $B_3^4(S)$ but, according to relation 2.73, the term $B_4^4(S)$ would be non zero unless all the second order $B_2^2(s_i)$ terms are zero. Indeed, in this symmetry, the sum of $B_2^2(s_i)$ terms must cancel out, but the sum of their square is not. Similar arguments could be applied to the $B_2^2(S)$ terms which in fact become zero, as symmetry requires,

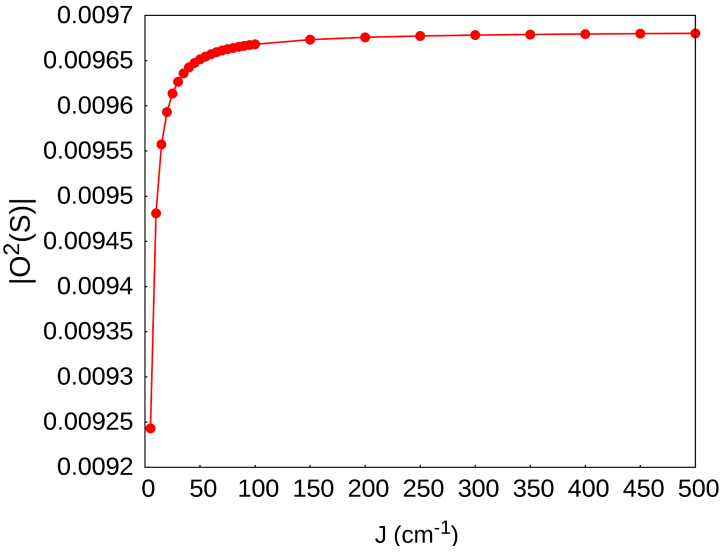

Figure 2.7: Second order giant spin tensor operator norm.

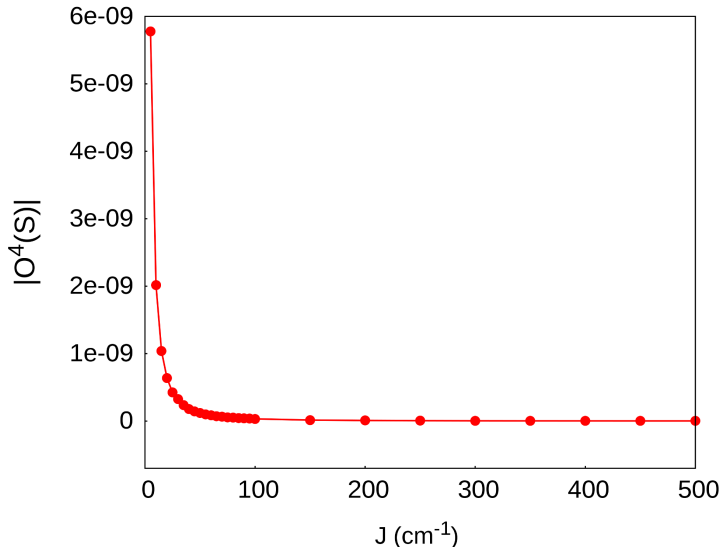

Figure 2.8: Fourth order giant spin tensor operator norm.

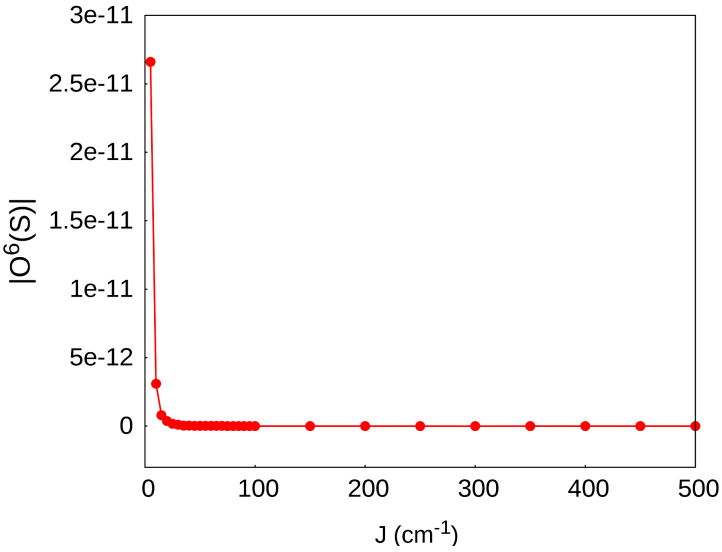

Figure 2.9: Sixth order giant spin tensor operator norm.

only in the $J \to \infty$ limit, where only first order terms of eq. 2.62 becomes relevant. Fig. 2.10 and 2.11 show these effect as dependence of J.

Notably, not all the singular terms of the giant spin hamiltonian converge to zero as 1/J but some of them experiences an oscillatory behavior superimposed to the decaying one, see for instance the $O_1^2(S)$ behavior reported in fig. 2.12.

This symmetry breaking effect might seem counter intuitive but it must be stressed out that the mapping of GSH in the presence of S-mixing effect is not formally strictly correct. Indeed, these terms are partially spurious and should be considered as mere additional fitting parameters needed to mimic the effects of excited states mixing with the ground state multiplet. As also pointed out by the RSS trend, the mapping is never completely fulfilled and this is because the fit with a GSH required a spin purification of the MSH eigenkets, operation which inevitably spoils part of the information provided by the MS description of the system. At this stage a comment on the work by Liu *et al.* is necessary[60]. In this paper the authors essentially present the same analysis just made but for a Mn_3 cluster with C_3 symmetry. Although the similarity of these problems, Liu and co-workers differently conclude that in zero field the only appearing giant spin terms are those allowed by symmetry, in contrast with the just showed findings. This difference essentially comes from the method used to extract

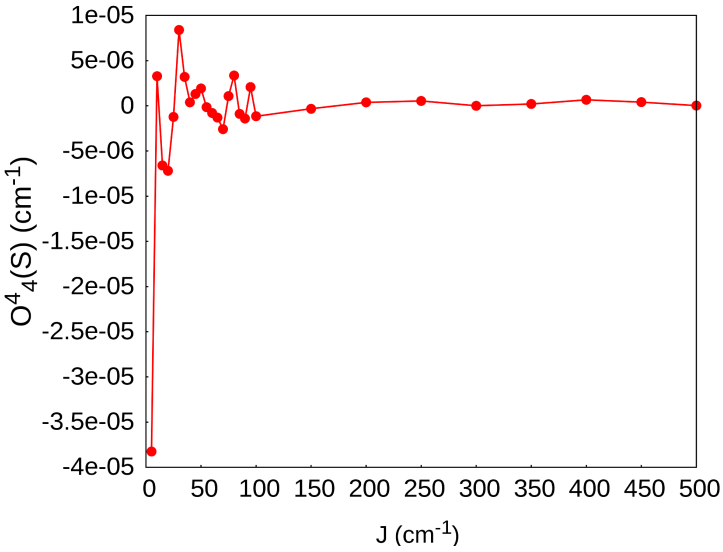

Figure 2.10: $O_4^4(S)$ behavior as function of isotropic exchange coupling J between chromium and peripheral ion ions.

these parameters. Indeed, Liu and co-workers use only the energy ladder obtained by the diagonalization of the multi spin hamiltonian and they did not introduce any information in the fitting about the eigenstates. The higher order GSH terms like O_0^4 and O_6^6 had been calculated according to the splitting between the $S_z = \pm 6$ and $S_z = \pm 3$ states and according to the the avoided crossing of all the other doublets all the other GSH terms had been excluded in the absence of non-collinearity between the C_3 symmetry axis and the single ion axial contributions. Accordingly, the simulations conducted over the Fe_3Cr with $\beta' = 0$ show a spectrum with the most important splitting between $S_z = \pm 6$ and $S_z = \pm 3$, however, a very small, but still over the machine precision, splitting is calculated for all the other states. More importantly, all the MSH eigenvectors show a deviation from the expected S_z eigenvalue, accordingly with the presence of S-mixing. The fitting method exploited here is based on the mapping of both eigenvalues and eigenvectors of GSH and MSH and it is therefore able to capture entirely the effect of S-mixing, the one contained in the eigenvectors included.

This analysis also points out the non necessity of non collinearity between easy axis of the peripheral ions, as it was excluded by construction. However, the dependence of S-mixing effects and non collinearity has been studied in order to access possible magneto structural correlations. The modulation of the giant spin operator norm by the

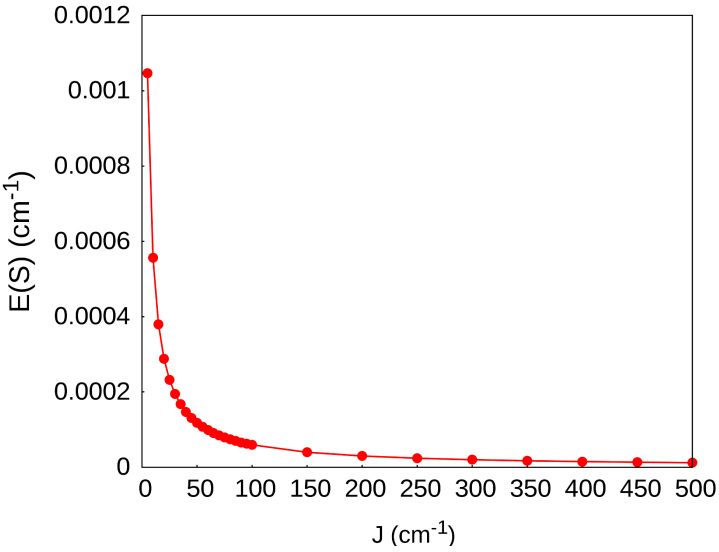

Figure 2.11: Rhombic term E behavior as function of isotropic exchange coupling J between chromium and peripheral ion ions.

angle β' shows an oscillating behavior for all the orders considered demonstrating the importance of the non collinearity over the S-mixing effect. These results could also be used to extract higher order GSH parameters in a DFT framework. Indeed, assuming that the multi spin hamiltonian already contains all the information about the spin system, the higher order spin hamiltonian terms completely comes from the S-mixing effect and could be easily calculated from single ion and exchange anisotropies.

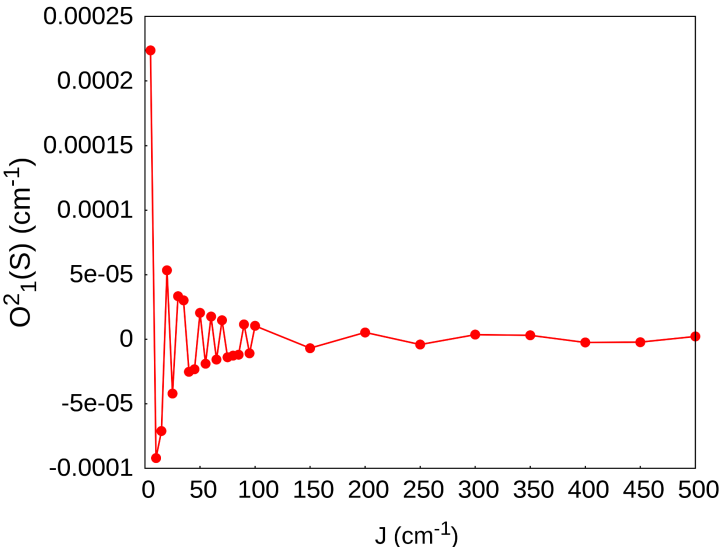

Figure 2.12: $O_1^2(S)$ behavior as function of isotropic exchange coupling J between chromium and peripheral ion ions.

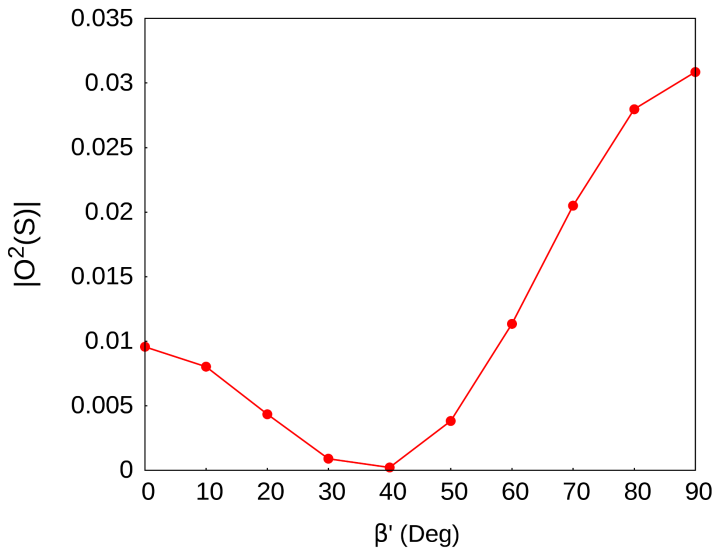

Figure 2.13: $O_q^2(S)$ norms behavior as function of the β' angle accounting for non collinearity.

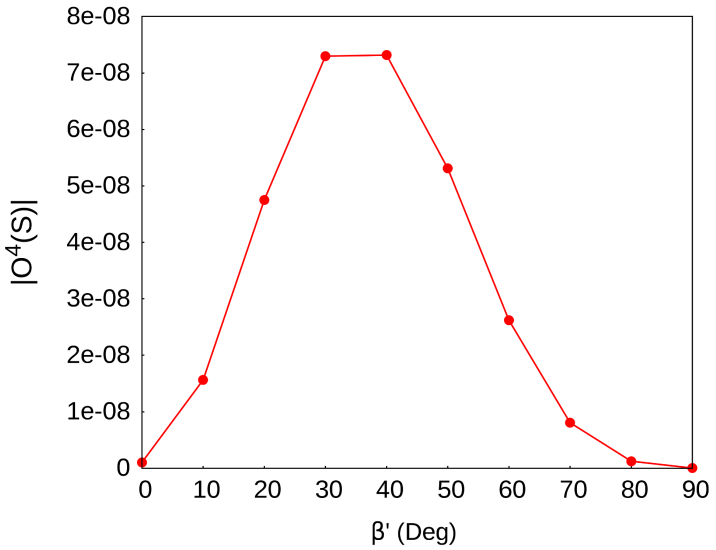

Figure 2.14: $O_q^4(S)$ norms behavior as function of the β' angle accounting for non collinearity.

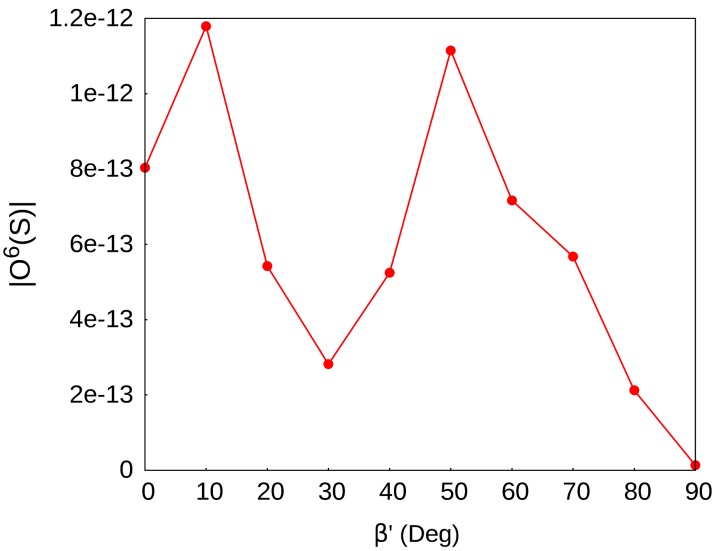

Figure 2.15: $O_q^6(S)$ norms behavior as function of the β' angle accounting for non collinearity.

Conclusions

A numerical investigation on the entity of higher order giant spin hamiltonian terms coming from the S-mixing effect in polynuclear clusters have been done exploiting the experimentally available Fe_3Cr spin hamiltonian parameters. This analysis, supported by perturbation theory arguments, shows that the best giant spin hamiltonian that fits the reference multi spin hamiltonian is affected by a symmetry breaking which is resolved only in the infinite exchange limit. Moreover, it has been proved that the S-mixing affects also the second order terms directly determined by the multi spin hamiltonian by means of the GSA. In the infinite J scenario the GSA approximation becomes both formally and quantitatively established and the mapping between the two kind of hamiltonian becomes exact. However, in a more realistic regime, where the isotropic interactions have a finite value, the giant spin hamiltonian and the multi spin one could never be exactly matched, due to the spin purification of the multi-spin low lying eigenstates spin components needed for their mapping.

2.6 Fe_2 Anisotropic Exchange

So far, many efforts have been devoted to the study of various spin hamiltonian terms that contribute to the Fe_4 family spectrum. Among them the most elusive one is by far the hamiltonian concerning the anisotropic exchange interaction. Although this interaction is generally neglected in the interpretation of experiments, this is not always correct and especially for those systems where single ion anisotropies not necessarily dominate the low lying part of the spin spectrum, this interaction might plays a fundamental role. Nevertheless helical pitch complexes fall inside this last category, the inclusion of anisotropic exchange in their spin hamiltonian has been attempted only recently[61]. As shown in the section 2.3 of this chapter, a possible route to its computation has been presented but unfortunately a conclusive claim about the goodness of its applicability has not been possible. The reason mainly lies in the lack of benchmark references, both of experimental and computational origin. In order to get some more insights on the importance of this interaction on Fe_4 like systems the most valuable strategy concerns the application of high level of theory with respect to DFT. Unfortunately this is not possible for system as big as the whole Fe_4 SMM and the study must be restrained to its most characteristic fragments. In this section the anisotropic exchange interaction for an high spin Fe^{+3} molecular dimer will be calculated through the methodology early described both at DFT and post Hartree Fock level of theory. The Fe^{+3}-oxo dimer $Fe_2(OCH_3)_2(dbm)_4$ with Hdbm = dibenzoylmethane (Fe_2 from now on) has been chosen as benchmark system mimicking the Fe_c-Fe_p inside the Fe_4 SMM structure (fig. 2.16 reports its structure). An experimental EPR study of Fe_2 shows that this system behaves as two S=5/2 iron ions whose spectrum is well described by the spin hamiltonian[42]

$$H_s(s_1, s_2) = J_{12}(\vec{\mathbf{s}}_1 \cdot \vec{\mathbf{s}}_2) + \vec{\mathbf{s}}_1 \cdot \mathbf{D}_{12} \cdot \vec{\mathbf{s}}_2 + \vec{\mathbf{s}}_1 \cdot \mathbf{D}_{11} \cdot \vec{\mathbf{s}}_1 + \vec{\mathbf{s}}_2 \cdot \mathbf{D}_2 \cdot \vec{\mathbf{s}}_2 \tag{2.77}$$

The leading interaction is the isotropic interaction J_{12} whose value is ~ 15 cm^{-1}. For symmetry reasons single ion anisotropic terms are equal and of the easy plane kind. The anisotropic exchange has been estimated to be of the same order of magnitude of the single ion term suggesting its importance in the final contribution to the magnetic behavior of this paramagnetic complex.

The DFT computation follows exactly the same procedure for Fe_4 series and requires the knowledge of both single ion tensors $\mathbf{D}_1$ and $\mathbf{D}_2$, evaluated through diamagnetic Ga^{+3} ions substitution, and the high spin S=5 anisotropy tensor $\mathbf{D}_{S=5}$. The same quantity have been calculated also with complete active space self consistent field

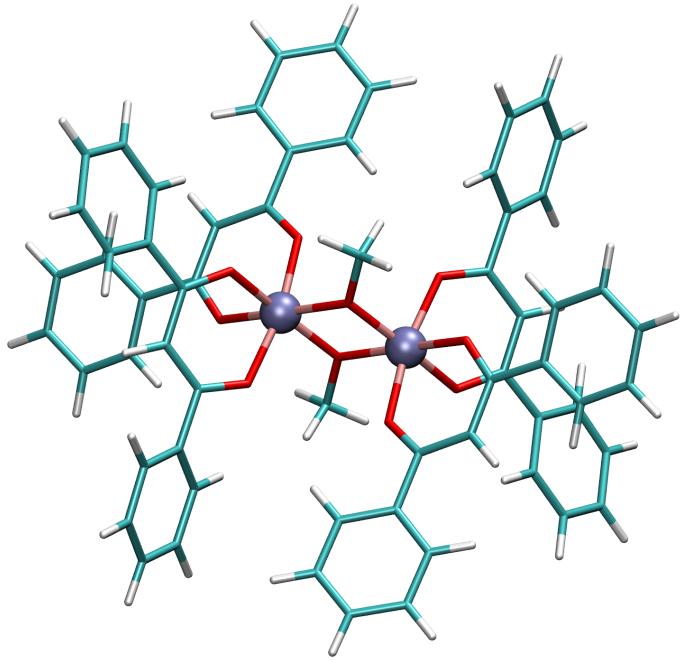

Figure 2.16: Fe_2 X-ray structure. Color code. Fe blue, O red, C green and H white.

(CASSCF) plus N-electron valence perturbation theory (NEVPT2) correction of the hamiltonian diagonal elements. The solutions obtained from this procedure have been then used to diagonalize the spin orbit coupling operator and, in the context of nearly degenerate perturbation theory (QDPT), the 2S+1 solutions of interest have been used as model space to fit the spin hamiltonian. For the CASSCF calculation of the electronic structure of the doped system a (5,5) active space including all d-like orbitals and the five unpaired electrons have been used and the sextuplet, all triplet and all doublet solutions have been included into the QDPT. While this strategy for extracting transition metal single ion anisotropy has already been widely validated[19], calculations on multi ion transition metals is still in its early stage and no practical guidelines are available in literature. So far, only active spaces extended over the d-like MOs have included in this kind of calculation and the same approach will be followed here in order to limit the already big computational demand[54, 62]. Nevertheless, as pointed out by many papers concerning the isotropic part of the

exchange, the inclusion of the MOs participating to the superexchange interaction might be fundamental. Such extension of the active space would be unaffordable and the effect of the ligand MOs correlation is included only at the perturbative level through NEVPT2 correction. For the DFT situation, the choice to project the D tensor on the high spin multiplet solution was forced but the impossibility of DFT to reproduce intermediate spin states but postHF calculations grant the access to each spin multiplicity. Although the choice of the spin multiplet where to project the D tensor is arbitrary, the high spin solution remains the most practical pathway as it is the one with the lower number of excitations. Moreover, as already discussed, this is also the solution less affected by S-mixing problems and therefore it is much more prone to be included in a spin hamiltonian mapping. On light of this discussion, only all the possible two higher spin multiplicity excitations have been introduced into the CASSCF plus QDPT machinery. CASSCF plus NEVPT2 calculation of the electronic structure makes also possible to extract the isotropic exchange coupling constant from the energy splitting between the S=10 and S=9 multiplet. Among the many S=9 solutions the one that should be considered for this purpose is the one corresponding to two misaligned local s=5/2 spins *i.e.* the solution with the biggest weight on determinants comprehending only on site excitations. At the CASSCF level, before applying the NEVPT2 corrections, this S=9 solution has the lowest energy among the whole S=9 multiplet and the isotropic exchange coupling constant J_{12} is -9.12 cm^{-1} and thus ferromagnetic, in net contrast to the experimental antiferromagnetic value. After the application of NEVPT2 correction, the S=11 and S=9 swap and J_{12} becomes 5.32 cm^{-1}. This value is still an underestimation of the experimental $\sim$15 cm^{-1} but the sign is recovered. Possible strategies to further improve this result would require the introduction of dictated CI procedure on top of the CASSCF instead of NEVPT2, but the computational demands for these treatments would require further fragmentation of the system and will not be addressed here. Table 2.8 reports all the results for both DFT and postHF anisotropy calculations and their respective experimental values. First of all it must be pointed out that experimental single ion value contains both spin-spin and soc contribution while the computed ones retain only soc contributions. Nevertheless, the lacking spin-spin contribution could not account for the big difference between the two and both DFT and postHF simulations underestimate the single ions contribution. As noted for the Fe_4Ph system, DFT overestimates the anisotropic exchange contribution while postHF methodologies give a result in good agreement with the experimental one both in sign and magnitude.

Table 2.8: Calculated Single Ion and Anisotropic Exchange Anisotropy Tensors.

	D_{SI}	E_{SI}/D_{SI}	D_{EX}	E_{EX}/D_{EX}	D_{HS}	E_{HS}/D_{HS}
DFT(PBE0)	0.231	0.321	-1.902	0.090	-0.484	0.170
postHF	0.329	0.113	-0.108	0.321	0.173	0.112
Exp.	0.749	0.097	-0.159	0.176	–	–

Conclusions

From a computational point of view, these results demonstrate that postHF calculation of magnetic properties is a valuable tool for qualitative and quantitative predictions and its increased computational cost, with respect to DFT, is well payed back by its robustness. Concerning the practical side of this study, the non negligible importance of the anisotropic exchange coupling inside iron-oxo dimers has been confirmed. Indeed, this interaction is found of the same order of magnitude of the single ion one and it might represents a fundamental ingredient to play with in the tailoring of SMM magnetism. This last point is particularly important as the most fruitful strategy to increase the global anisotropy barrier of a multi spin SMM has been showed to be the control of specific building block anisotropies, more than just increases the total S values.

2.7 Cr_5 EMACs

In the last sections I showed the ability of DFT to reproduce iron cluster magnetic properties. Results for single ion anisotropy and isotropic exchange parameters are exceptionally good and a qualitative agreement is achieved only for anisotropic exchange calculations. However, the good quality of these results is in striking contrast with the few DFT computed values available in literature, where even single ion properties usually carry errors much higher than a few percentage points. The explanation lies in the electronic structure of the transition metal considered. Indeed, so far, all the calculations presented concern Fe^{+3} ion properties. This ion has an S=5/2 ground state arising form a completely half-filled d shell, giving a total symmetric ground state. The absence of angular momentum degeneracy *i.e.* almost no static correlation contributions, makes the Fe^{+3} ions as the best candidates to be treated at the DFT level of theory. In this section I will show results for a different transition metal in order to highlight DFT limits in the prediction of spin hamiltonian parameters and the need to employ higher level of theory for a much robust computational strategy.

Extended metal atom chains (EMACs) are a class of transition metal clusters characterized by a linear arrangement of the paramagnetic ions. The interest in this class of compound has many origins that range from a classic chemical point of view, with the study of metal metal multiple bond nature, to a more practical side, concerning possible applications in the molecular magnetism based device realm. Last but not least, the big synthetic versatility of this class of compounds offers the possibility to engineer both ligands and metallic core nature, resulting in a valuable tool for a systematic study of all the properties listed above. In the context of this thesis I will focus on the description of their electronic structure as propaedeutic step for the following discussion about their magnetic properties. Specifically, the molecules studied are two synthetic variants of the Cr_5 system. The metallic core of these systems is made by five Cr^{+2} ions arranged in a linear fashion. Each ion is coordinated by four azo-ligand lying in perpendicular planes to the metal chain direction. Along the metal axis, each ion saturates its octahedral coordination by two Cr^{+2} ions, except for the two terminal ions whose pseudo octahedral coordination shell is completed by one L^- ligand each. Results for L^-=Cl^-,SCN^- will be discussed.

Clearly, the magnetic behavior of these compounds is strongly related to the number of unpaired electrons and consequently to the nature of the metal-metal bonds inside the chain. Chromium clusters are the prototype of multiple metal metal bond compounds and the existence of fourth order multiple bonds in chromium dimers is

commonly belief on the basis of their diamagnetism and short metal-metal distance. From a computational point of view this claim has been partially reviewed and the presence of a slightly lower bond order has been demonstrated[63]. The origin of this discrepancy lies on the very low energy lying nature of the δ^* molecular orbital in the Cr dimer, which is slightly occupied by means of electronic correlation effects, resulting in a partial lowering of the bond order. As the bond order is critically correlated to intra metal distance, in order to predict EMAC magnetic and electronic structure features, the knowledge of high quality structural parameters is mandatory. In this context, conflicting claims about EMAC structure have been reported in literature. The PES shallow nature along the metal chain direction makes the assessments of the intra-metal distance quite challenging from both experimental and computational points of view and a short assay of available results from literature is here required. A comprehensive study on Cr_3 EMACs[64] showed the occurrence of three different bond patterns inside the chromium trimer depending on the degree of symmetry between the two Cr-Cr bonds: symmetric and slightly or largely asymmetric. The modulation between the three possible structures occurs with the interchanging of the two axial terminal ligands according to their ligand field effect. Ligands favoring a large d orbital splitting as CN^- give symmetric structures while weak σ ligands produce asymmetric structures with one very short metal metal distance. Intermediate σ donors as Cl^- and SCN^- produce less asymmetric structures. The Cr_5Cl molecule can be regarded as a Cr_3Cl molecule where an axial Cl^- is substituted by a ligand made by a chromium dimer[65] and, according to literature[66], the alternating intra-metal spacing demonstrates the weak σ donor power of the Cr_2Cl building block. Moreover, magnetic studies on this compound reveled an S=2 ground state which, together with the structure analysis, suggests that two chromium couples are involved in a fourth order bond each, while the fifth Cr ion is single bonded to a Cr-Cr couple. Interestingly, Cr_5Cl behaves as a SMM under external applied field thanks to a D=-1.6 cm^{-1} and a E/D$\sim$ 0[67]. The high axial symmetry felt by the metallic ions makes this system a good candidates for typical SMM applications, but in order to enhance its property even further a better knowledge about the origin of its magnetic behavior it is mandatory. Specifically, the dependence of the whole magnetic properties of the EMAC on the terminal high Cr^{+2} ion and its small coupling to the diamagnetic chromium couples must be proved. A detailed knowledge of EMAC magnetic and electronic structure would also pave the ground for a rational engineering of its properties.

Cr_5X Structure Optimization

X-Ray diffraction techniques have been used to determine Cr_5Cl and Cr_5SCN structures. The structure of Cr_5Cl have been reported multiple times and a common agreement on the presence of alternating short and long CrCr distances is reported in literature. Although Cr_5SCN structure is expected to have an isostructural core to the Cr_5Cl one, the Cr-Cr distances show instead a symmetric pattern evidenced by the crystallographic analysis[68]. However, the interpretation of X-ray results for this class of system is not always straightforward and to shed some light on the structural properties of the two systems their geometries have been optimized. Despite CASSCF calculations would be preferable in this case (*vide infra*), the computational demand for a structure optimization at this level of theory is too high and DFT is the only tool able to tackle such problem.

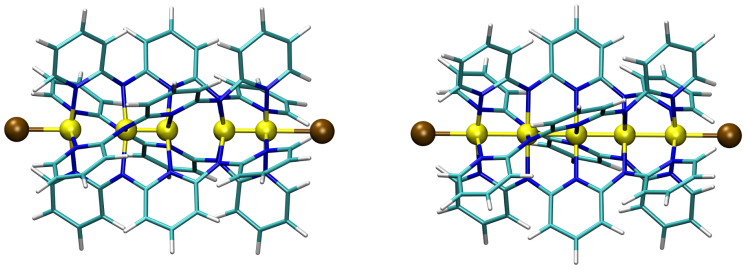

Figure 2.17: Cr_5Cl asymmetric and symmetric optimized structures. Chromium ions are numbered from 1 to 5 from left to right.

Cr_5Cl and Cr_5SCN structures have been optimized with both symmetric and asymmetric Cr-C bonds arrangements as starting geometries. Accordingly with literature, the energy difference between these structures is very small and because of the shallow form of the PES, DFT does not let the structure evolve significantly during the optimization and both minima are found stable at this stage. However, as expected by precedent works, the asymmetric structures have been found as the most stable of about 2.5 kcal/mol for both compounds, in agreement with the discussion above (see Fig. 2.17). The same optimizations have also been carried out with the inclusion of CH_2Cl_2 solvent effects through the COSMO model but not appreciable differences have been noted. Structural parameters of interest are reported in Table 2.9. The difference between Cr-Cr distances with L=Cl or L=SCN are not significant and they show the same trend for the symmetric and asymmetric species. Symmetric species shows the two inner Cr-Cr distances shorter than the outer two. The asymmetric

molecules show two short Cr-Cr distances of about 1.9 Å, a computed value which is in agreement with the usual distance associated to a fourth order bond.

Table 2.9: Chromium Intra-Chain Distances.

	Cl				**SCN**			
	Cr_{1-2}	Cr_{2-3}	Cr_{3-4}	Cr_{4-5}	Cr_{1-2}	Cr_{2-3}	Cr_{3-4}	Cr_{4-5}
Symmetric	2.32	2.21	2.22	2.31	2.33	2.20	2.22	2.31
Asymmetric	2.55	1.86	2.60	1.90	2.55	1.87	2.60	1.91

Figs. 2.18, 2.19 and 2.20 report unrestricted natural orbitals (UNOs) at the end of the optimization for the asymmetric Cr_5Cl structure (Cr_5SCN are qualitatively the same). This kind of orbitals are not associated with any single particle energy, like the corresponding unrestricted Kohn-Sham canonical molecular orbitals, but provide the information about the mean occupation number of electrons associated with a specific spatial single particle density probability. In this framework, UNOs fractional occupation numbers are well defined and points out correlation effects. UNOs show an almost complete separation between orbitals of Cr_1 with those of the Cr_{2-5} unit. This result is in line with the long distance between Cr_1 and Cr_2 ions. Unrestricted natural orbital occupation numbers show that the σ, π, π, δ orbitals of the Cr_{2-5} unit are sensibly less than completely filled (13 out of 16 electrons) and at the same time the anti boding orbitals are more than totally empty by the same amount of electrons. However, occupation number of d like UNOs localized on Cr_1 show a half occupation except for the $d_{x^2-y^2}$ which is totally empty. This result suggests that Cr_5 could be considered as the superposition of two sub units, which are only marginally interacting between them. Only Cr_1 d_{z^2} like UNO is slightly delocalized over the Cr_{2-5} part of the chromium chain. Although the same consideration are valid for the Cr_{2-3} and Cr_{4-5} units, their d_{z^2} like UNOs are totally mixed due to their shorter bond. However, all these features could be exploited in order to rationalize EMACs behavior on the basis of sub unit magnetism.

Unrestricted natural orbitals for the symmetric Cr_5Cl optimized structure (Cr_5SCN are qualitatively the same) are reported in figs. 2.21, 2.22 and 2.23. Although the occupation numbers follow the same pattern as in the asymmetric situation, the UNOs shape is completely different. The saparation of UNOs observed in the previous example is completely lost and the one particle electronic density is spread all over

the five Cr ions. Notably, the singly filled UNOs are made by d like orbitals located on the Cr_1,Cr_3 and Cr_5. This particular configuration might imply a completely different anisotropic magnetic behavior with respect to the asymmetric case.

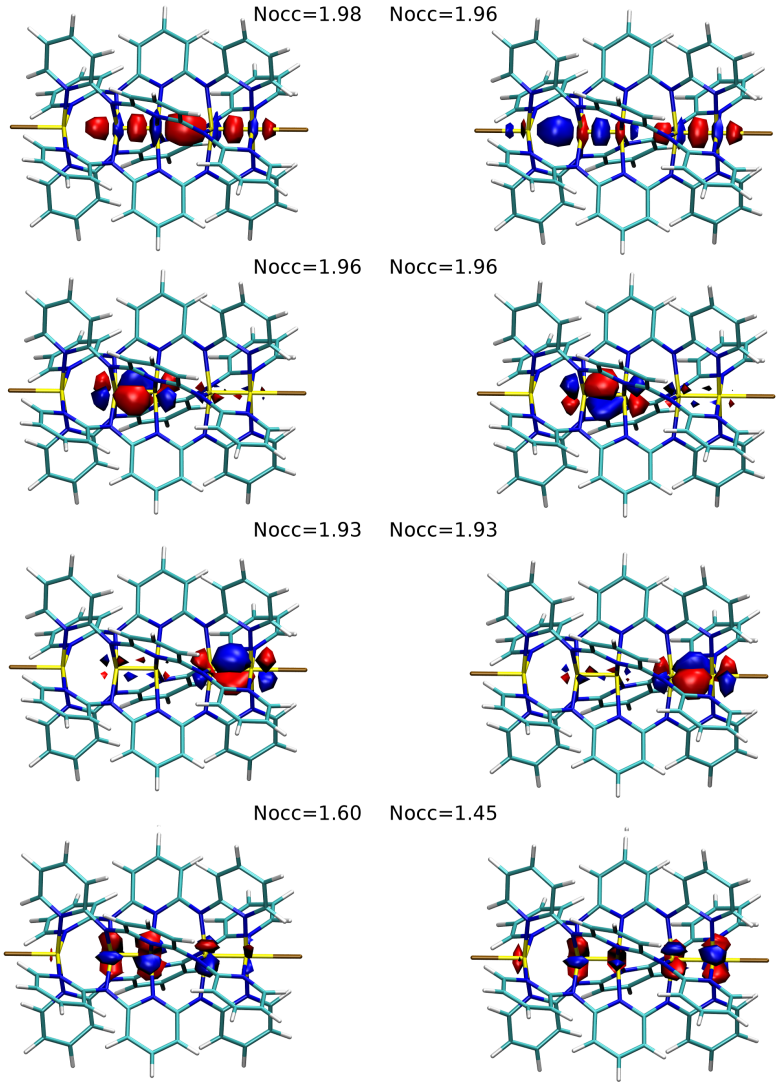

Figure 2.18: Cr_5Cl asymmetric optimized structure UNOs.

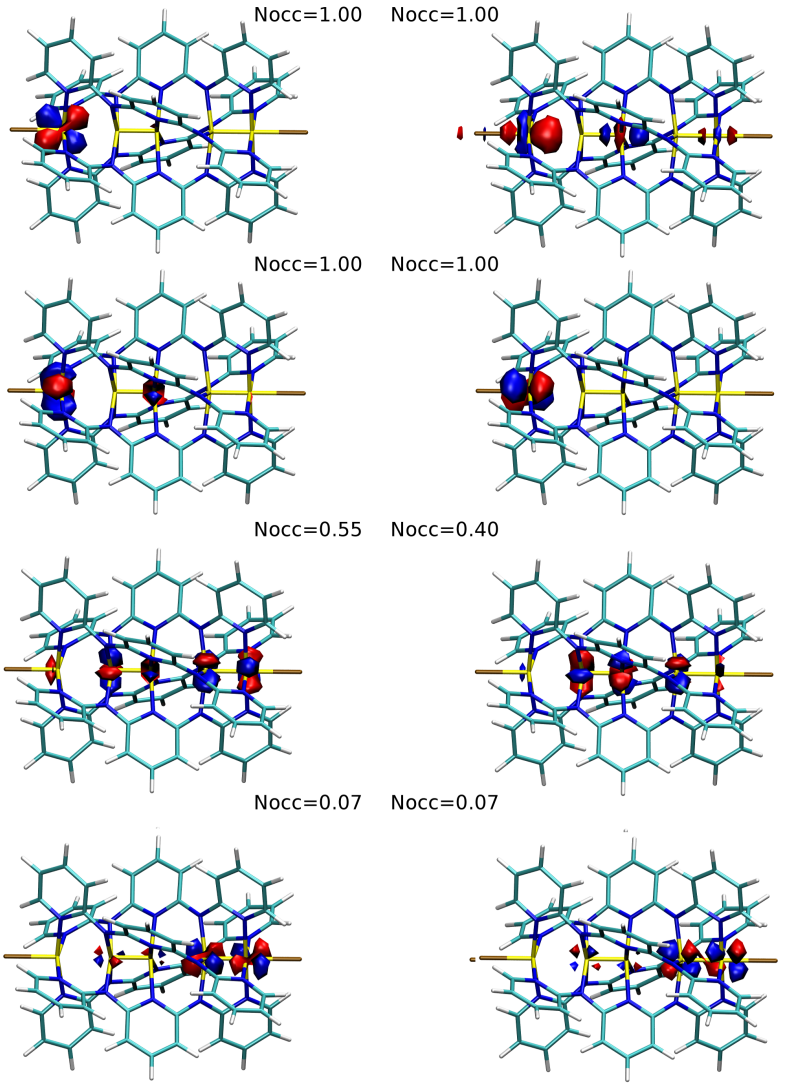

Figure 2.19: Cr_5Cl asymmetric optimized structure UNOs.

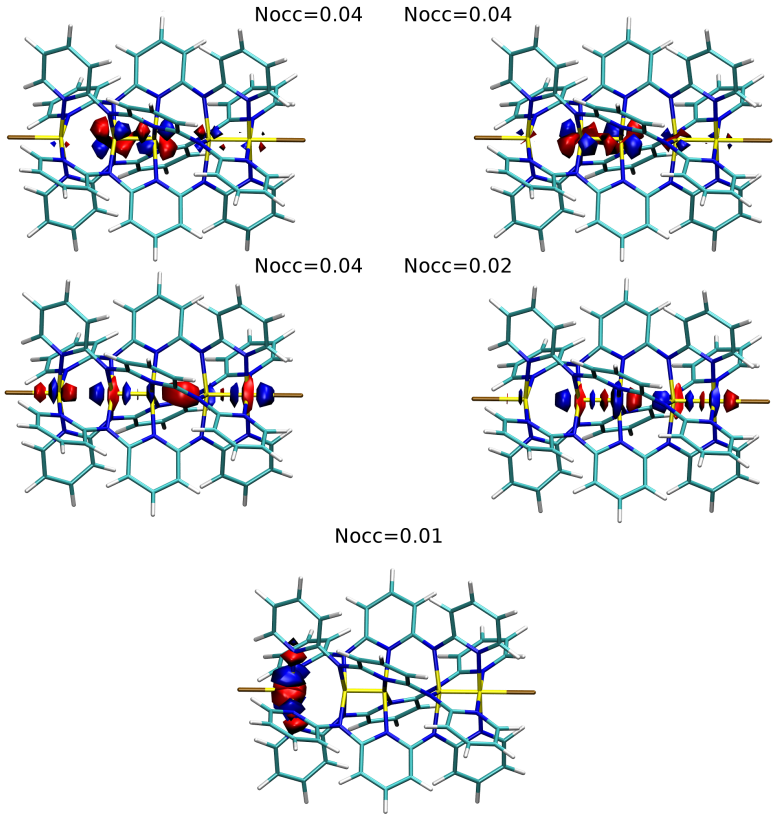

Figure 2.20: Cr_5Cl asymmetric optimized structure UNOs.

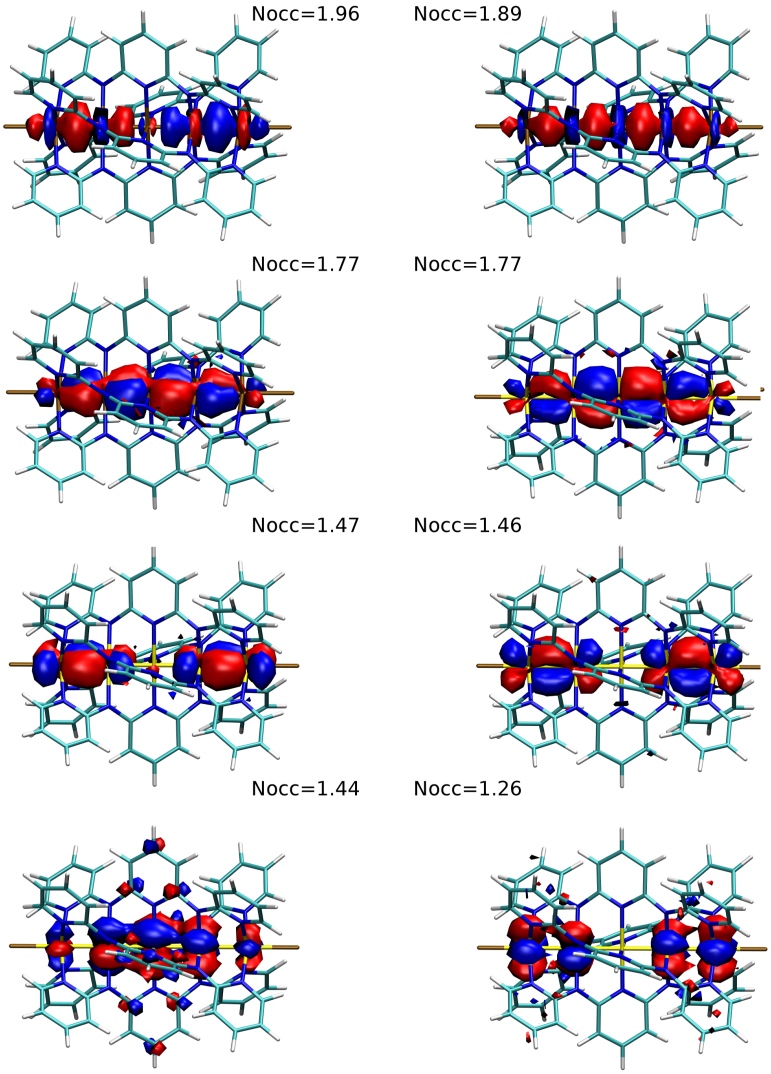

Figure 2.21: Cr_5Cl symmetric optimized structure UNOs.

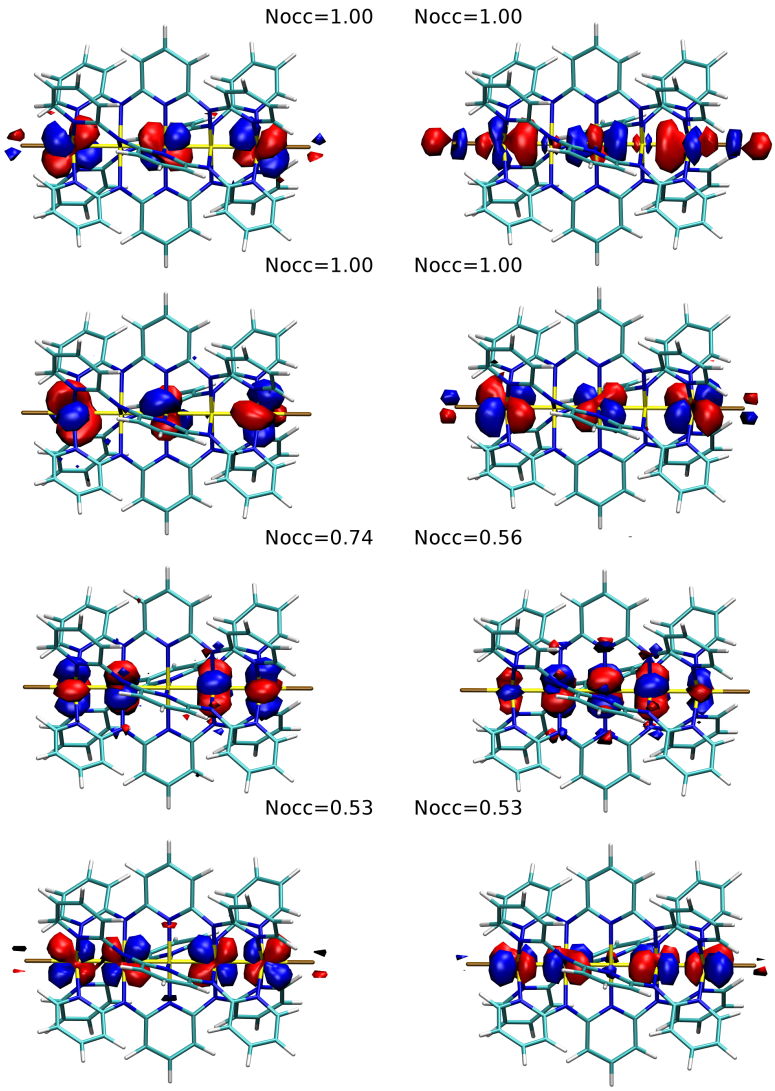

Figure 2.22: Cr_5Cl symmetric optimized structure UNOs.

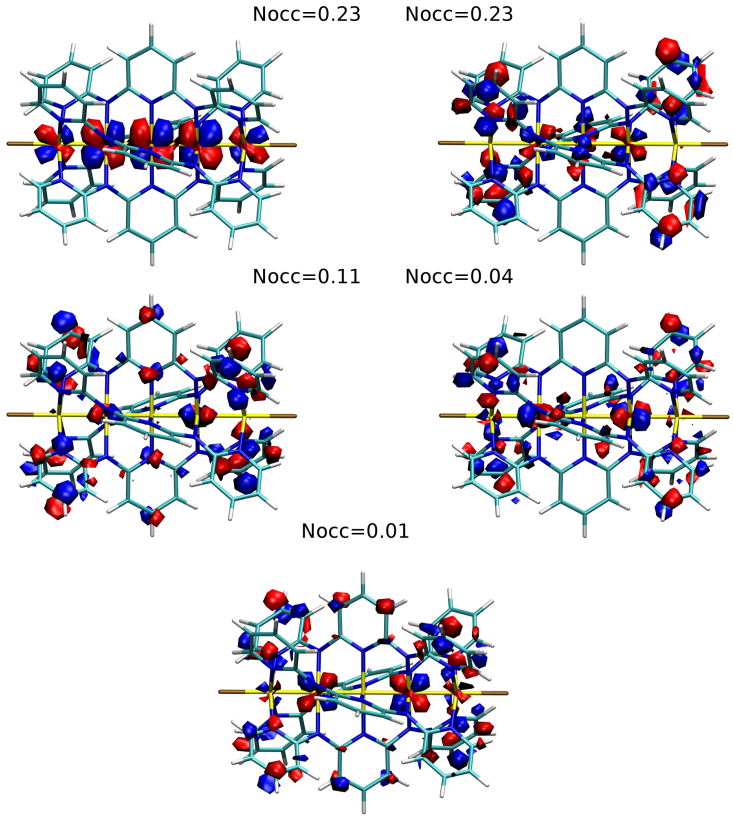

Figure 2.23: Cr_5Cl symmetric optimized structure UNOs.

Magnetic Property Modeling

The study of magnetism will be restricted to the asymmetric molecules as they are the more stable configurations. As previously discussed, anisotropy tensor calculations at the unrestricted DFT level of theory require the electronic spin density of the system to be consistent with an S^2 eigenstate. For all the structures just presented this is not the case. Indeed the $\langle S^2 \rangle_{DFT}$ are significantly deviating from the expected value $\langle S^2 \rangle = 6$. For this reason the straightforward DFT calculation of **D** is not possible. The natural orbitals show a significant spread of the occupation number already at the DFT level pointing out the need of a the theoretical method able to handle high level of correlation. CASSCF is particularly fitted for these purposes but in this situation it would require the calculation of an extended active space comprehensive of all the Cr_1 five d like MOs and the sixteen Cr_{2-5} bonding and anti-bonding MOs. Although this kind of calculations could be handled with some computational scheme as ORMAS or GASSCF, the computational demand remains enormous and in this thesis I will restrain the discussion to the analysis of sub units magnetism.

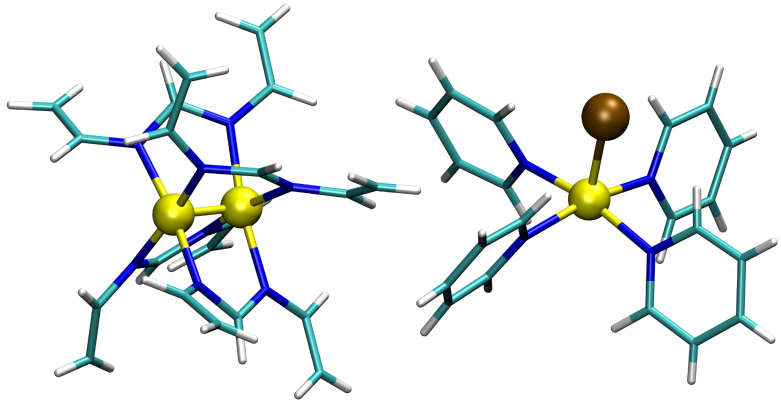

Figure 2.24: Cr_{2-3} and Cr_1 model structures.

The Cr_1 unit is a typical mononuclear Cr^{2+} ion in a square planar pyramid coordination geometry with the chromium ion only slightly out of the plane of the N ligands. The calculation of its electronic structure has been done at both DFT and CASSCF (4,5) level and the axial anisotropy constant for this model has been calculated as D=-0.464 cm^{-1} and D=-1.51 cm^{-1}, respectively. The origin of such discrepancy is hard to tell. The lacking of static correlation in DFT is not expected to play an

important role here as the ground state of Cr_1 is well described by a single Slater determinant. Both computational methods predict E/D$\sim$ 0, in agreement with the presence of a C_4 symmetry axis collinear with the metal chain axis. CASSCF result is in excellence agreement with the experimental anisotropy D_{exp}=-1.6 cm^{-1}. The truncated Cr_1 model with the SCN ligand gives similar CASSCF results: D=-1.59 cm^{-1}. The experimental value D=-1.8 cm^{-1} is in remarkable agreement with CASSCF also in this case. Moreover, CASSCF is able to predict the slight decrease passing from Cl to SCN.

Cr_{2-3} is the next studied fragment.

According to the shorter bond length and confirmed by UNOs, the two Cr^{+2} ions are strongly coupled and for this reason both static and dynamic correlations are supposed to be relevant. Therefore, CASSCF(8,8) has been used to determine the electronic structure for this fragment. The active space has been built with σ, π, π, δ and $\sigma^*, \pi^*, \pi^*, \delta^*$ orbitals. Two ground state selected calculations have been carried out converging the wave function on the first triplet and singlet CI solution, respectively. Energy difference for these two simulation give the singlet state more stable than the triplet of 3927.95 cm^{-1}. The big energy distance between the solutions demonstrates that the Cr_{2-3} unit could be considered as a diamagnetic fragment. Natural orbital analysis gives an interesting insight on the nature of the Cr-Cr bond. The bond order could be defined as the half difference between bond and anti-bond natural orbital occupation numbers and for the singlet ground state solution it is only 2.27, value significantly departed from the expected 4. As also reported in literature this is due to the partial occupation of anti bonding orbital as effect of electron correlation. The value reported here is even more dramatically small than other similar systems reported in literature, and the explanation lies in the partial twist of the two squares perpendicular to the Cr axis and containing the nitrogen ligands. Indeed, departures of the alignment between the two set of ligands make the overlap between d_{xy}, d_{xz} and d_{yz}, *i.e.* π and δ interactions, less effective and the energy splitting between bonding and anti bonding pairs of MOs gets reduced. The reduction of the band gap is then reflected on a higher spread of electron occupation numbers all over the Fermi energy region which consequently reduces the effective bond order of the chromium pair.

Accordingly to the above discussions, it is natural to expect the Cr_1 ruling the magnetism of the whole asymmetric EMACs. Indeed, the Cr_{2-5} is expected to behave only as diamagnetic ligands only marginally affecting the electronic structure of Cr_1. Moreover, the long distance between Cr_1 - Cr_2 and the almost complete separation

between UNO of different sub sections, make this hypothesis quite solid.

In order to put the last result in more solid theoretical ground, even though qualitative, lets study the D dependence from a perturbation mimicking the C_{1-2} interaction. Although D formulas in terms of spin multiplets splitting for an S=2 exist[69, 70], a formulation in terms of MOs would be advisable for clarity purpose. Lets start recalling that atomic d orbital are tesseral function defined from spherical harmonics $|l, m\rangle$ as

$$|d_{z^2}\rangle = |2, 0\rangle, \tag{2.78}$$

$$|d_{x^2-y^2}\rangle = \frac{1}{\sqrt{2}}(|2, 2\rangle + |2, -2\rangle), \tag{2.79}$$

$$|d_{zy}\rangle = \frac{i}{\sqrt{2}}(|2, 1\rangle + |2, -1\rangle), \tag{2.80}$$

$$|d_{zx}\rangle = -\frac{1}{\sqrt{2}}(|2, 1\rangle - |2, -1\rangle), \tag{2.81}$$

$$|d_{xy}\rangle = \frac{1}{i\sqrt{2}}(|2, 2\rangle - |2, -2\rangle) \tag{2.82}$$

where (l_x, l_y, l_z) and (l_+, l_-) are orbital angular momentum operators

$$l_z|l, m\rangle = m|l, m\rangle \tag{2.83}$$

$$l_+|l, m\rangle = \sqrt{(l-m)(l+m+1)}|l, m+1\rangle \tag{2.84}$$

$$l_-|l, m\rangle = \sqrt{(l+m)(l-m+1)}|l, m-1\rangle \tag{2.85}$$

$$l_x = \frac{1}{2}(l_+ + l_-) \tag{2.86}$$

$$l_y = \frac{1}{2i}(l_+ - l_-) \tag{2.87}$$

From second order perturbation theory the SOC contribution to **D** in terms of MOs is expressed by eq. 2.51. As discussed by Neese, this sum over states formula could be obtained from the general second order perturbation treatment of a regular many body wave function in absence of the exchange term[39], and therefore it readily applies to the unrestricted DFT framework, where states are expressed by means of non orthogonal unrestricted MOs. This property is of paramount importance in the context of practical calculations as spin polarization effects, arising from it, account for general properties of paramagnetic molecules. However, in this context it makes

impossible to extract practical information on D. In order to overcome this flaw a slightly different formulation of eq. 2.51 should be used. Based on the discussion of Neese[39], unrestricted MOs could be converted into orthogonal unrestricted natural orbitals, divided in double occupied, singly occupied and non occupied MOs, where the former sub space is associated with alpha Fock operator eigenvalues and the latter with beta Fock operator eigenvalues. The MOs belonging to the remaining sub space are dressed with the average value between spin up and spin down Fock operator eigenvalues. Although containing a degree of arbitrariness, this kind of transformation (quasi restricted orbitals) provides proper results in excellent agreement with the more general eq. 2.51. The only contributions to the Cr^{+2} anisotropy comes from the S=2 and S=1 multiplets and their effects in terms of single particle excitations is given by $\alpha \rightarrow \alpha$ and $\alpha \rightarrow \beta$ spin excitations. Clearly the most important ones are those localized into the d like MOs of the chromium ion and the discussion will be restrained to them.

Cr_1 coordination geometry is a square pyramid geometry and its ground state could be described by a configuration $(d_{xy})^1(d_{zx})^1(d_{zy})^1(d_{z^2})^1(d_{x^2-y^2})^0$ where the energies ladder is about $E(d_{xy}) < E(d_{zx}) \sim E(d_{zy}) < E(d_{z^2}) < E(d_{x^2-y^2})$, according to the MOs ordering provided by the CASSCF calculation. The only $\alpha \rightarrow \alpha$ excitation contributions are

$$D_{zz} \propto -\frac{|\langle d_{x^2-y^2}|l_z|d_{xy}\rangle|^2}{\epsilon_{d_{x^2-y^2}} - \epsilon_{d_{xy}}} = -\frac{4}{\epsilon_{d_{x^2-y^2}} - \epsilon_{d_{xy}}} \tag{2.88}$$

$$D_{xx} \propto -\frac{|\langle d_{x^2-y^2}|l_x|d_{zy}\rangle|^2}{\epsilon_{d_{x^2-y^2}} - \epsilon_{d_{zy}}} = -\frac{1}{\epsilon_{d_{x^2-y^2}} - \epsilon_{d_{zy}}} \tag{2.89}$$

$$D_{yy} \propto -\frac{|\langle d_{x^2-y^2}|l_y|d_{zx}\rangle|^2}{\epsilon_{d_{x^2-y^2}} - \epsilon_{d_{zx}}} = -\frac{1}{\epsilon_{d_{x^2-y^2}} - \epsilon_{d_{zx}}} \tag{2.90}$$

$$\tag{2.91}$$

while the $\alpha \rightarrow \beta$ excitations are

$$D_{zz} \propto +\frac{|\langle d_{zx}|l_z|d_{zy}\rangle|^2}{\epsilon_{d_{zx}} - \epsilon_{d_{zy}}} = \frac{1}{\epsilon_{d_{zx}} - \epsilon_{d_{zy}}} \tag{2.92}$$

$$D_{xx} \propto +\frac{|\langle d_{zx}|l_x|d_{xy}\rangle|^2}{\epsilon_{d_{zx}} - \epsilon_{d_{xy}}} + \frac{|\langle d_{z^2}|l_x|d_{zy}\rangle|^2}{\epsilon_{d_{z^2}} - \epsilon_{d_{zy}}} = \frac{1}{\epsilon_{d_{zx}} - \epsilon_{d_{xy}}} + \frac{3}{\epsilon_{d_{z^2}} - \epsilon_{d_{zy}}} \tag{2.93}$$

$$D_{yy} \propto +\frac{|\langle d_{zy}|l_y|d_{xy}\rangle|^2}{\epsilon_{d_{zy}} - \epsilon_{d_{xy}}} + \frac{|\langle d_{z^2}|l_y|d_{zx}\rangle|^2}{\epsilon_{d_{z^2}} - \epsilon_{d_{zx}}} = \frac{1}{\epsilon_{d_{zy}} - \epsilon_{d_{xy}}} + \frac{3}{\epsilon_{d_{z^2}} - \epsilon_{d_{zx}}} \tag{2.94}$$

Therefore, $D = D_{zz} - \frac{1}{2}(D_{xx} + D_{yy})$ for the $\alpha \rightarrow \alpha$ excitations is

$$D_{\alpha\rightarrow\alpha} \propto -\frac{4}{\epsilon_{d_{x^2-y^2}} - \epsilon_{d_{xy}}} + \frac{1}{2}(\frac{1}{\epsilon_{d_{x^2-y^2}} - \epsilon_{d_{zy}}} + \frac{1}{\epsilon_{d_{x^2-y^2}} - \epsilon_{d_{zx}}}) \tag{2.95}$$

while for the $\alpha \rightarrow \beta$ excitations it is

$$D_{\alpha\rightarrow\beta} \propto \frac{1}{\epsilon_{d_{zx}} - \epsilon_{d_{zy}}} - \frac{1}{2}(\frac{1}{\epsilon_{d_{zx}} - \epsilon_{d_{xy}}} + \frac{3}{\epsilon_{d_{z^2}} - \epsilon_{d_{zy}}} + \frac{1}{\epsilon_{d_{zy}} - \epsilon_{d_{xy}}} + \frac{3}{\epsilon_{d_{z^2}} - \epsilon_{d_{zx}}}) \tag{2.96}$$

From relation 2.95 it comes out that D becomes more negative as d_{xy} and $d_{x^2-y^2}$ get closer or $d_{x^2-y^2}$ - d_{zx}/d_{zy} split gets larger. From relation 2.96, D becomes more negative if d_{z^2} or d_{xy} get closer to d_{zx}, d_{zy}. All these conditions are coherent with those found out in the work of Barra *et al.*[69] for the iso electronic high spin Mn^{+3}. Interestingly these MOs based formulas take into accounts all the main contributions reported by Liakos *et al.*[70], for a Jahn Teller distorted $Cr(II)(H_2O)_6$, in the context of many body perturbation theory. Indeed, eqs. 2.95 and 2.96 correctly accounts for sign, symmetry and magneto structural correlation for both quintet excitations ($^5E_g \rightarrow ^5 T_{2g}$) and the two most important triplet excitations ($^5E_g \rightarrow ^3 T_{1g}$ and $^5E_g \rightarrow ^3 T_{2g}$) contribution to D. From the UNOs analysis at the beginning of the sections was evident that the major contribution to the Cr_1 Cr_{2-5} interaction comes from the overlap between the Cr_1 d_{z^2} MO and the Cr_{2-5} σ MO. As the Cr_1 d_{z^2} lies more near to the bonding σ orbital, with respect to the anti bonding σ^*, this interaction would increase the d_{z^2} energy and consequently its gap with d_{yz} and d_{xz}, resulting in a decrease of the anisotropy absolute value. The same effect would be provided by π interactions which would increase d_{zy} and d_{zx} energy difference from $d_{x^2-y^2}$, leading to a more negative $D_{\alpha\rightarrow\alpha}$ contribution. Clearly, this discussion is completely qualitative and it does not give information on the magnitude of D reduction due to the sigma overlap with the Cr_{2-5} fragment. Although the explicit inclusion of the Cr_{2-5} ions is too expensive as already discussed, a small step toward a refinement of the truncated Cr_1 model might be done with the inclusion of a diamagnetic substitution (Zn^{2+} ions) in the Cr_5 structure without any structural relaxation. Although this kind of substitution is not expected to be realistic and experimentally feasible, it could at least give an indication of the importance of a charged transition metal near the Cr_1 site. A summary of results for Cr_1 and $CrZn_4$ model anisotropy calculations, with both Cl and SCN ligands, are reported in Table 2.10. After the inclusion of Zn^{+2} ions, the anisotropy constants are slightly diminished with respect to the truncated Cr_1 model, in agreement to the D analysis above. Although this tiny variations could

hardly be considered quantitative, the comparison between the two models clearly shows the small influence of the axial ligand on the Cr_1 magnetism.

Table 2.10: CASSCF Calculated Cr_1 Anisotropy.

	Cl		SCN	
	D (cm^{-1})	E/D (cm^{-1})	D (cm^{-1})	E/D (cm^{-1})
Cr_1	-1.513	0.000	-1.592	0.000
$CrZn_4$	-1.441	0.000	-1.248	0.000
Exp	-1.6	–	-1.8	–

Conclusions

This study meant to give a rationalization of the origin of the slow relaxation rate of the magnetization for a recently proposed Cr^{+2} based SMM. The ambiguity on the possible source of the zero field splitting have been addressed by means of postHF calculations which elucidates the importance of only one chromium ion inside the Cr_5 EMAC chain. The possible effect of the nearby chromium ions has been investigated through perturbation theory and diamagnetic substitution techniques which proved the Cr-Cr interaction to be almost negligible. A short discussion of the electronic structure of an alternative geometry has also been provided suggesting the possibility to modify sensibly the EMAC magnetism changing the external axial ligands σ donor power.

2.8 Summary

In this chapter the importance of the various terms of the spin hamiltonian for polynuclear SMMs has been investigated. Fe^{+3} iron clusters have been at the center of the investigation due to the wide interested they have recently capture and a comprehensive characterization of the fundamental properties of a Fe_4 family have been addressed through a DFT plus post-HF approach. This proposed computational scheme makes possible to elucidate the nature of magneto-structural correlations inside the helical pitch family and to unambiguously weight all the multi spin interactions concurring to their spin hamiltonian. Moreover, a practical way to calculate the anisotropic exchange part of the multi spin hamiltonian has been proposed and tested on the Fe_4Ph SMM at the DFT level, and over the Fe_2 cluster at both DFT and postHF levels, demonstrating the not negligible weight of this interaction. Although the assessment of the DFT protocol has been very positive, this study pointed out the necessity to use a higher level of theory for evaluation of the exchange coupling tensor. The limits of the GSA approximation have also been tested and the possibility to access computationally the higher order giant spin hamiltonian terms has been investigated. First a theoretical description of the nature of these higher order terms has been provided by means of perturbation theory and then a numerical analysis through the exact diagonalization of the multi spin hamiltonian has been done shedding some light on their value dependence on both isotropic exchange coupling and spin non-collinearity. Finally, metal-metal bond effects on the spin hamiltonian have been studied in the context of chromium based EMACs showing the possibility to change the easy axis anisotropic of a Cr^{+2} ion modulating it distance inside the linear metallic ions chain.

2.9 Computationl Methods

CP2K and ORCA[71] packages of software have been used to perform DFT calculations of isotropic exchange coupling constants and all the other properties, respectively. The evaluation of the isotropic part of the spin Hamiltonian J_{ij} has been carried out with the PBE0 [72] functional. To solve the UKS equations in CP2K, the Gaussian and plane waves (GPW) formalism was used. Double-ζ polarized basis sets (DZVP-MOLOPT-SR[73]) with Goedecker-Teter-Hutter norm conserving pseudopotentials[74, 75] have been employed. The auxiliary Plane Wave basis set has been truncated to an energy of 400 Ry. DZVP-MOLOPT-SR for iron and SZV-MOLOPT-SR for all the other elements have been used as auxiliary basis-sets for the exchange integrals evaluation[76]. A convergence criteria on the maximum element of the wave function gradient was sets to 1.0E-07. The DFT evaluation of all the anisotropic tensors, made with the package ORCA, has been carried out with both PBE [77] and PBE0 functionals. All the calculations have been done with a def2-TZVP [78] basis set for all the elements. The RI-J approximation along with the def2-TZVP/J auxiliary basis set[79] and the COSX approximation[80] to the Fock operator building when dealing with hybrid functionals have also been exploited. Speaking in the ORCA notation, grids were set to 5 and VeryTightSCF convergence criteria were used. As shown by Neese *et al.*[39] the two fundamental ingredients for the anisotropy relativistic calculations are spin-orbit (SOC) and spin-spin (SS) interactions and both were taken into account for the calculations. SOC have been evaluated with UKS orbitals and with Van Wüllen et al's[38] receipt for the pre-coefficients of integrals. The SS contribution to **D** have been evaluated utilizing the unrestricted natural orbitals (UNO) obtained from UKS orbitals as suggested by Sinnecker *et al.*[81]. Magnetic properties of SMMs are strictly related to geometries and even small variations of the structural parameters could affect the computed final values. For this reason, X-ray crystal structures were used for all calculations if not differently specified. All the calculations have been carried out on a single molecule without any approximations as, for instance, ligands truncation. All the Fe_4 molecules considered crystallize with four or six molecules per unit cell and, except for Fe_4C_5, Fe_4C_4, and Fe_4C_1, the crystal lattice owns only one crystallographically-independent molecule. For what concerns Fe_4C_5, Fe_4C_4, and Fe_4C_1, the crystallographically distinct molecules exhibit very similar geometries and essentially differ only in the orientation of the alkyl chains. The Heisenberg Hamiltonian chosen to describe the isotropic spin-spin interaction is:

$$H = J_1'(\vec{\mathbf{s_1}} \cdot \vec{\mathbf{s_2}}) + J_1''(\vec{\mathbf{s_1}} \cdot \vec{\mathbf{s_3}}) + J_1'''(\vec{\mathbf{s_1}} \cdot \vec{\mathbf{s_4}}) + J_2(\vec{\mathbf{s_2}} \cdot \vec{\mathbf{s_3}} + \vec{\mathbf{s_2}} \cdot \vec{\mathbf{s_4}} + \vec{\mathbf{s_3}} \cdot \vec{\mathbf{s_4}}) \tag{2.97}$$

To calculate the Js values[82], the energy of the high spin state has been calculated, S=10 (HS) and all the broken symmetry states (BSx, x =1-4) obtained by all the possible single spin flips on the four iron ions. The system of linear equations $\Delta E(HS-BSx) = 2\sum_{ij} J_{ij} s_i s_j \lambda_{ij}$ (where λ_{ij} differs from zero only if, for the selected BS, s_i and s_j have opposite sign) can then be used. The anisotropic part of the spin Hamiltonian is chosen of the form $\mathrm{H}=\sum_{i=1}^{N=4} \vec{\mathbf{s_i}} \cdot \mathbf{D_i} \cdot \vec{\mathbf{s_i}} + \sum_{i=1,j\neq i}^{6} \vec{\mathbf{s_i}} \cdot \mathbf{D_{ij}} \cdot \vec{\mathbf{s_j}}$ where each ion and each couple contribution has been evaluated explicitly, without making any symmetry assumptions.

For what concerns the postHF calculations they have been done with ORCA employing a def2-TZVP [78] basis set for magnetic elements and their first neighbors, while def2-SVP basis set has been used for all the other atoms. The RI-J approximation along with the def2-TZVP/J auxiliary basis set[79] for all the elements has been used. Speaking in the ORCA notation, grids were set to 5 and VeryTightSCF. This set up has been test in the context of CASSCF method with respect to calculations done with the def2-TZVP basis set on every atomic kind and no significant differences have been noted on the energy ladder of the excited states.

Chapter 3

Spin Relaxation

Contents

The study of interactions between spins and their surrounding manifold of phonons is a key problem in physics as it is related to a broad area of phenomena. For instance, the spin phonon interaction is responsible for relaxation in magnetic materials and moreover, due to the fermionic nature of electrons, spin phonon interaction deeply affects charge and spin transport properties with consequences for (super)conductance and spintronic phenomena. The importance of an exhaustive description of the spin phonon interaction could be hardly overestimated and the addressing of fundamental questions about the microscopic quantum origin of this mechanism is of broad interest. For what concern SMMs, as their key properties arise from non equilibrium dynamics, spin-phonon relaxation acts as the limiting factor to their range of applicability and for this reason this interaction has been extensively studied in this context for almost

twenty years, with the final goal to extend the SMMs operating temperature to the ambient one. Generally, relaxation time of SMMs exhibits an Arrhenius like temperature behavior $\tau = \tau_0 exp(U_{eff}/k_b T)$[27] and therefore the effective spin-flip barrier U_{eff} has been of central interest in order to enhance the magnetization life time τ. U_{eff} has been linked to the spin excited state energies and this connection has been used as guideline to increase U_{eff}[83]. Although a lot of efforts have been done in order to increase U_{eff} value, and remarkable results have been obtained following this route[84, 85], several discrepancies between the expected barrier, obtained through optical methods, and the effective one have been observed[86–88], leading to severe limitations about their properties engineering. Moreover, although hundreds kelvin effective barriers have been reached through extensive molecular structure manipulations and ligands design, relaxation time scales are still confined in the sub-ms regime and only at low temperature. This effect is observed because responsible interactions for high spin-flip barriers are the same that made the spin couples to the phonon bath and therefore, the strategy to enhance U_{eff} commonly leads to τ_0 reductions at the same time. This situation clearly points out the need to extend current strategies to significantly extend spin life-times and in order to accomplish such a result, a more detailed theory is needed. So far, the formal theory describing spin-phonon coupling in molecular crystals is the same firstly derived in the context of paramagnetic ionic crystals by Orbach[89]. Clearly at the time a phenomenological approach was the only possible route and the description of this dynamics in an ab initio fashion has become feasible only in the last few years. In that framework, only the effect of acoustic phonon branches was considered and no details on the effective coupling strength between normal modes and spin degrees of freedom was specified. However, although all this approximation, the original theory of the first 60s has been at the center of experiment interpretations up today with remarkable results. Clearly, various specialization of this theory to molecular system has been attempted over the years but the phenomenological ground has never been left. For instance, also librational modes have been addressed to explain spin relaxation in molecular magnets but the use of the Debye phonon model in order to get rid of explicit phonon feature dependencies has always been introduced[90]. Although these arguments have been used ever since the firsts Orbach's spin-phonon relaxation models, a clear proof of their validity has never been provided.

In this chapter a review of the basic theory of the spin phonon coupling mechanism will be provided making a fundamental step toward a realistic description of this interaction. For the first time, the anharmonicity of normal modes and its temperature dependence has been introduced into the theory lifting the too extreme harmonic

approximation. A few simple models will be discussed in order to highlight differences with the former theory and to introduce new predictable spin dynamics features. Moreover, in section 3.5, thanks to recent progresses in both electronic structure theory and computing facilities, it will be discussed the *ab initio* evaluation of all the spin-phonon coupling coefficients for the periodic cell of a prototypical mononuclear transition metal based SMM, which has been used to put to test the new formal theory in a realist playground. The realistic modeling of the complexity of both the spin system and its vibrational environment, makes possible to unambiguously reveal the dramatic effects of the phonon bath thermal fluctuations over the SMM spin dynamics and their connection with the effective spin reversal barrier reduction has been established. Finally, the possibility to calculate the spin phonon coupling coefficient for a real molecular system, for the first time, makes possible to access the weight of specific modes to the global spin dynamics paving the ground for a rational tailoring of molecular structural features in order to scale up spin life time.

3.1 Spin-Environment Dynamics

The low energy lying part of SMM spectrum is generally composed by a manifold of spin levels whose degeneracy is removed by relativistic interactions, therefore the total hamiltonian of the spin system H_0 is generally described as the sum of the Born-Oppenheimer hamiltonian H_{BO} and the spin orbit coupling hamiltonian H_{SOC} *i.e.* $H_0 = H_{BO} + H_{SOC}$. The spin relaxation phenomena took place through the modulation of the spin components of the wave function during molecular motion. This coupling between spin and nuclear degrees of freedom open an energy exchange path which makes the manifold of phonon modes to act as a thermal bath for the spin system. Therefore, the bath hamiltonian could be expressed in terms of normal modes q_α, occupation number operators $\hat{n}_\alpha = a_\alpha^\dagger a_\alpha$ and vibrational frequencies ω_α. Assuming a weak coupling between phonon bath and spin degrees of freedom the interaction hamiltonian H_{s-ph} could be modeled as

$$H_{s-ph} = \sum_\alpha \Big(\frac{\partial H_0}{\partial q_\alpha}\Big)_0 q_\alpha \tag{3.1}$$

Assuming a weak coupling between phonon bath and spin degrees of freedom H_{s-ph} can be modeled as

$$H_{sph} = \sum_k \Big(\frac{\partial H_0}{\partial q_k}\Big)_0 q_k + \frac{1}{2}\sum_{kl} \Big(\frac{\partial^2 H_0}{\partial q_k q_l}\Big)_0 q_k q_l ... \tag{3.2}$$

The dynamics of the spin and bath systems can be described by means of density operator, whose equation of motion in the interaction picture reads:

$$\frac{d\rho(t)}{dt} = -\frac{i}{\hbar}[H_{sph}(t), \rho(t)] \tag{3.3}$$

From now on $H \sim H_{sph}$ and all the operator will be intended in the interaction picture if not differently specified.

3.2 First Order Spin-Phonon Coupling

As the interest is on dynamics of only spin degrees of freedom it is convenient to define a reduced density operator taking trace over bath degrees of freedom: $\rho_s(t) = tr_B(\rho(t))$ After a formal integration of equation 3.3:

$$\frac{d\rho_s(t)}{dt} = -\frac{1}{\hbar^2}\int_0^t ds \quad tr_B[H(t),[H(s),\rho(s)]] \tag{3.4}$$

Where $tr_B[H(t),\rho(0)] = 0$ has been assumed. The first term of 3.1 already satisfy this condition. If the second term is considered, it is still possible to define a new $H'_{sph} = H_{sph} - Tr_B(H_{sph}\rho(0))$ without any needs of changing the subsequent results. Equation 3.4 is only formally independent by bath dynamics. In order to remove this dependence, it is useful to make the *Born* approximation: $\rho(t) = \rho_s(t)\otimes\rho_{eq}^B$. In virtue of the supposed weak coupling between bath and spin degrees of freedom the *Born* approximation assumes the bath to relax much faster than the spin system. Before to explicitly write H also the *Markov* approximation should be done, in order to let ρ_s to be a dynamical semi-group. To do so, the substitution $t' = t - s$ should be done and the t' superior integration boundary should be bring to $+\infty$:

$$\frac{d\rho_s(t)}{dt} = -\frac{1}{\hbar^2}\int_0^\infty dt' tr_B[H(t),[H(t-t'),\rho_s(t)\otimes\rho_B]] \tag{3.5}$$

Now let's consider $H = \sum_\alpha V_\alpha L_\alpha$ corresponding to the first term in equation 3.1 as $V_\alpha = \frac{\partial H_0}{\partial q_\alpha}$ and $L_\alpha = q_\alpha$:

$$\frac{d\rho_s(t)}{dt} = -\frac{1}{\hbar^2}\int_0^\infty dt' \sum_\alpha \Big\{ \tag{3.6}$$

$$\Big[V_\alpha(t)V_\alpha(t-t')\rho_s(t) - V_\alpha(t)\rho_s(t)V_\alpha(t-t')\Big] \tag{3.7}$$

$$Tr_B\Big(L_\alpha(t)L_\alpha(t-t')\rho_B^{eq}\Big) - \tag{3.8}$$

$$\Big[V_\alpha(t-t')\rho_s(t)V_\alpha(t) - \rho_s(t)V_\alpha(t-t')V_\alpha(t)\Big] \tag{3.9}$$

$$Tr_B\Big(L_\alpha(t-t')L_\alpha(t)\rho_B^{eq}\Big)\Big\} \tag{3.10}$$

Taking the matrix elements of $\rho_s(t)$ in the eigenket basis of $H_0|a\rangle = E_a|a\rangle$ is possible to obtain:

$$\frac{d\rho^s_{ab}(t)}{dt} = -\frac{1}{\hbar^2}\int_0^\infty dt' \sum_\alpha \sum_{cd} \Big\{ \tag{3.11}$$

$$\Big[V^\alpha_{ac}(t)V^\alpha_{cd}(t-t')\rho^s_{db}(t) - V^\alpha_{ac}(t)\rho^s_{cd}(t)V^\alpha_{db}(t-t')\Big] \tag{3.12}$$

$$Tr_B\Big(L_\alpha(t)L_\alpha(t-t')\rho^{eq}_B\Big) - \tag{3.13}$$

$$\Big[V^\alpha_{ac}(t-t')\rho^s_{cd}(t)V^\alpha_{db}(t) - \rho^s_{ac}(t)V^\alpha_{cd}(t-t')V^\alpha_{db}(t)\Big] \tag{3.14}$$

$$Tr_B\Big(L_\alpha(t-t')L_\alpha(t)\rho^{eq}_B\Big)\Big\} \tag{3.15}$$

Now let's explicit the time dependencies of spin degrees of freedom coming back to the Scroedinger picture: $V_{ab}(t) = \langle a|e^{iH_0 t}Ve^{-iH_0 t}|b\rangle = e^{i\omega_{ab}t}V_{ab}$

$$\frac{d\rho^s_{ab}(t)}{dt} = -\frac{1}{\hbar^2}\int_0^\infty dt' \sum_\alpha \sum_{cd} \Big\{ \tag{3.16}$$

$$\Big[V^\alpha_{ac}V^\alpha_{cd}\rho^s_{db}(t)e^{i\omega_{ac}t}e^{i\omega_{cd}t}e^{-i\omega_{cd}t'} - V^\alpha_{ac}\rho^s_{cd}(t)V^\alpha_{db}e^{i\omega_{ac}t}e^{i\omega_{db}t}e^{-i\omega_{db}t'}\Big] \tag{3.17}$$

$$Tr_B\Big(L_\alpha(t)L_\alpha(t-t')\rho^{eq}_B\Big) - \tag{3.18}$$

$$\Big[V^\alpha_{ac}\rho^s_{cd}(t)V^\alpha_{db}e^{i\omega_{ac}t}e^{i\omega_{db}t}e^{-i\omega_{ac}t'} - \rho^s_{ac}(t)V^\alpha_{cd}V^\alpha_{db}e^{i\omega_{cd}t}e^{i\omega_{db}t}e^{-i\omega_{cd}t'}\Big] \tag{3.19}$$

$$Tr_B\Big(L_\alpha(t-t')L_\alpha(t)\rho^{eq}_B\Big)\Big\} \tag{3.20}$$

Doing some algebra is possible to lead equation 3.20 to a linear system of linear differential equation:

$$\frac{d\rho^s_{ab}(t)}{dt} = -\frac{1}{\hbar^2}\int_0^\infty dt' \sum_\alpha \sum_{cd} \Big\{ \tag{3.21}$$

$$\Big[V^\alpha_{ac}V^\alpha_{cd}\rho^s_{db}(t)e^{i\omega_{ad}t}e^{-i\omega_{cd}t'} - V^\alpha_{ac}\rho^s_{cd}(t)V^\alpha_{db}e^{i\omega_{ac}t}e^{i\omega_{db}t}e^{-i\omega_{db}t'}\Big] \tag{3.22}$$

$$Tr_B\Big(L_\alpha(t)L_\alpha(t-t')\rho^{eq}_B\Big) - \tag{3.23}$$

$$\Big[V^\alpha_{ac}\rho^s_{cd}(t)V^\alpha_{db}e^{i\omega_{ac}t}e^{i\omega_{db}t}e^{-i\omega_{ac}t'} - \rho^s_{ac}(t)V^\alpha_{cd}V^\alpha_{db}e^{i\omega_{cb}t}e^{-i\omega_{cd}t'}\Big] \tag{3.24}$$

$$Tr_B\Big(L_\alpha(t-t')L_\alpha(t)\rho^{eq}_B\Big)\Big\} \tag{3.25}$$

Rearranging the first and the last term as:

$$\sum_{ij} V^{\alpha}_{ai} V^{\alpha}_{ij} \rho^{s}_{jb}(t) e^{i\omega_{aj}t} e^{-i\omega_{ij}t'} = \tag{3.26}$$

$$\sum_{icd} \delta_{bd} V^{\alpha}_{ai} V^{\alpha}_{ic} \rho^{s}_{cd}(t) e^{i\omega_{ac}t} e^{-i\omega_{ic}t'} = \sum_{cd} \big[\sum_{i} \delta_{bd} V^{\alpha}_{ai} V^{\alpha}_{ic} e^{i\omega_{ac}t} e^{-i\omega_{ic}t'} \big] \rho^{s}_{cd}(t) = \tag{3.27}$$

$$\sum_{cd} \big[\sum_{i} \delta_{bd} V^{\alpha}_{ai} V^{\alpha}_{ic} e^{i\omega_{bd}} e^{i\omega_{ac}t} e^{-i\omega_{ic}t'} \big] \rho^{s}_{cd}(t) \tag{3.28}$$

$$\sum_{ij} V^{\alpha}_{ij} V^{\alpha}_{jb} \rho^{s}_{ai}(t) e^{i\omega_{ib}t} e^{-i\omega_{ij}t'} = \tag{3.29}$$

$$\sum_{ijc} \delta_{ca} V^{\alpha}_{dj} V^{\alpha}_{jb} \rho^{s}_{cd}(t) e^{i\omega_{db}t} e^{-i\omega_{dj}t'} = \sum_{cd} \big[\sum_{j} \delta_{ca} V^{\alpha}_{dj} V^{\alpha}_{jb} e^{i\omega_{db}t} e^{-i\omega_{dj}t'} \big] \rho^{s}_{cd}(t) = \tag{3.30}$$

$$\sum_{cd} \big[\sum_{j} \delta_{ca} V^{\alpha}_{dj} V^{\alpha}_{jb} e^{i\omega_{ac}} e^{i\omega_{db}t} e^{-i\omega_{dj}t'} \big] \rho^{s}_{cd}(t) \tag{3.31}$$

Then, taking the secular approximation: $e^{i(\omega_{ac}+\omega_{db})t} = 1$, equation 3.25 becomes

$$\frac{d\rho^{s}_{ab}(t)}{dt} = R_{ab,cd} \rho^{s}_{cd}(t) \tag{3.32}$$

$$R_{cd} = -\frac{1}{\hbar^2} \sum_{\alpha} \Big\{ \tag{3.33}$$

$$\sum_{j} \delta_{bd} V^{\alpha}_{aj} V^{\alpha}_{jc} \int_0^{\infty} dt' e^{-i\omega_{jc}t'} Tr_B \Big(L_{\alpha}(t) L_{\alpha}(t-t') \rho^{eq}_{B} \Big) \tag{3.34}$$

$$- V^{\alpha}_{ac} V^{\alpha}_{db} \int_0^{\infty} dt' e^{-i\omega_{db}t'} Tr_B \Big(L_{\alpha}(t) L_{\alpha}(t-t') \rho^{eq}_{B} \Big) \tag{3.35}$$

$$- V^{\alpha}_{ac} V^{\alpha}_{db} \int_0^{\infty} dt' e^{-i\omega_{ac}t'} Tr_B \Big(L_{\alpha}(t-t') L_{\alpha}(t) \rho^{eq}_{B} \Big) \tag{3.36}$$

$$+ \sum_{j} \delta_{ca} V^{\alpha}_{dj} V^{\alpha}_{jb} \int_0^{\infty} dt' e^{-i\omega_{dj}t'} Tr_B \Big(L_{\alpha}(t-t') L_{\alpha}(t) \rho^{eq}_{B} \Big) \Big\} \tag{3.37}$$

Equilibrium Bath Correlation Function

The term $\int_0^{\infty} dt' e^{-i\omega_{ij}t'} Tr_B \Big(L_{\alpha}(t) L_{\alpha}(t-t') \rho^{eq}_{B} \Big)$ is the single phonon bath equilibrium green function and it contains all the information on the bath dynamics, temperature dependence included. Clearly, the form of this function rules the temperature behavior

of the spin relaxation and for this reason its evaluation is of paramount importance. This mathematical object is usually studied in perturbative way where the harmonic approximation is used as the ground for the Dyson's equation while anharmonic interactions between phonon represent the perturbation acting on normal modes. The presence of anharmonic interactions makes the life time of phonon finite and consequently the bath spectral shape broadened. Clearly, the spectral shape of the bath is a key ingredient in this relaxation theory and its features are expected to sensibly affect the overall magnetization dynamics. In order to access this information about the bath, the calculation of the anharmonic frequencies and phonon self energy would be required[91]. Basically the formalism used so far for the spin-phonon interaction should be recast for the phonon-phonon interaction. An alternative way to proceed is offered by the Caldeira-Leggett model which solves the problem though a phat-integral approach[92]. In the Caldeira-Leggett model the hamiltonian is composed by a single harmonic oscillator interacting with a bath of harmonic oscillator through a linear coupling, equivalently to the anharmonic hamiltonian previously discussed. Consequently, the total set of anharmonic coupling parameters is required also in this framework. Moreover, although the path integral solution makes possible to overcome possible failure of perturbative green function series, it makes the results less transparent and the connection between specific phonon-phonon interactions may be lost.

In the context of this thesis I have decided to tackle this problem through a stochastic approach, which has the advantage of not needing all the information about the single phonon-phonon interactions. In this framework, the bath hamiltonian is considered of the harmonic form $H_{ph} = \sum_\alpha \hbar\omega_\alpha(\hat{n}_\alpha + \frac{1}{2})$ and all the anharmonic features are included in a statistical way, according to the fact that the interaction of a modes with its bath, (made by all the other modes) is the same interaction that drives it to the thermal equilibrium described by the canonical distribution. If a phonon is considered at thermal equilibrium its energy experiences fluctuations and consequently, a certain H_{ph} eigenstates would have finite life time. Clearly there is an equivalence between the statistical picture and the mechanistic microscopic description of the phonon phonon-bath system. In order to bridge the statistical description of the system and the microscopic one, the phonon Hamiltonian is considered time dependent with a time propagator $e^{-i\int_0^{t'} d\tau H(\tau)}$. The expression for the time dependent bath operators L will be

$$L(t) = e^{i\int_0^t d\tau H_B(\tau)} q e^{-i\int_0^t d\tau H_B(\tau)} \tag{3.38}$$

Therefore

$$Tr_B\Big(L_\alpha(t)L_\alpha(t-t')\rho_B^{eq}\Big) = \tag{3.39}$$

$$Tr_B\Big(e^{i\int_0^t d\tau H_b(\tau)}q_\alpha e^{-i\int_0^t d\tau H_b(\tau)}e^{i\int_0^{t-t'} d\tau H_b(\tau)}q_\alpha e^{-i\int_0^{t-t'} d\tau H_b(\tau)}\rho_B^{eq}\Big) = \tag{3.40}$$

$$Tr_B\Big(e^{i\int_0^t d\tau H_b(\tau)}(a_\alpha^\dagger + a_\alpha)e^{-i\int_0^t d\tau H_b(\tau)}e^{i\int_0^{t-t'} d\tau H_b(\tau)}(a_\alpha^\dagger + a_\alpha)e^{-i\int_0^{t-t'} d\tau H_b(\tau)}\rho_B^{eq}\Big) \tag{3.41}$$

The time dependence of H_B is in the entity ω_α that can be expressed as $\omega_\alpha(t) = \langle\omega_\alpha\rangle + \delta\omega_\alpha(t)$. According to the choice of $\rho_B(t) \sim \rho_B^{eq}$ it is natural to suppose that the bath relaxes at equilibrium as its equilibrium fluctuations do, in a fluctuation-dissipation theorem fashion. Therefore, the phonon's energies will be considered randomly fluctuating around the NVE $\langle\omega_\alpha\rangle$ frequencies with a gaussian distribution of amplitude $\Delta = \sqrt{\langle\delta E^2\rangle} = \sqrt{\langle E^2\rangle - \langle E\rangle^2}$ where all the mean values are taken at the NVT equilibrium. As the time dependent part of the bath hamiltonian is not due to its operator part $[H_B(t), H_B(t')] = 0$ and thus $e^{i\int_0^t d\tau H_B(\tau)} = \prod_{n=0}^t e^{i\Delta\tau H_B(\tau_n)}$, where all the exponential commute. According to this, it is then possible to demonstrate that

$$e^{i\int_0^t d\tau H_B(\tau)}a_\alpha^\dagger e^{-i\int_0^t d\tau H_B(\tau)} = e^{i\int_0^t d\tau\omega_\alpha(\tau)}a_\alpha^\dagger \tag{3.42}$$

$$e^{i\int_0^t d\tau H_B(\tau)}a_\alpha e^{-i\int_0^t d\tau H_B(\tau)} = e^{-i\int_0^t d\tau\omega_\alpha(\tau)}a_\alpha \tag{3.43}$$

Equation 3.41 then becomes

$$Tr_B\Big((e^{i\int_0^{t'} d\tau\omega_\alpha(\tau)}a_\alpha^\dagger a_\alpha + e^{-i\int_0^{t'} d\tau\omega_\alpha(\tau)}a_\alpha a_\alpha^\dagger)\rho_B^{eq}\Big) \tag{3.44}$$

Before to proceed it should be assumed that

$$\begin{aligned} &Tr_B\Big((e^{i\int_0^{t'} d\tau\omega_\alpha(\tau)}a_\alpha^\dagger a_\alpha + e^{-i\int_0^{t'} d\tau\omega_\alpha(\tau)}a_\alpha a_\alpha^\dagger)\rho_B^{eq}\Big) = \\ &\quad Tr_B\Big(e^{i\int_0^{t'} d\tau\omega_\alpha(\tau)}\rho_B^{eq}\Big)Tr_B\Big(a_\alpha^\dagger a_\alpha\rho_B^{eq}\Big) + Tr_B\Big(e^{-i\int_0^{t'} d\tau\omega_\alpha(\tau)}\rho_B^{eq}\Big)Tr_B\Big(a_\alpha a_\alpha^\dagger\rho_B^{eq}\Big) \end{aligned} \tag{3.45}$$

Finally, according to Kubo's model[93, 94]

$$Tr_B\Big(e^{i\int_0^{t'}\omega_\alpha(\tau)}\rho_B^{eq}\Big) = \langle e^{i(\langle\omega_\alpha\rangle+\int_0^{t'}\delta\omega_\alpha(\tau))}\rangle = e^{i\langle\omega_\alpha\rangle t'}\langle e^{i\int_0^{t'}\delta\omega_\alpha(\tau)}\rangle = e^{i\langle\omega_\alpha\rangle t'}F(t') \tag{3.46}$$

Expanding F(t') as a cumulant expansion of averages and taking advantage of the gaussian statistic of fluctuation

$$F(t') = exp\Big(-\frac{1}{2}\int_0^{t'}\int_0^{t'} d\tau' d\tau''\langle\delta\omega(\tau')\delta\omega(\tau'')\rangle\Big) \tag{3.47}$$

making the substitution $\tau = \tau' - \tau''$

$$F(t') = exp\Big(-\int_0^{t'} d\tau(t'-\tau)\langle\delta\omega(\tau)\delta\omega(0)\rangle\Big) \tag{3.48}$$

assuming that the fluctuation correlation function decay as an exponential $\langle\delta\omega(\tau)\delta\omega(0)\rangle = \Delta^2 exp(-\tau/\tau_c)$

$$F(t) = exp\Big(-\Delta^2\tau_c^2(exp(-t/\tau_c) + t/\tau_c - 1)\Big) \tag{3.49}$$

According to the Born-Markov approximation the spin dynamics is in a regime where $t \gg \tau_c$, and therefore $F(t) = exp(-\Delta^2\tau_c t)$. Choosing τ_c according to the Heisenberg principle: $\tau_c = \hbar\Delta E^{-1} = \Delta^{-1}$ and so $F(t) = exp(-\Delta t)$.

In the end it is possible to define the phonon spectral shape according to the phonon Green's function:

$$G(\omega_{ij},\omega_\alpha) = \int_0^\infty dt' e^{-i\omega_{ij}t'} Tr_B\Big(L_\alpha(t)L_\alpha(t-t')\rho_B^{eq}\Big) = \tag{3.50}$$

$$\int_0^\infty dt'\big[e^{-i(\omega_{ij}-\omega_\alpha)t'}e^{-\Delta t'}\bar{n}_\alpha + e^{-i(\omega_{ij}+\omega_\alpha)t'}e^{-\Delta_\alpha t'}(\bar{n}_\alpha+1)\big] = \tag{3.51}$$

$$\frac{\Delta_\alpha}{\Delta_\alpha^2+(\omega_{ij}-\omega_\alpha)^2}\bar{n}_\alpha + \frac{\Delta_\alpha}{\Delta_\alpha^2+(\omega_{ij}+\omega_\alpha)^2}(\bar{n}_\alpha+1) \tag{3.52}$$

$\bar{n}_\alpha = \frac{1}{e^{\beta\hbar\omega_\alpha}-1}$ is the phonon occupation number according to Bose Einstein statistics, while

$$\Delta_\alpha^2 = \frac{\partial\langle H\rangle}{\partial\beta} = \frac{(\hbar\omega_\alpha)^2 e^{\beta\hbar\omega_\alpha}}{(e^{\beta\hbar\omega_\alpha}-1)^2} \tag{3.53}$$

Eq. 3.53 shows the temperature dependence of the phonon spectra line width. At low temperature Δ converges to zero asymptotically and a $1/\beta$ linear divergence is observed for $\beta \to 0$. About the same trend in temperature is experimentally observed through the determinations of homogeneous contribution to the phonon line width[95–97]. Although Eq. 3.53 qualitatively describes the correct observed behavior for Δ, a few discrepancies between this model and experiments exist. First of all, the experimental line width approaches a finite value different from 0 for $T \to 0$. Moreover, this model treat on the same footing every modes while experimentally the rapidity of Δ divergence depends on the anharmonicity of the mode considered. However, given its extreme simplicity, the model proposed represents an appealing way to introduce anharmonic contribution in the bath green function without any further requirements apart from harmonic modes calculation.

Master Equations

According to the last two sections the time evolution of the reduced density operator for the spin system is :

$$\frac{d\rho^s_{ab}(t)}{dt} = -\frac{1}{\hbar^2}\sum_{\alpha} \Big\{ \sum_j \delta_{bd} V^\alpha_{aj} V^\alpha_{jc} G(\omega_{jc},\omega_\alpha) - V^\alpha_{ac} V^\alpha_{db} G(\omega_{db},\omega_\alpha) - V^\alpha_{ac} V^\alpha_{db} G(\omega_{ca},\omega_\alpha) + \sum_j \delta_{ca} V^\alpha_{dj} V^\alpha_{jb} G(\omega_{jd},\omega_\alpha) \Big\} \rho^s_{cd}(t) \quad (3.54)$$

where it was used $\int_0^\infty dt' e^{-i\omega_{ij}t'} Tr_B\Big(L_\alpha(t-t')L_\alpha(t)\rho^{eq}_B\Big) = G(\omega_{ji},\omega_\alpha)$.

Let's study the case of population transfer:

$$\frac{d\rho^s_{aa}(t)}{dt} = -\frac{1}{\hbar^2}\sum_{\alpha} \Big\{ \sum_j \delta_{ac} V^\alpha_{aj} V^\alpha_{jc} G(\omega_{jc},\omega_\alpha) - V^\alpha_{ac} V^\alpha_{ca} G(\omega_{ca},\omega_\alpha) - V^\alpha_{ac} V^\alpha_{ca} G(\omega_{ca},\omega_\alpha) + \sum_j \delta_{ca} V^\alpha_{cj} V^\alpha_{ja} G(\omega_{jc},\omega_\alpha) \Big\} \rho^s_{cc}(t) \quad (3.55)$$

$$\frac{d\rho^s_{aa}(t)}{dt} = -\frac{1}{\hbar^2}\sum_{\alpha} \Big\{ \sum_j V^\alpha_{aj} V^\alpha_{ja} G(\omega_{ja},\omega_\alpha) - V^\alpha_{ac} V^\alpha_{ca} G(\omega_{ca},\omega_\alpha) - V^\alpha_{ac} V^\alpha_{ca} G(\omega_{ca},\omega_\alpha) + \sum_j V^\alpha_{aj} V^\alpha_{ja} G(\omega_{ja},\omega_\alpha) \Big\} \rho^s_{cc}(t) \quad (3.56)$$

$$\frac{d\rho^s_{aa}(t)}{dt} = \frac{2}{\hbar^2}\sum_{\alpha} \Big\{ -\sum_j |V^\alpha_{aj}|^2 G(\omega_{ja},\omega_\alpha) + |V^\alpha_{ac}|^2 G(\omega_{ca},\omega_\alpha) \Big\} \rho^s_{cc}(t) \quad (3.57)$$

Equation 3.57 is exactly the same result it would have been obtained if the derivation would have started with the probability density coming from the second Fermi's golden rule, integrated over the bath degrees of freedom:

$$P_{a\to b} = \sum_{\alpha\beta} P_\alpha \frac{2\pi}{\hbar} |\langle a\alpha | H_{sph} | b\beta \rangle|^2 \delta(\omega_{ab} + \omega_{\alpha\beta}) \quad (3.58)$$

as a density matrix for master matrix approach to the time evolution of H_0's eigenstates. Equation 3.57 could be used instead of the complete 3.54 if a the starting time the system is expressed as a incoherent superposition of H_0 eigenstates.

S=1/2 and S=1 Models

Pseudo S=1/2 with 1 mode

Let's consider a spin system composed by a doublet of $|0\rangle$ and $|1\rangle$ whose energy difference $E_1 - E_0 = |\delta| \sim 0$.

According to Eq. 3.57 the population (p_0 and p_1) of the states dynamic is reproduced by the system of linear differential equation:

$$\begin{cases} \frac{dp_0}{dt} = k_2 p_1 - k_1 p_0 \\ \\ \frac{dp_1}{dt} = k_1 p_0 - k_2 p_1 \end{cases} \quad (3.59)$$

Solutions of the system 3.59 are:

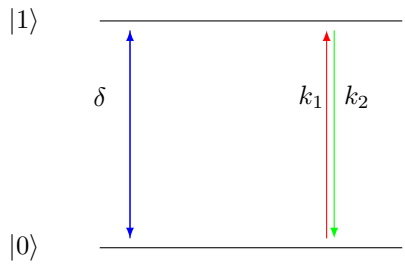

Figure 3.1: Energy level diagram for the one phonon model. Blue lines displays energy differences, red lines represent population transfers due to a phonon absorption and green lines represent population transfers due to a phonon emission. For graphical reasons the energy differences are not proportional to their real value. See the text for details.

$$\begin{aligned} p_0(t) = &\quad (p_0(0) - p_0(\infty))e^{-(k_1+k_2)t} + p_0(\infty) \\ p_1(t) = &\quad p_1(\infty)(1 - e^{-(k_1+k_2)t}) \end{aligned} \tag{3.60}$$

Assuming the reference frame with the z component aligned along an external magnetic field, or equivalently with z oriented in order to reduce rhombic terms in the spin hamiltonian, $\langle 0|M|0\rangle \sim -\langle 1|M|1\rangle$ and thus

$$M(t) \propto ((p_0(0) - p_0(\infty) - p_1(\infty))e^{-(k_1+k_2)t} + p_0(\infty) + p_1(\infty) \tag{3.61}$$

For such a kind of model the magnetization vector relax to its equilibrium value with a relaxation time $\tau = \frac{1}{k_1+k_2}$.

If $\hbar\omega > \delta \sim 0$ and a finite line width for the bath green function is assumed, k_1 and k_2 expressions are identical to $\alpha(2n(\hbar\omega) + 1)G(\delta, \hbar\omega)$. $\hbar\omega$ here stands for the energy associated to the phonon mode with frequency ω and α is the phonon assisted transition probability between the two states. In this scenario the transition between the two almost degenerate states is induced by the tail at ~ 0 of the Lorentzian phonon spectra, as no other modes are included.

case 1: $\hbar\omega >> k_bT$

In this situation the population of the normal mode is approximately zero and therefore $k_1 = k_2 \propto G(\delta, \omega)$. According to relation 3.52, and introducing the definition of Δ

$$k_1 = k_2 = \alpha \frac{\Delta}{\Delta^2 + (\delta - \hbar\omega)^2} \sim \alpha \frac{\Delta}{\Delta^2 + \hbar\omega^2} \sim \frac{\alpha}{\hbar\omega} e^{-\frac{\beta\hbar\omega}{2}} \tag{3.62}$$

and so the relaxation time follows an Arrhenius like temperature dependence

$$\tau = \tau_0 e^{\beta U_{eff}} \qquad \tau_0 = \frac{\hbar\omega}{\alpha} \qquad U_{eff} = \frac{\hbar\omega}{2} \tag{3.63}$$

case 2: $k_b T >> \hbar\omega$

In this case $k_1 \sim k_2 \propto n(\hbar\omega) G(\delta, \omega)$ and therefore:

$$k_1 = k_2 = \alpha \frac{1}{e^{\beta\hbar\omega} - 1} \frac{\Delta}{\Delta^2 + (\delta - \hbar\omega)^2} = \frac{\alpha}{\hbar\omega} \frac{e^{\frac{\beta\hbar\omega}{2}}}{(e^{\beta\hbar\omega} - 1)^2 + e^{\beta\hbar\omega}} \sim \frac{\alpha}{\hbar\omega}(1 - \frac{1}{2}\beta\hbar\omega) \tag{3.64}$$

In the limit for $\beta \to 0$, $\tau \sim \frac{\hbar\omega}{\alpha}(1 - \frac{1}{2}\beta\hbar\omega))^{-1} \sim \frac{\hbar\omega}{\alpha}(1 + \frac{1}{2}\beta\hbar\omega)$.

Pseudo S=1 with 1 mode

Let's now suppose there is an additional exited states $|2\rangle$ whose energy is higher than $|0\rangle$ and $|1\rangle$: $E_2 > E_1 \sim E_0$ *i.e.* $E_2 - E_1 \sim E_2 - E_0 = \lambda$ and $E_1 - E_0 =\sim 0$.

The kinetic equations for this kind of system are:

$$\begin{cases} \frac{dp_0}{dt} = -k_1 p_0 + k_2 p_2 - k_3 p_0 + k_3 p_1 \\ \frac{dp_1}{dt} = -k_3 p_1 + k_3 p_0 - k_1 p_1 + k_1 p_2 \\ \frac{dp_2}{dt} = -2k_2 p_2 + k_1 p_0 + k_1 p_1 \end{cases} \tag{3.65}$$

Assuming $\delta \to 0$ the various kinetic constants are

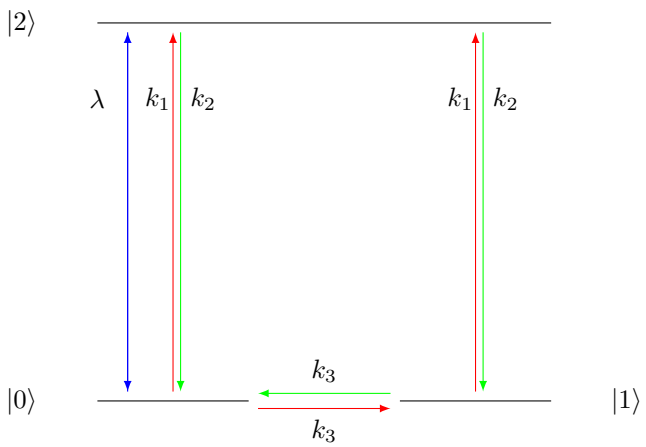

Figure 3.2: Energy level diagram for the one phonon model. The blue line display the zero field splitting energy, red lines represent population transfers due to a phonon absorption and green lines represent population transfers due to a phonon emission.

$$k_1 = \alpha n(\hbar\omega) G(\lambda, \hbar\omega) \tag{3.66}$$

$$k_2 = \alpha (n(\hbar\omega) + 1) G(-\lambda, \hbar\omega) \tag{3.67}$$

$$k_3 = \alpha (2n(\hbar\omega) + 1) G(\delta, \hbar\omega) \tag{3.68}$$

Assuming as before $M_z(t) = p_0 - p_1$, and thus subtracting the first and the second equation of 3.65

$$\frac{dM_z(t)}{dt} = \frac{d(p_0 - p_1)}{dt} = -(2k_3 + k_1)(p_0 - p_1) = -(2k_3 + k_1) M_z(t) \tag{3.69}$$

In order to understand the nature of this relaxation it is necessary to obtain eigenvectors and eigenvalues of the whole system 3.65. Instead of solving the system 3.65, it is more instructive to split the problem between pure direct intra ground state doublet population transfer and through excited state mechanism (Orbach mechanism) forcing k_1=k_2=0 and k_3=0, respectively. In the k_1=k_2=0 case, a system equivalent to the one already solved for the pseudo S=1/2 case is found and so the same solutions apply here to describe the direct relaxation mechanism. The system with k_3=0, describing a pure Orbach relaxation mechanism, has two eigenvalues besides the null one: k_1 and $2k_2 + k_1$. The eigenvector corresponding to k_1 is the same as for the pseudo S=1/2 spin and it corresponds to a population transfer from 0 to 1 and vice versa:

$$\begin{pmatrix} p_0 \\ p_1 \\ p_2 \end{pmatrix} = \begin{pmatrix} 1 \\ -1 \\ 0 \end{pmatrix} \tag{3.70}$$

Interestingly, this process, which introduces the k_1 kinetic constant in the magnetization decay profile, does not produce population on the excited states, contrary to common belief, but involve a virtually instantaneous excitation and emission of the system. It must be noted that even though the population of the excited state $|2\rangle$ is not involved in this process, the presence of this state is indirectly accounted for in the definition of the kinetic transfer rate constant k_1. The effect on the system of the eigenvalue $2k_2 + k_1$ is different from the former one and it corresponds to an eigenvector of the form

$$\begin{pmatrix} p_0 \\ p_1 \\ p_2 \end{pmatrix} = \begin{pmatrix} 1/\sqrt{6} \\ 1/\sqrt{6} \\ -2/\sqrt{6} \end{pmatrix} \tag{3.71}$$

This kind of eigenvector does not produce relaxation but merely adjust the population of the excited state to its equilibrium value and indeed it does not appear in the M(t) rate equation 3.69.

Focusing on the sole through excited state mechanism, the transition rate is

$$k_1 = \frac{\alpha}{\hbar\omega} e^{\frac{\beta\hbar\omega}{2}} \frac{1}{e^{\beta\hbar\omega} + \frac{(\lambda-\hbar\omega)^2}{(\hbar\omega)^2}(e^{\beta\hbar\omega} - 1)^2} \tag{3.72}$$

in the resonance condition this becomes

$$k = \frac{\alpha}{\hbar\omega} e^{-\frac{\beta\hbar\omega}{2}} \tag{3.73}$$

for all temperatures. However, in the low T regime, the general expression 3.72 imply a relaxation time constant

$$\tau_{Orbach} = \frac{\hbar\omega}{\alpha}[e^{\frac{\beta\hbar\omega}{2}} + \frac{(\lambda - \hbar\omega)^2}{(\hbar\omega)^2} e^{\frac{3}{2}\beta\hbar\omega}] \tag{3.74}$$

Expressions 3.62 and 3.73, corresponding to the direct and Orbach relaxation mechanism respectively, differ from those usually reported in literature[89, 98, 99]. The

direct mechanism is here T dependent also in the $\hbar\omega >> k_bT$ limit and it exhibits an Arrhenius like behavior. Notably, the effective spin flip barrier for both relaxation pathways is related to the half energy of the phonon. Although at a first sight it might seems counter intuitive the independence of the U_{eff} by λ in the Orbach mechanism, the spin splitting magnitude dependence is indirectly established. Indeed, in a most realistic situation, where multiple phonons are available, the most efficient ones are those near the resonant condition $\lambda \sim \hbar\omega$ and consequently $U(eff) \sim \lambda/2$. However, with the introduction of a finite life time the contemporary effect of more then one mode might be observed and each out of resonance node would contribute to the final magnetization rate expression according to the whole eq. 3.74. Finally it is important to stress out that all the formulas displayed above become coincident with the classical formulas available in literature if the anharmonicity of bath is neglected and an infinite phonon life-time is assumed.

The introduction of fluctuations into relaxation theory has already been explored before in the context of the U_{eff} reduction[100, 101] but, in contrast to this treatment, the line width broadening was phenomenologically applied to spin excited state energy levels instead to the bath vibrational levels. Although the former approach was virtually able to explain small U_{eff} reductions, it is not applicable to more recent dramatic barrier reductions, which would imply astronomically big excited states line width, in clear contrast to optical measurements.

Pseudo S=1 with Continuum Phonon DOSs

The discussion of the single phonon models clearly points out the importance of the phonon spectra features over the spin dynamics. Indeed, even for single mode models, different behaviors of the $\ln(\tau)$ v.s 1/T plot, with respect to the expected ones, could be derived once the temperature dependence of the phonon spectra line width is considered. Clearly, in this framework also the form of the phonon density of states is expected to play an important role. In order to investigate this further dependency, the S=1 model has been studied also once embedded in a pseudo continuum phonon density of states. This analysis has been done numerically by the integration of eq. 3.57 for 200 normal modes homogeneously spaced between 1 cm^{-1} and 200 cm^{-1}. The spin hamiltonian has been assumed to contain only the O_0^2 term and moreover, in order to study only the more relevant Orbach relaxation mechanism, the only spin hamiltonian derivatives different from zero has been assumed to be $O_{\pm1}^2$ in order to completely quench the direct relaxation mechanism. The spin dynamics has been investigated in the 4 K $<$ T $<$ 120 K range. Results of simulations for different O_0^2

values have been reported in fig. 3.3. The various lines all show a similar non linear behavior in the explored temperature range, however, for small barrier energies, the curvature is sensibly reduced and a linear behavior with a slope corresponding to the excited state energy is recovered. Interestingly, the slope of the pseudo linear behavior at high temperature (1/T<0.05) for big O_0^2 is about the same value of the excited state energy. Fig. 3.4 reports an increment of the high T region of the plot. The linear regression results (lines), superimposed over the simulated ones (points), predict effective barriers in good accord with the expected ones. These date, are in nice accord with experimental observations which commonly show Arrhenius behaviors for non strongly anisotropic compounds while big discrepancies appears in compounds with big zero field splitting.

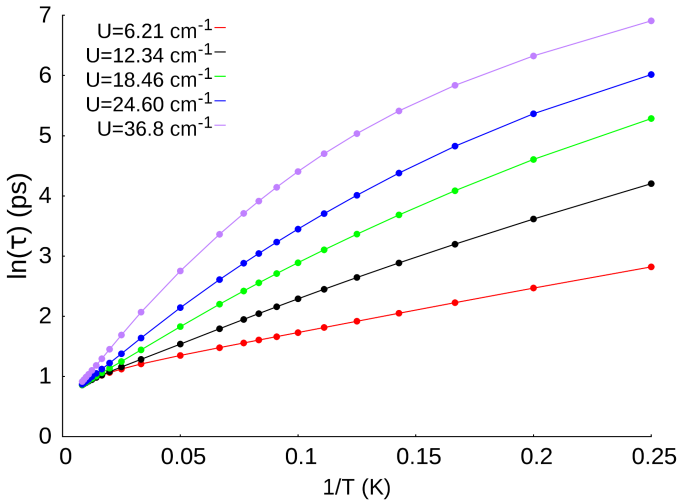

Figure 3.3: Temperature trend of relaxation times of a S=1 spin embedded in continuum of normal modes. The key reports the expected barrier *i.e.* the energy of the excited state.

Accordingly with the former theory, if a very narrow function *e.g.* a Gaussian function with 1 cm^{-1} of width at half height, is used instead of a Lorentzian function with Δ width, the same plot changes. Fig. 3.5 shows that the linear Arrhenius like behavior at low T, as predicted by Orbach's theory, is recovered if a the phonon energy fluctuations are small enough in order for the spin transition to be efficiently selected. Indeed, the slope of all the lines reported in fig. 3.5 in the range $0.01 < 1/T < 0.25$ is with

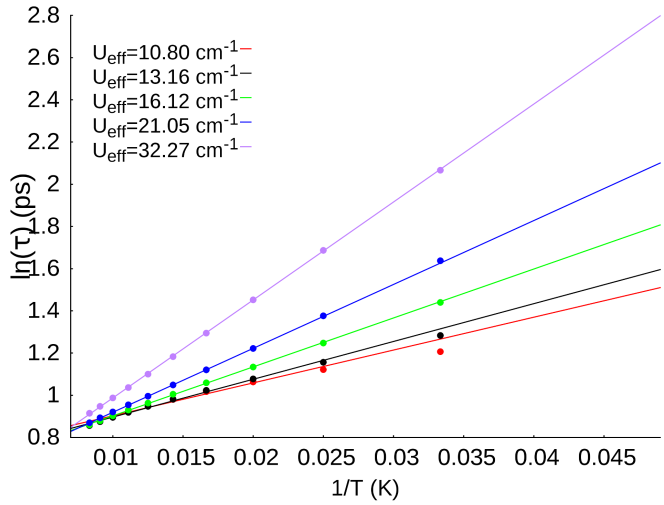

Figure 3.4: Linear fitting of the temperature trend of relaxation times of a S=1 spin embedded in continuum of normal modes in the high T regime. The key reports the effective barrier *i.e.* the slope of the reported fitted lines.

good approximation the same value of the excited state energy. Finally, it worth a comment the effect of neglecting the temperature dependence of phonon life time. *i.e.* a Lorentzian line shape of phonon spectra is assumed. Fig. 3.6 reports the results for these simulations where the Lorentzian line shape of phonons is assumed constant and equal to 0.01 cm^{-1}. The plots behavior appeared to be a mix between the two limiting cases just discussed. For small O_0^2 value the dynamics resembles the one deduced by selecting only a single phonon, while moving to higher energy excited states, features of the dynamics with a temperature dependent phonon line width are recovered. These last simulations clearly show that the phonon density of states is another key element for the rationalization of the spin dynamics and even without considering its temperature dependence, a significant different behavior, from the one expected for a totally harmonic crystal theory, is observed.

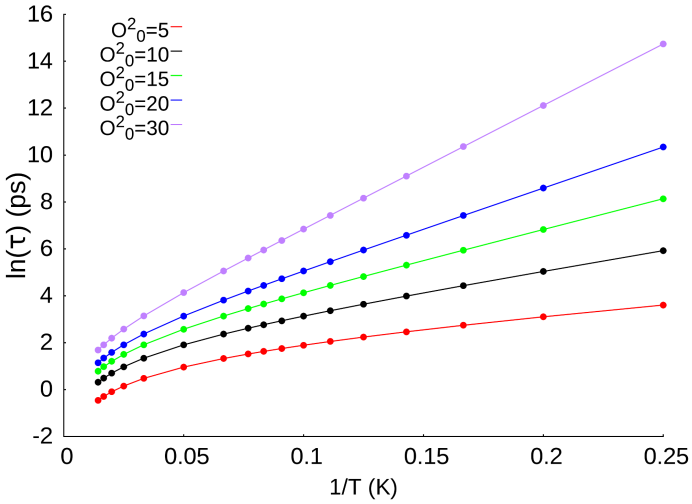

Figure 3.5: Temperature trend of relaxation times of a S=1 spin embedded in continuum of normal modes when a Gaussian function with 1 cm^{-1} of width at half height is used as phonon life time.

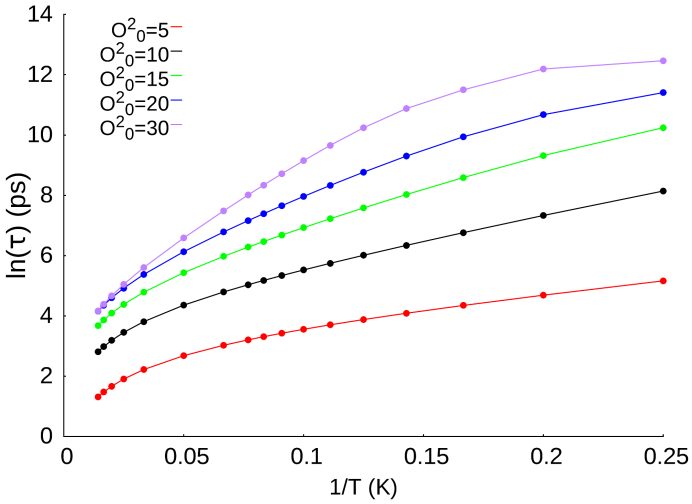

Figure 3.6: Temperature trend of relaxation times of a S=1 spin embedded in continuum of normal modes.

Conclusions

In this section the theoretical ground for the discussion of the spin phonon coupling mechanism has been developed through the specialization of the Redfiled equation for this interaction. A fundamental step forward, with respect to current theories, has been done introducing a more detailed description of the phonons green function. The anharmonic terms and the subsequent finite phonon life-time an have been introduced into the theory within a stochastic approach as the computational overhead for a detailed ab-initio computation of a molecular crystal green function is still far beyond the reach of modern hardware. On the contrary, the stochastic approach proposed here, although not quantitative, makes possible to get an estimation of phonons life-time with a simple analytical expression without any need of powerful computational resources. Another advantage of the presented set of equations is their generality with respect to the nature of the phonon that the spin is interacting with. Indeed, no assumptions have been made so far in order to let the theory be adaptable to a general ab initio treatment of phonons. The full set of density matrix equations of motion has been used to study a few simple models in order to extract some handily information on the spin dynamics. The analytic solutions for a pseudo S=1/2 and pseudo S=1, interacting with a single phonon, show the dramatic contribution of the temperature dependence of the phonon line width. In this framework both direct and Orbach relaxation mechanisms show a different temperature dependence with respect to the former Orbach's theory pointing out the importance of phonons features on the spin dynamics. The introduction of finite phonons life-time also switch on the effect of phonon density of states on the spin dynamics. Indeed, as demonstrated by the numerical analysis of a pseudo S=1 in a continuum of phonons, the spin dynamics could be driven by multiple phonons at the same time resulting in non Arrhenius like $ln(\tau) v.s. 1/T$ plots. Notably, an Arrhenius behavior with an effective spin-flip barrier of the same value of the excited state could be recover in two distinct situation: in the low T - low barrier and high T - high barrier regimes. All these foundings, although qualitative in nature, are in remarkable accord with a lot of experimental data showing the same trend in the two region of the barrier-T space and points out the need to consider the explicit phonon structure in order to correctly interpret experimental analysis. Specifically, an Arrhenius trend should not necessarily be expected and the slope of the $ln(\tau) v.s. 1/T$ plots might strongly depends on the temperature region the experiments is conducted. This partial loss of the U_{eff} meaning also point out the need to focus on other parameters as rule of thumb to increase SMMs quality.

3.3 First Order Spin-Spin Relaxation

Although spin-phonon interactions are the leading one at *high* temperature, usually under a few K the SMM relaxation is usually driven by spin-spin interactions. The source of these interactions lies both in presence of other SMMs in the crystal and in the presence of nuclear spins. In order to study this relaxation pathway eq. 3.32 and 3.57 could still be used as long as the interaction hamiltonian is replaced with the Zeeman interaction $H_{ss} = \vec{\mathbf{S}} \cdot \mathbf{g} \cdot \vec{\mathbf{B}}_{eff}(t)$. Differently from the spin-phonon situation where the nuclear dynamics was assumed faster than the spin one and thus integrated out of the equations of motion, here is not clearly possible to follow this route as $\vec{\mathbf{B}}_{eff}(t)$ is, at least in part, originated by the same spin which are evolving in time. The effective magnetic field felt by each spin is generated by the magnetic vector of all the other molecules inside the crystal. In a good approximation this can be calculated as sum of point dipole contributions

$$\vec{\mathbf{B}}_{eff}(t) = \sum_i -\frac{\mu_0 \mu_B g_s}{4\pi} \Big(\frac{3\vec{\mathbf{r}}(\vec{\mathbf{r}} \cdot \langle \vec{\mathbf{S}}_i \rangle)}{r^5} - \frac{\langle \vec{\mathbf{S}}_i \rangle}{r^3} \Big) \tag{3.75}$$

where the sum is extended to the whole periodic crystal molecules and $\langle \vec{\mathbf{S}}_i \rangle$ is the time dependent part of it as the expectation value is calculated over an evolving wavefunction. It must here be noted that in principle there is another time dependent part in this expression coming from the dependence on the molecule inter distance coordinate r. Accordingly to the point like dipole approximation only acoustic nuclear displacements are able to module such interaction. Clearly, this is a simplification of much more involved situation where also libration and optical modes act as a perturbation on both absolute value and orientation of $\langle \vec{\mathbf{S}}_i \rangle$. At very low temperature, when the only acoustic populated states are those near the Γ point, the effect of nuclear displacements could be neglected and no temperature effect is provided by phonons. In this regime Eq. 3.32 could be numerically integrated with time steps small enough to consider $\vec{\mathbf{B}}_{eff}(t)$ constant in that lapse of time. In this scenario the magnetic field generated by all the other SMMs in the crystal act as a static perturbation and thus introduces a transition probability only between degenerate levels. In conclusion, the master equations defining the i-spin dynamics are

$$\frac{\rho^s_{aa}(t)}{dt} = \frac{2}{\hbar^2} \Big\{ -\sum_j |V_{aj}|^2 \delta(\omega_{ja}) + |V_{ac}|^2 \delta(\omega_{ca}) \Big\} \rho^s_{cc}(t) \tag{3.76}$$

where $V_{ac} = -g_s \langle a|\vec{\mathbf{B}}_{eff} \cdot \langle \vec{\mathbf{S}}_i \rangle |c\rangle$.

This kind of relaxation pathway is usually called *quantum tunneling* relaxation mechanism because of its similarity with the tunneling effect of particles through potential barriers. However, the connection between the two effects is only virtual as proper tunneling is not an irreversible process as the one discussed in this section. Indeed, proper quantum tunneling has its origin in the oscillation of the phase component of a wave function which is not a system eigenstate, while spin-spin relaxation acts independently from the wave function of the system, as it is originated by the open-system nature of the molecule embedded in a spin bath.

3.4 Spin Hamiltonian Connection

The theory just outlined is expressed as function of hamiltonian derivatives. Although they could be evaluated by means of analytic derivatives machinery, an expression as function of a few parameters would be much more convenient. Moreover, in order to obtain more physical insights on the various contribution to the relaxation, a clear connection to the spin hamiltonian formalism would be desirable. Considering the system described by an effective Spin Hamiltonian $H_s = \sum_{kq} B_{kq}\hat{O}_{kq}(\vec{\mathbf{s}})$[25], H_0 matrix element derivatives could be evaluated as follows:

$$\sum_{i\ldots j}\langle SM_S|\frac{\partial^n H_0}{\partial q_i\ldots\partial q_j}|SM'_S\rangle = \sum_{i\ldots j}\frac{\partial^n}{\partial q_i\ldots\partial q_j}\langle SM_S|H_0|SM'_S\rangle = \tag{3.77}$$

$$\sum_{i\ldots j}\frac{\partial^n}{\partial q_i\ldots\partial q_k}\langle SM_S|H_{spin}|SM'_S\rangle = \sum_{i..j}\sum_{kq}\frac{\partial^n B_{kq}}{\partial q_i\ldots\partial q_j}\langle SM_S|\hat{O}_{kq}(\vec{\mathbf{s}})|SM'_S\rangle \tag{3.78}$$

Deriving 3.78 it has been took advantage of the non dependency of spin wave function with respect to bath normal modes ($\frac{|SM_S\rangle}{\partial q} = 0$) and of the spin hamiltonian definition $\langle SM_S|H_0|SM'_S\rangle = \langle SM_S|H_s|SM'_S\rangle$. At the best of my knowledge, this is the first time that a connection between general theory of spin-phonon relaxation and spin hamiltonian formalism has been reported. These relations also suggest a practical way to evaluate the spin phonon coupling coefficients on the basis of electronic structure calculations presented on the last chapter, indeed once normal mode displacements of the systems are known, it is easily possible to numerically derive the spin hamiltonian parameters.

3.5 Fe(II)tpa^{Ph} SMM

Spin dynamics has been carried out for the anion Fe(tpa^{Ph}) SMM[102] (structure and magnetization easy axis are reported in fig. 3.7), where tpa^{Ph} = tris(pyrrolyl-phenyl-methyl)amine is the ligand of the S=2 high spin Fe^{+2} ion. The trigonal pyramidal coordination geometry of the amine ligands around the Fe^{+2} center makes the first excited S=2 state almost degenerate with the ground state. This situation makes the spin orbit coupling interaction especially effective to split the degeneracy of S=2 ground state multiplet, producing a remarkable easy axis zero field splitting with D=-27.5 cm^{-1} with an almost vanishing rhombicity. Fe(tpa^{Ph}) crystallizes in a $P_{\bar{1}}$ space symmetry group with a primitive cell that comprehends two SMMs units and two co-precipitate Na ion coordinated by three dimethoxyethane solvent molecules each, for a total of 228 atoms. The Fe(tpa^{Ph}) structure has been optimized both for the isolated molecules and for the periodic unit cell in the gamma point approximation. The structures produced by the two optimization schemes are very similar, accordingly with the high stiffness of the ligands cage. Normal modes and harmonic frequencies have been calculated for both the isolated and periodic structure. From now on this two models will be denoted as *Isol Model* and *Bulk Model*, respectively.

Phonon density of states (DOSs) for both Isol Model and Bulk Model are displayed in Fig. 3.8. Major differences between the two models are evident, especially in the low energy part of the DOSs. The latter difference clearly comes from the appearance of lattice vibrations. Interestingly, the Isol Model shows a non zero density of states at very low energy values. Further differences come from the presence in the periodic cell of co-precipitate molecules which clearly contribute to the global DOS, see for instance the appearance of DOSs at about 3000 cm^{-1}. Moreover, intermolecular interactions are expected to introduce further modulation on the DOSs shape.

CASSCF calculations have been done in order to determine Fe(tpa^{Ph}) ZFS. All magnetic property calculations have been done on a single isolated molecule as periodic boundary condition are not implemented for correlated calculations. For instance, for the Bulk Model only one of the two Fe(tpa^{Ph}) molecules in the primitive cell has been characterized but this does not represent a problem as they are symmetry reported inside the crystal. However, the elimination of the explicit surrounding of the SMM during the anisotropy calculation poses a serious limitation to the model as the crystal is made of charged molecules. Despite dipole and polarizability long range effects due to the packing are usually neglected during these kind of calculations, reports about the importance of stark effects on the magnetic structure of SMMs exist[103].

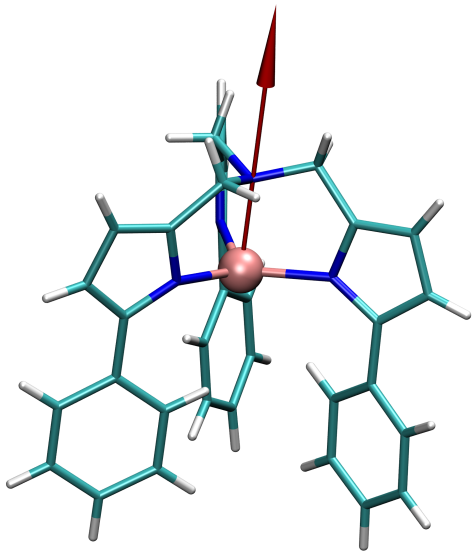

Figure 3.7: $(tpa^{Ph})Fe$ optimized structure. Iron ion is shown in pink, nitrogen atoms in blue, carbon atoms in green and hydrogen atoms in white. The red arrow displays the easy axis magnetization direction.

For this reason, a point charge modeling of the charge density of the periodic crystal has been attempted. Various point charge methods have been tested: Mulliken, density derived point charges (DDAPC)[104], RESP[105] and CHELPG[106]. The first two methods rely on the projection of the DFT electronic structure on atomic localized functions, while the last two are based on a fitting of the electrostatic potential outside the vdW volume of the molecule coming from the DFT charge distribution. Although all these parametrization schemes give similar results, final CASSCF calculations have been done with RESP point charges as this procedure is the one usually employed for force field development and thus much more tested and robust. Fig. 3.9 shows preliminary results about the stark effect on ZFS coming from charged co-precipitate molecules. Results coming from the introduction in the CASSCF simulation cell of the nearest co-precipitate molecule (red bars) show the dramatic impact of the stark effect on both the ZFS and its derivatives, the last one calculated along a low energy internal vibrational mode. The substitution of the explicit co-precipitate molecule with its fitted RESP point charges reproduces very nicely the latter results. It also must be stressed that the explicit molecule model is not necessarily the most accurate one, indeed the co-precipitate charged molecules is treated at the HF level of

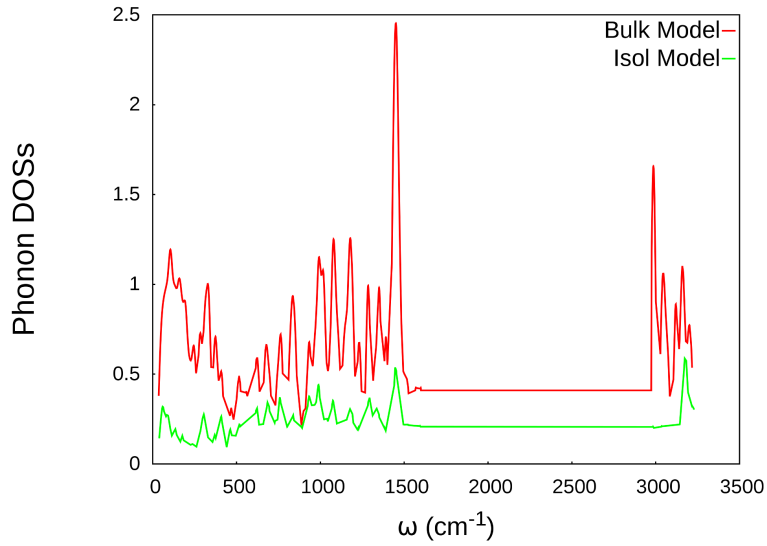

Figure 3.8: Phonon density of states. A gaussian broadening of 10 cm^{-1} has been applied to all the modes.

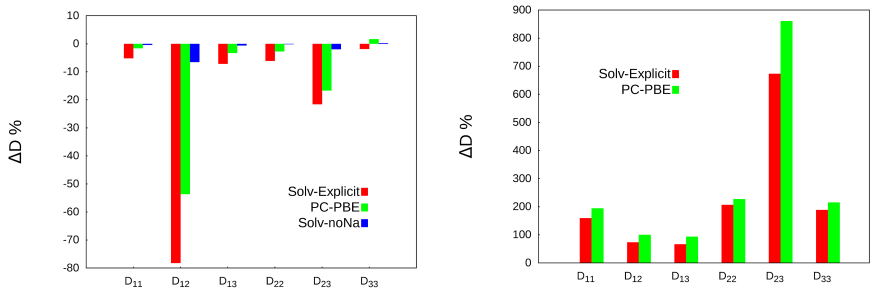

Figure 3.9: Stark effect on D and its derivatives along an internal displacement. Data are expressed as percentage difference with respect to the isolated molecule results. Red bars show results for the calculation that includes the explicit nearest co-precipitate cation molecule. Blue bars show the results for the same model after the quenching of the co-precipitate charge through the removing of the Na^{+1} ion. Green bars show the results for the model with RESP point charges in place of the co-precipitate molecule.

theory which is known to overestimated both dipole moment and polarizability.[107] Accordingly, DFT GGA fitted RESP point charges predict a smaller stark effect. Calculation with the explicit co-precipitate molecule without the sodium ion have also been done. The quenching of the net charge shows that dipole and polarizability effects have only a small impact on the magnetism of the SMM. In order to complete this analysis, it is interesting to compare the D tensor derivatives displayed on fig. 3.9 with those obtained by reciprocal translation of the two molecule. Both longitudinal and transverse movements produce spin-phonon coupling coefficients at least one order of magnitude smaller than those produced by the internal coordinates used to test point charge models, suggesting an intrinsic poor effect of acoustic phonons on relaxation. Clearly this is only a preliminary result and a more systematic study is needed. In order to mimic the periodic surrounding, the single explicit SMM has been embedded in a 21X21X21 lattice of point charges. The model that includes the point charge correction will be called *Bulk PC Model*. This model shares the same structure and phonon structure of the Bulk Model. Table 3.1 reports the calculated anisotropy parameters for all the models equilibrium structures.

Table 3.1: Calculated Fe(tpa^{Ph}) Models Anisotropy

Model	Exp	X-ray	Isol	Bulk	Bulk-PC
D cm^{-1}	-27.5	-27.54	-33.75	-30.74	-31.01
E/D	0.08	0.03	0.01	0.05	0.06

The D axial anisotropy constant calculated retaining the X-ray structure (X-ray model), without any optimization, is found very close to the experimental one demonstrating the ability of CASSCF to handle this problem, as also previously noted by Atanasov *et al.*[108]. Looking at the various models it is possible to observe a small deviation from the X-ray value. Bulk Model is the one which better reproduces the experimental value, accordingly with the higher level of environment quality. Interestingly, the effect of point charge correction is almost negligible. Although preliminary calculations predict an important effect of an externally applied electrostatic field on anisotropy, here the local filed is everywhere zero due to the crystal symmetry and thus ineffective.

Although the calculated axial anisotropy parameters are in nice accord with the experimental value, the reproduction of the whole ground state S=2 multiplet spectrum

is poor. Indeed, energy levels of the second pseudo doublet are overestimated of about 15 cm^{-1} with respect to the calculated ones while the energy of the highest energy spin level is underestimated of about the same quantity. The breaking down of the fit quality on a spin hamiltonian containing only the second order Stevens term is in line with the high anisotropy of the molecules. Indeed, the big ZFS observed for this SMM originates from the presence of two almost degenerate electronic energy levels with the same spin multiplicity, which mix to create the S=2 ground state spin multiplet once the SOC is turned on. As discussed in the chapter 2, this is the situation when the spin hamiltonian formalism itself is expected to fail. However as the ground state multiplet does not suffer from S-mixing effects the quality of its description could be raised employing higher order terms in the spin hamiltonian. Indeed, tests on this direction showed an increased quality of the CASSCF spin levels when fourth order terms are added to the spin hamiltonian. However, the introduction of these terms does not change the results discussed in the next sections, except for an overall speed up of the relaxation process thanks to new spin-phonon coupling terms. For this reason all the discussion on the spin dynamics will be done over the data obtained with a spin hamiltonian $H_s = \sum_{ij} D_{ij} s_i s_j$ without any loss of generality.

Magnetization Dynamics

Magnetization dynamics driven by spin-phonon interactions can be studied solving eq. 3.32. In order to reproduce a relaxation experiment the starting density matrix could be chosen accordingly to a pure state representing or not an eigenket of the spin hamiltonian. Fig. 3.10 display the dynamics of the magnetization component parallel to the external B field at 5 K, where the density matrix is initialized as pure maximally polarized S_z eigenket and as the pure lowest energy lying H_s eigenket, respectively.

Clearly in the latter situation coherences are zero at all times and a well defined exponential decay is observed. In the former situation the exponential decay is superimposed to an oscillating function arising from the phase dynamics. This fast ($\geq$ THz) wave function oscillations are the analog of a particle through barrier tunneling effect. Indeed, if a generic quantum system is not initialized as an eigenstate, it will oscillate coherently between its eigenstates or part of them, and this is exactly what happens to the spin system as long as it is not interacting with any bath. Clearly this effect is not by itself a relaxation mechanism as the phase state oscillating dynamics is not damped. Only as soon as the bath interaction is switched on, every density

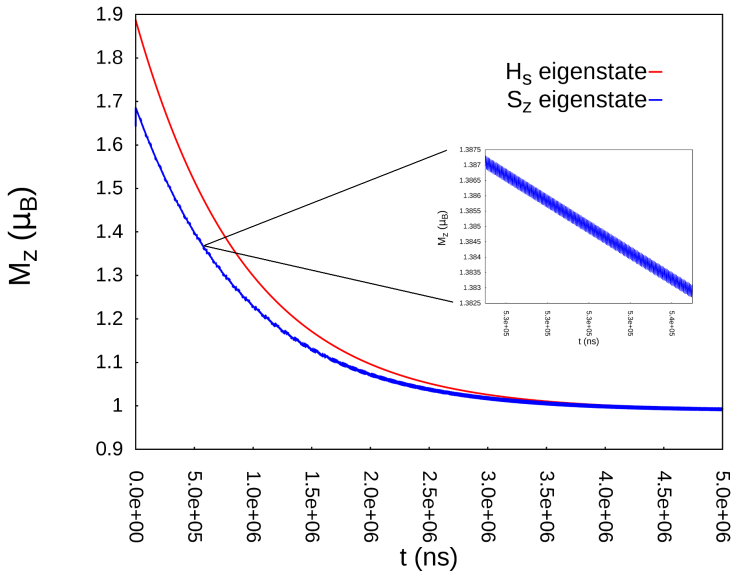

Figure 3.10: Temperature Dependence of Relaxation Time at 5 K. Red line corresponds to the dynamics of an H_s eigenstate, while the blue one corresponds to the dynamics of an S_z eigenstate.

matrix element will start decaying. This effect must not be confused with the so called *quantum tunneling relaxation*, which will be discussed later in the context of spin-spin interactions. Even though the starting magnetization is different in the two cases, the exponential decay characteristic time is the same. This is simply because the nature of the equilibrium driving force is unchanged in the two experiments and the population decaying part of the equation remains the same. For this reasons, in the next sections, all the calculations concerning T_1 will be done utilizing the master matrix equation 3.57 without any loss of generality. A final comment on the possibility to access the global dephasing time T_2 is here needed. Apart from inhomogeneous contributions, transverse relaxation time is due both to pure population decay (T_1) ad pure dephasing (T_2^*):

$$\frac{1}{T_2} = \frac{1}{T_1} + \frac{1}{T_2^*} \tag{3.79}$$

The pure dephasing relaxation time T_2^* arises from the asynchronous SMM relaxations

inside the crystal and thus, in order to compute it, the dynamics of both spin and nuclei of all the SMMs inside the crystal is required. Eq. 3.32 has been obtained through the trace over all the bath degrees of freedom and for this reason all the information about the explicit nuclear dynamics is lost. Indeed, all the three cartesian components of the magnetization vector relax according to the same exponential function and the oscillatory part of it persist as long as there is population, *i.e.* $T_2^* = 0$.

The inclusion of the spin-spin relaxation pathways through eqs. 3.76 necessarily needs the inclusion of more than one molecule inside the simulation cell. In order to do so, the Fe(tpa^{Ph}) unit cell, containing two molecules, has been reproduced along the three Bravais lattice vectors 5 times each for a total of 250 molecule in the simulation cell. The $\vec{\mathbf{B}}_{eff}(t)$ has then been calculated over these ensemble of spins within the point dipolar approximation and exploiting periodic boundary condition along all the three space directions in order to mimic the infinite crystal cell. $\vec{\mathbf{B}}_{eff}(t)$ is updated every spin dynamics step, which has been chosen in order to resolve smooth variation of the effective field. For this simulation the Dirac's delta appearing in eq. 3.76 has been chosen as a Lorentzian function with 0.0001 cm^{-1} broadening. The magnetization dynamics obtained from a simulation at 2 K with only this interaction would produce a $M(t)$ decay as showed by the red line in fig. 3.11.

the decaying profile could be fitted with a double exponential function (see blue and green line in fig. 3.11). This decay form arises from the presence of two different phase of the relaxation: at the beginning, the whole sample is polarized in the same direction (all the molecules have been initialized in their lowest energy H_s spin eigenstate) the relaxation is faster with respect to the last phase of the dynamics when the sample has almost completely lost its magnetization and the local magnetic field felt by the spins is almost zero. However, in perfect agreement with former simulation and experimental observations[109, 110], the two exponential decay could be also fitted with a stretched exponential

$$M(t) = (M(t=0) - M(t=\infty))exp(-(\frac{t}{\tau})^{\gamma}) + M(t=\infty) \tag{3.80}$$

This peculiar form of decaying profile is equivalent to a double exponential decay for $\gamma < 1$ (γ would have been 0.37 in the previous plot). The stretched exponential makes possible to extract a single relaxation time constant τ which can be monitored through temperature modulations as for the spin-phonon decay but, as the spin-spin dynamics has been introduced as a temperature independent effect, the spin-spin τ constant would produce a straight line in the $ln(\tau)v.s.1/T$ plots. Moreover, as the effective

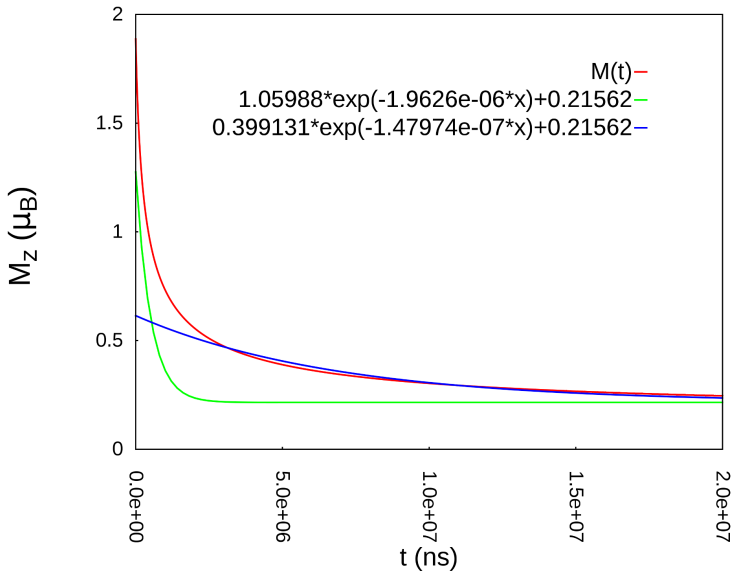

Figure 3.11: The red line reports the simulated behavior of M in time. The blue and green lines stands for the two exponential whose sum perfectly fits the M decay.

line width associated with the energy conservation condition in 3.76 has not been addressed, this remain an adjustable parameter which deeply affects the value of τ and for this reason no further discussion of the spin-spin dynamics will be provided in the next, leaving it for further studies. However, even at this stage an important information could be provided by this simulation. When both spin-spin and spin-phonon channel are potentially operative, the most efficient one is selected by the temperature and at low T the spin-spin pathway becomes dominant. Interestingly the region on transition is confined in few K and at higher temperature the parameter γ becomes one and exactly the same dynamics provided by the solely spin-phonon mechanism is recovered. On the contrary, only from a few K under the transition temperature the spin-spin relaxation becomes the only active relaxation mechanism and γ approaches ~ 0.4. These data lead to the very important conclusion that spin-spin dynamics, which involves only the ground state doublet due to the severe energy conservation condition, does not affect the thermally activated relaxation regime. Consequently, the so called tunneling of the magnetization could not be used as argument to explain the reduction of the effective barrier.

Temperature Dependence

Fig. 3.12 (red dots) shows the results for the magnetization dynamics simulation at various temperature for the $(tpa^{Ph})Fe$ crystal. The $ln(\tau)$ v.s. $1/T$ plot shows a linear behavior in the low temperature region with 1/T>0.2, a second linear behavior, but with different slope, is observed in the range 0.1<1/T<0.2 and finally a deviation from a linear trend is observed for small values of 1/T. The two linear behavior slopes correspond to $U_{eff} = 19.7\ cm^{-1}$ for the low T regime and $U_{eff} = 55.7\ cm^{-1}$ for the intermediate T regime. Experimental date are available only up to 0.2 K^{-1} and report an effective barrier value of 25 cm^{-1}, in good agreement with the present founding. For instance, both values are in net disagreement with the first spin excited state energy value, calculated at $\sim$94 cm^{-1} from the ground state.

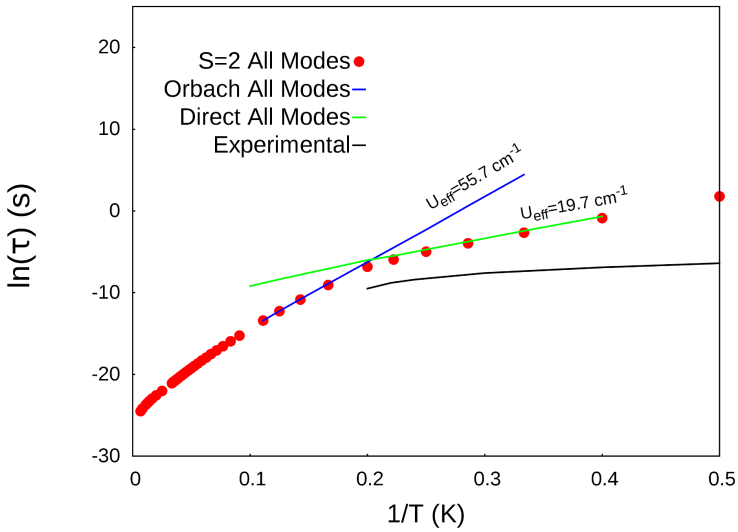

Figure 3.12: Temperature Dependence of Relaxation Time for Selected Modes

In order to individuate the nature of the relaxation mechanism at different temperatures, the same simulation has been done retaining only the effect of the almost degenerate ground doublet states in one case and totally neglecting it in a second case. In the former case, the direct mechanism is selected and the green line in fig. 3.12 represent its behavior. On the opposite, in the latter situation only the Orbach mechanism is retained and reported in fig. 3.12 with the blue line. The two different

pathways have been schematically reported in fig. 3.13.

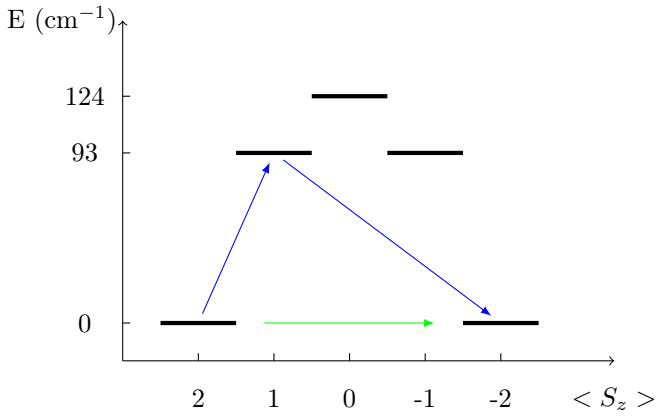

Figure 3.13: Horizontal black lines show the energy ladder of the five spin states. The S_z expectation values are calculated for the molecule orientated with its easy axis along the external magnetic field. The first four states are only slightly non degenerate ($\sim 0.5 \div 1\ cm^{-1}$) and their energy difference could not be appreciated from the figure. The green arrow represents the direct relaxation pathway and the blue arrows represent the Orbach relaxation mechanism.

The two linear regimes have been found generated by these two distinct mechanisms, with the direct one active at small temperature and the Orbach one active from 0.2 K^{-1} on. Interestingly, up to 0.1 K^{-1} the dynamics is driven by only the first few low energy lying normal modes and the observed slopes are in remarkable agreement with what expected by the S=1 model proposed in the previous section. Indeed, the lowest energy phonon has a frequency of $\sim 36cm^{-1}$ and it generates a pseudo Arrhenius behavior with $U_{eff} = 36/2 = 18cm^{-1}$ for the direct mechanism and a pseudo Arrhenius behavior with $U_{eff} = 3 * 36/2 = 54cm^{-1}$ for the Orbach mechanism. It should be noted from eq. 3.74 that the Orbach mechanism induced by an out of resonance mode contributes to the effective barrier with $\frac{3}{2}\hbar\omega$, differently from a resonance mode which contributes with $\frac{1}{2}\hbar\omega$. The effect of multiple phonons becomes active only at higher temperature where a drift form the Arrhenius law is observed. Fig. 3.14 highlights this scenario showing explicitly the contribution of different number of modes, counting from the lowest energy one, in the high T part of the former plot.

The experimental AC measurement results are reported in fig. 3.12 as well. The evidence of the relaxation time scale agreement between simulated and experimental one

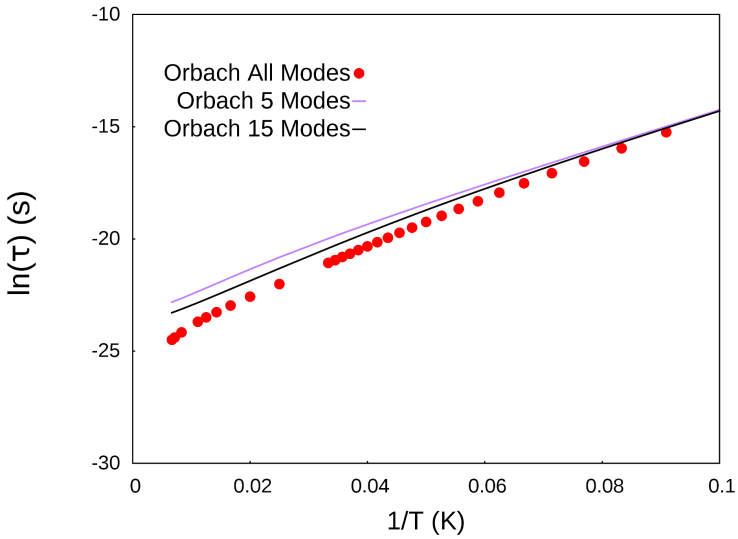

Figure 3.14: Temperature Dependence of Relaxation Time for Selected Modes

is a remarkable results, especially considering the huge number of ab initio calculations needed to produce these results. Moreover, although the simulated time scales are slightly longer (about a factor of 10 of difference between calculated and experimental τ at 5 K), this difference is expected to further reduce with the introduction of other relaxation pathways as those provided by second order relaxation processes or those provided by the inclusion of higher order spin hamiltonian parameters in both the spin hamiltonian and the spin-phonon coupling hamiltonian. For what concerns the comparison between calculated and experimental U_{eff} is important to note that the experiments were conducted without a diamagnetic dilution of the SMM crystal and therefore at low T a pseudo plateau is expected in virtue of the overcoming spin-spin dipolar relaxation pathways and, for this reason, it is not possible to unambiguously compare the low T simulation with the available experiments. At T higher than $\sim$ 0.25 K^{-1} a more pronounced $ln(\tau)$ temperature dependence is observed, signaling the overcoming of spin-phonon processes. The authors provided an $U_{eff} \sim 26$ cm^{-1} obtained fitting the Arrhenius law over the last three points available in this temperature region. In the original work of Harman *et al.* [102], the relaxation at higher T, with respect to those obtained in the AC measurements, are obtained by means of

Mössbauer experiments. The authors report the presence of two relaxation regimes for T $<$ 30 K, one in agreement with the AC fit of $\sim$ 26 cm^{-1} and the other one in agreement with the expected full barrier provided by the first excited spin state. Besides the difficulties related to a direct comparison of experimental and simulated data it is however possible to point out a qualitative agreement between the two. Indeed, both set of data show a small and comparable U_{eff} Arrhenius behavior at low T with a progressive recovering of a big U_{eff} close to the first spin excited state energy for high T.

As discussed previously, although its extreme simplicity, the model proposed to evaluate the energy fluctuations is able to account for the major features of the phonon homogeneous line width. However, the specific temperature dependence of Δ for each normal modes is related to the anharmonic nature of the mode itself. Therefore, discrepancies between experimental and the calculated U_{eff} trend are expected. However, at the same time, the dependence of the slope on the specific properties of phonons elucidates the presence of many different behavior reported in literature. The inclusion of the explicit bath dynamics in the ab initio protocol would require the calculation of the phonon self energies through the evaluation of high order derivatives of the molecular potential with respect to normal mode displacements. These kinds of calculations are quite expensive and at present beyond the scope of this thesis.

Despite the complex dependence over the system details does not make possible to easily predict the value of the effective barrier, a few main guidelines to increase U_{eff} may be provided by this analysis. The direct process is slowed down both increasing the lowest phonon frequency and reducing the spin-phonon coupling coefficients. While the former strategy might be an hard nut to crack, the second one is readily accomplished with the usual quantum tunneling reduction methods such as employing highly axial symmetry Kramer-ions. Although the Orbach mechanism is expected to be slower than the direct one in virtue of its higher U_{eff}, it is always the faster one at high temperature, as also observed for the molecule under exam. The reason is that in the pseudo Arrhenius regimes, its pre-exponential coefficient (see eq. 3.62 and eq. 3.74) is always smaller than the one of the direct relaxation mechanism because both depending on the value of the phonon frequency inducing the relaxation. Clearly the phonons most effective for an Orbach process are those near the resonance with the excited states and therefore those modes with a higher frequency with respect to those inducing the direct mechanism, which are the low energy ones. Therefore, although U_{eff} increases passing from direct to Orbach mechanism, the intercept of the Arrhenius plot is sensibly reduced with a resulting effect of fastening the Orbach

dynamics at high T instead of slowing it down with respect to the direct mechanism. The same argument applies to different and competitive Orbach mechanism involving different excited states. Indeed, an Orbach relaxation pathway through an higher energy excited states would involve the dynamics of higher energy phonons resulting in higher U_{eff} but also higher τ_0 at the same time. Indeed, if a continuum like phonon spectra is available, τ_0 of each mode increases as $\hbar\omega$ does and the sum of all the contribution would resemble the curvilinear trend observed for the S=1 model in the previous section. This effect points out that an increase of the excited state energy would imply an increasing of τ_0 at the same time of U_{eff} and since these two parameters have opposite effects the final magnetization relaxation rate is not slowed down as expected by the solely increase of U_{eff}. Although tricky to exploit, a possible strategy to quench the Orbach mechanism is to modulate the spin excited state energy value in order to obtain a non resonant condition with the phonon spectrum. However, as already discussed, more attention on other parameters besides U_{eff} (τ_0 among all) is mandatory in order to produce significant spin life-time extensions.

Internal-External Displacement Contribution

According to the discussion above, the most effective way to quench spin-phonon relaxation might be to selectively engineer the spin-phonon coupling coefficients. However, in order to do so, it is first necessary to understand the nature of the modes that couple with the spin. Nuclear displacements for molecular systems could be divided into two main classes: External and Internal displacements. In the first case the displacements are called acoustic and libration and correspond to translations and rotations of the rigid molecules inside the electrostatic potential generated by the crystalline surrounding. Instead, internal displacements are those who generate optical branches of phonons and correspond to internal vibrations of molecules. Figure 3.15 reports the ration between the cartesian norm of total and internal cartesian displacements $\sqrt{\Delta X^2_{Tot}}/\sqrt{\Delta X^2_{int}}$, for each crystal's normal mode, as function of frequency. As expected, external displacements are much more localized on low frequency modes due to the big inertia of such movements, however, there is not a clear separation between acoustic, librational and optical branches which are always mixed together. This is mostly due to the existence of very low energy internal vibrations such as those that involve heavy elements displacements.

Considering a spin hamiltonian such as $H_s = \sum_{ij} D_{ij} s_i s_j$, each mode contributes to the coupling between states a and b through:

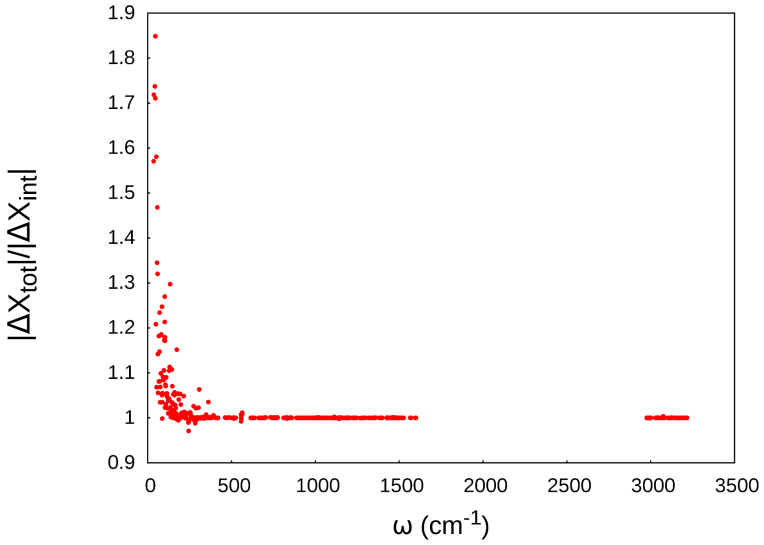

Figure 3.15: Contribution of External Displacements to Crystal Normal Modes

$$\sum_{ij} \frac{\partial D_{ij}}{\partial q_\alpha} \langle a|s_i s_j|b\rangle G(\omega_{ab}, \omega_\alpha) \tag{3.81}$$

Considering only the part of eq. 3.81 which does not depend on temperature, there are 5 independent elements for each mode $(\partial D_{ij}/\partial q)$ plus the dependence on the nature of the matrix elements on the wave function composition. Moreover, if an external field is applied, the elements $\langle a|s_i s_j|b\rangle$ would also depend on the orientation in space of the system. In order to let the dependence of the spin phonon coupling intensity on the phonon's nature to become more evident it is convenient to first convert the $\mathbf{D}$ cartesian tensor derivatives (shortly $\delta\mathbf{D}$ in the next), appearing in expression 3.81, into the corresponding spherical tensors of second order $H_{sph} = \sum_{-q}^{q} \delta X_q^2 \delta T_q^2(\vec{\mathbf{s}})$ and then to study its norm behavior (see 2.11 for the definition). Fig. 3.16 shows the frequency dependence of the spin phonon coupling coefficients. Nicely, an homogeneous behavior is not observed and there are two spectral region where a more pronounced phonons effect is evident: around 400 cm^{-1} and 1300 cm^{-1}. In order to split the effect of internal and external modes to the total 3.16 behavior, cartesian displacements coming from calculated normal modes have been projected into rotational translational and internal displacements[111]. All the D tensor derivatives have been calculated for two new model: *Bulk PC Proj Int* and *Bulk PC Proj Rot*, containing only internal and

rotational displacements respectively.

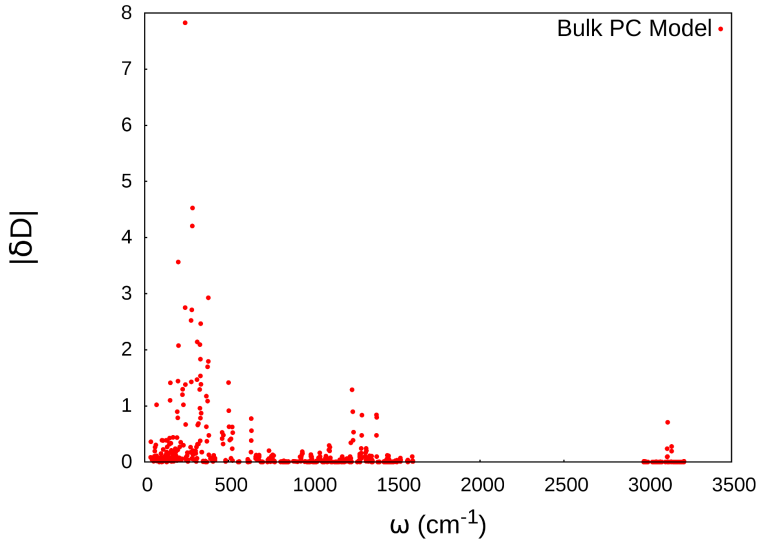

Figure 3.16: Contribution of External Displacements to the spin phonon coupling coefficients

The difference between $|\delta\mathbf{D}|$ norm for Bulk PC and Bulk PC Proj Int models is really small as shown by the ration between $|\delta D_{int}|$ and $|\delta D_{tot}|$ (see Fig. 3.17). The very first few modes are those which report the biggest difference, which reach a factor of more than ten for a couple of modes. Nevertheless, it is evident that the modulation of $|\delta\mathbf{D}|$ by internal modes is much more important than that produced by external displacements.

Fig. 3.18, reports the $ln(\tau)$v.s.1/T plots obtained for Bulk-PC, Bulk-PC-Proj-Int and Bulk-PC-Proj-Rot models. Accordingly with calculated spin phonon coefficients displayed in fig. 3.16, the relaxation coming from internal modes is more efficient with respect to the one induced by rotations with the exception of an intermediate temperature region where rotations becomes more effective. These results show that in order to correctly evaluate the effect of a normal mode it must be taken into account both the spin coupling coefficient and its temperature dependence deduced from the bath green function. Notably, the inclusion of the crystal structure by means of point charges does not influence the calculation of H_s's derivatives and the simulations for the Bulk model (not shown) are identical to the Bulk-PC model. The inclusion of electrostatic effects coming from the periodic crystal surrounding should affects the

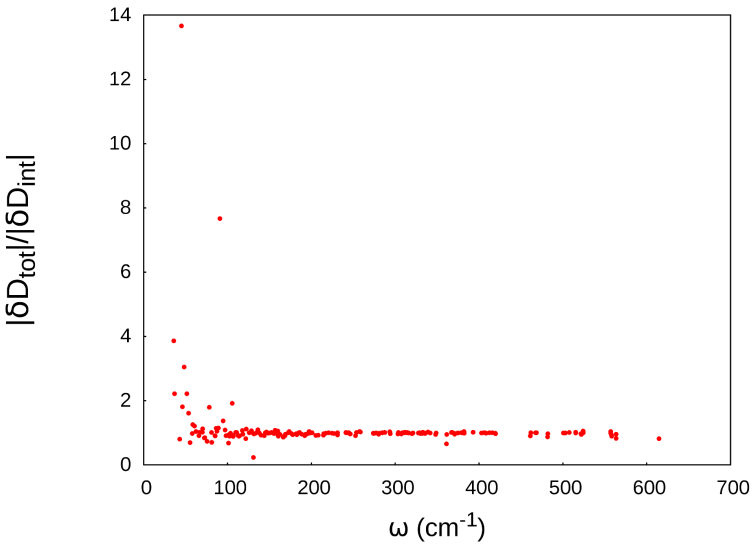

Figure 3.17: Contribution of External Displacements to the spin phonon coupling coefficients

calculation of the spin hamiltonian derivatives for every degrees of freedom. However, the most important effect is expected for acoustic phonons because , differently from rotations and internal vibrations, translations do not intrinsically change the spin hamiltonian elements and they are necessarily connected to the interaction between SSM and its surrounding. Consequently, translations can only affect the SMM anisotropy due to long range electrostatic interactions between different molecules. Electronic delocalization effects along different molecules are excluded as molecular crystal paramagnetic centers are efficiently screened by organic ligands. Therefore, as the inclusion of surrounding electrostatic interactions is found totally ineffective, the demonstration that acoustic modes are totally ineffective in this crystal is provided. However, as the symmetry of the crystal ($P_{\bar{1}}$) prevents the formation of a finite electrostatic field inside the crystal, such behavior was expected. This situation is not general and electrostatic field effects might be operative in other systems.

The importance of internal modes on the spin dynamics is a remarkable result and it is in line with the very short range effects of the spin orbit coupling, whose modulation induce such relaxation phenomena. In this context the enormous amount of magneto-structural correlations developed over the years might be dressed with renew interest and exploited to tune SMM spin-phonon coupling coefficients. Clearly,

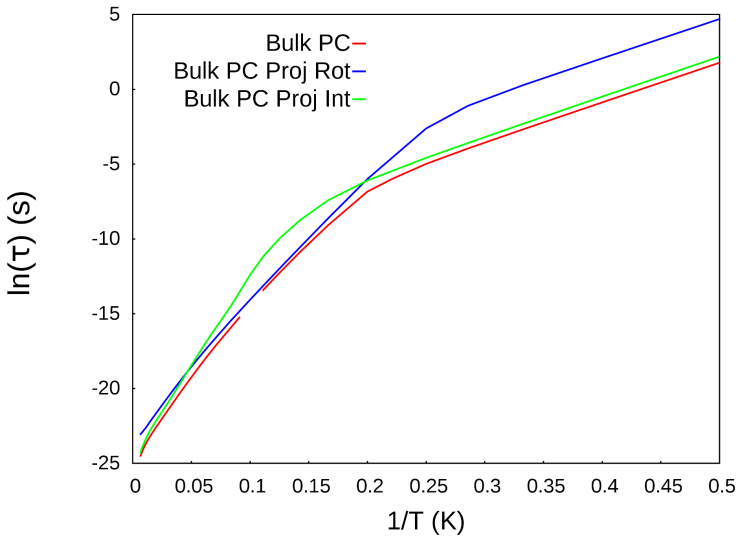

Figure 3.18: Temperature Dependence of Relaxation Time

following from the short range nature of the SOC, the most relevant modes for the spin relaxation are those whom induce large modification of the paramagnetic ions anisotropies and therefore those involving the first shell of coordination of the metal. Fig. 3.19 shows the frequency dependence of phonon cartesian displacements involving iron and nitrogen atoms inside the Fe(tpa^{Ph}) molecule for the Bulk Model. The maximum modulation of these structural parameters is found very close to the spin phonon coupling coefficients dispersion of fig. 3.16. However, a strict correlation between the two set of data is absent and a more refined collective variable, function of internal displacements, must be introduced in order to find a magneto structural correlation in the spin-phonon coupling context.

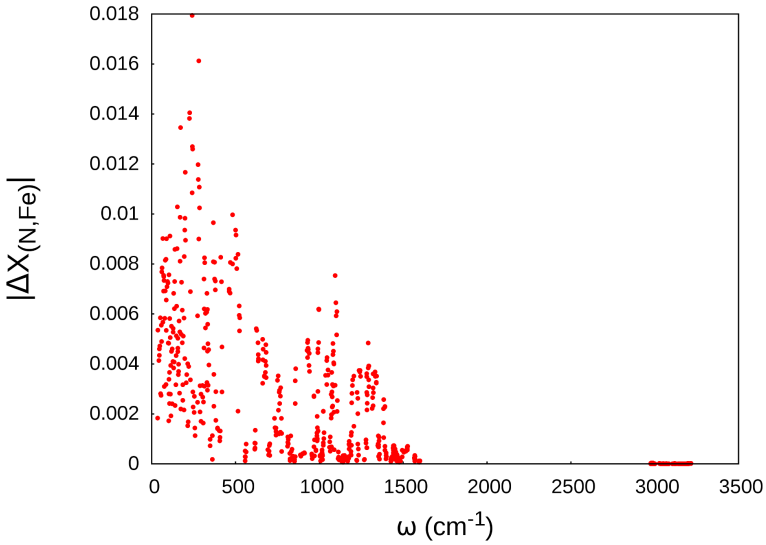

Figure 3.19: Temperature Dependence of Relaxation Time

3.6 Conclusion

The theory outlined in the previous sections of this chapter has been applied to a real chemical system through a rigorous ab initio treatment of both nuclear and electronic structure of the benchmark Fe(tpa^{Ph}) SMM. The magnetization dynamics has been studied under the effect of both spin-phonon and spin-spin interactions revealing the fundamental information that the quantum tunneling of the magnetization, induced by spin-spin dipolar interactions, does not affect the temperature active spin-phonon mechanism. Indeed, simulations showed that spin-spin and spin-phonon coupling mix together only in the narrow temperature range where the transition between the two regime takes place. This consideration has a deep impact on the general understanding of spin relaxation phenomena in molecular magnets as the magnetization tunneling has been usually used as argument to interpret the reduction of the effective spin flip barrier. The rest of the work focused on the spin-phonon relaxation and its temperature dependence. Due to the lacking of phonons under the frequency of 36 cm^{-1} for Fe(tpa^{Ph}) at the gamma point, the low temperature regime dynamics is driven by the first mode and only at higher temperature (T $>$ 10 K) more modes become active. The spin dynamics has been found dominated by a direct relaxation mechanism at T $<$ 5 K and by an Orbach mechanism at higher temperatures pointing out the needs to calculate all the spin-phonon coupling coefficients in order to predict such features as the transition between different regimes is connected with the relative spin-phonon coupling strength between different phonons. The results obtained for Fe(tpa^{Ph}) have also been interpreted with the results of the pseudo S=1 model discussed previously showing that the consideration made in the previous sections also apply in a more realistic context. The effects observed for $(tpa^{Ph})Fe$ are believed to be quite general and help to shed some lights upon the typical puzzling situation encountered in the context of highly anisotropic SMMs, where the low temperature relaxation rate follows an Arrhenius like trend but without a clear correlation with the expected U_{eff}. In light of this discussion this strict correlation must be lifted because both Orbach and direct processes follow an Arrhenius law which depends on the specific phonon structure. Reports available in literature, support this theory and give the chance to explain some conflicting situation. For instance, an experimental observation of multi Orbach mechanism has been reported for a Dy^{+3} SMM[112]. Specifically, the low temperature spin dynamics was found to be characterized by a double Arrhenius like trends with both effective barriers (334 K and 94 K) lower than the first accessible spin exited state (430 K). The presence of two separate Arrhenius like trend, both with an effective barrier below the first excited state, point out the existence of two different

mechanism which, in light of our discussion, could be attributed to the effect of two different normal modes. The possibility of processes, different from the Orbach one, showing an Arrhenius like trend in lanthanides based SMMs has been also proposed very recently by Pedersen *et al.* on the basis of experimental data[86]. However, the conclusions outlined in that work are essentially different from this thesis claims, since discrepancies between theory and experiments had been addressed by them introducing a second order Raman effect contribution. Here we have shown that is possible to conciliate theory and experiments without requiring second order effects (Raman relaxation) to prevail over first order ones (Orbach and direct relaxations). The study of Fe(tpa^{Ph}) has been extended also in order to understand which are the most important nuclear displacements able to induce large spin-phonon couplings. The phonon displacements have been analyzed in terms of their projection on internal and external movements of the single SMM molecule inside the unit cell. This study revealed that internal degrees of freedom are highly efficient in order to promote the spin relaxation in virtue of both their higher density of states (especially at high T) and of their intrinsic intensity. Nevertheless, also rotations affect the spin dynamics in the low temperature region and again, in order to predict such features for realistic system, a detailed ab initio modeling of all the SMM parts is mandatory. However, in light of an high temperature application of SMMs, the engineering of internal vibrations seems to be most fruitful path to be followed. In light of this consideration a first attempts to rationalized the correlation between the spin-phonon coupling coefficients and the internal degrees of freedom has been done and the prominent effect of the metal-ligand local distortions has been highlighted.

3.7 Summary

In this chapter the spin dynamics in SMMs has been discussed. The spin-phonon origin of relaxation has been addressed through a quantum mechanics first order perturbative approach where both harmonic and anharmonic terms have been introduced in the phonons Green function. Consequences of this theoretical framework have been investigated in the context of toy models as pseudo S=1/2 and pseudo S=1, which revealed the most important consequence of the introduction of a phonon finite lifetime. Both the temperature dependence of the phonon spectral width and the phonon density of states have been found to be key elements for what concern the temperature dependence of the magnetization relaxation time. A prototypical real SMM has been studied in an ab initio context revealing the need to carefully weight all the ingredients of the theory in order to make quantitative prediction of relaxation phenomena. The study of Fe(tpa^{Ph}) makes possible to investigate the joint presence of spin-spin and spin-phonon relaxation pathways demonstrating that the effective spin flip barrier reduction in the temperature triggered relaxation regime could not be possibly addressed to the quantum tunneling of the magnetization. Most importantly, the ab initio study point out the importance of the internal modes for the spin relaxation suggesting the possibility to chemically engineer specific degrees of freedom in order to extend the spin relaxation time. In this context, from a perspective point of view, a specif effort to offer practical guidelines for SMMs structures tailoring has been done, hoping to stimulate further experimental and theoretical investigations.

3.8 Computational Details

All the calculation concerning structure and frequency determination have been done with the cp2k software. To solve the UKS equations in CP2K, the Gaussian and plane waves (GPW) formalism was used. Double-ζ polarized basis sets (DZVP-MOLOPT-SR[73]) with Goedecker-Teter-Hutter norm conserving pseudopotentials[74, 75] have been employed. The auxiliary Plane Wave basis set has been truncated to an energy of 400 Ry for isolated systems and up to 600 Ry for crystals. The PBE functional has been used throughout all the calculations with Grimme's D3 vdW corrections. Several vdW correction schemes were tested on the periodic cell optimization. All the method tested showed an underestimation of all the lattice parameters. D3 and rvv10 corrrections showed similar result, with D3 performing slightly better. df and df-2 non local corrections have also been tested but both perform worse than D3 and rvv10. The chosen set up guaranteed a maximum error on lattice parameters of less than 5%. RESP point charges have been evaluated, with Cp2k, for all the four molecules inside the unit cell one at the time. The charge of the Fe ion has been constrained to its DDAPC value. All the other constraints were used with their default value. Hessian calculation has been done with a 0.001 a.u. numerical integration step, with a convergence criteria on the maximum element of the wave function gradient sets to 1.0E-08. The evaluation of all the anisotropic tensors, made with the package ORCA[71], has been carried out at the CASSCF level of theory. All the calculations have been done with a def2-TZVP [78] basis set for N and Fe elements while def2-SVP basis set has been used for C and H. The RI-J approximation along with the def2-TZVP/J auxiliary basis set[79] for all the elements has been used. Speaking in the ORCA notation, grids were set to 5 and VeryTightSCF. This set up has been test with respect to calculations done with the def2-TZVP basis set on every kind and no significant difference has been noted. All the spin-phonon coupling coefficients have been numerically evaluated differentiating calculated **D** tensor values along each of the normal coordinates obtained from the hessian diagonalization. The numerical integration step has been chosen as 0.2 normal mode units, in order to guaranteed a linear dependence of **D** elements with respect to displacements.

Chapter 4

SMMs on Au(111) Surface

Contents

So far, a detailed understanding of the atomic scale scenario of surface deposited molecules is missing and, therefore, one of the main open challenge in this field is about the understanding of the nature of the interaction between surfaces and molecules, the so-colled spinterface. The possibility to retain SMM properties after the adsorption is the first fundamental question to be addressed. However, the importance of such studies is also grounded by the interesting effects originated by molecule-surface interaction, which might thus be exploited as an additional tuning parameter in order to address molecules with new properties. Indeed, the possibility to combine effects such surface electron screening with the inherent quantum complexity of SMM might leads to a further enrichment of molecular properties. In this last chapter the interaction between SMMs and a metallic surfaces will be addressed. Once again the helycal pitch SMMs will be at the center of the investigation. Indeed, several molecules of the propeller-shaped family[113] have been showed to be robust

enough to retain their magnetic hysteresis loop[114] once grafted on Au(111), resulting as appealing candidates for a throughout analysis on how the magnetic properties change upon deposition on a metallic surface. A detailed experimental characterization of SMMs@Au(111) can be achieved only through an interplay between different techniques.[115] In particular, the difficult access to accurate structural information poses major limitations onto the full understanding of deposited SMMs properties. Indeed, the absence of an atomically resolved structure makes the assessments of the origin of the observed magnetic phenomena difficult to be unambiguously rationalized. In this scenario a cutting-edge theoretical description of SMMs deposited on surfaces becomes mandatory to fill up the missing information and therefore to draw a final picture of the SMM@Au(111) system.

A methodology able to provide the SMM@Au(111) structure without a reliable starting reference represents the first issue to be solved. X-ray derived geometries are commonly used for the calculation of magnetic properties of SMMs and in some studies, to account for the effects of adsorption on surfaces, the structures have been optimized at the level of theory of choice.[116–118] However, static optimization approaches can not be always sufficients to describe a complex configurational space that could present multiple minima, as it is expected to be the case by deposition of SMMs on surfaces. In this framework, ab initio molecular dynamics (AIMD) represent the proper computational tool to provide a reliable sampling of the accessible space of configurations at finite temperature. The generated trajectory is expected to visit the accessible structures according to their statistical probability at the selected thermodynamic conditions. In this respect, the MD simulation samples the free energy surface (FES) underlying the dynamic of the system of interest, and reproduces its characteristic thermal fluctuations. Recently AIMD has been applied to the study of Spin crossover magnetic systems containing Fe^{2+} ions.[119, 120] However, at the best of my knowledge, this computational strategy has never been applied before to study hybrid systems (adsorbate@surface) containing hundreds of heavy atoms and with a complex magnetic structure as the one observed for SMMs. Indeed, a similar statistical analysis restricted to only isotropic magnetic properties has been previously computed only at the QM/MM level for a metalloprotein system [121] containing two iron ions bridged by di-sulfuric bridge as catalytic center. The AIMD application to the study of the grafting process of Fe_4C_5@Au(111), will be reported in the first section of this chapter, where both dynamical information and steady state structures, which could well statistically describe the molecular geometry once the SMM is grafted on Au(111), will be discussed. The so computed accurate atomistic picture of the system is of fundamental importance in order to understand how the deposition

on a metallic surface affects the molecular magnetic properties and in section 4.2 the same methodology will be applied to a series of Fe_4 where the dependence of structure and magnetism over the surface-linking group nature will be provided. In section 4.3 the limits of AIMD will be tackled extending the time scales of the dynamics investigation through a force filed (FF) parametrization of all the main interaction involved in the hybrid SMM plus substrate system. The realization of an *ad hoc* effective potential for the Fe_4Ph@Au(111) system makes possible to confirm the AIMD results and, using a combined approach FF+AIMD, the self assembling process and the two dimensional crystal packing effects over the SMM magnetism will be investigated. The determination of the importance of structural deformations introduced by the substrate paves the ground for the final step: the determination of the weight of the substrate purely electronic effects on the SMM and their dependence on the SMM nature. In section 4.4 two structurally identical SMMs, but with different transition metal ions, have been studied: Fe_3CrC_5@Au(111) and Fe_4C_5@Au(111). The study of this topic will be performed for the isotropic exchange interactions inside polynuclear systems, as they have been recognized as a promising property to be exploited to build an I/O spintronic devices[15, 122]. Moreover, such a property has deep effects on the whole rich quantum magnetic behavior of SMMs it represent the first step before to propagated the discussion to anisotropic terms.

4.1 Surface Grafting Structural Effects

Fe_4C_5, whose X-ray structure is reported in fig. 4.1, represents the first SMM positively grafted on Au(111) with the retaining of its magnetic properties and in this section its structural evolution on a gold slab will be addressed through AIMD calculations. Before to proceed with the results an outline of the protocol used is required. When a trend of physical properties must be evinced, it is of fundamental importance

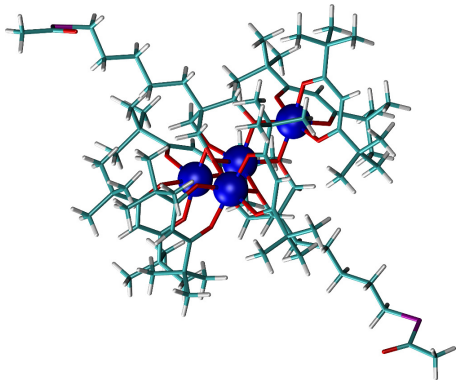

Figure 4.1: Sketch of Fe_4C_5 molecule. Iron atoms are colored in blue, oxygen atoms in red, sulfur atoms in purple, carbon atoms in green and hydrogen atoms in white.

to handle all the elements of the ensemble with the same computational procedure. Such a care must be used in order to enforce the homogeneity of the results and reduce the source of errors coming from unbalanced computational treatments. Since the geometry of grafted species can not be determined at the experimental level (it can only be qualitatively extrapolated in simple cases, *e.g.*, adsorbed porphyrins [123]), the calculation of the relaxed geometry, through structure optimization, of the SMM on the surface becomes mandatory. Therefore, in order to study the evolution of the magnetic properties from the bulk to the grafted scenario, the same optimization procedure must be applied also to the SMM bulk phase. The magnetic data computed on optimized geometries become the reference values to compare to those computed in the grafted scenario. In order to have comparable magnetic properties, each spin Hamiltonian parameter must be computed with the same electronic structure approach before and after the grafting. The choice of the computational protocol clearly depends on the properties one isinterested in. GGA DFT calculations are known to accurately determine optimized structures of large systems. However, the accurate calculation of magnetic properties, *e.g.* the calculation of exchange coupling parameters, may

require the use of hybrid functionals. The mixed computational protocol proposed in this work allows us to determine the evolution of the SMM's magnetic properties from bulk to the grafted scenario. The reference bulk structure optimization and the AIMD simulations have been carried out with the TPSS functional[124] corrected for the dispersion forces using the Grimme's formalism[125]. The calculation of exchange coupling parameters would require the use of hybrid functionals, while the anisotropic part of the spin Hamiltonian could be accurately calculated with the less demanding PBE functional. However, applying hybrid functionals to large periodic systems (SMM bulk and grafted on a surface) and over many configurations becomes computationally unaffordable. For this reason, the isotropic exchange coupling constants have been calculated at the PBE+U level of theory. [126] PBE0 calculations have been carried out for isolated systems and compared to the PBE+U results, in order to asses the reliability of the parametric Hubbard correction (see Methods for further details).

Bulk Structural and Magnetic Properties

One of the main issues related to the calculations of the magnetic properties at the quantum-mechanical level is the choice of the geometrical data. X-ray structures have often been considered as the best choice[127], since optimization procedures might be not accurate enough. Slight distortions of the most important geometrical parameters have significant effects on the computed magnetic properties. Indeed, the geometry optimization of molecules in the gas phase can hardly provide structures corresponding to the experimentally determined magnetic properties, which are generally measured in the solid state. Hence, in order to get a reliable bulk reference state, it is crucial to quantify the effects on the computed magnetic properties ascribed to the optimization at the DFT level and to the crystalline environment. To this purpose, the Fe_4C_5 molecule has been optimized both in vacuum (Opt-Isol model) and inside the periodic crystallographic cell (Opt-Bulk model). Optimizations have been carried out with the TPSS+D3 functional converging the electronic structures on the $S = 5$ BS state (see the Methods section for more details). The resulting Root Mean Square Deviation (RMSD) of the the Opt-Bulk model with respect to the X-ray structure is 0.10 Å. The larger contribution to the RMSD value comes from the C_5 aliphatic chains, which, however, are not well resolved in experiment. Instead, the RMSD of the iron and oxygen atoms of the magnetic core is only 0.03 Å. For the Opt-Isol model the global RMSD amounts to 0.12 Å, while it is reduced to 0.04 Å considering only the core of the molecule. Considering the strong dependence of the magnetic properties on

structural parameters, particular attention has been devoted to check the agreement between experimental and computed Fe_cOFe_p and γ-pitch angles of the propeller structure.

The latter is defined as the dihedral angle between the irons' plane and the plane $Fe_cO_2Fe_p$ defining the blades of the propeller structure, see fig.2.3. As already discussed, the isotropic exchange coupling between central and peripheral irons and the axial anisotropy intensity strongly depend on the Fe_cOFe_p and the γ-pitch angles, respectively. The mean value of the Fe_cOFe_p angle for the Opt-Isol and the Opt-Bulk models deviates from the corresponding X-ray values of 1.5% and 0.9%, respectively. The average γ-pitch angle deviates of about 1.5% for both Opt models. To verify the effect of these deviations on the magnetic properties, the isotropic exchange coupling and the anisotropy tensors have been evaluated for the Opt-Bulk and Opt-Isol models (see Tables 4.1 and 4.2). The same successful approach used to calculate these properties for the X-ray structures of a Fe_4 family has been exploited here. The isotropic exchange coupling constants are obtained at both PBE0 and PBE+U level of theory. The PBE+U results show a slight overestimation of the antiferromagnetic contributions comparing to the PBE0 ones(see Table 4.1). The difference between PBE+U and PBE0 can be ascribed to the fact that the used Hubbard U parameters for Fe and O were fitted at the DFT rev-PBE level.[128] Nevertheless, these results show the good transferability of the U parameters within the Fe_4 class of SMMs.

Table 4.1: Fe_4C_5 Crystal Magnetic Properties

	Functional	X-ray[a]	Opt-Bulk[a]	Opt-Isol[a]	Exp
J_{12} (cm^{-1})	PBE0	17.4	13.2	9.8	-
	PBE+U	21.5	16.2	13.9	
J_{13} (cm^{-1})	PBE0	15.3	8.1	5.0	-
	PBE+U	19.2	11.7	8.8	
J_{14} (cm^{-1})	PBE0	15.3	7.8	8.6	-
	PBE+U	19.1	11.4	12.5	
J_1 (cm^{-1})[b]	PBE0	16.4	9.7	7.8	16.74
	PBE+U	19.9	13.4	11.8	
J_2 (cm^{-1})	PBE0	0.2	0.1	0.1	0.5
	PBE+U	0.4	0.2	0.2	

[a] Selected molecule inside the Fe_4C_5 crystal;
[b] J_{12}, J_{13} and J_{14} average value.

The effective C_2 symmetry of the molecule is correctly retained only in the Opt-Bulk model, which turns out to be less antiferromagnetic than the corresponding X-ray structure (see Table 4.1). A further decrease of J has been obtained for the Opt-Isol model. The same trend has been observed for both the PBE0 and PBE+U approaches. This confirms the strong dependence of the magnetic properties on small geometrical variations, thus emphasizing the importance of accurate reference structures. Previous studies on iron dimers and Fe_4 molecules [129, 130] suggest that the FeOFe angle variations have the largest effect on J_1. Instead, in the Opt-Bulk model a large decrease of J_1 seems to be induced by a slightly changed Fe_cOFe_p angle. Most of the structural differences between X-ray and Opt-Bulk come from the rotation of the two tripodal ligands along the pseudo C_3 symmetry axis. This rotation occurs without changing the position of the oxygen atoms. It rather modifies the out-of-plane angle of the alchoxy-nearest carbon with respect to the Fe_c-O-Fe_p plane. Test calculations over an iron dimer model support the hypothesis that also this degree of freedom could affect the isotropic exchange interaction between μ-alchoxy bridged iron clusters (see ESI for further explanations).

Table 4.2: Fe_4C_5 Crystal Magnetic Properties

	Functional	X-ray[a]	Opt-Bulk[a]	Opt-Isol[a]	Exp
D_1 (cm^{-1})	PBE	-1.105	-1.050	-1.046	-
E/D_1		0.03	0.01	0.11	
D_2 (cm^{-1})	PBE	0.818	0.639	0.650	-
E/D_2		0.16	0.20	0.21	
D_3 (cm^{-1})	PBE	0.731	0.619	0.540	-
E/D_3		0.17	0.18	0.22	
D_4 (cm^{-1})	PBE	0.731	0.628	0.591	-
E/D_4		0.17	0.18	0.20	
$D_{S=5}$ (cm^{-1})	PBE	-0.475	-0.426	-0.425	-0.451
$E/D_{S=5}$	PBE	0.02	0.03	0.06	0.01

[a] Selected molecule inside the Fe_4C_5 crystal;

For what concerns the axial anisotropy parameter, D, the symmetry properties are correctly retained in the Opt-Bulk model and this seems to be sufficient to get a good agreement with experiment. Apparently, the structural changes generated by the optimization have a marginal effect on this quantity. These results shed light

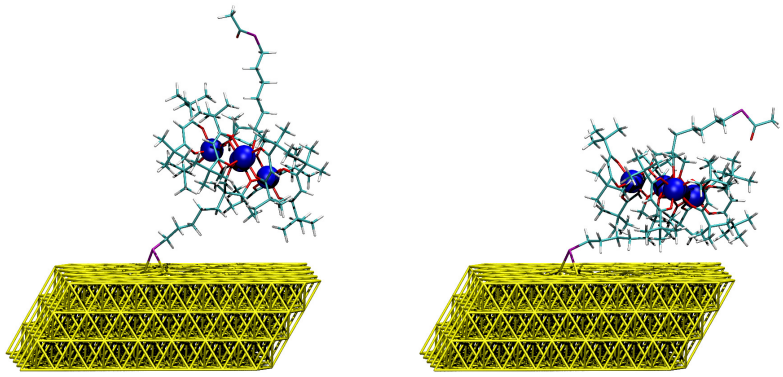

Figure 4.2: On the left the Fe_4C_5@Au(111) starting configuration used for the AIMD simulation (GeoUp). On the right one snapshot extracted from the trajectory after thermalization (GeoDown). Color code as in Fig. 4.1. Yellow is used for the gold atoms.

on the importance of studying the condensed phase to reproduce the experimental properties.

As a summary, the Opt-Bulk model is preferable to reproduce both geometrical and magnetic features of Fe_4C_5 and thus it is selected as reference model.

Fe_4C_5@Au(111) Molecular Dynamics and Structures Relaxation

The DFT-optimized structure published by Mannini *et al.*[113] was obtained with the bare TPSS functional as were not available vdW correction methods at the time. This structure has been optimized with the computational set up explained in the Methods section but the inclusion of D3 corrections does not significantly change the Fe_4C_5@Au(111) structure. This geometry (GeoUp model, Fig. 4.2 left panel), already found by Mannini *et al.*[113] is the starting configuration for the AIMD simulations. The initial thermalization run at 200 K ($\sim$ 3 ps) has produced important structural changes and a stabilization of about 77 kcal mol^{-1}. The new relaxed geometry (GeoDown model, see Fig. 4.2 right panel) is characterized by the collapse of the aliphatic C_5 chain on the gold surface, so that the organic scaffold of the magnetic irons core is significantly closer to both the surface and the aliphatic chain itself. Moreover, the angle θ, defined as the angle between the normal to the plane of the

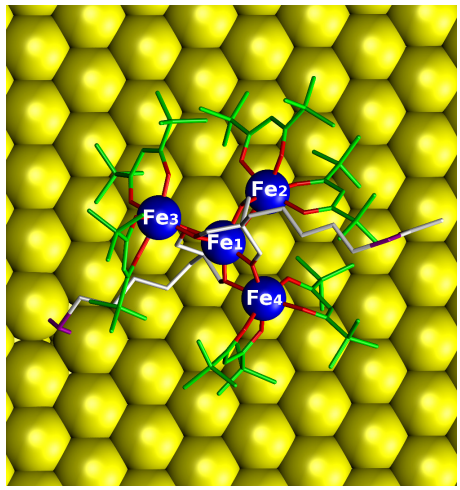

Figure 4.3: Top view of an AIMD snapshot. Color code as in Fig. 4.2 but for the C_5 aliphatic chains' carbon atoms colored in white.

four irons and the surface normal, is significantly smaller (see Fig. 4.2). θ is related to the easy-axis direction of the spin ground state anisotropy. As a consequence of this rearrangement, also the magnetic core undergoes a strong deformation, with the loss of the C_2 symmetry axis along the Fe_1-Fe_2 bond.

In order to sample the configurational landscape of Fe_4C_5@Au(111) at finite temperature, eight independent AIMD simulations have been started from the minimum structure found after the thermalization. In order to generate independent trajectories spanning the accessible phase space, the velocities have been differently initialized (details in Methods). Each independent run consists of a thermalization part at 200 K, followed by a sampling part at equilibrium. The sum of all eight sampling times amounts to 20 ps, which can be used for the analysis of the equilibrium properties of Fe_4C_5@Au(111) at 200 K. All trajectories span the same region of the configurational space, which suggests that a stable minimum is already reached during the thermalization. The C_5 aliphatic chain remains in close contact with one dpm ligand of Fe_3, while the other dpm are free to lay in contact with the surface (see Fig. 4.3). As a consequence, the molecule turns out to be tilted with respect to the surface normal and the symmetry elements of the Fe_4C_5 magnetic core are completely removed.

The statistical distributions of Fe_cOFe_p, γ-pitch, and θ angles, reported in Fig. 4.4 and Fig. 4.5, provide an interesting overview on the observed distortions. The mean value of the Fe_cOFe_p angle, averaged over the three Fe_c-Fe_p couples inside the molecule,

Table 4.3: AIMD Walkers Final Energies

	GeoUp	GeoDown	Walker1	Walker2	Walker3	Walker4	Walker5	Walker6	Walker7	Walker8	Avg.[a]
E (Kcal mol^{-1})	0.0[f]	-76.95	-83.43	-79.02	-79.09	-79.97	-81.54	-81.73	-81.16	-79.40	-80.67
RMSD[b]	0.64	0.00[f]	0.16	0.25	0.38	0.20	0.21	0.20	0.28	0.34	0.25
Fe_cOFe_p[c]	102.37°	102.94°	103.15°	103.54°	102.95°	103.65°	104.88°	104.23°	105.23°	104.07°	103.73
θ[e]	29.0°	14.7°	18.5°	18.0°	16.5°	16.9°	16.3°	13.9°	14.3°	17.5°	16.5°
γ-pitch[d]	67.3°	71.5°	71.1°	71.2°	68.2°	70.6°	72.7°	69.1°	70.8°	78.0°	71.4°

[a] This averaged value is calculated over the eight final AIMD structure only;
[b] Evaluated considering irons and oxygens from magnetic core region only;
[c] Averaged over the molecule, Exp. Value 102.89°;
[d] Averaged over the molecule, Exp. Value 70.45°;
[e] Estimated upper limit value by Mannini *et al.*[113] 35°;
[f] Reference value.

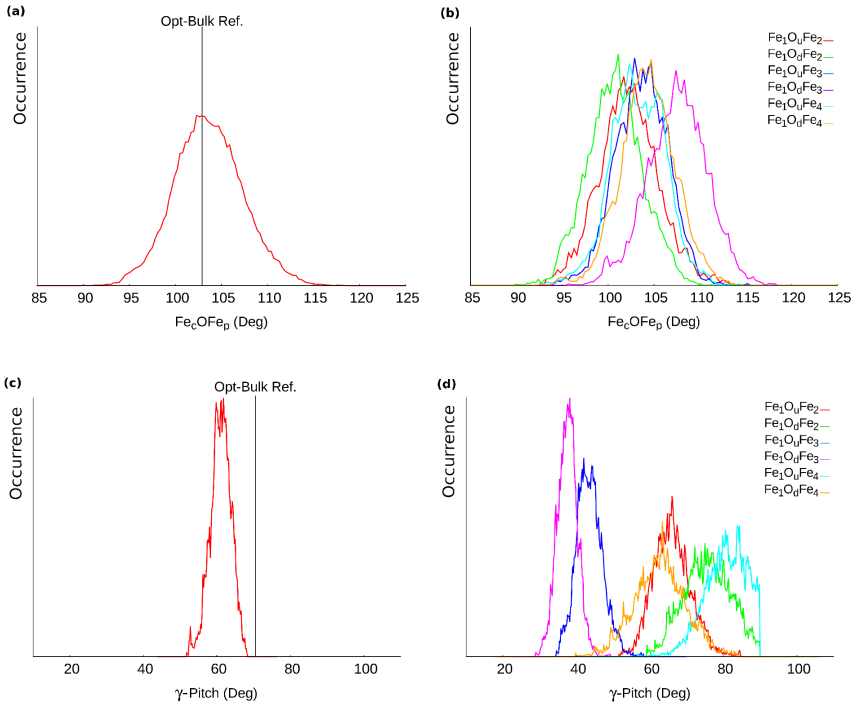

Figure 4.4: (a): Molecular average FeOFe angle's normalized distribution. (b): Single FeOFe angle's normalized distributions. (c): Molecular average γ-pitch angle's normalized distribution. (d): Single γ-pitch angle's normalized distributions.

is 103.8° (Fig. 4.4a). This value is only slightly larger than the value characterizing the X-ray geometry: 102.6°. Splitting the average into the single angle contributions, both for the oxygen above (O_u) and below (O_d) the iron ions' plane, as showed in Fig. 4.4b, it is noticed that the $Fe_1O_dFe_3$ distribution is shifted with respect to the others. On the other hand, the single γ-pitch angles fluctuate around quite different mean values, while the molecular average is strongly peaked at 61.1° (Fig. 4.4c *vs* Fig. 4.4d). In both cases, the larger deviation from the molecular average value is observed for the Fe_3 ion's properties. Such different behavior can be ascribed to the fact that this ion is the one in direct contact with the C_5 chain.

Even though Fe_4C_5@Au(111)'s local magnetic centers undergo severe geometrical distortions upon grafting, the differences are partially averaged at the molecular level. Fig. 4.5 shows that θ explores angles between 10° and 25° with a mean value of 16.7°. This means that the magnetization easy-axis does not sample all the direc-

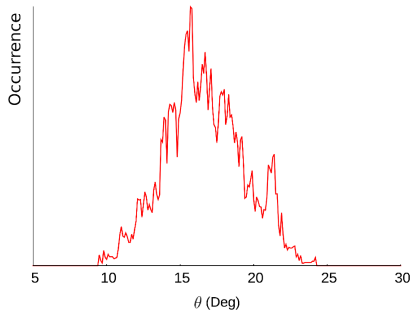

Figure 4.5: The angle between the irons' plane normal and the surface's normal.

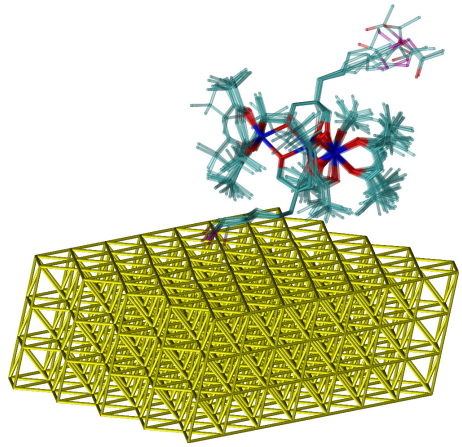

Figure 4.6: Overlapped structure of all the Fe_4C_5 Walkers. Walkers' geometries have been translated over the Au(111) slab minimizing the displacement between equivalent iron ions. Color code as in Fig. 4.2.

tions inside a cone, as expected.[113] Instead, it moves inside an hollow cone, avoiding the structures strictly perpendicular to the surface. The observed behavior is due to the presence of the C_5 carbon chain which remains under the organic scaffold of the Fe_4 core, thus imposing the tilt. The not innocent influence of the functionalization group of the tripod ligand on the final grafted geometry is even more evident. Indeed, if a flexible aliphatic chain can ensure a lower angle θ, it can also induce larger geometrical perturbations at the magnetic core level, which in turn might alter the Fe_4C_5 magnetic properties. SMMs magnetism becomes experimentally evident only at temperature of a few K, while AIMD generates a structural sampling at 200 K.

In principle, starting from the sampled configurations, an estimate of the magnetic properties could be extrapolated from structural magneto-correlations. However, it is preferable to get rid of the entropic contributions, *i.e.* to derive from the FES exploration the corresponding equilibrium structures on the PES. Even though on the FES the system has remained in one single basin of attraction, the underlying PES is topographically corrugated, *i.e.* is characterized by several local minima. The structural features distinguishing among these minima determine fluctuations of the magnetic properties that might become important for the understanding of the experimentally observed behaviour. In order to identify possible different minima on the PES, a simulated thermal annealing (from 200 K to a few K) has been applied to the final configuration of each of the eight generated trajectories. Each annealing has been followed by a structure optimization. Energies, RMSD and selected geometrical parameters for the eight optimized geometries (Walker1-8 from now on) are summarized in Table 4.3. All the structures are in a range of few kcal mol^{-1} in energy. With respect to the GeoDown model, they are approximately 4 kcal mol^{-1} more stable. RMSD (only for iron and oxygen atoms) values and Fe_cOFe_p and θ angles are close to the averages of the corresponding distributions as obtained along the AIMD sampling, and differ substantially from those calculated for the GeoUp model. The most evident structural parameter that distinguishes the eight Walkers is the position of the dangling C_5-SAc aliphatic chain, as illustrated by the overlap of eight sets of coordinates in Fig. 4.6. Small, but significant from the magnetic point of view, deviations in the core region are also observed, which point to a distribution of the values of certain magnetic properties, even though these structures belong to the same minimum on the FES.

Magnetic Properties Analysis

As discussed above, in order to employ a consistent electronic structure method to compare magnetic properties of Bulk-Opt model and the Fe_4C_5@Au(111), the PBE+U approach has been adopted to evaluate isotropic exchange coupling constants. As for Bulk-Opt, Fe_4C_5@Au(111) retains antiferromagnetic exchange interaction between iron ions and the $S = 5$ ground state multiplicity. The average values of the Js reported in the last column of Table 4.4 reveal a stronger antiferromagnetic character for Fe_4C_5@Au(111) than for Opt-Bulk. In particular, J_1 increases of about 11 cm^{-1} and J_2 of about 0.2 cm^{-1}. The bulk pseudo C_3 symmetry is here lost and the individual J_{12}, J_{13} and J_{14} values are quite different one from each other. According to the structural analysis made in the last section, these J_{1x} differences could be attributed

Table 4.4: Isotropic Magnetic Properties - Fe_4C_5@Au(111) Models

	Functional	Walker1	Walker2	Walker3	Walker4	Walker5	Walker6	Walker7	Walker8	Avg
J_{12}	PBE+U	20.8	16.7	17.3	11.7	13.3	20.1	15.1	16.6	16.5
J_{13}	PBE+U	26.2	17.4	24.3	29.1	31.1	33.1	43.9	39.6	30.6
J_{14}	PBE+U	20.2	26.4	28.7	27.7	25.3	29.9	33.1	17.8	26.1
J_1 [a]	PBE+U	22.4	20.2	23.4	22.8	23.3	27.7	30.7	23.8	24.3
J_2	PBE+U	0.2	-0.3	-0.5	0.3	0.7	1.1	1.2	0.7	0.4

All reported values are in cm^{-1}.
[a] J_{12}, J_{13} and J_{14} average value.

Table 4.5: Isotropic Magnetic Properties - Fe_4C_5@Au(111) Models

	Functional	Walker1	Walker2	Walker3	Walker4	Walker5	Walker6	Walker7	Walker8	Avg
J_{12}	PBE0	17.5	13.0	11.0	7.8	11.0	14.8	12.0	13.7	12.6
	PBE+U	21.5	17.8	16.7	11.6	14.0	19.5	15.8	17.0	16.7
J_{13}	PBE0	23.4	16.7	19.0	26.5	29.4	29.8	39.0	32.9	27.1
	PBE+U	27.9	21.0	25.1	31.6	34.2	35.2	46.8	38.3	32.5
J_{14}	PBE0	16.3	22.1	24.0	24.6	23.4	29.4	29.7	15.2	23.1
	PBE+U	20.9	25.1	30.2	29.6	27.6	35.0	33.7	17.7	27.5
J_1 [a]	PBE0	19.1	17.4	18.0	19.6	21.3	24.7	26.9	20.6	21.0
	PBE+U	23.4	21.3	24.0	24.3	24.0	29.9	32.1	24.4	25.4
J_2	PBE0	0.2	0.2	0.1	0.2	0.1	0.1	0.2	0.2	0.2
	PBE+U	0.0	-0.1	1.8	0.4	0.3	0.4	0.2	0.3	0.4

All reported values are in cm^{-1}.
[a] J_{12}, J_{13} and J_{14} average value.

Table 4.6: Anisotropic Magnetic Properties - Fe_4C_5@Au(111) Models

	Functional	Walker1	Walker2	Walker3	Walker4	Walker5	Walker6	Walker7	Walker8	Avg
D_1	PBE	1.555	-1.138	-1.058	-1.177	-1.106	-1.105	-1.107	-1.167	-0.789
E/D_1		0.23	0.12	0.08	0.26	0.09	0.23	0.18	0.18	0.17
D_2	PBE	0.651	0.557	0.573	0.614	0.480	0.508	0.529	0.610	0.565
E/D_2		0.13	0.16	0.13	0.13	0.15	0.16	0.13	0.15	0.14
D_3	PBE	-0.375	0.536	-0.407	-0.390	-0.447	-0.362	-0.434	-0.465	-0.293
E/D_3		0.21	0.25	0.20	0.18	0.30	0.14	0.20	0.26	0.22
D_4	PBE	0.461	0.488	0.515	0.591	0.634	0.410	-0.384	0.747	0.433
E/D_4		0.24	0.23	0.21	0.17	0.14	0.23	0.32	0.19	0.22
$D_{S=5}$	PBE	-0.390	-0.403	-0.583	-0.376	-0.378	-0.343	-0.343	-0.409	-0.403
$E/D_{S=5}$	PBE	0.12	0.02	0.19	0.05	0.04	0.07	0.15	0.08	0.09
ζ		18.6°	14.2°	36.7°	15.1°	14.7°	12.2°	13.9°	15.3°	17.6°

All reported D and E/D values are in cm^{-1}.

to the removal of any symmetry elements for the four iron ions upon grafting. The J_1 values are all larger than the bulk reference, as expected from the increase of the Fe_cOFe_p angles. It is interesting to note that the standard deviations for the two exchange coupling parameters are 3.0 cm^{-1} and 0.6 cm^{-1}, respectively. This means that the energy separation from the first excited state, $S = 4$, can range from 46 cm^{-1} to 70 cm^{-1}. The estimate for the Opt-Bulk model is significantly lower, 32 cm^{-1}, once more strongly supporting the not innocent role of the Au(111) surface. These results pose a question on the nature of the effects induced by the grafting process. In order to separately address steric effects and electronic contributions of the gold surface, the gold slab has been removed, computing the magnetic properties keeping the same molecular coordinates, Fe_4C_5@Au(111) model. In this case the Ac· group has been reintroduced at the S radical site, in order to avoid spurious spin contributions. Indeed, in the grafted scenario, at this site a strong Au-S bond is present. For a check on the reliability of the DFT+U correction for geometries different than the equilibrium one, the Js of the Fe_4C_5@Au(111) model have been also computed at the PBE0 level. Confirming the trend observed for the Bulk and Isolated models (see Table 4.1), the PBE0 values in Table 4.5 are systematically lower than the PBE+U ones. Otherwise, the two series of calculations over the eight walkers show the same type of fluctuations, validating the reliability of the PBE+U approach. The exchange interaction between iron ions is always antiferromagnetic and the ground state multiplicity is still $S = 5$. The comparison between J values in Tables 4.4 and 4.5 reveals that the explicit presence of the metallic substrate induces an homogeneously reduction of the J_1 values of about 1 cm^{-1}.

These data clearly show that structural rearrangements induced by the grafting process are mostly responsible for the evolution of the magnetic properties of Fe_4C_5 and the electronic effects induced by the presence of the metallic slab can be considered negligible.

Also the anisotropy parameters have been calculated for the Fe_4C_5@Au(111) system. Given the negligible effect of the Au(111) explicit presence, these parameters are expected to properly approximate the Fe_4C_5@Au(111) values. From the study of the anisotropic part of the spin Hamiltonian (reported in Table 4.6), a significant increase in the rhombicity of the single ion anisotropy tensor for the central iron ion is observed, with respect to the bulk calculated values. The local distortions of the octahedral environment around Fe_c are responsible for this behavior. Except for Walker1, the easy axis kind of anisotropy is retained. While no big differences with respect to the crystalline system are recorded for Fe_2 and Fe_4, the magnetic behavior

of Fe_3 is modified. The dpm ligands of Fe_3 are always found to lie above the C_5 aliphatic chain. This causes the change in sign of its axial anisotropy parameter in all cases, except for Walker2, leading to an easy-axis anisotropy, in contrast with the easy plane anisotropy observed for the Opt-Bulk model. To be stressed that in spite of all these not negligeble modifications, the orientation of the single ion tensors resemble the bulk one. The easy-axis of both the central iron and the peripheral ions are almost parallel to the irons plane normal, *e.g.* the mean inclination angle of the Fe_3 easy-axis with respect to the normal is $4.8° \pm 3.7°$. The global molecular anisotropy, evaluated for the $S = 5$ ground states in the GSH approximation, is an easy-axis anisotropy and, for all the adsorbed molecules except for Walker3, its value is diminished of about the 11%, with respect to the Bulk-Opt model. The easy-axis orientation, with respect to the irons' plane normal, is retained: the easy-axis direction deviates from the peripherals irons' plane normal of about 4°. Moreover, the easy-axis direction inclination (ζ) with respect to the surface normal, evaluated from the $\mathbf{D}_{S=5}$ tensor, well matches with the angle θ for all the Walkers, except for Walker3. For Walker1, Walker3 and Walker7 the increase of the rhombicity term with respect to the Opt-Bulk model is also observed. The significant increase in the rhombic anisotropy induced by the interaction with the surface well compares with experimental observation of an increased tunnelling relaxation efficiency. Indeed, the simulation of the hysteresis loops detected by XMCD experiments by Mannini *et al.*[113] requested an increases of the E/D ratio up to 0.1 as well as the inclusion of higher order terms in the spin Hamiltonian. It should however be considered that in that case the formation of a densely packed monolayer of grafted molecules could partially limit the interaction of the aliphatic chain with the surface, reducing the deformation of the magnetic core.

Conclusions

In this section a computational study of the Fe_4C_5 SMM adsorbed on Au(111) has been presented. The proposed new computational protocol revealed to be able to predict the evolution of both structural and magnetic properties going from the bulk to the adsorbed scenario. The importance of the AIMD approach to properly take into account the distribution of accessible configurations and to reveal, after annealing, the roughness of the PES has been highlighted. Selected geometrical parameter, crucial for the SMM magnetism, have been monitored both at finite and zero temperature and considerable modifications, with respect to the bulk reference values, have been observed. The relevant conclusion is that the retention of the S = 5 as ground state in the transition from bulk to @Au(111) is not due to the rigidity of the Fe_4 core

but on accidental balanced structural distortions of it. In particular the not innocent influence of the C_5 aliphatic carbon linker, on the final adsorbed geometry, have been discussed. The combination of AIMD sampling, annealing procedures, and magnetic properties calculations at the DFT level of theory allowed to shed light on the effects of structural rearrangements and of the surface coupling on grafted SMMs. A first attempt to get a quantitative estimation of the importance of electronic effects on the magnetic orbitals coming from metal density of states has been tackle with a DFT+U approach in its common phenomenological fashion. Although at this state the relaxation of screening effects inside the U parameters have been neglected an important information about sign and magnitude of this interaction over the isotropic exchange coupling constant has been obtained: the leading J_1 constant is marginally affected by this interaction, with respect to the weight of structural rearrangements, toward more ferromagnetic values.

4.2 Linking Group Effects

According to the main conclusion of the last section, the linking group used to graft the Fe_4 SMM to the Au(111) surface is expected to play a very important role and for this reason the analysis of the magnetism dependence on this degrees of freedom has been addressed. A series of three molecules, namely Fe_4C_X with X=2-4, has been studied by means of the tools proposed in the previous section. Around 4 ps of AIMD have been performed for the Fe_4C_{2-4}@Au(111) systems in order to relax their X-ray structures over the gold slab and let them be comparable with the Fe_4C_5@Au(111) structure (only walker1 will be discussed in this section). Following, a thermal annealing down to ~ 0 K in ~ 1 ps plus structure optimization has been done in order to produce sufficiently reliable Fe_4C_X@Au(111) structures. At this stage only the magnetism of the extrapolated geometries Fe_4C_X@Au(111) will be studied and a more detailed description of the electronic effects of metallic substrate is left to the next section. Accordingly with the previous section discussion, the C_X aliphatic chains of the Fe_4C_X@Au(111) structures, reported in fig. 4.7, remains parallel to the surface. For this reason small differences between C_{3-5} are indeed observed as the Fe_4 magnetic core lies all the same over the linking chain. A different scenario is observed for Fe_4C_2, whose linking chain is short enough not to directly interact with the external dpm ligands and remains directly under the Fe_4 core, imposing a more tilted configuration to the SMM.

For the reasons reported above the discussion of the Fe_4C_2 will be separated from the Fe_4C_{3-5} ones. Similar trends for isotropic exchange coupling constants have been computed within the Fe_4C_{3-5} systems. Indeed, the J_{13} interaction has been found to be the larger one and the less altered by the grafting process for the three considered structures. Interestingly, this is the interaction between the central iron and the iron approximately lying over the aliphatic chain. The other two constants show a more pronounced modulations toward smaller values passing from the C_5 to C_3, resulting in a slight reduction of the mean J_1 constant. J_2 is always observed very small and antiferromagnetic regardless system changes. Surprisingly, isotropic interactions inside Fe_4C_2 show a dramatic enhancement almost up to the double of the other element of the series. Similar features are reported for the anisotropic part of the spin hamiltonian. Indeed, while the Fe_4C_{3-5} possess similar properties, Fe_4C_2 shows dramatic changes in its single ion anisotropy properties. As discussed in the last section and further highlights in tab. 4.8, small modulations of the single ion anisotropy tensor lead to almost identical ground state $D_{S=5}$. Nevertheless, Fe_4C_2 single ion anisotropic tensors are so remarkably different from the expected values

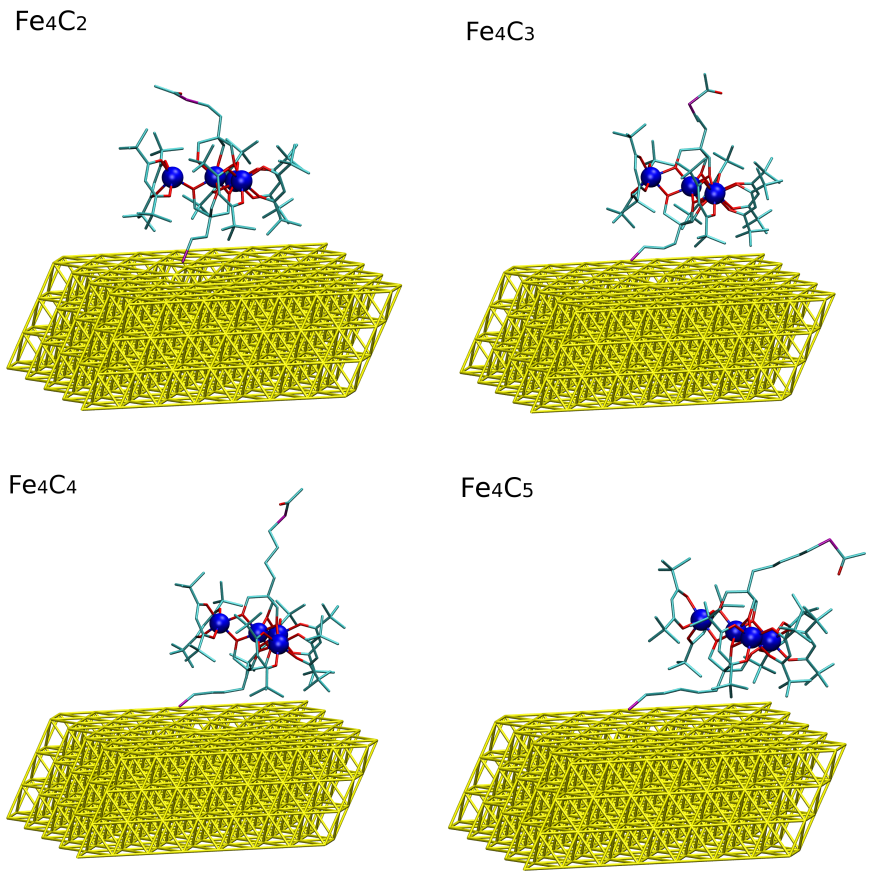

Figure 4.7: Fe_4C_{2-5}@Au(111) model structures. Hydrogen atoms are not displayed for sake of clarity.

that the projected $D_{S=5}$ change its sign, leading to an overall easy plane anisotropy. In tab. 4.8 there are also reported the molecular easy axis tilt angle θ with respect to the surface normal vector, which shows a mildly pronounced rising of the SMMs over the substrate passing from Fe_4C_5 to Fe_4C_2, in agreement with the qualitative analysis reported at the beginning of the section. The dramatic changes in the Fe_4C_2@Au(111) magnetic structure deserves a further comment. Due to the interaction between the sulfur and gold and the short linking chain, this SMM is strongly pulled toward the substrate with a consequent molecular stress induced by the steric repulsion between Au(111) slab and external dpm ligands. Due to this compression the $Fe_c\widehat{O}_uF_p$ angles

are larger spread and the final mean $Fe_c\widehat{O}F_p$ value reach 104.2°. However, as already pointed out in the previous section regarding the Fe_4C_5@Au(111) isotropic exchange coupling correlations with the aforementioned angle, this magneto structural correlation is no more strictly valid for highly distorted structures as those examined here and other parameters might be introduced in the analysis. For what concerns the extremely high easy plane anisotropy of the central iron ions it could be interpreted in terms of its trigonal compression. Indeed, the same molecular stress leading to the increase of the $Fe_c\widehat{O}F_p$ angles also increase this second structural parameter which is known to produce easy plane anisotropy in high spin d^5 transition metal ions.

Table 4.7: Crystal and adsorbed Fe_4C_X@Au(111) Isotropic Exchange Couplings.

	Fe_4C_2	Fe_4C_3	Fe_4C_4	Fe_4C_5
J_{12} (cm^{-1})	26.37	10.46	7.24	17.49
J_{13} (cm^{-1})	43.10	25.00	22.61	23.42
J_{14} (cm^{-1})	32.92	13.53	16.07	16.33
J_1 (cm^{-1})	34.13	16.33	15.31	19.08
J_2 (cm^{-1})	0.20	0.13	0.07	0.18

Conclusions

The main results of the last section have been confirmed here with the extension of the study to other three homologous SMMs, *i.e.* Fe_4C_{2-4}@Au(111) and a progression on structural and magnetic properties for the series has been demonstrated. The computed results hint the possibility to play with the linking group in order to control the SMM magnetic properties from a pure synthetic chemistry point of view in a bottom up approach, leading to the fundamentally important possibility to reach a dense-oriented packing of molecules on the substrate. Interestingly, in a covalent grafted scenario, a too short linking chain seems to induce a molecular stress, due to structural perturbations, enough to spoil the SMM easy axis magnetic properties. Once again, the importance of structural rearrangements coming together a deposition have been highlighted pointing out the necessity to carefully tailor the grafting chemical group in order to let the SMM to retain its bulk properties once adsorbed.

Table 4.8: Crystal and adsorbed Fe_4C_X@Au(111) Magnetic Anisotropies.

	Fe_4C_2	Fe_4C_3	Fe_4C_4	Fe_4C_5
D_1 (cm^{-1})	4.50	-1.118	-1.126	1.556
E/D_1	0.23	0.03	0.22	0.23
D_2 (cm^{-1})	0.331	0.518	0.739	0.651
E/D_2	0.30	0.15	0.13	0.13
D_3 (cm^{-1})	-0.363	0.418	-0.375	-0.375
E/D_3	0.27	0.32	0.19	0.21
D_4 (cm^{-1})	0.346	0.656	0.557	0.460
E/D_4	0.27	0.18	0.18	0.24
$D_{S=5}$ (cm^{-1})	0.697	-0.391	-0.380	-0.390
$E/D_{S=5}$	0.30	0.10	0.03	0.13
θ (°)	10.2	16.5	15.5	18.5

4.3 Self Assembling and Packing Effects

AIMD has been proved to be a valuable and very powerful tool to explore configurational landscape of complex system like adsorbed molecules with many degrees of freedom. However, the big computational cost does not make possible to access to large system and/or long time scales. Indeed, the application of AIMD has been possible only for a single adsorbed molecule and for a few ps of acquisition time. Although many important effects have been proved to be captured with this approach, the study of different and at the same time important effects requires an extension of the system size and the simulation time. For instance, the possibility to include the description of multi SMM collective dynamics can give access to fundamental information about the self-assembling process. Clearly, the possibility to do that would necessarily require the lowering of the level of theory and the introduction of a partial amount of parametrization into the atomic forces definition. Among the many possible schemes, the complete parametrization of the electronic structure through an analytical force field has been chosen. Although it may resemble a drastic solution, it is the only one that makes possible to access time scales as long as ns and for system containing a number of atoms as large as thousands.

Force Field Description and Validation

In order to produce an *ad hoc* force field for the Fe_4Ph@SMM system the most natural choice is to assemble it from existing exportable force fields. The classic hamiltonian of the hybrid system SMM@Au(111) is considered as the sum of three main parts, addressed separately for purpose of discussion, *i.e.* $H = H_{mol} + H_{slab} + H_{mol-slab}$. The H_{mol} describes the interactions occurring inside the Fe_4Ph SMM. The most widely used FF form for the description of molecular systems is in terms of internal degrees of freedom *i.e.* stretching, bonding, torsion, wagging and pairwise potentials describing vdW and electrostatic forces. For what concerns organic compounds, there exist many different robust and exportable parametrization for these interactions and among them the general amber force field (GAFF) has been used to describe the ligand parts of the SMM[131]. Major efforts have been devoted to the parametrization of the interaction involving metal centers. Indeed, due to the complex three dimensional nature of the coordinative bonds and their not transferability properties, a general and readily usable parametrization of these interaction does not exist. In this work the metal-ligands interaction has been described by means of a GAFF-like form of the potential whose parametrization has been done following the scheme proposed by

Seminario[132]. This very simple recipe makes possible an automated parametrization on the basis of a DFT description of the Fe_4Ph hessian through the interface between the software Hess2FF and the software Gaussian[133, 134]. Clearly this was not the only possible solution and many other more refined computational set up are available to solve this task. Following the discussion of Hu *et al.*[135], a DFT B3LYP optimization followed by an analytical hessian calculation has been done to evaluate stretching, bending and torsion involving the iron ions. vdW interactions have been chosen accordingly with the GAFF recipe as described by 6-12 Lennard Johns potential forms, whose parameters have been selected from literature. The fully bonded FF obtained has been tested over its ability to reproduce the structure and stability of both isolated and crystalline Fe_4Me SMM. This specific Fe_4 family member has been chosen as it is the only one that crystallizes with one independent molecule inside its primitive cell.

Table 4.9: Experimental values compared to the computed DFT and FF ones for the Isolated Fe_4Me

	Fe_c-O-Fe_p (°)	Fe_c-Fe_p (Å)	Fe_p-Fe_p (Å)
FF	103.2	3.05	5.28
DFT	102.4	3.11	5.39
Exp.	102.9	3.09	5.35

Table 4.9 shows the structural results for the isolated Fe_4Me SMM at different level of theory. The agreement between the FF and experimental structural values is remarkable and well within the DFT-exp error. The choice of testing the FF on the periodic cell has been done to check the FF reliability to reproduce the SMM-SMM interactions which are of capital importance in driving the self-assembling process. In table 4.10 are reported cell and geometrical parameters computed at the FF level for the Fe_4Me crystal. The very nice agreement with the experimental findings is evident. Moreover, an MD study, within the NPT ensemble, of the crystal has been performed in order to demonstrate the stability of the crystal structure at finite temperature and pressure. Indeed, an error of about the 3% has been introduced with respect to static calculations. Nevertheless, this difference is consistent with the thermal expansion of the lattice at finite temperature. These structural and dynamical tests point out the high quality of the produced FF. A more detailed description of these and other tests is reported in the master thesis of Fernandez Garcia together with the complete list of the new FF parameters[136].

For what concerns the H_{slab} hamiltonian the 6-12 Lennard Jones description of the

Table 4.10: Calculated and experimental Fe_4Me cell parameters and RMSD with respect to exp. geometry.

	Cell Opt.	NPT	Exp
a (Å)	16.554	17.165	16.189
b (Å)	16.554	17.275	16.189
c (Å)	56.707	57.111	56.712
$\alpha(^\circ)$	89.99	89.99	90
$\beta(^\circ)$	90.01	90.05	90
$\gamma(^\circ)$	119.99	119.96	120
RMSD (Å)	0.4052	0.4636	
RMSD without H (Å)	0.3370	0.3805	

Au-Au interaction has been chosen[137]. This choice is particularly appealing as it makes possible to combine the Au-Au interaction parameters with those of the GAFF in order to readily obtain the $H_{mol-slab}$ hamiltonian[138]. However, this scheme must be carefully tested and the adsorption energy of a single phenyl ring on Au(111) (E(Ph-Au(111)) has been chosen as our master benchmark, since lot of computational and experimental data are available in literature. Moreover, even because the Ph-Au(111) interaction is supposed to be pretty important in the Fe_4Ph adsorption process. When such kind of interactions are present, the choice of the dispersion forces corrections to DFT becomes extremely important. At this regard we calculated the E(Ph-Au(111) both with D3 and rVV10 schemes (see table 4.11).

Table 4.11: E(Ph-Au(111)) benchmark with both FF and DFT schemes.

	TPSS+D3	TPSS+rVV10	GAFF	DFT[a]	Exp[b]
ΔE_{ads} Kcal/mol	-30.53	-21.26	-27.30	-16.83	-17.06

[a] Computational value obtained with PBE+vdW^{Surf} from [139];
[b] Experimental values taken from [140].

Both TPSS+D3 and GAFF overestimate E(Ph-Au(111)). Although recently the highly accurate PBE+vdW^{Surf} functional has been developed, here the TPSS+rVV10 functional, available in the CP2K software, has been used as reference for a new FF parametrization of the atomic kinds involved in the Ph@Au(111) interaction. This choice relies in the perspective to use an homogeneous DFT-FF protocol in order to reduce source of discrepancies in the results coming from different levels of theory. Aromatic carbon and hydrogen atomic kinds (C_α and H_α) are the only ones, of those involved in the Fe_4Ph@Au(111) interaction, that are expected to be those that weight

more in the final results, indeed Fe_4Ph is only physisorbed on Au(111) and its Ph ring is the part which interacts more strongly with the substrate. Accordingly, only the parametrization of aromatic carbon and hydrogen atomic kinds is expected to be important for in the final results. The energy profile of the phenyl ring, lying flat with respect to the Au(111) surface, has been calculated at various distances from the metal slab. A first attempts to fit this energy profile with a Lennard-Jones potential has been done but with unsatisfactory results. Accordingly to other parametrization tests reported in literature, the Lennard-Jones potential form is ineffective to capture surface-adsorbate interactions and more degrees of freedom in the potential function are needed. A Morse kind of potential has then be used to complete this task.

$$E_{ij} = D[e^{-2(r-r_0)} - 2e^{-(r-r_0)}] \tag{4.1}$$

The use of three parameters inside the definition of the interaction potential makes possible to fit with excellent accuracy all the points of the DFT calculated energy profile and it has been used throughout all the next calculations. The fitted parameters are reported in table 4.12.

Table 4.12: Morse Potential Fitted Parameters.

	D (kcal/mol)	α Å^{-1}	r_0 (Å)
E(C_α-Au)	0.42717	1.2460	3.5554
E(H_α-Au)	0.14130	1.1105	3.3359

Isolated SMM@Au(111)

The FF just described has been used to perform MD runs of a single Fe_4Ph@Au(111). The study of this system has a twofold importance: it is the fundamental final test for the FF proposed and it is also useful to check the stability of the fully ab initio results obtained for Fe_4C_5@Au(111) and Fe_3CrC_5@Au(111) over a longer time scale. The Fe_4Ph@Au(111) DFT optimized structure proposed by Ninova *et al.* has been used as starting point for the MD. A simulation of 20 ns at 300 K shows diffusion of the SMM molecule on the surface.

Fig. 4.8 reports the distribution of the single and mean γ-pitch values and the single and mean $Fe_c\widehat{O}Fe_p$ values. Differently from the AIMD Fe_4C_5@Au(111) corresponding values, the single distribution are much more similar among them and readily resemble their mean distribution. Although these results point to an high stiffness of Fe_4Ph during molecular motion, it should be stress that it might be due to the bonded

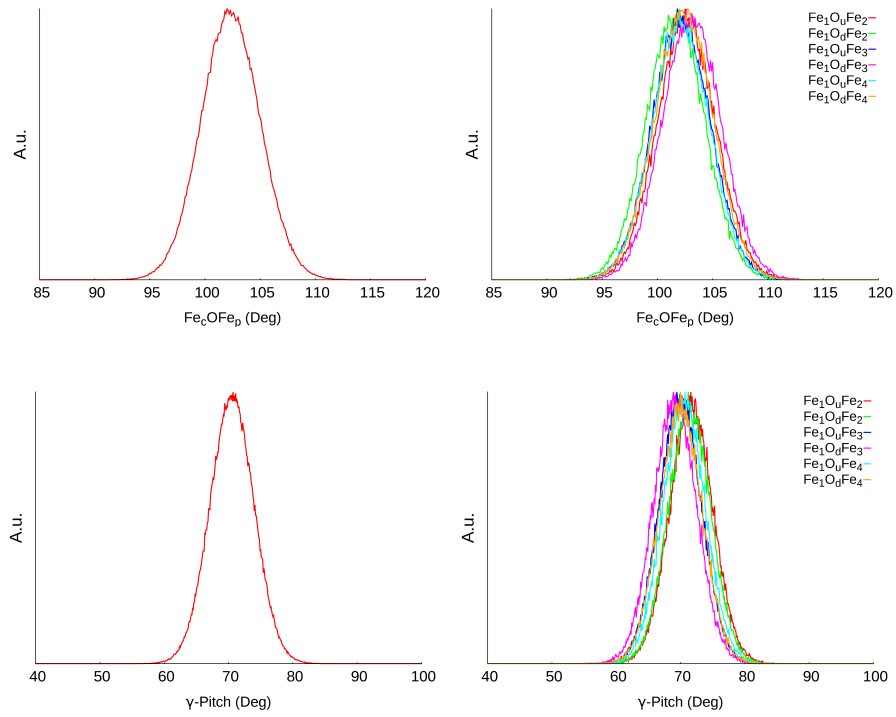

Figure 4.8: (a): Molecular average $Fe\widehat{O}Fe$ angle's normalized distribution. (b): Single FeOFe angle's normalized distributions. (c): Molecular average γ-pitch angle's normalized distribution. (d): Single γ-pitch angle's normalized distributions.

form of the FF used. Indeed, as the equilibrium geometry is the only one used for the FF parameters fit and because of the harmonic form of the potential, big reorganization of the SMM structure are impossible to be observed in this framework. The MD simulation has been followed by a thermal annealing down to 200 K in turns followed by a thermal annealing at the DFT level down to 0 K in 0.1 ps. A final geometry optimization at the DFT level reveals a final structure different from the starting one (see fig. 4.10). The main difference between the two lies in the phenyl ring in direct contact with the substrate whose bending angle with the molecular pseudo symmetry axis is reduce of 12.3°. Although this is not a dramatic distortion, it is important to underline that it modifies the position of the whole molecule over the surface, with consequences for the SMM easy axis orientation. For instance, the presence of the phenyl ring as physisorbing linking unit makes the easy axis direction of the Fe_4Ph

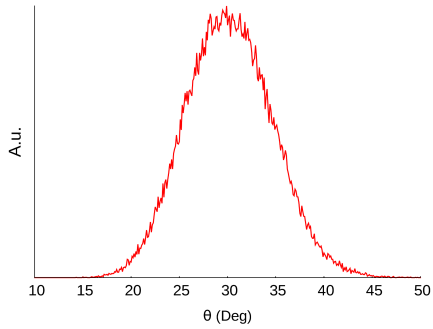

Figure 4.9: Distribution of the iron ions plane normal vector inclination with respect to the surface normal vector.

SMM inclined of about 30° with respect to the surface normal vector as showed by fig. 4.9, differing less than 5° with respect the starting geometry. This value should be also compared to the $\sim 15°$ observed for the Fe_4C_5@Au(111), demonstrating again the importance of the surface linking group. In table 4.13 there are reported the ad-

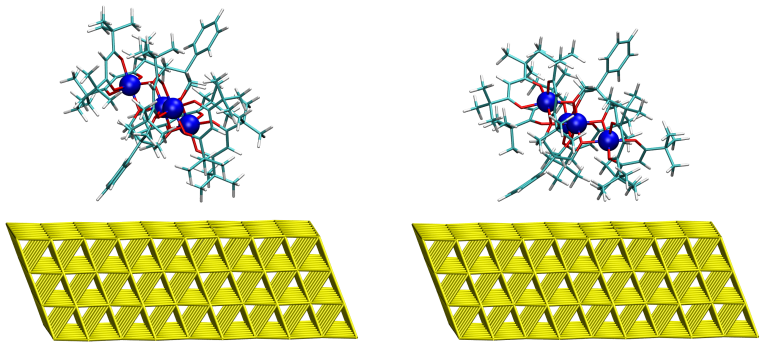

Figure 4.10: On the left the Fe_4Ph@Au(111) starting configuration used for the MD simulation (GeoUp). On the right one snapshot extracted from the trajectory after the FF based MD + DFT thermalization (GeoDown).

sorption energies of both the starting and final Fe_4Ph@Au(111) geometries and their energy difference ($\Delta E_{up-down}$). The good agreement between FF and DFT energetics validates even further the new proposed FF and they both predict the down structure as the more stable. For comparison, a FF without the adjusted phenyl-Au(111) interaction would has predicted a value of $\Delta E_{up-down} = 49.11$ kcal/mol in net dis-

Table 4.13: Structural values for the Isolated Fe_4Me

	ΔE_{ads}^{up} (kcal/mol)	ΔE_{ads}^{down} (kcal/mol)	$\Delta E_{up-down}$ (kcal/mol)
FF	-46.2	-83.4	-17.0
DFT	-53.1	-92.3	-12.1

agreement with the more efficient DFT scheme, demonstrating the importance of the new parametrization proposed. In order to study in more detail the time evolution of the SMM structure during the MD simulation, the probability density plot of oxygen and iron ions has been computed and reported in fig. 4.11together with the SMM mean structure. These data have been calculated along the whole 20 ns trajectory after the elimination of the external degrees of freedom. Accordingly with the discussion about the MD mean values distributions, the magnetic core ions experience small displacements with an almost spherical distribution. For comparison, the thermal annealed final structure, whose energetics has just been discussed, is slightly different from the mean one but still inside the probability density plot.

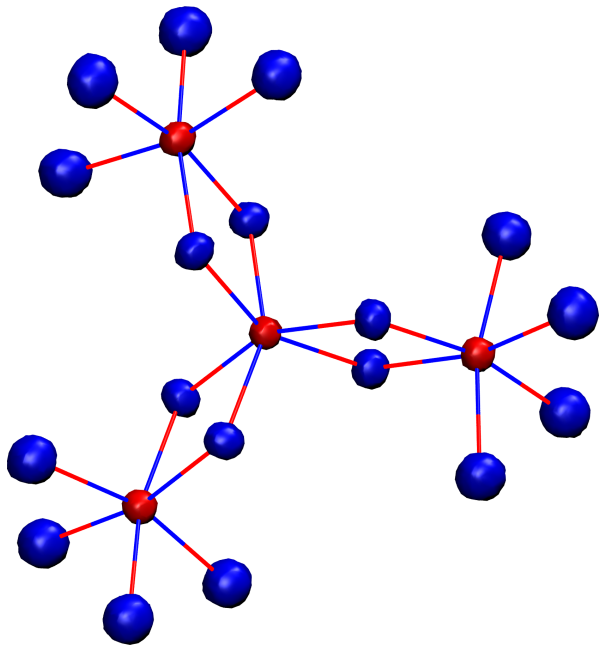

Figure 4.11: Mean Fe_4Ph core structure and its space probability distribution. Blue volumes correspond to the oxygen space probability and the red volumes correspond to iron ions space probability.

It must be noted that the DFT refinement of the structures produced by the FF based MD simulation is a mandatory steps in order to access the SMM magnetism. Indeed, while the FF is believed accurate enough to described qualitatively the dynamics of the adsorbed molecules and its interaction with the substrate, does not account for an accurate description of the internal degrees of freedom involving the metallic ions. This is mostly due to the already discussed dramatic dependency of magnetic properties over these structural parameters which impose the need to address them more carefully. The magnetism of the X-ray, Opt-Isol and final adsorbed structures, reported in table 4.14 and 4.15, has been evaluated for the extrapolated geometries with the usual PBE0 and PBE approach. The comparison between Opt-Isol and X-ray models reveal the already observed partial spoils of the structure quality with the consequent lowering of magnetic properties accuracy. Regarding the mean J_1 constant, its value increases from 11.19 cm^{-1} to 16.05 cm^{-1} once Fe_4Ph is adsorbed on gold. Although the same trend was observed for the Fe_4C_X series, in this case the entity of the variation is less dramatic, confirming the higher rigidity of the Fe_4Ph core observed also during the MD run. The same observations also apply to the anisotropic part of the spin hamiltonian whose projection on the ground S=5 state in increased of 0.007 cm^{-1} in absolute value. However, the $E_{S=5}/D_{S=5}$ ration increases of one order of magnitude accordingly with the loss of symmetry after the deposition.

Table 4.14: Crystal and adsorbed Fe_4Ph Isotropic Exchange Couplings.

	X-ray	Opt-Isol	Fe_4Ph@Au(111)	Exp Bulk
J_{12} (cm^{-1})	13.30	13.48	9.37	–
J_{13} (cm^{-1})	13.00	16.90	20.66	–
J_{14} (cm^{-1})	13.10	3.18	18.13	–
J_1 (cm^{-1})	13.10	11.19	16.05	16.37
J_2 (cm^{-1})	0.24	0.14	0.19	0.29

Table 4.15: Crystal and adsorbed Fe_4Ph Magnetic Anisotropies.

	X-ray	Opt-Isol	Fe_4Ph@Au(111)	Exp Bulk
D_1 (cm^{-1})	-1.100	-1.027	-1.144	–
E/D_1	0.06	0.12	0.25	–
D_2 (cm^{-1})	0.728	0.716	0.485	0.710
E/D_2	0.16	0.17	0.19	0.108
D_3 (cm^{-1})	0.618	0.527	0.491	0.602
E/D_3	0.23	0.28	0.25	0.168
D_4 (cm^{-1})	0.641	0.543	0.675	0.602
E/D_4	0.22	0.25	0.18	0.168
$D_{S=5}$ (cm^{-1})	-0.456	-0.388	-0.395	-0.421
$E/D_{S=5}$	0.00	0.06	0.18	0.023

Self Assembled Monolayer of SMM@Au(111)

On the basis of results obtained for the isolated SMM@Au(111) it is now possible to proceed to the study of molecule-molecule interaction on the surface. For this purpose an half coverage monolayer of 36 Fe_4Ph has been assembled as shown in fig. 4.12. A rearrangement of the SMMs distribution to form clusters of molecules is observed already at the beginning of the simulation run. Panel b) of fig. 4.12 reports the half monolayer structure at the end of the MD simulation after 10 ns. Although the presence of border effects on the clusters, due to the lacking of SMMs that prevent the formation of a fully periodic phase, the formed island of SMMs clearly show a regular pattern (see for instance the white hexagonal marked group in panel b) of fig. 4.12). Interestingly, exotic orientations of Fe_4Ph have also been observed. For instance a quasi isolated molecules lying with it pseudo symmetry axis parallel to the surface has been identified (see the red mark in panel b) of fig. 4.12). This structure, called Fe_4Ph_{side}@Au(111) from now on, has also been optimized alone over a slab of Au(111) (see fig. 4.13). Notably, this configuration had not been observed in the single SMM MD simulation and became accessible only with the presence of SMM-SMM interactions. It must be pointed out that the choice of the starting disposition of the SMM molecules on the Au(111) slab is in principle a big issue as it might biases the subsequent results. However, in this case, the high tendency of the SMM to create a regular two dimensional structure different from the starting one and the excellent agreement with experimental findings (*vide infra*), suggests the overcoming of this MD pathological issue. Nevertheless, a refinement of the MD results on the basis of more sophisticated methodology, *e.g.* metadynamics and replica exchange methods, to extend the exploration of the configurational phase space of this SMM@Au(111) might be an interesting evolution of this study.

The regular structures observed in the half monolayer simulation and their high stability suggest the possibility the SMMs can form a two dimensional crystal of packed SMMs. A simulation cell comprehending 72 SMMs on Au(111) slab has been prepared (see panel a) of fig. 4.15) and simulated following the same procedure used for the single adsorbed molecule: an MD run of 10 ns at 300 K has been produced and followed by a thermal annealing down to 200 K. Clearly in order to proceed to the DFT refinement of the periodic 2D structure is first necessary to reduce the system size down to a cell of less then a thousand of atoms. Thanks to the periodic properties of the self assembled monolayer it has been possible to shape an hexagonal unit periodic cell containing one SMM. This structure has been then cooled down to $\sim$0 K and optimized at the DFT level (Fe_4Ph_{2D}@Au(111) model from now on). The

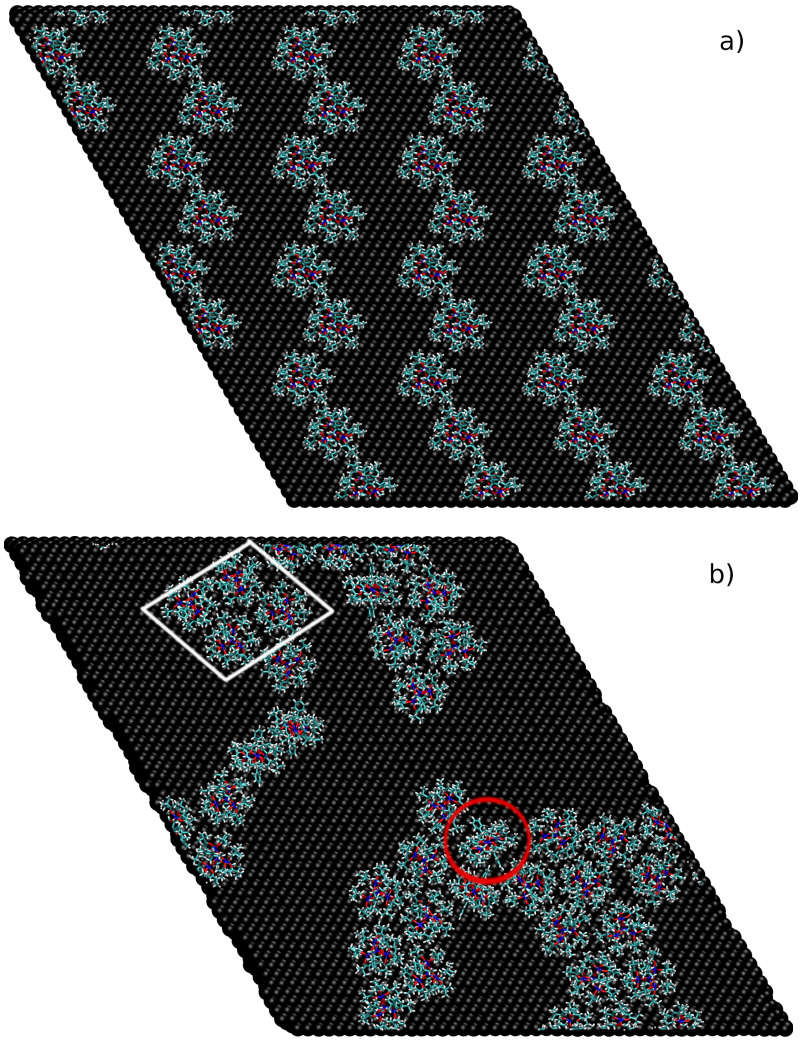

Figure 4.12: Panel a): Starting distribution of the half monolayer of Fe_4Ph molecules on Au(111). Panel b): Final distribution of the half monolayer of Fe_4Ph molecules on Au(111). The Au(111) color has been switched to black in order to enhance the contrast of the molecules.

mean probability distribution P(r) to find two Fe_4Ph at distance r, reported in panel a) of fig. 4.14, shows a regular pattern of picks corresponding to the crystallographic positions of a 2D hexagonal Bravais lattice. Notably, P(r) almost reach 0 between the picks pointing out the lacking of diffusion inside the crystal. The residual diffusion is

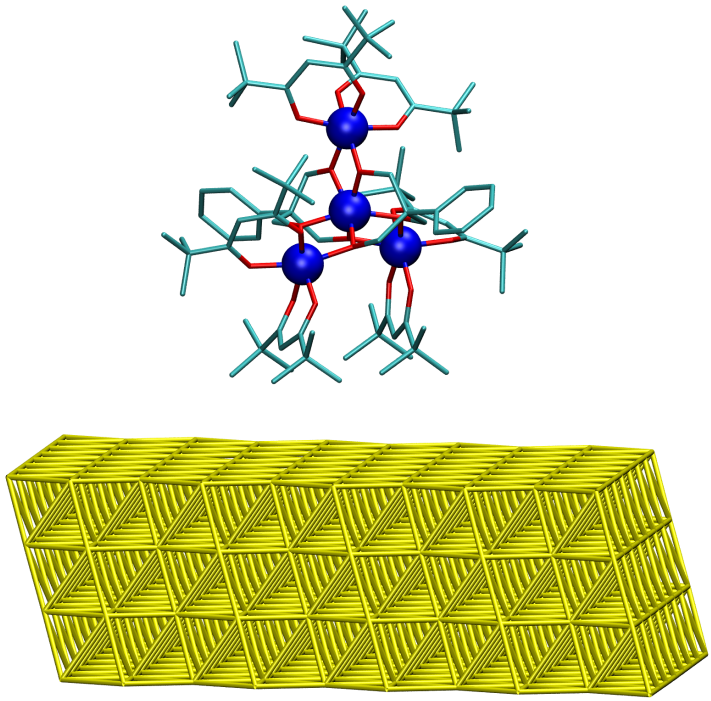

Figure 4.13: Fe_4Ph_{side}@Au(111) optimized structure.

probably due to the holes in the surface coverage. Accordingly, a qualitative analysis of the overall SMMs distribution at the end of the MD simulation shows that although the majority of the molecules remains in a sufficiently well defined two dimensional crystal scenario (see for instance the white marked group in panel b) of fig. 4.15), the observation of other structures as Fe_4Ph_{side}@Au(111) (see the red mark in panel b) of fig. 4.12) is still possible. This is further highlighted by the distribution of the SMMs easy axis inclination with respect to the surface normal reported in panel b) of fig. 4.14. The red line reports distribution of the molecular easy axis inclination angle and clearly shows the presence of at least three molecular orientations. The first one, centered at $\sim 30°$ corresponds about to the same structure observed in the single molecule scenario. A second pick, less intense, corresponds to a more tilted kind of molecule probably due to transient configurations explored by molecules on the border of the more bulky phase and finally the small pick at 90° points out the

presence of the Fe_4Ph_{side}@Au(111) structure. The very small distributions above $\sim 150°$ corresponds to the same structures with $\sim 30°$ due to the 90° periodicity of the property under study. Notably, if the mean value of the tilting angle is taken before the distribution is evaluated, *i.e.* the distribution shows the entire cell mean value, the second pick is averages out (green line in panel b) of fig. 4.14). The difference between the two distribution reflect the potential difference between a local (red distribution) and massive (green distribution) probe of this property.

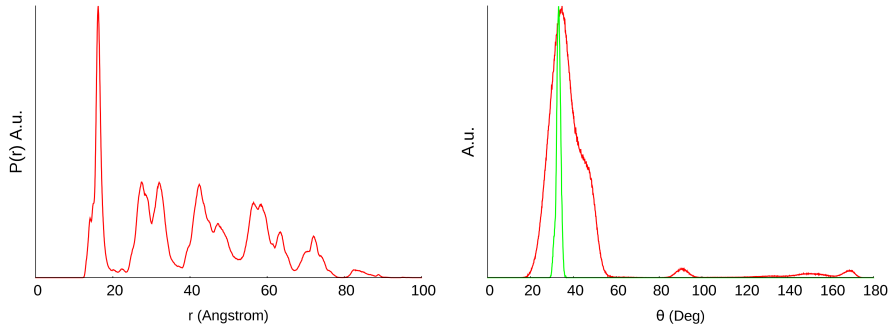

Figure 4.14: (a): Probability distribution of funding two SMMs at distance r. (b): Probability distribution of the cell mean easy axis inclination in reported in green and the mean probability distribution of the molecular easy axis inclination in reported in red.

Isotropic exchange coupling constants and anisotropy tensors for the Fe_4Ph_{2D}@Au(111) and Fe_4Ph_{side}@Au(111) structures have been calculated with the PBE0 and PBE approach and reported in tab. 4.16 and 4.17, together with the previous results for Fe_4Ph@Au(111). The isotropic exchange coupling constant increase passing from the Fe_4@Au(111) models to those coming from the self assembled monolayer. Notably, Fe_4Ph_{side}@Au(111) and Fe_4Ph_{2D}@Au(111) show the same increase of the mean J_1 constant. The same apply also to the anisotropies which show a small increase in their absolute value.

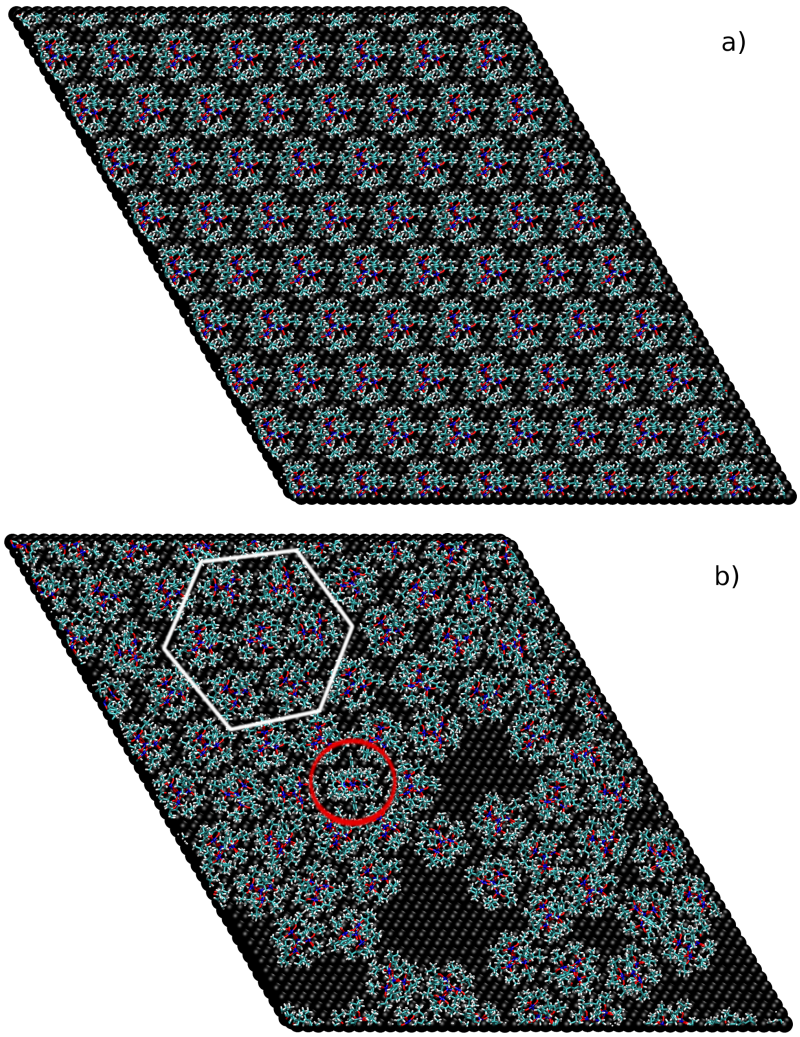

Figure 4.15: Panel a): Starting distribution of the full monolayer of Fe_4Ph molecules on Au(111). Panel b): Final distribution of the full monolayer of Fe_4Ph molecules on Au(111). The Au(111) color has been switched to black in order to enhance the contrast of the molecules.

Table 4.16: Full Monolayer Fe_4Ph Isotropic Exchange Couplings.

	Fe_4Ph@Au(111)	Fe_4Ph_{side}@Au(111)	Fe_4Ph_{2D}@Au(111)
J_{12} (cm^{-1})	9.37	22.57	21.04
J_{13} (cm^{-1})	20.66	18.26	23.91
J_{14} (cm^{-1})	18.13	23.87	19.13
J_1 (cm^{-1})	16.05	21.57	21.36
J_2 (cm^{-1})	0.19	0.03	0.25

Table 4.17: Full Monolayer Fe_4Ph Magnetic Anisotropies.

	Fe_4Ph@Au(111)	Fe_4Ph_{side}@Au(111)	Fe_4Ph_{2D}@Au(111)
D_1 (cm^{-1})	-1.144	-1.146	1.315
E/D_1	0.25	0.18	0.28
D_2 (cm^{-1})	0.485	0.568	0.403
E/D_2	0.19	0.21	0.28
D_3 (cm^{-1})	0.491	0.508	0.615
E/D_3	0.25	0.22	0.17
D_4 (cm^{-1})	0.675	0.633	0.712
E/D_4	0.18	0.19	0.17
$D_{S=5}$ (cm^{-1})	-0.395	-0.417	-0.418
$E/D_{S=5}$	0.18	0.07	0.14

Conclusions

The FF based MD simulation of a single Fe_4Ph@Au(111) confirms the main outcomes about the AIMD study of the similar Fe_4C_5@Au(111), where the influence of the linking group that makes the SMM bound to the substrate has been revealed. The proposed FF set up has been demonstrated a reliable and powerful tool and has been used to simulate the self-assembled monolayer at two different coverage: half and full monolayer. The study of the self-assembled monolayer points out the importance of inter molecular interactions in the modulation of SMM magnetic properties and, as also observed for SMM-substrate interactions, the isotropic exchange couplings are the most affected parameters of the spin hamiltonian while the axial anisotropic ground state parameters $D_{S=5}$ are modulated to a lesser extent by structural reorganization. Interestingly, inter molecular interactions lead to the observation of several structures, not explored by the MD simulation of the single Fe_4Ph@Au(111), which differ mainly for the orientation of the SMM easy axis. However, although the most probable structure is associated to a periodic 2D crystal, where the orientation of the single units resemble the orientation of the isolated one, the need to engineer SMM structures in order to lead to a specific and regular self assembled monolayer became evident. This need becomes especially relevant as the lacking of a surface covalent grafting is suggested to be at the origin of a reduction of the 2D crystallinity, due to the stabilization of SMM configurations with an unwanted easy axis parallel to the surface.

4.4 Surface Grafting Screening Effects

Density Functional Theory (DFT), in its LDA or GGA flavor, is the commonly used method for calculations of electronic and magnetic properties of transition metal ion clusters. For both isotropic exchange coupling constants and density of states prediction this tool is known to give poor results.[141, 142] For what concerns isotropic exchange coupling constants, the overestimation of the magnetic orbitals delocalization, due to spurious self-energy interactions, results in an overestimation of the antiferromagnetic interaction between unpaired spins, while the lacking of non-local interactions inside the exchange-correlation potential exclude the renormalization of molecular MOs while approaching metallic substrates, thus providing unreliable DOSs and related magnetism. This last point becomes especially important in the context that is going to be discussed in this section, as the effects of electronic interaction between localized d-like SMM states and itinerant s-like Au(111) states will be addressed. An interesting way through these technical problem is provided by the hubbard correction[126] and in the last section a first attempt to the determination of the importance of electronic effects coming from the substrates surface states has been done in this framework. However, this correction scheme has been implemented in its native phenomenological approach with parameters prepared *ad hoc* to reproduce the bulk magnetic scenario. In order to overcome this theoretical limitation, in this section the DFT+U procedure will be considered in its linear response framework[143]. The possibility to calculate the Hubbard correction within DFT theory, enables us to define it for different chemical environments without the necessity to modulate it on the basis of experimental data, which are not always available. However, most importantly, it must be stress out that this practical advantage of the DFT+U_{LR} is not the only appealing property of this computational scheme and its validity on the scenario of molecular magnets deposited above metallic substrates is grounded on strong theoretical considerations. Lets start noting that the DFT+U_{LR} approach already introduce into the theory a key element for the description of bulk SMMs. Indeed, as pointed out by Pemmaraju *et al.*[144] the hubbard correction could be interpreted as self interaction correction acting on a subset of localized MOs and, in fact, it has been already showed that accurate exchange coupling constant could be extracted from such an approach once the hubbard correction is applied over both transition metals and those ions responsible for super exchange interactions[145]. The account of the weak hybridization between itinerant and localized electrons is one of the most investigated problems in the realm of computational chemistry as the flaws in its description make the assessment of all the properties related to the adsorbed

system quasi particle spectra unreliable. The source of errors in the description of this property arises from the lacking of proper non-local interactions inside the Kohn-Sham potential which in turn exclude the formation of the correct band gap due to the absence of the discontinuity of the total energy with respect to the system occupation numbers. As nicely discussed by Himmetoglu *et al.*[146], the introduction of the DFT+U_{LR} correction would dress the system exactly with these lacking features. A formal connection with higher level of theory as G_0W_0, already known to give reliable states renormalization for physisorbed molecules, has also been provided [147]. It is also interesting to note that a strategy formally equivalent to the DFT+U_{LR} approach in the context of surface induced band gap renormalization has been exploited by Sau *et al.* and Souza *et al.*[148, 149], with the only difference that they had applied the correction to the HOMO and LUMO orbitals instead to the magnetic ones. Clearly this two framework would coincide when magnetic orbitals lies near the Fermi level. Moreover, as this correction is applied only to the localized d-like states of the transition metals of the SMM, the GGA part of the functional is still taking care of the description of delocalized states of the metal, which are known to be sufficiently well described by GGA functional.

According to the discussion above, linear response calculated Hubbard correction is the perfect candidate to represent the extension of the state of art computational treatment for this system, as it is able to take into accounts the aforementioned properties, which are all at the same time needed to correctly reproduce SMM electronic features once deposited on a metallic substrate. Although these such intriguing features sound very appealing, DFT+U_{LR} has been applied only a few times[150] to systems similar to the one discussed here and this work represent the first attempt to use it for the determination of surface induced polarization effects on molecular magnetism.

The computational strategy follows the same outline of the last sections. Magnetic and electronic characterization have been produced for both the gas-phase optimized structures (Opt-Isol Models), the adsorbed SMM relaxed structures (SMM@Au(111)) and finally for the extrapolated models (SMM@Au(111)), where the last one is obtained from the SMM@Au(111) model just removing the Au(111) slab without changing the SMM structure (see Methods section for more details). The comparison between these three models makes possible to capture from a microscopic point of view the weight of structural and electronic modifications upon SMM magnetism induced by the adsorption process.

The relaxed structure of Fe_4C_5@Au(111), obtained through AIMD and thermal an-

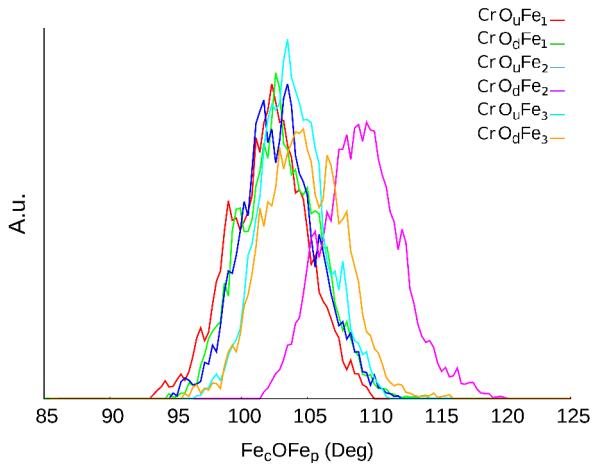

Figure 4.16: CrOFe angle's normalized distributions.

nealing calculations, have been reported and discussed in the last section and here its analysis will be restrained to the Walker1 geometry. In order to study the dependence of helical pitch magnetism on the nature of its magnetic ions, an AIMD calculation has been performed on Fe_3CrC_5@Au(111) (see Methods for details) showing that its time evolution is similar to the one already observed for Fe_4C_5@Au(111). As already discussed elsewhere (see section 2.4) for the Fe_4C_5 system, it exists a correlation between the angle Fe_cOFe_p and the isotropic exchange coupling parameter which couple the two iron ions. Although the same correlation has never been highlighted for the CrOFe moiety, its validity could be extend to the system under study. The thermal fluctuations of the CrOFe angles has been reported in Fig. 4.16 for the adsorbed system. Comparing the Opt-Isol model's CrOFe angle average value (101.0°) with the mean distributions reported in Fig. 4.16 is possible to observe that the interaction of Fe_3CrC_5 with Au(111) distorts the SMM's structure producing an overall increase of these parameters value. The violet curves in Fig. 4.16 shows that the $CrOFe_2$ angle is the most affected by the grafting process and it is due to the interaction of Fe_2 with the C_5 aliphatic chain that bind the SMM to the substrate. These finding are in perfect agreement with what already reported for Fe_4C_5@Au(111). The two SMMs share about the same relaxed geometry and the structural effect on magnetism due to the substrate could be readily compared.

The Hubbard on-site coefficients have been therefore evaluated for all transition metal ions and ligands oxygen ions separately for all models in order to include screening

effects due to surrounding environment changes. As the calculation of the hubbard correction for every different atomic kind requires two self consistent field energy calculations each, only two oxygen kinds have been used: oxygen atoms belonging to the tripod ligands (O_p) and oxygen atoms belonging to the dpm external ligands (O_e). The calculation of the hubbard correction for these two kinds has been done for only two representative atoms bonded to Fe_3. The results are reported on Table 4.18. The U values for the Opt-Isol model transition metals are in remarkable agreement with those phenomenologically introduced in section 4.1. While the effect of pure geometric distortions on transition metals U values is negligible for Fe_4C_5@Au(111), the on-site U correction for Fe_3CrC_5@Au(111) increases of about 0.5 eV. Interestingly, the sole effect of the surface is able to increment the U value for the central ion in Fe_4C_5@Au(111) of about 0.8 eV. An increase on the Cr ions of about 0.3 eV upon inclusion of the gold slab is also observed. The effect of structural and electronic perturbations on the chromium ion U value is additive and it results in a total increase of 0.8 eV passing from the Opt-Isol to Fe_3CrC_5@Au(111) model. This effect worth a further comment. As briefly discussed in the introduction of this section, the hubbard correction is deeply connected with the opening of the molecular band gap due to the restoration of the discontinuity in the Kohn-Sham energy profile. Moreover, as the hubbard correction has been calculated for every different scenario it is also able, at least to some extent, to take into account the screening effect due to the metallic surface. The variation of the hubbard correction upon inclusion of the gold slab is a clear manifestation of this effect, which is believed to be of fundamental importance in order to retain the calculated results reliable. The on-site Hubbard correction values of oxygen ions remain about the same for all the models considered. Although only two oxygen atoms have been monitored, the selected ones are those most influenced by structural rearrangements, pointing out the robustness of the hubbard correction for oxygen atomic kinds. However, differences of about 1 eV between the U correction associated to the dpm oxygen ions for Fe_4C_5 and Fe_3CrC_5 have been noted. Besides the differences already discussed, the magnitude of the U corrections calculated for transition metals have been found similar to the phenomenologically fitted values used in the last section. The same is not true for the corrections on oxygen ions. Indeed, the linear response calculation provides values more than 100% higher. This discrepancy mainly arises from the different chosen MOs sub set where the hubbard correction is applied. In the last section the hubbard parameters where fitted and used over the projection of MOs over a set of Löwdin orthonormalized metal d states while in this context the correction is applied over non-orthogonal atomic-like metal d states. The choice of the nature of the sub space where to apply the hubbard correction

represent the only *arbitrary* part of this formalism and it must be chosen accordingly to both common sense and quality of the results. Preliminary test of DFT+U_{LR} on iron dimer and other Fe_4C_5 SMMs point out the necessity to use non orhogonal d-like MOs as definition of localized states. Although this choice is reasonable for the transition metal ions, the use of pure p atomic orbital for the oxygen ions is probably less acceptable as the corresponding MOs have a more pronounced hybridization with respect to the d counterpart.

Table 4.18: Fe_3M Calculated On-Site Hubbard Parameters

U (eV)	Opt-Isol		Fe_3M@Au(111)		Fe_3M@Au(111)	
	Cr	Fe	Cr	Fe	Cr	Fe
M	3.8	4.3	4.3	4.4	4.6	5.2
Fe_1	4.8	4.4	5.3	4.5	4.6	4.3
Fe_2	4.8	4.4	5.2	4.5	4.8	4.5
Fe_3	4.8	4.4	5.2	4.5	4.8	4.5
O_p	10.5	9.5	10.4	10.8	10.7	10.2
O_e	11.4	10.0	11.3	11.2	11.3	10.6

At this stage, only the evaluation of the mean isotropic coupling constant J acting between the central ion and the peripheral ones has been calculated at the DFT+U_{LR} and results for Fe_4C_5 and Fe_3CrC_5 are reported in Table 4.19. Isotropic exchange coupling constants for Fe_3CrC_5 Opt-Isol model is in good agreement with experimental data, which place it at slightly less antiferromagnetic values with respect to Fe_4C_5 SMM. Despite the DFT prediction is in line with the expected behavior, the Fe_4C_5 Opt-Isol J value is found overestimated of about 6 cm^{-1} with respect to both experimental value and the results reported in the last two sections. From the comparison of results for Opt-Isol and SMM@Au(111) models it has been found that the mean J constant is enhanced as a result of structural rearrangements of the magnetic core after the deposition of the SMMs. Although the same trend was observed in the last sections, where hybrid and phenomenological DFT+U approach were exploited, here the effect of structural rearrangements on Fe_4C_5 is less dramatic. However, it must be noted that the J value of the Fe_4C_5@Au(111) model is in remarkable agreement with the previous analysis and that this discrepancy comes from an overestimation of the Opt model J.

The comparison between SMM@Au(111) and SMM@Au(111) models revealed that the sole electronic contribution of the metal substrate reduces the mean J_1 constant of about 6 cm^{-1} (36 %) for Fe_3CrC_5@Au(111) and of 3.4 cm^{-1} (14 %) for

Fe_4C_5@Au(111). This is a twofold remarkable result: firstly it shows that the metal acts to reduce the antiferromagnetic contribution to J and, secondly, it highlights the dependence of its magnitude on the nature of the transition metals involved. Although the similar structure of the two SMM are almost identical, the final J values for the adsorbed systems are significantly different. This result could be used to reconcile two apparent contradictory experimental reports. The mean J values for both SMM@Au(111) have been measured by means of two different experimental methods. In the case of Fe_4C_5@Au(111) the authors claimed to observe an increases of J of about $\sim 60\%$ with respect to the bulk value. A completely different scenario has been observed for Fe_3Cr@Au(111) where no significant variations on J was observed[151]. On light of the calculations just discussed, this could be explained considering the different activity of the metal substrate, that compensate the structure deformation effects only for the Fe_3CrC_5.

Table 4.19: Fe_3CrC_5 and Fe_4C_5 Isotropic Exchange Coupling Parameter.

J (cm^{-1})	Opt-Isol	SMM@Au(111)	SMM@Au(111)	Exp-Bulk	Exp@Au(111)
Fe_3CrC_5	12.2 cm^{-1}	16.6 cm^{-1}	10.7 cm^{-1}	13.0-15.6 cm^{-1} [a]	14.0-15.6 cm^{-1} [b]
Fe_4C_5	21.4 cm^{-1}	24.2 cm^{-1}	20.8 cm^{-1}	15.6 cm^{-1}	25.7 cm^{-1} [c]

[a] Value taken from the work of Totaro *et al.*[152] and Tancini *et al.*[24]
[b] Value taken from the work of Tancini *et al.*[151]
[c] Value taken from the work of Salman *et al.*[153]

In order to get some insights on the nature of such interaction Löwdin charges and projected DOSs have been evaluated. The difference between the löwdin charge carried by transition metal and oxygen ions between SMM@Au(111) and SMM@Au(111) models is 0.088 and 0.092 atomic charge unit for Fe_3CrC_5 and Fe_4C_5, respectively. Therefore, although for both system a very small depletion of charge in the core region is observed, according to its modest value, it is possible to exclude a significant charge transfer effect between surface and magnetic core. This is indeed expected because of the insulate barrier created by organic ligands. As demonstrated by the analysis of the Löwdin charges, the magnetic core region could be considered as a physisorbed unit. Indeed, nevertheless the SMMs are chemisorbed through a S-Au(111) bond to the substrates, the C_5 alyphatic chain ensure the independence of magnetic core from the bonding region. Consequently, the screening effects due to the metal charge density stands as the prominent interaction operating in this framework, coherently with common observation about physisorbed molecules upon metal substrates.

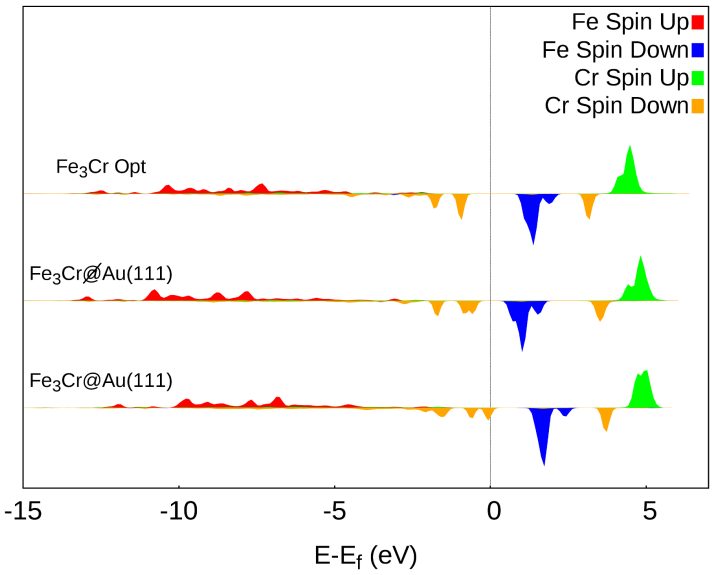

Figure 4.17: Fe_3CrC_5 projected DOSs on 3d orbitals of Cr and one Fe_p Ions.

Pojected DOSs on 3d atomic like orbitals of Cr and Fe ions for both Fe_3CrC_5 and Fe_4C_5 SMMs are reported in Fig. 4.17 and 4.18, respectively. The DOSs is reported for all the models in order to show the effects of specific interactions. The density of occupied states for Fe_3CrC_5 Opt-Isol model are characterized by two peaks near the Fermi energy. The density of states corresponding to d orbitals of peripheral iron ions are shifted at lower binding energies with respect to Cr states and are much more spread in energy, displaying the effect of a less pronounced local symmetry with respect to the distorted octahedral environment of the central Cr ion. Fe_3CrC_5@Au(111) density of states show that structure distortions produce a shift of iron d orbitals to lower energies with respect to the Opt-Isol model, while the energy of Cr d orbitals is slightly shifted toward the Fermi energy. Moreover, the degeneracy of the two high lying d orbitals of the Cr ion is removed producing two different peaks. The comparison between Fe_3CrC_5@Au(111) and Fe_3CrC_5@Au(111) models DOSs show that the proximity of Au(111) electronic density shifts the occupied d orbital energies towards the Fermi energy. Notably, the Fe_3CrC_5 becomes half metallic when adsorbed on Au(111). The DOSs for peripheral iron ions in Fe_4C_5 follows a trend similar to the corresponding ions in Fe_3CrC_5. Due to the broad and not well defined line shape

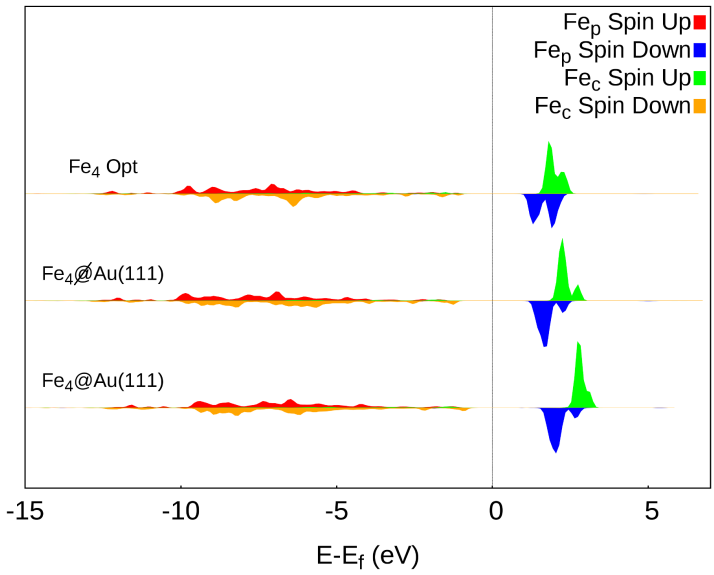

Figure 4.18: Fe_4C_5 projected DOSs on 3d orbitals of Fe_c and one Fe_p Ions.

of Fe_c in Fe_4C_5, the evolution of its DOSs is not easily rationalized and follows about the same changes of the three Fe_p.

Although there is not a straightforward procedure to extract from the DOSs the single contribution to the isotropic exchange coupling, an attempt to give e qualitative interpretation on the basis of Hoffmann's theory will be performed. The resulting total exchange coupling between two paramagnetic ions may be considered as the sum of exchange couplings between all the possible couples of electrons, each located on different magnetic centers. Moreover, each electrons couple produces an antiferromagnetic contribution to the total J constant proportional to $(E_g - E_u)^2$, where E_g and E_u are, respectively, the energy of the gerade and ungerade combination of the two d orbitals containing the selected couple of electrons. Taking a look at the projected DOSs, it is clear that d orbital of Cr and Fe are poorly mixed inside MOs and therefore, it is possible to approximate $(E_g - E_u)^2$ to $(E(d_{Fe}) - E(d_{Cr}))^2$. Comparing the energies of occupied d_{Fe} and d_{Cr} orbitals for Opt-Isol and Fe_3CrC_5@Au(111) it is possible to observe an overall increases in their energy separation. According to the above considerations, an increase in the antiferromagnetic contribution to the isotropic exchange coupling constants is expected and indeed observed by calculations.

Comparing the energies of occupied d_{Fe} and d_{Cr} orbitals for Fe_3CrC_5@Au(111) and Fe_3CrC_5@Au(111) models is possible to observe the opposite trend. The energy of both d_{Cr} and d_{Fe} orbitals get closer to the Fermi Energy but with a reduction of their energy difference. Therefore, isotropic exchange coupling constants are expected to be reduced by the electronic interaction between Fe_3CrC_5 and substrates. Also in this case our simple model is in accord with DFT+U_{LR} calculations. The same reasoning is expected to apply also to Fe_4C_5 but unfortunately the complexity of its DOSs does not allow to verify it. However, in this framework, as Fe_4C_5 DOSs changes are less evident with respect to Fe_3CrC_5 ones, a weak effect on J is expected.

At this stage it is not possible to unambiguously demonstrate the source of these different shifts in the Fe_3CrC_5 and Fe_4C_5 DOSs and more tests will be needed. However, excluding the charge transfer effect as the driving interaction between SMM and substrate on the base of the previous discussion, the image-charge effect is the best candidate to explain the presented features. From a classical point of view, this effect arises when a charge distribution $\rho(\vec{\mathbf{r}})_{mol}$ is placed near a surface. According to Maxwell equations, the electrostatic potential $\phi(\vec{\mathbf{r}})$ inside the substrate would follows the solution of the screened Poisson equation

$$(\bigtriangledown^2 - \chi)\phi(\vec{\mathbf{r}}) = \rho(\vec{\mathbf{r}})_{mol} \tag{4.2}$$

where χ represent the surface susceptibility. Therefore, the $\rho(\vec{\mathbf{r}})_{mol}$ density induces a response in the slab, polarizing it, which in turns generates an electrostatic field acting on $\rho(\vec{\mathbf{r}})_{mol}$ itself. This effect is known as image-charge effect and it is at the origin of molecular electronic level renormalization induced by a substrate. The potential acting on the molecules is of the form

$$\phi(z) = \frac{qq'}{4|z - z_0|} \tag{4.3}$$

where $z - z_0$ is the distance from the surface, q is the test charge out of the surface a distance $z - z_0$ and q'=q(1-ϵ)/(1+ϵ) is the image charge in the surface with $\epsilon = 1 + \chi$. According to this form of the potential, the molecular electronic levels energies would be shifted according to their MO shape and distance from the surface slab. Concluding, all these effects might play together in order to shift different MO energies in different ways, producing a modulation of the J constants as expected from Hoffman theory.

Conclusions

The addressing of the tricky effect of the weak hybridization between localize d-like and itinerant metal electrons has been attempted through a linear response DFT+U framework in order to obtained a balance description of all the electronic features. Application to Fe_3CrC_5@Au(111) and Fe_4C_5@Au(111) SMMs revealed that screening effects are operative on their magnetic core, which act over the main J_1 isotropic exchange coupling constant to reduce its absolute antiferromagnetic value. The analysis of Löwdin charges and DOSs suggests that the principal source of screening is the polarization of the surface due to the molecular charge density and only small charge transfer screening is operative. A qualitative interpretation of the computational data by mean of classical image-charge surface effect and Hoffman theory has been provided paving the ground to future, more extended, studies. Indeed, as the reciprocal spin states energy difference is at the origin of all the magnetic properties described by means of the spin hamiltonian, the possibility to shift them through an interplay with surface itinerant states might has deep effects also on the anisotropic properties of SMMs.

4.5 Summary

In this chapter the adsorption of SMMs over a metallic surface has been studied with particular attention to decouple effects coming from different kind of interactions *i.e.* SMM-Au(111) and SMM-SMM, where the former ones have been further divided between effects coming from pure structural rearrangements and pure electronic interaction with the gold itinerant electrons. In all the studied scenario the basic magnetic features of the helical pitch SMM family have been retained *i.e.* the ground state S=5 and its negative axial anisotropy $D_{S=5}$ remain qualitatively the same. However, from a multi spin point of view, the spin hamiltonian parameters are deeply influenced by the many interactions occurring in the complex surface scenario.

The study of the series of grafted Fe_4C_X@Au(111) and the physisorbed Fe_4 Ph@Au(111) revealed the important effect of structural rearrangements over SMMs magnetism. Indeed, vdW forces between substrate and molecules lead to a strong interaction between the two, with consequent severe modification of the molecular structure. This effect, generally not recognized in literature, is expected to be particular important for this class of system because of their complex structure with many degrees of freedom. The surface linking group itself has been revealed a key element in the modulation of the magnetism on the surface, mainly because it is responsible for the SMMs orientation on the substrate. Indeed, if a long spacer chain can ensure a facilitate grafting procedure, it can also induce larger geometrical perturbations at the magnetic core level risking to alter the Fe_4 magnetic structure. On the other hand, a too short linking group might induces an exceedingly molecular stress leading to the loss of SMM properties *e.g.* Fe_4C_2. The possibility to employ a physisorption process instead to a covalent grafting has been addressed with the study of a single Fe_4Ph@Au(111), which showed the same qualitative features of the Fe_4C_X@Au(111) series in addiction to an high on surface molecular mobility. Fe_4Ph has been also used to study the effect of inter molecular interactions once a self assembled monolayer is formed. Both the half and full monolayer coverages have been simulated, showing that on surface packing interactions play a role in the modulation of easy axis orientation and single molecule properties. Interestingly, the lacking of a covalent grafting and the possibility of interaction among molecules leads the SMMs to assume multiple configurations unexplored by the single molecule scenario.

Finally, the effect of the weak hybridization of SMM magnetic orbitals with the metal itinerant electrons has been addressed for Fe_4C_5 and Fe_3CrC_5 systems. The sole effect of molecular level reorganization has been found operative in both system leading to

a decrease of the main isotropic exchange coupling interaction inside the magnetic core. However, the magnitude of this effect has been found dependent on the nature of the magnetic ion involved in the interaction showing a more pronounced effect for Fe_3CrC_5@Au(111). Although a more detailed study is mandatory in order shed more lights on this effect, a possible interpretation on the basis of image charge effect has been provided, suggesting that the alignment between the metal E_F and molecular levels, the shape of the magnetic orbital and their distance from the surface might play a fundamental role in this interaction. Moreover, according to this interpretation, the possibility to tune the surface response to the molecular deposited charge density, *e.g.* applying an electrostatic bias or changing the surface itself, might lead to interesting magnetic properties modulations. Although in the context of this thesis only the effect over isotropic exchange coupling constants has been addressed, it is believed that both single ion anisotropy and exchange anisotropy might be affected.

Finally, from a computational point of view, in this chapter a big amount of work has been devoted to development of a multiscale protocol able to address and disentangle the many interactions separately. This goal has been achieved through the interplay of different level of theory and different computational approaches which have been selectively used in the respective area of interest. For instance, once the need of molecular dynamics to study the structural arrangements had been realized, the high quality fully ab initio approach has been restricted to the single molecule scenario while a more computationally light FF parametrization has been developed to stress the time scale limits and system sizes up to nano seconds and more than twenty thousands of atoms for the study of the self assembling process. The same approach has been followed for the study of magnetic properties where the use of highly demanding hybrid PBE0 functional has been restricted to the isolated and extrapolated scenario where it was known to well describe localized d states, leaving the place for DFT+U approaches for the more demanding adsorbed scenario where a more balanced description of localized and itinerant electrons was needed.

4.6 Computational Methods

Models

The Au(111) surface has been modeled as a four layers slab of gold. Each layer consists of 80 gold atoms. The dimensions of the simulation cell are 23.05 x 25.0 x 60.0 Å. Periodic boundary conditions are always applied, but the size of the box is sufficient to avoid interactions between periodic images of the Fe_4C_5 units, which are about 10 Å apart from each other. From experimental and computational evidances it can be assessed that both thioacetyl and simple thiols undergo an homolithyc cleavage of the S-Ac (S-H) bond with the formation of a sulfur radical, which is the species that effectively binds the metallic substrate.[154, 155] The Fe_4C_5 molecule has two side chains, each containing one thioacetyl group. Thanks to the steric hindrance of the magnetic core, only one of the two chains can actually bind to the substrate[156]. According to literature[154, 155, 157, 158], the initial configuration was prepared grafting the X-ray structure of Fe_4C_{2-5} upon the Au(111) after the removal of one $Ac^{\cdot}$ group from one aliphatic chain, while leaving intact the other one. The starting geometry of Fe_3CrC_5 has been chosen simply replacing the Fe_c ion with a Cr^{+3} ion in the Walker1 structure as discussed in section 4.4.

MD and optimizations

AIMD calculations within the Born-Oppenheimer framework have been performed optimizing the wave function at each MD step. Electronic structure and nuclear forces have been calculated at the meta-GGA DFT level of theory, applying the Gaussian and plane wave (GPW) method[159, 160], as implemented in CP2K[161]. The GPW approach is based on the expansion of the valence electron molecular orbitals in Gaussian type orbital basis sets, for which we use molecule optimized basis sets of the DZVP-MOLOPT-SR-GTH type.[73] The auxiliary plane wave basis set is needed for the representation of the electronic density in the reciprocal space and the efficient solution of the Poisson's equation. We truncate the plane wave basis set at 400 Ry. The interactions between valence electrons and atomic cores are described by means of Godecker-Teter-Hutter pseudopotentials.[74, 75] In particular, we used the TPSS[124] functional together with the Grimme's D3 corrections[125] to account for the dispersion forces. The computational set up has been tested on bulk Au, Au(111) surface energy and cohesive energy of Benzene on Au(111) (available on ESI). The selected set up can adequately reproduce the structure of both gold slab and grafted

molecule. PBE and non local dispersion corrections (rvv10) have been used for both optimizations and AIMD runs only for the Fe_4Ph SMM simulations (see section 4.3 for further discussions). Electronic energy calculations have been carried out with the direct diagonalization of the Kohn-Sham matrix until the maximum gradient of the wave function was less than 1.0E-05 for AIMD and 1.0E-06 for geometry optimizations. In order to reach rapidly the convergence criteria we used both a Broyden mixing procedure and a smearing of the MOs' occupation numbers with a Fermi-Dirac distribution set at 1500 K.

Hamiltonian equations of motion are numerically integrated using the velocity Verlet algorithm and a time step of 1 fs. Canonical distribution of momenta at 200 K is enforced with the canonical stocastic rescaled velocity (CSVR) thermostat[162] with a time constant of 100 fs during thermalization and 500 fs during acquisition runs. When requested, independent trajectories starting from the same initial configuration have been generated by first initializing the velocities at 100 K and then annealing the system up to 200 K by different ramp procedures. Total energy conservation has been obtained with a smearing of molecular orbitals' occupation numbers with a Fermi-Dirac distribution at 1500 K and with a convergence threshold criteria on the maximum wave function's gradient of 1.0E-5.

When dealing with multispin systems, the DFT solution which can be used to evaluate forces is not unequivocally defined. Various spin solutions, described by broken symmetry (BS) states, are available. For what concern the overall structure of the complex and its interaction with the surface, the choices of one spin DFT solution instead of another is not important and no appreciable differences should be expected. For this reason, all the AIMD calculations are carried out with forces evaluated from the electronic configuration that better describes the lowest energy spin multiplet ($S = 5$ for Fe_4 and $S = 6$ for Fe_3Cr): the central iron (Fe_c or Fe_1) / chromium is down polarized while the peripheral irons (Fe_p or Fe_{2-4}) are up polarized (schematically DUUU).

All the force field based MD calculations have been done with the software LAMMPS. The single molecule simulations has been done on a cell of 46.08x50x60 Åwith a 6 layer slab of gold (1902 Au atom in total) while for the half and full coverage monolayers simulations a simulation cell of 138.24x134.28x80 Åwith a 6 layer slab (33000 Au atom in total) of gold has instead been used. Non-bonded interactions cutoff has been set at 20 Åand pppm summations have been exploited with an integration accuracy of 1.0E-7.

Magnetic Properties Calculations

The nearby metallic substrate could affects Fe_4C_5 magnetic properties both by geometrical distortions and electronic effects. In order to decouple and independently estimate these two contributions we evaluated the magnetic properties both on the entire system (mol@Au(111)) and on the molecule by itself in vacuum (mol@Au(111)). This procedure was applied only for the isotropic exchange coupling constants calculations while for the anisotropy parameters calculations it was possible to study only the extrapolated case. Nevertheless it is not possible to exclude *a priori* an electronic contribution from the metal to the anisotropic magnetic properties of the SMM and this topic is left for future studies. Magnetic properties analysis have been carried out utilizing both CP2K and ORCA software. For what concerns the extrapolated geometries we used the same procedure of section 2.4 for the Fe_4 SMMs. This procedure consists in two steps. The first one requires the CP2K code with the hybrid PBE0 functional[72] for the calculation of the isotropic exchange coupling constants. The PW cutoff have been set to 400 Ry, DZVP-MOLOPT-SR basis sets with GTH pseudo potentials have been chosen for all the elements. For the evaluation of exact exchange integrals we take advantage of an auxiliary basis set[76]: the DZVP-MOLOPT-SR basis set has been used for iron ions while the SZV-MOLOPT-SR basis set was chosen for carbon, hydrogen, oxygen and sulfur atoms. Convergence criteria over the maximum component of the wavefunction's gradient were set to 1.0E-6. Following the Noodleman formulation of the BS approach[32, 82], isotropic exchange coupling constants have been extracted solving the linear system

$$\Delta E\big(HS - BS(\{s_k\})\big) = \sum_{ij} 2J_{ij}s_i s_j \lambda_{ij}^{BS} \tag{4.4}$$

where s_i and s_j are the value of the single ion spins, J_{ij} their exchange interaction and λ_{ij} is equal to one if, for the specific BS state considered with the appropriate s_k value, the couple of spin (i,j) are misaligned, zero otherwise. The SH considered to model the multiplet structure of the Fe_4C_5 is given in Equation 2.55. In order to solve the system 4.4 for the SH model 2.55 we used four different energy differences built up by the HS state and the four BS determinants: DUUU, UDUU, UUDU and UUUD. Once the non relativistic multiplets structure is obtained, it is then possible to proceed with the second step, where the calculation of the anisotropy tensors is performed. For this second task the software ORCA has been utilized. The computationally cheap GGA (PBE) functional has been used, since the expensive PBE0 is found not to improve the results. We used the def2-TZVP basis set for all the elements and the

RI approximation for the coulomb operator integral evaluation have been employed with the def2-TZVP/J auxiliary basis set. Speaking in the ORCA notation, Grid 5 and Very Tight convergence criteria were used. The protocol used to compute anisotropy splittings follows the route of the diamagnetic substitution. We evaluated single ion tensors making the substitution of all but one iron ions with Ga^{3+} ions at turn. Both Spin Orbit Coupling (SOC) and Spin Spin (SS) interactions were take into accounts for single ion anisotropy tensor calculations.[37, 38] For what concerns the anisotropic exchange coupling interaction between iron ions we decided to take into account only spin dipole pair interaction. Moreover, although a few differences between DFT and point-dipole like calculation of this interaction exist,[53] we decided to use the second one which is less computational demanding. This procedure makes possible to directly map the multispin Hamiltonian H=$\sum_i \vec{\mathbf{s}}_i \cdot \mathbf{D_i} \cdot \vec{\mathbf{s}}_i + \sum_{i,j \neq i} \vec{\mathbf{s}}_i \cdot \mathbf{D_{ij}} \cdot \vec{\mathbf{s}}_j$ from DFT calculations. Thanks to the quite large J coupling constants, compared to anisotropy splitting, it was possible to take advantage of the strong exchange limit and use the Giant Spin Hamiltonian (GSH) H=$\vec{\mathbf{S}} \cdot \mathbf{D_{S=5}} \cdot \vec{\mathbf{S}}$, which is generally used to interpret experimental data. The multispin Hamiltonian and the GSH are related by the equation

$$\mathbf{D_S} = \sum_i d_i^S \mathbf{D_i} + \sum_{ij} d_{ij}^S \mathbf{D_{ij}} \tag{4.5}$$

where the projection coefficients d_i^S and d_{ij}^S were evaluated as:

$$\begin{aligned} d_i^S &= \frac{\langle \alpha S || T_2(\mathbf{s}_i, \mathbf{s}_i) || \alpha S \rangle}{\langle \alpha S || T_2(\mathbf{S}, \mathbf{S}) || \alpha S \rangle} \\ d_{ij}^S &= \frac{\langle \alpha S || T_2(\mathbf{s}_i, \mathbf{s}_j) || \alpha S \rangle}{\langle \alpha S || T_2(\mathbf{S}, \mathbf{S}) || \alpha S \rangle} \end{aligned} \tag{4.6}$$

where $\langle \alpha S || \cdots || \alpha S \rangle$ stands for an irreducible matrix element of spherical tensor T_{kq}. Once the eigenket of the Heisenberg Hamiltonian (Eq. 2.55) $|\alpha S M_S\rangle$ have been evaluated by numerical diagonalization, d_i^S and d_{ij}^S could be calculated taking advantage of the Wigner-Eckart theorem.

The straightfoward application of this procedure to the calculation of the isotropic exchange coupling once the Au(111) metallica slab is considered is not possible. Although the hybrid formulation of DFT usually improves the results for system described by localized states, when delocalized states are considered, as is the case of metallic systems, GGA functionals give better results. Moreover, the computational

cost for a periodic extended system like those treated in this work poses several limitation to the application of hybrid functional to this class of systems. However, it is well known that DFT at the GGA level overestimates the delocalization of the charge density leading to unacceptable overestimation of antiferromagnetic interactions. In order to solve this situation, we employed a GGA+U methodology[126] for the study of SMMs and Au(111) substrate at the same time. This procedure makes possible to correct part of the GGA deficiency on the treatment of localized states, without loosing high speed performances of non-hybrids functionals. In section 4.1 we tested the DFT+U in its phenomenological formulation with the CP2K software, choosing the U correction for Fe, O and Au elements of 4.1 eV, 3.0 eV and 0.60 eV, respectively. These values were taken from the works of Ninova and Malavolti *et al.*[128, 163]. In section 4.4 this approach has been extended to its parameters-free linear response formulation (U_{LR}) and applied to Fe_4C_5 and Fe_3CrC_5 SMMs. In this context, U_{LR}, Density of States (DOSs) and isotropic exchange coupling constants calculations have all been done with Quantum Espresso software.[164] PBE functional with PAW pseudo potentials have been used together with a plane wave cutoff of 50 Ry for the kinetic energy and 300 Ry for the electronic density. Such values for the plane wave expansion cutoff were carefully testes in order to get well converged multiplet energy differences. The computation of the on-site Hubbard correction have been applied to all transition metal atoms and all oxygen ions. The inclusion of the correction for the latters has been shown to be crucial to get a quantitatively agreement between simulation and experiments.[145, 165, 166] The Hubbard U values has been computed as the second derivative of the ground state electronic energy (E) with respect to the i-site occupation number (n_i)[]. We chose to define the i-site occupation number n_i through the projection of the electronic density on the non-orthogonalized d and p atomic orbitals for the metal and oxygens ions, respectively. The computation of the energy derivatives is performed through the application of an external α potential acting on the sub manifold of projected atomic orbitals:

$$U_i = (\chi_{i0}^{-1} - \chi_i^{-1}), \quad \chi_i = \left(\frac{\partial n_i}{\partial \alpha_i}\right)_{\alpha=0} \tag{4.7}$$

where χ_i is computed with self consistent converged wave function and χ_{i0} is calculated with the wave function after the first diagonalization with the applied α potential. The derivatives are numerically evaluated thorugh α variation of 0.1 eV.

Chapter 5

Final Remarks and Perspectives

In this thesis a systematic theoretical and computational approach has been applied to the main research aree concerning SMMs. The state of the art about SMMs modeling has been used and pushed forward in order to investigate their properties in different environments: isolated, embedded in molecular crystals and deposited on a metallic surface.

Besides the results presented and discussed, this thesis is also expected to stimulate further investigations on the here presented topics. Indeed, from a perspective point of view, the results on spin relaxation phenomena can represent a very promising starting point in the SMMs field. Thanks to it, indeed, it would be possible to answer to many questions and open it to new developments. For instance, the extension of the formalism here developed would make possible its straightforward extension to higher order perturbation treatments, making an ab initio determination of the second order Raman effects on relaxation. Most importantly, a more detailed analysis on normal modes contribution to the several relaxation pathways is expected to be a breakthrough in the comprehension of this phenomena with consequences also for experimental studies. It is important to stress out that the microscopic description of time dependent spin phenomena represents an aspect of paramount importance in physics due to its broad impact over many aree. Knowing how spins relax in function of time would allow the design of new magnetic data storage devices, non-volatile memories, high frequency resonators, etc. Among the various mechanisms for spin relaxation, spin-phonon interaction is dominant for a vast class of materials. For

instance, this interaction determines the Curie and Neel temperatures in bulk magnets and furthermore affects the transport properties such as the conductance and spin currents generation in spintronic materials. An important step forward toward a full understanding of deposited SMMs related phenomena has also been done. The combination of a multi scale computational approach has made possible to address separately the many aspects of the SMM@Au(111) interactions, revealing their respective importance. The whole study on SMM@Au(111) is expected to change drastically the actual conception on deposited systems. Indeed, the realization of the dramatic effect produced by the deposition is starting only recently to enter in the scientific debates and a full realization of the not necessary robustness of SMMs and similar systems, with respect to adsorption process, is expected to induce a more careful design of SMMs and its *a priori* computational characterization for specific deposition purpose, instead of completely relying on the SMM crystalline phase properties. Also in this field, numerous evolution pathways arose from the present study. The realization of a computational protocol able to address different sizes and time-scales might be further enriched, for instance, by the mixing of the present schemes within a QM/MM approach[167]. On the basis of the results presented in this thesis, such an approach can represent a valuable tool capable to account in large part the accuracy of the AIMD and the efficiency of the FF MD approaches. In the same context, another very promising evolution of the presented studies is represented by the use of more advanced computational schemes for the free energy surface scan as metadynamics and replica exchange methods[168, 169]. These approaches, together with the FF description of forces, are expected to be a valuable tool to explore different configurational phases of adsorbed SMMs in a more systematic way. Moreover, the conclusion of the study on the sole electronic effect on the SMMs magnetism is expected to produce interesting results showing an innovative way to control magnetism in deposited scenario with a wide appeal also in slightly different context with respect to SMMs field.

Bibliography

[1] R. Sessoli, D. Gatteschi, A. Caneschi, and M. A. Novak, Nature **365**, 141 (1993).

[2] G. Christou, D. Gatteschi, D. Hendrickson, and R. Sessoli, MRS Bull. , 66 (2000).

[3] D. Gatteschi and R. Sessoli, Angew. Chem. Int. Ed. **42**, 268 (2003).

[4] J. Luzon and R. Sessoli, Dalton Trans. **41**, 13556 (2012).

[5] M. Cavallini, J. Gomez-Segura, D. Ruiz-Molina, M. Massi, C. Albonetti, C. Rovira, J. Veciana, and F. Biscarini, Angew. Chemie - Int. Ed. **44**, 888 (2005).

[6] W. Wernsdorfer, N. Aliaga-Alcalde, D. N. Hendrickson, and G. Christou, Nature **416**, 406 (2002).

[7] S. Hill, R. S. Edwards, N. Aliaga-Alcalde, and G. Christou, Science **302**, 1015 (2003).

[8] M. N. Leuenberger and D. Loss, Nature **410**, 789 (2001).

[9] A. Ardavan, O. Rival, J. J. L. Morton, S. J. Blundell, A. M. Tyryshkin, G. a. Timco, and R. E. P. Winpenny, Phys. Rev. Lett. **98**, 057201 (2007).

[10] C. Schlegel, J. Van Slageren, M. Manoli, E. K. Brechin, and M. Dressel, Phys. Rev. Lett. **101**, 1 (2008).

[11] G. A. Timco, S. Carretta, F. Troiani, F. Tuna, R. J. Pritchard, C. a. Muryn, E. J. L. McInnes, A. Ghirri, A. Candini, P. Santini, G. Amoretti, M. Affronte, and R. E. P. Winpenny, Nat. Nanotechnol. **4**, 173 (2009).

[12] F. Troiani and M. Affronte, Chem. Soc. Rev **40**, 3119 (2011).

[13] S. a. Wolf, D. D. Awschalom, R. a. Buhrman, J. M. Daughton, S. von Molnár, M. L. Roukes, a. Y. Chtchelkanova, and D. M. Treger, Science **294**, 1488 (2001).

[14] A. Fert, Rev. Mod. Phys. **80**, 1517 (2008).

[15] S. Sanvito, Chem. Soc. Rev. **40**, 3336 (2011).

[16] J. S. Moodera, B. Koopmans, and P. M. Oppeneer, MRS Bull. **39**, 578 (2014).

[17] L. Bogani and W. Wernsdorfer, Nat. Mater. **7**, 179 (2008).

[18] F. Neese, Coord. Chem. Rev. **253**, 526 (2009).

[19] M. Atanasov, D. Aravena, E. Suturina, E. Bill, D. Maganas, and F. Neese, Coord. Chem. Rev. **289-290**, 177 (2015).

[20] O. Waldmann, A. Ako, H. U. Gudel, and A. K. Powell, Inorg. Chem. **47**, 3486 (2008).

[21] H. Oshio and M. Nakano, Chem. - Eur. J. **11**, 5178 (2005).

[22] O. Waldmann, Inorg. Chem. **46**, 10035 (2007).

[23] S. Accorsi, A. Barra, A. Caneschi, G. Chastanet, A. Cornia, A. C. Fabretti, D. Gatteschi, C. Mortalò, E. Olivieri, F. Parenti, P. Rosa, R. Sessoli, L. Sorace, W. Wernsdorfer, and L. Zobbi, J. Am. Chem. Soc. **128**, 4742 (2006).

[24] E. Tancini, M. J. Rodriguez-Douton, L. Sorace, A.-L. Barra, R. Sessoli, and A. Cornia, Chem. - Eur. J. **16**, 10482 (2010).

[25] W. Tennant and C. Walsby, J. Phys. Condens. Matter **9481** (2000).

[26] C. Rudowicz and M. Karbowiak, Coord. Chem. Rev. **287**, 28 (2015).

[27] D. Gatteschi, R. Sessoli, and J. Villain, *Molecular Nanomagnets*, Mesoscopic Physics and Nanotechnology (OUP Oxford, 2006).

[28] F. Neese and E. I. E. Solomon, Inorg. Chem. **37**, 6568 (1998).

[29] R. Maurice, R. Bastardis, C. Graaf, N. Suaud, T. Mallah, and N. Guihéry, J. Chem. Theory Comput. **5**, 2977 (2009).

[30] P. Löwdin, Phys. Rev. **97**, 1490 (1955).

[31] P. Löwdin, Rev. Mod. Phys. **34**, 80 (1962).

[32] L. Noodleman, J. Chem. Phys. **74**, 5737 (1981).

[33] K. Yamaguchi, T. Tsunekawa, Y. Toyoda, and T. Fueno, Chem. Phys. Lett. **143**, 371 (1988).

[34] A. P. Ginsberg, J. Am. Chem. Soc. **102**, 1 (1980).

[35] D. Dai and M.-H. Whangbo, J. Chem. Phys. **114**, 2887 (2001).

[36] M. Pederson and S. Khanna, Phys. Rev. B **60**, 9566 (1999).

[37] F. Neese, J. Chem. Phys. **127**, 164112 (2007).

[38] S. Schmitt, P. Jost, and C. van Wüllen, J. Chem. Phys. **134**, 194113 (2011).

[39] F. Neese, J. Am. Chem. Soc. **128**, 10213 (2006).

[40] C. van Wüllen, J. Phys. Chem. A **113**, 11535 (2009).

[41] E. M. V. Kessler, S. Schmitt, and C. van Wüllen, J. Chem. Phys. **139**, 184110 (2013).

[42] P. ter Heerdt, M. Stefan, E. Goovaerts, A. Caneschi, and A. Cornia, J. Magn. Reson. **179**, 29 (2006).

[43] F. Neese, J. Chem. Phys. **115**, 11080 (2001).

[44] A. Barra and A. Caneschi, J. Am. Chem. Soc. **121**, 5302 (1999).

[45] E. Tancini, *Organizing Single-Molecule Magnets on Surfaces by Chemical Tailoring*, Ph.d., Università degli Studi di Modena e Reggio Emilia (2013).

[46] A.-L. Barra, A. Caneschi, A. Cornia, F. Fabrizi de Biani, D. Gatteschi, C. Sangregorio, R. Sessoli, and L. Sorace, J. Am. Chem. Soc. **121**, 5302 (1999).

[47] F. Le, F. Fabrizi, D. Biani, A. Caneschi, P. Cinelli, A. Cornia, A. C. Fabretti, and D. Gatteschi, Inorganica Chim. Acta **262**, 123 (1997).

[48] L. Gregoli, C. Danieli, A.-L. Barra, P. Neugebauer, G. Pellegrino, G. Poneti, R. Sessoli, and A. Cornia, Chem. - Eur. J. **15**, 6456 (2009).

[49] J. Ribas-Arino, T. Baruah, and M. R. Pederson, J. Chem. Phys. **123**, 044303 (2005).

[50] J. Cirera, E. Ruiz, S. Alvarez, F. Neese, and J. Kortus, Chem. - Eur. J. **15**, 4078 (2009).

[51] C. Duboc, D. Ganyushin, K. Sivalingam, F. Neese, and M.-N. Collomb, J. Phys. Chem. A **114**, 10750 (2010).

[52] L. Sorace, M.-E. Boulon, P. Totaro, A. Cornia, J. Fernandes-Soares, and R. Sessoli, Phys. Rev. B **88**, 104407 (2013).

[53] C. Riplinger, J. P. Y. Kao, G. M. Rosen, V. Kathirvelu, G. R. Eaton, S. S. Eaton, A. Kutateladze, and F. Neese, J. Am. Chem. Soc. **131**, 10092 (2009).

[54] R. Maurice, K. Sivalingam, D. Ganyushin, N. Guihéry, C. de Graaf, and F. Neese, Inorg. Chem. **50**, 6229 (2011).

[55] A. Bencini and D. Gatteschi, *EPR of Exchange Coupled Systems*, Dover Books on Chemistry Series (Dover Publications, Incorporated, 2012).

[56] S. Carretta, E. Liviotti, N. Magnani, P. Santini, and G. Amoretti, Phys. Rev. Lett. **92**, 207205 (2004).

[57] S. Datta, O. Waldmann, a. Kent, V. Milway, L. Thompson, and S. Hill, Phys. Rev. B **76**, 052407 (2007).

[58] A. Wilson, E.-C. Yang, D. N. Hendrickson, and S. Hill, Polyhedron **26**, 2065 (2007).

[59] E. Liviotti, S. Carretta, and G. Amoretti, J. Chem. Phys. **117**, 3361 (2002).

[60] J. Liu, E. del Barco, and S. Hill, Phys. Rev. B **85**, 012406 (2012).

[61] K. C. M. Westrup, M. Boulon, P. Totaro, G. G. Nunes, D. F. Back, A. Barison, J. M, C. Paulsen, D. Gatteschi, L. Sorace, A. Cornia, J. F. Soares, and R. Sessoli, Chem. - Eur. J. **20**, 13681 (2014).

[62] R. Maurice, N. Guihéry, R. Bastardis, and C. D. Graaf, J. Chem. Theory Comput. **6**, 55 (2009).

[63] M. Brynda, L. Gagliardi, and B. O. Roos, Chem. Phys. Lett. **471**, 1 (2009).

[64] J. F. Berry, F. A. Cotton, T. Lu, C. a. Murillo, B. K. Roberts, and X. Wang, J. Am. Chem. Soc. **126**, 7082 (2004).

[65] M. Nippe and J. Berry, J. Am. Chem. Soc. , 12684 (2007).

[66] F. A. Cotton, L. M. Daniels, T. Lu, C. A. Murillo, and X. Wang, Dalt. Trans. **5**, 517 (1999).

[67] A. Cornia, L. Rigamonti, S. Boccedi, R. Clérac, M. Rouzières, and L. Sorace, Chem. Commun. **50**, 15191 (2014).

[68] A. Cornia, Personal Communication .

[69] A. Barra, D. Gatteschi, R. Sessoli, G. Abbati, A. Cornia, A. C. Fabretti, and M. G. Uytterhoven, Angew. Chem. Int. Ed. Engl. **36**, 2329 (1997).

[70] D. G. Liakos, D. Ganyushin, and F. Neese, Inorg. Chem. **48**, 10572 (2009).

[71] F. Neese, Wiley Interdiscip. Rev. Comput. Mol. Sci. **2**, 73 (2012).

[72] J. P. Perdew, M. Ernzerhof, and K. Burke, J. Chem. Phys. **105**, 9982 (1996).

[73] J. VandeVondele and J. Hutter, J. Chem. Phys. **127**, 114105 (2007).

[74] C. Hartwigsen, S. Gœ decker, and J. Hutter, Phys. Rev. B **58**, 3641 (1998).

[75] M. Krack, Theor. Chem. Acc. **114**, 145 (2005).

[76] M. Guidon, J. Hutter, and J. VandeVondele, J. Chem. Theory Comput. **6**, 2348 (2010).

[77] J. P. J. Perdew, K. Burke, and Y. Wang, Phys. Rev. B **54**, 533 (1996).

[78] F. Weigend, R. Ahlrichs, and F. K. Gmbh, Phys. Chem. Chem. Phys. **7**, 3297 (2005).

[79] F. Weigend, Phys. Chem. Chem. Phys. **22**, 1057 (2006).

[80] F. Neese, F. Wennmohs, A. Hansen, and U. Becker, Chem. Phys. **356**, 98 (2009).

[81] S. Sinnecker and F. Neese, J. Phys. Chem. A **110**, 12267 (2006).

[82] A. Bencini and F. Totti, J. Chem. Theory Comput. **5**, 144 (2009).

[83] F. Neese and D. a. Pantazis, Faraday Discuss. **148**, 229 (2011).

[84] R. J. Blagg, L. Ungur, F. Tuna, J. Speak, P. Comar, D. Collison, W. Wernsdorfer, E. J. L. McInnes, L. F. Chibotaru, and R. E. P. Winpenny, Nat. Chem. **5**, 673 (2013).

[85] J. M. Zadrozny, D. J. Xiao, M. Atanasov, G. J. Long, F. Grandjean, F. Neese, J. R. Long, and J. R. Long, Nat. Chem. **5**, 577 (2013).

[86] K. S. Pedersen, J. Dreiser, H. g. Weihe, R. Sibille, H. V. Johannesen, M. a. Sø rensen, B. E. Nielsen, M. Sigrist, H. Mutka, S. Rols, J. Bendix, and S. Piligkos, Inorg. Chem. , 150722135227000 (2015).

[87] J. M. Zadrozny and J. R. Long, J. Am. Chem. Soc. **133**, 20732 (2011).

[88] D. E. Freedman, W. H. Harman, T. D. Harris, G. J. Long, C. J. Chang, and J. R. Long, J. Am. Chem. Soc. **132**, 1224 (2010).

[89] R. Orbach, Proc. R. Soc. A **264**, 458 (1961).

[90] E. Chudnovsky, D. Garanin, and R. Schilling, Phys. Rev. B **72**, 094426 (2005).

[91] S. Califano, V. Schettino, and N. Neto, *Lattice dynamics of molecular crystals*, Vol. 26 (Springer Science & Business Media, 2012).

[92] a. J. Leggett, S. Chakravarty, a. T. Dorsey, M. P. a. Fisher, A. Garg, and W. Zwerger, Rev. Mod. Phys. **59**, 1 (1987), arXiv:arXiv:0806.0992v2 .

[93] R. Kubo, J. Math. Phys. **4**, 174 (1963).

[94] R. Kubo and K. Shuler, Advances in Chemical Physics **15**, 101 (1969).

[95] R. Torre, R. Righini, L. Angeloni, and S. Califano, J. Chem. Phys. **93**, 2967 (1990).

[96] R. Bini, S. Califano, B. Eckert, and H. J. Jodl, J. Chem. Phys. **106**, 511 (1997).

[97] J. P. Pinan, R. Ouillon, P. Ranson, M. Becucci, and S. Califano, J. Chem. Phys. **109**, 5469 (1998).

[98] A. Abragam and B. Bleaney, *Electron paramagnetic resonance of transition ions* (Oxford University Press, 2012).

[99] K. Shrivastava, Phys. status solidi **437** (1983).

[100] S. K. Lyo, Phys. Rev. B **5**, 795 (1972).

[101] B. Young and H. Stapleton, Phys. Lett. **21**, 498 (1966).

[102] W. H. Harman, T. D. Harris, D. E. Freedman, H. Fong, A. Chang, T. D. Rinehart, A. Ozarowski, M. T. Sourgrati, F. Grandjean, J. G. Long, J. R. Long, and C. J. Chang, J. Am. Chem. Soc. **132**, 18115 (2010).

[103] G. Cucinotta, M. Perfetti, J. Luzon, M. Etienne, P.-E. Car, A. Caneschi, G. Calvez, K. Bernot, and R. Sessoli, Angew. Chem. Int. Ed. Engl. **51**, 1606 (2012).

[104] P. Blöchl, The Journal of chemical physics **103**, 7422 (1995).

[105] C. I. Bayly, P. Cieplak, W. Cornell, and P. A. Kollman, The Journal of Physical Chemistry **97**, 10269 (1993).

[106] C. M. Breneman and K. B. Wiberg, J. Comput. Chem. **11**, 361 (1990).

[107] a. L. Hickey and C. N. Rowley, J. Phys. Chem. A **118**, 3678 (2014).

[108] M. Atanasov, D. Ganyushin, D. A. Pantazis, K. Sivalingam, and F. Neese, Inorg. Chem. **50**, 7460 (2011).

[109] C. Sangregorio, T. Ohm, C. Paulsen, R. Sessoli, and D. Gatteschi, Phys. Rev. Lett. **78**, 4645 (1997).

[110] A. Cuccoli, A. Fort, A. Rettori, E. Adam, and J. Villain, Eur. Phys. J. B - Condens. Matter **46**, 39 (1999).

[111] N. Neto and L. Bellucci, Chem. Phys. **328**, 259 (2006).

[112] A. Watanabe, A. Yamashita, M. Nakano, T. Yamamura, and T. Kajiwara, Chem. - Eur. J. **17**, 7428 (2011).

[113] M. Mannini, F. Pineider, C. Danieli, F. Totti, L. Sorace, P. Sainctavit, M.-A. Arrio, E. Otero, L. Joly, J. C. Cezar, A. Cornia, and R. Sessoli, Nature **468**, 417 (2010).

[114] M. Mannini, F. Pineider, P. Sainctavit, C. Danieli, E. Otero, C. Sciancalepore, A. M. Talarico, M.-A. Arrio, A. Cornia, D. Gatteschi, and R. Sessoli, Nat. Mater. **8**, 194 (2009).

[115] A. Cornia, M. Mannini, P. Sainctavit, and R. Sessoli, Chem. Soc. Rev. **40**, 3076 (2011).

[116] F. Totti, G. Rajaraman, M. Iannuzzi, and R. Sessoli, J. Phys. Chem. C **117**, 7186 (2013).

[117] S. Barraza-Lopez, M. C. Avery, and K. Park, J. Appl. Phys. **103**, 07B907 (2008).

[118] J. Dreiser, C. Wackerling, M. E. Ali, C. Piamonteze, F. Donati, A. Singha, K. S. Pedersen, S. Rusponi, J. Bendix, P. M. Oppeneer, T. A. Jung, and H. Brune, ACS Nano **8**, 4662 (2014).

[119] K. Tarafder, S. Kanungo, P. M. Oppeneer, and T. Saha-Dasgupta, Phys. Rev. Lett. **109**, 1 (2012).

[120] P. Maldonado, S. Kanungo, T. Saha-Dasgupta, and P. M. Oppeneer, Phys. Rev. B **88**, 1 (2013).

[121] N. Nair, J. Ribas-Arino, V. Staemmler, and D. Marx, J. Chem. Theory Comput. **6**, 569 (2010).

[122] F. Zu, Z. Liu, K. Yao, G. Gao, H. Fu, S. Zhu, Y. Ni, and L. Peng, Sci. Rep. **4**, 1 (2014).

[123] J. Otsuki, Coord. Chemi. Rev. **254**, 2311 (2010).

[124] J. Tao, J. Perdew, V. Staroverov, and G. Scuseria, Phys. Rev. Lett. **91**, 146401 (2003).

[125] S. Grimme, J. Antony, S. Ehrlich, and H. Krieg, J. Chem. Phys. **132**, 154104 (2010).

[126] S. L. Dudarev, G. A. Botton, S. Y. Savrasov, C. J. Humphreys, and A. P. Sutton, Phys. Rev. B **57**, 1505 (1998).

[127] C. Adamo, V. Barone, A. Bencini, F. Totti, and I. Ciofini, Inorg. Chem. **38**, 1996 (1999).

[128] S. Ninova, V. Lanzilotto, L. Malavolti, L. Rigamonti, B. Cortigiani, M. Mannini, F. Totti, and R. Sessoli, J. Mater. Chem. C **2**, 9599 (2014).

[129] F. Le Gall, F. Fabrizi de Biani, A. Caneschi, P. Cinelli, A. Cornia, A. C. Fabretti, and D. Gatteschi, Inorg. Chim. Acta **262**, 123 (1997).

[130] A. Lunghi and F. Totti, J. Mater. Chem. C **2**, 8333 (2014).

[131] J. Wang, R. R. M. Wolf, J. W. Caldwell, P. a. Kollman, and D. a. Case, J. Comput. Chem. **25**, 1157 (2004).

[132] J. SEMINAR10 and J. SEMINARIO, Int. J. Quantum Chem. **30**, 1271 (1996).

[133] K. Nilsson, D. Lecerof, E. Sigfridsson, and U. Ryde, Acta Crystallogr. Sect. D **59**, 274 (2003).

[134] M. Frisch, G. Trucks, H. Schlegel, G. Scuseria, M. Robb, J. Cheeseman, G. Scalmani, V. Barone, B. Mennucci, G. Petersson, *et al.*, Gaussian Inc., Wallingford (2009).

[135] L. L. Hu and U. Ryde, J. Chem. Theory Comput. **7**, 2452 (2011).

[136] G. Fernandez Garcia, *Single molecule ,agnets on surface: an integrated MM and QM computational approach. A step forward to study real complex systems in silica.*, Master, Università degli studi di Firenze (2013).

[137] H. Heinz, R. a. Vaia, B. L. Farmer, and R. R. Naik, J. Phys. Chem. C **112**, 17281 (2008).

[138] H. Heinz, B. L. Farmer, R. B. Pandey, J. M. Slocik, S. S. Patnaik, R. Pachter, and R. R. Naik, J. Am. Chem. Soc. **131**, 9704 (2009).

[139] J. Carrasco, W. Liu, A. Michaelides, and A. Tkatchenko, J. Chem. Phys. **140**, 084704 (2014).

[140] W. Liu, A. Tkatchenko, and M. Scheffler, Acc. Chem. Res. (2014), 10.1021/ar500118y.

[141] E. Ruiz, S. Alvarez, J. Cano, and V. Polo, J. Chem. Phys. **123**, 164110 (2005).

[142] C. Toher, a. Filippetti, S. Sanvito, and K. Burke, Phys. Rev. Lett. **95**, 146402 (2005).

[143] M. Cococcioni and S. de Gironcoli, Phys. Rev. B **71**, 035105 (2005).

[144] C. D. Pemmaraju, T. Archer, D. Sánchez-Portal, and S. Sanvito, Phys. Rev. B **75**, 045101 (2007).

[145] C. Cao, S. Hill, and H.-p. Cheng, Phys. Rev. Lett. **167206**, 2 (2008).

[146] B. Himmetoglu, A. Floris, S. de Gironcoli, and M. Cococcioni, Int. J. Quantum Chem. **114**, 14 (2014).

[147] H. Jiang, R. I. Gomez-Abal, P. Rinke, and M. Scheffler, Phys. Rev. B - Condens. Matter Mater. Phys. **82**, 1 (2010).

[148] J. D. Sau, J. B. Neaton, H. J. Choi, S. G. Louie, and M. L. Cohen, Phys. Rev. Lett. **101**, 11 (2008).

[149] a. M. Souza, I. Rungger, C. D. Pemmaraju, U. Schwingenschloegl, and S. Sanvito, Phys. Rev. B **88**, 1 (2013), arXiv:arXiv:1309.6981v1 .

[150] U. G. E. Perera, H. J. Kulik, V. Iancu, L. G. G. V. Dias Da Silva, S. E. Ulloa, N. Marzari, and S. W. Hla, Phys. Rev. Lett. **105**, 1 (2010).

[151] E. Tancini, M. Mannini, P. Sainctavit, E. Otero, R. Sessoli, and A. Cornia, Chem. - Eur. J. **19**, 16902 (2013).

[152] P. Totaro, K. C. M. Westrup, M.-E. Boulon, G. G. Nunes, D. F. Back, A. Barison, S. Ciattini, M. Mannini, L. Sorace, J. F. Soares, A. Cornia, and R. Sessoli, Dalton Trans. **42**, 4416 (2013).

[153] Z. Salman, S. J. Blundell, S. R. Giblin, M. Mannini, L. Margheriti, R. Sessoli, E. Morenzoni, T. Prokscha, A. Suter, and A. Cornia, , 1arXiv:arXiv:0909.4634v1 .

[154] H. Häkkinen, Nat. Chem. **4**, 443 (2012).

[155] M. Jaccob, G. Rajaraman, and F. Totti, Theor. Chem. Acc. **131**, 1150 (2012).

[156] P. Totaro, L. Poggini, A. Favre, M. Mannini, P. Sainctavit, A. Cornia, A. Magnani, and R. Sessoli, Langmuir **30**, 8645 (2014).

[157] F. Pineider, M. Mannini, C. Danieli, L. Armelao, F. M. Piras, A. Magnani, A. Cornia, and R. Sessoli, J. Mater. Chem. **20**, 187 (2010).

[158] G. Rajaraman, A. Caneschi, D. Gatteschi, and F. Totti, Phys. Chem. Chem. Phys. **13**, 3886 (2011).

[159] J. VandeVondele, M. Krack, F. Mohamed, M. Parrinello, T. Chassaing, and J. Hutter, Comput. Phys. Commun. **167**, 103 (2005).

[160] J. Hutter, M. Parrinello, and G. Lippert, Theor. Chem. Acc. **103**, 124 (1999).

[161] J. Hutter, M. Iannuzzi, F. Schiffmann, and J. VandeVondele, Wiley Interdiscip. Rev.: Comput. Mol. Sci. **4**, 15 (2014).

[162] G. Bussi, D. Donadio, and M. Parrinello, J. Chem. Phys. **126**, 014101 (2007).

[163] L. Malavolti, V. Lanzilotto, S. Ninova, L. Poggini, I. Cimatti, B. Cortigiani, L. Margheriti, D. Chiappe, E. Otero, P. Sainctavit, F. Totti, A. Cornia, M. Mannini, and R. Sessoli, Nano Lett. **15**, 535 (2015).

[164] P. Giannozzi, S. Baroni, N. Bonini, M. Calandra, R. Car, C. Cavazzoni, D. Ceresoli, G. L. Chiarotti, M. Cococcioni, I. Dabo, A. Dal Corso, S. de Gironcoli, S. Fabris, G. Fratesi, R. Gebauer, U. Gerstmann, C. Gougoussis, A. Kokalj,

M. Lazzeri, L. Martin-Samos, N. Marzari, F. Mauri, R. Mazzarello, S. Paolini, A. Pasquarello, L. Paulatto, C. Sbraccia, S. Scandolo, G. Sclauzero, A. P. Seitsonen, A. Smogunov, P. Umari, and R. M. Wentzcovitch, J. Phys. Condens. Matter **21**, 395502 (2009).

[165] S. Ninova, V. Lanzilotto, L. Malavolti, L. Rigamonti, B. Cortigiani, M. Mannini, F. Totti, and R. Sessoli, J. Mater. Chem. C **2**, 9599 (2014).

[166] S. Gangopadhyay, A. E. Musunov, and S. Kilina, J. Phys. Chem. C **118**, 20605 (2014).

[167] H. Lin and D. Truhlar, Theoretical Chemistry Accounts **117**, 185 (2007).

[168] A. Laio and F. F. L. Gervasio, Reports Prog. Phys. **71**, 126601 (2008).

[169] R. Zhou, Methods Mol. Biol. **350**, 205 (2007).